CYCLIC SIMPLE SHEAR BEHAVIOUR OF COWDEN TILL

by

ZHENGHUI (MARK) QIU



A thesis submitted for the degree of

Doctor of Philosophy

at the University of Oxford

Wolfson College, Hilary Term 2023

Abstract

Cyclic Simple Shear Behaviour of Cowden Till

A thesis submitted for the degree of Doctor of Philosophy

Zhenghui (Mark) Qiu
Wolfson College, Oxford
Hilary Term 2023

Offshore wind turbines (OWT) are subject to complex cyclic loads throughout their design life. This includes loads induced by the wind and waves as well as the turbine operation. The interaction of the structure and the soil on which the OWT is founded is fundamental in geotechnical design situations. Several studies have investigated unidirectional cyclic loading of OWT foundations at high amplitudes, but this is not representative of the loads experienced by an OWT, which are generally random and multidirectional. Published data on high-quality multidirectional soil element tests are limited, meaning their effects or impact are yet to be addressed in current design methods.

The material investigated in this thesis, known as Cowden till, is a stiff, low plasticity, highly overconsolidated glacial till, a type of soil commonly encountered in the North Sea. This research explores the behaviour of Cowden till under cyclic loading. Therefore, a test plan using a novel multidirectional direct simple shear apparatus was devised to investigate these effects at element scale. The apparatus features orthogonal actuators situated on the horizontal plane which can apply complex load or displacement paths by adjusting the frequency, cyclic amplitude and mean load. Furthermore, realistic user-defined storm load histories are also able to be simulated. The test programme began with standard monotonic direct simple shear tests to characterise the undrained shear strength profile of the site. Next, cyclic tests ranging from standard unidirectional constant amplitude to more complex multidirectional and multi-amplitude cyclic loading tests were performed.

The experimental results were used to calibrate a multi-surface kinematic hardening model formulated in the Hyperplasticity framework and then used to predict the behaviour of the soil under complex cyclic loading scenarios, including realistic storm loading tests. Furthermore, the experiments were used to evaluate the performance of the underlying components of the model. This made it possible to identify the key components affecting the soil's response to realistic cyclic loading, thus providing a basis for improved offshore foundation design.

Acknowledgements

For their constant guidance and support, I would like to thank my supervisors Professors Byron Byrne and Chris Martin. This work would not have been possible without them. I am deeply grateful and consider myself lucky to have been given such an opportunity. I also want to express my gratitude to my former supervisor at the University of Cape Town, Prof. Denis Kalumba, for encouraging me to take up the studentship.

I would like to thank the team at Fugro, Wallingford, for providing me with training and accommodating my research interests. In particular, I thank Dr Amin Rismanchian for his useful advice on advanced element testing during my time there. Thanks, must also go to Yusuke Suzuki from NGI for providing wired-reinforced membranes and helpful suggestions.

The experience at Oxford has been truly enriching and I thank all those involved. From the department, I thank Dr Wayne Wu for his enthusiasm over monopiles and discussions on rate effects, Sarah Martin for her medium-scale field test data, and Dr Jamie Crispin for his support with calibrating the constitutive model and advice on optimising my Python script. I am also grateful to Dr Jonathan White for his assistance in the lab and to Dr Toby Balaam for his help with all things Hyperplasticity. Furthermore, I want to thank friends in the Jenkin building who were always up for a discussion about anything, which was much appreciated on days when testing did not go so well. I am also thankful to Alison May for her help in procuring various items in the lab. Special thanks must also go to the REMS contingent for this memorable experience, and Ørsted and the EPSRC for their financial support.

Outside of the department, I am thankful to the many friends who have supported me during my time at Oxford, those at Wolfson College, those back home in South Africa, and those friends elsewhere in the world. Finally, I want to thank my parents, brother and sister for always being there for me. This doctorate is just as much mine as it is yours. Last but not least, to my wonderful partner, May Wun Cheung, thank you for all that you do for me. I could not have done this without you.

Contents

Chapter 1 **8**

1 Introduction **8**
1.1 Background 8
1.2 Offshore wind turbine foundation development 9
1.3 Loading on offshore wind turbine foundations 10
1.4 Design of monopile foundations under lateral loading 12
1.4.1 API/DNVGL method 12
1.4.2 PISA method 13
1.5 PICASO Project 14
1.6 Research objectives 15
1.7 Thesis outline 16

Chapter 2 **18**

2 Literature review **18**
2.1 Introduction 18
2.2 Monotonic loading 18
2.2.1 Framework for clay behaviour 18
2.2.2 Critical state concept 19
2.2.3 Stress-strain behaviour in direct simple shear apparatus 21
2.2.4 Stress distribution 23
2.2.5 Failure states in direct simple shear 25
2.2.6 Rate effects in cohesive soils 29
2.3 Cyclic loading 30
2.3.1 Cyclic loading framework for simple shear tests 30
2.3.2 Factors affecting cyclic behaviour 33
2.3.3 Stiffness and energy loss factor 35
2.3.4 Multidirectional and multi-amplitude loading 37
2.3.5 Realistic storm loading at element scale 42
2.4 Soil constitutive model 43
2.4.1 Hyperplasticity framework 43
2.4.2 Evolution of multi-surface kinematic hardening model 46
2.5 Summary 49

Chapter 3 **50**

3 Apparatus description **50**
3.1 Introduction 50
3.2 Variable direction dynamic cyclic simple shear apparatus (VDDCSS) 50
3.2.1 Equipment overview 50
3.2.2 Sample size and preparation for DSS tests 52
3.3 Test procedure 54
3.3.1 Setup 55

3.3.2 Saturation 56
3.3.3 Consolidation 56
3.3.4 Static shear 57
3.3.5 Cyclic stage 58
3.4 Commissioning of VDDCSS 58
3.4.1 System corrections 59
3.4.2 Lateral stress measurement 63
3.4.3 Wired reinforced membrane 66
3.4.4 VDDCSS cyclic control 66
3.4.5 Validation and repeatability 67
3.5 Supplementary element tests 69
3.5.1 Oedometer apparatus 70
3.5.2 Triaxial apparatus 71
3.5.3 Equipment specification 75
3.6 Summary 76

Chapter 4 **77**

4 Site description and soil characterisation **77**
4.1 Introduction 77
4.2 Cowden till formation 77
4.3 Soil sampling 80
4.4 Sample quality 82
4.5 Index properties of test material 84
4.6 Grading and composition 86
4.7 CPT profiles 87
4.8 Estimate of undrained shear strength, K_0 and OCR 88
4.9 Soil sensitivity 91
4.10 Summary 92

Chapter 5 **93**

5 Monotonic testing of Cowden till **93**
5.1 Introduction 93
5.2 Testing programme 94
5.3 1-D compression results 97
5.3.1 Oedometer test programme 97
5.3.2 Behaviour of Cowden till in 1D compression 99
5.3.3 Swelling sensitivity 101
5.3.4 Coefficients of compressibility, consolidation, and permeability 102
5.4 DSS test results 104
5.4.1 Constant volume NL tests in upper soil (RL: 10.8 to 6.0m) 107
5.4.2 Constant volume OL tests in upper soil (RL: 10.8 to 6.0m) 108
5.4.3 Constant volume NL tests in lower soil (RL: 6.0 to -5.0m) 109
5.4.4 Constant volume OL tests in lower soil (RL: 6.0 to -5.0m) 110

5.5 General observations of DSS tests across depth profile 111
5.5.1 Stress-strain behaviour and the effect of confining stress 111
5.5.2 Pore pressure response 113
5.5.3 Effect of shearing rate 114
5.5.4 Effect of sample confinement method 117
5.6 Stress distribution and lateral stress estimation in DSS tests 120
5.7 Triaxial test results 123
5.7.1 Triaxial test programme 123
5.7.2 Test results 124
5.7.3 General observations 127
5.7.4 Comparison with DSS results 129
5.8 Stiffness estimate 133
5.9 Undrained shear strength profile of PICASO Cowden site 138
5.10 Summary 143

Chapter 6 **145**

6 Cyclic simple shear tests **145**
6.1 Introduction 145
6.2 Test plan 145
6.3 Standard cyclic simple shear tests (CSS) 147
6.3.1 Test programme 148
6.3.2 Test schedule results and general observations 148
6.3.3 Strain accumulation and cycles to failure 155
6.3.4 Post-cyclic behaviour 159
6.3.5 Stiffness degradation 160
6.3.6 Energy loss factor (damping behaviour) 163
6.3.7 Cyclic contour diagrams 164
6.4 Perpendicular cyclic simple shear tests (PCSS) 166
6.4.1 Test programme 166
6.4.2 Test schedule results and general observations 168
6.4.3 Strain accumulation 170
6.4.4 Stiffness degradation and energy loss factor 173
6.5 Random loading cyclic simple shear tests (RCSS) 176
6.5.1 Test programme 177
6.5.2 Test schedule results and general observations 178
6.5.3 Strain accumulation 180
6.5.4 Stiffness degradation 182
6.6 Random packaged cyclic simple shear tests (RPCSS) 182
6.6.1 Test programme 183
6.6.2 Test schedule results and general observations 186
6.6.3 Strain accumulation 186
6.6.4 Post-cyclic behaviour 188
6.6.5 Stiffness degradation 189

6.7 Challenge cyclic simple shear tests (CCSS) 190
6.7.1 Test programme 190
6.7.2 Test schedule results 191
6.8 Comparison of the VDDCSS tests with medium-scale field test results 192
6.8.1 Outline 192
6.8.2 Ratcheting comparison 194
6.8.3 Stiffness degradation comparison 195
6.8.4 Energy loss comparison 196
6.8.5 Random loading tests 197
6.8.6 Scaling potential 200
6.9 Summary 200

Chapter 7 **202**

7 Soil constitutive modelling **202**
7.1 Introduction 202
7.2 Numerical implementation 203
7.3 Validation of model 204
7.4 Calibration of model 206
7.4.1 Calibration procedure 206
7.4.2 Sensitivity study 215
7.4.3 Selected calibration parameters 221
7.5 Performance and predictions of model 223
7.5.1 Synthesising cyclic contour plots 223
7.5.2 Complex cyclic loading predictions 224
7.5.3 Discussion 233
7.6 Summary 235

Chapter 8 **237**

8 Conclusions and recommendations **237**
8.1 Introduction 237
8.2 Major contributions 237
8.3 Future work 240

References **242**

Appendix A **251**
Model backbone recalibration by Crispin et al. (2022) 251

Chapter 1

Introduction

1.1 Background

Europe is one of the world leaders in wind energy and is set to increase its wind power capacity by an average of 21 GW p.a. over the next three years, giving 318 GW of installed capacity by 2025 (see Figure 1-1). The rapid growth of this sector is fuelled by international pressure to reduce CO_2 emissions and limit the rise in global temperatures by 2°C as outlined in the 'Paris Agreement', a global framework aimed at avoiding dangerous climate change (United Nations, 2015). Europe, in particular, aims to cut greenhouse gas emissions by 55% by 2030 in its quest for climate neutrality by 2050 (Wind Europe, 2021a).

Of the total installed wind turbines in the UK, offshore wind turbines (OWTs) account for 49% of the operational capacity and have continued to increase in production year on year (RenewableUK, 2022). The benefits of OWTs include higher energy yield, stable energy production, and fewer size limitations. As a result, bidding for OWT projects has become increasingly competitive (4C Offshore, 2019). With the increased demand showing no signs of slowing down, it has become pertinent to reduce the levelised cost of electricity (LCOE) by improving OWT design and construction methods.

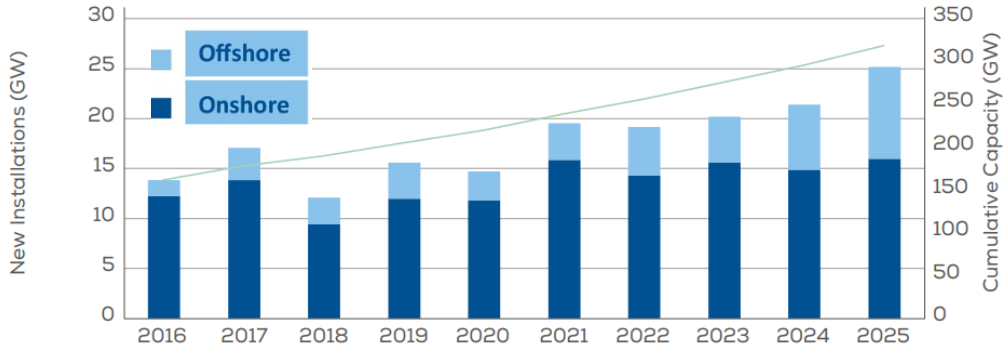


Figure 1-1: New and cumulative wind turbine installations in Europe and forecasts up to 2025
Source: (Wind Europe, 2021b)

With foundations contributing a significant cost component of OWTs, their design has had significant focus within the industry. Predictions of foundation behaviour are typically made using numerical modelling techniques, such as finite element analysis (FEA). These techniques require selecting and calibrating suitable constitutive models that describe the mechanical behaviour of soils. However, for soils subjected to complex cyclic loads, including the multidirectional and multi-amplitude loads that are imposed on OWT foundations, these constitutive relationships are not as well developed as those for unidirectional loads. Therefore, an extensive database of high-quality experimental tests to investigate this type of loading is needed, from which existing constitutive models may be calibrated and improved constitutive models can be developed.

1.2 Offshore wind turbine foundation development

The majority (~80%) of the installed and planned offshore wind turbine foundations have been founded on monopile foundations (BVG Associates, 2019). Over time these tubular structures have become larger, in both diameter and length, to accommodate the increased size of current and future wind turbines. However, advancements in design methods, such as those from the PISA project (Byrne et al., 2015), and the expanding market suggest that finding a balance is essential. This involves optimising monopile size to accommodate larger turbines while ensuring an efficient design and reducing the Levelized Cost of Energy (LCOE). These factors have driven the push for better design methods for OWT monopile

foundations. While other foundation types (e.g. suction caissons, gravity-base, floating wind turbines moored with anchors) as shown in Figure 1-2, have gained traction in deeper waters, their numbers are reasonably modest in comparison. However, as these turbines become larger, going from 2MW turbines back in 2000 to turbines >10MW today (IRENA, 2019; Wind Europe, 2019), the monopile-type foundation will inevitably reach a limit, particularly for developers that need to exploit deeper waters for installation. Furthermore, countries such as Japan and USA have few shallow-water sites (IRENA, 2019). This is a major limitation of the monopile, as increasing its size to accommodate these factors has extreme knock-on effects on its fabrication, transportation, installation, and economic viability. Nonetheless, while offshore monopile foundations may not be the right choice for deeper sites, for many sites now and in the future, they will remain the economic choice. Nevertheless, it is useful to highlight how this may change in a rapidly evolving market.

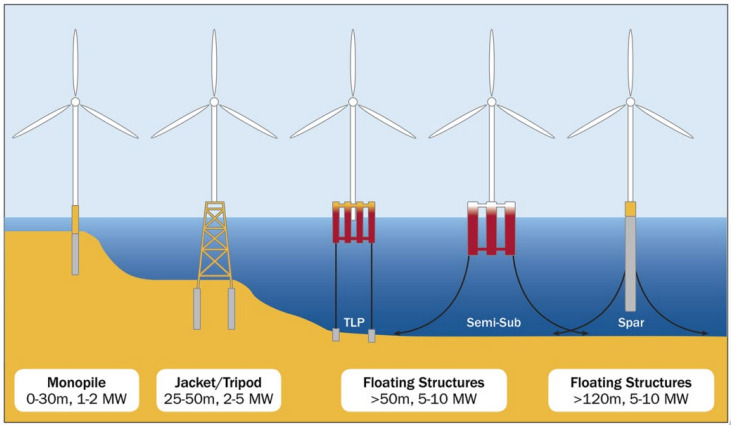


Figure 1-2: Types of offshore wind turbine foundations
Source: (Bailey et al., 2014)

1.3 Loading on offshore wind turbine foundations

An OWT foundation is subjected to loads induced by its self-weight, wind and waves as well as turbine operation (see Figure 1-3(a)). At the foundation level, seen in Figure 1-3(c), these load components are presented in terms of combined horizontal (H), vertical (V) and moment (M) loading. Typical dynamic loads under working conditions arise from wind, waves and rotor action. When combined, the loads are considered to be pseudo-random,

increasing and decreasing with time as shown by the example in Figure 1-3(b). While also referred to as cyclic loading, these loads are irregular and complex due to variations in loading frequency, magnitude of loading, directionality and eccentricity (M / H) (Balaam, 2021). Out of the three dynamic loads, waves are usually the dominant cyclic component with a cyclic frequency of around 0.1 Hz (Richards, 2019). Dynamic loads arising from seismic action may also be a design consideration in some regions of the world, but this type of loading is not common in the North Sea.

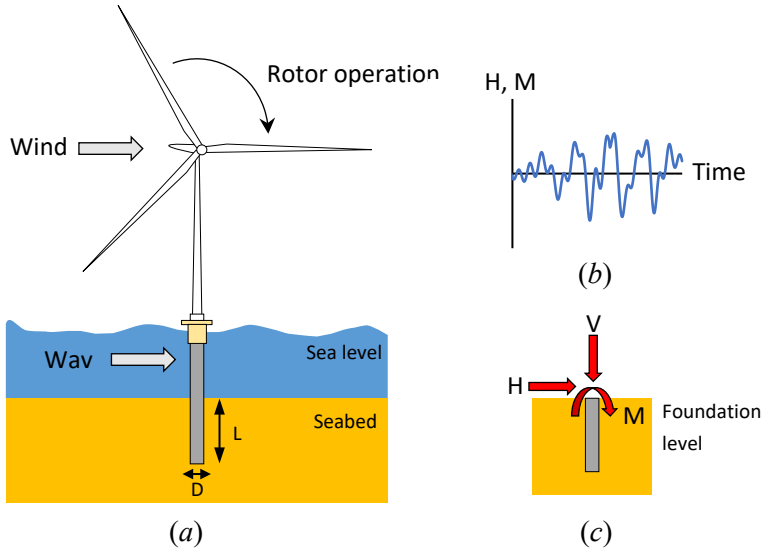


Figure 1-3: Illustration of (*a*) loading on OWT monopile foundation, (*b*) example of pseudo-random cyclic loading and (*c*) idealised combined Moment, Vertical and Horizontal load Modified from (Balaam, 2021)

Monopile foundations are simple in design and vary according to their embedded length L, diameter D, and wall thickness t. Monopiles currently have diameters up to 10m, lengths ranging from 30 to 40m, and thicknesses that can be as much as 150 to 200 mm, with the next generation of OWTs expected to have foundations with even larger dimensions (Byrne et al., 2020). The parameters are chosen to limit horizontal displacement u and rotation θ, and withstand material yield and failure of the pile according to criteria based on design standards such as the DNVGL-ST-0126 standard 'Support structures for wind turbines' (DNVGL-ST-0126, 2016).

The research also focusses on the directionality of realistic wind and wave loads. Figure 1-4 presents the wind and wave spatial distributions for an example site located in the Dutch North Sea (Fischer et al., 2010). While site-specific, all sites are exposed to multidirectional environmental loading (Richards, 2019). Additional complexities include the potential misalignment between wind and wave loading, and the variation in load amplitude with time.

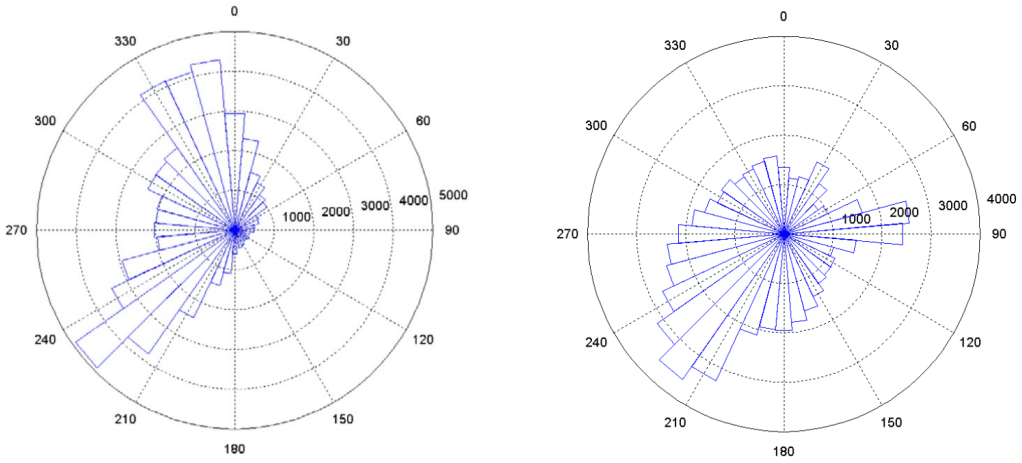


Figure 1-4: Example of (*a*) wind and (*b*) wave direction distribution in the North Sea
Source: (Fischer et al., 2010)

1.4 Design of monopile foundations under lateral loading

1.4.1 API/DNVGL method

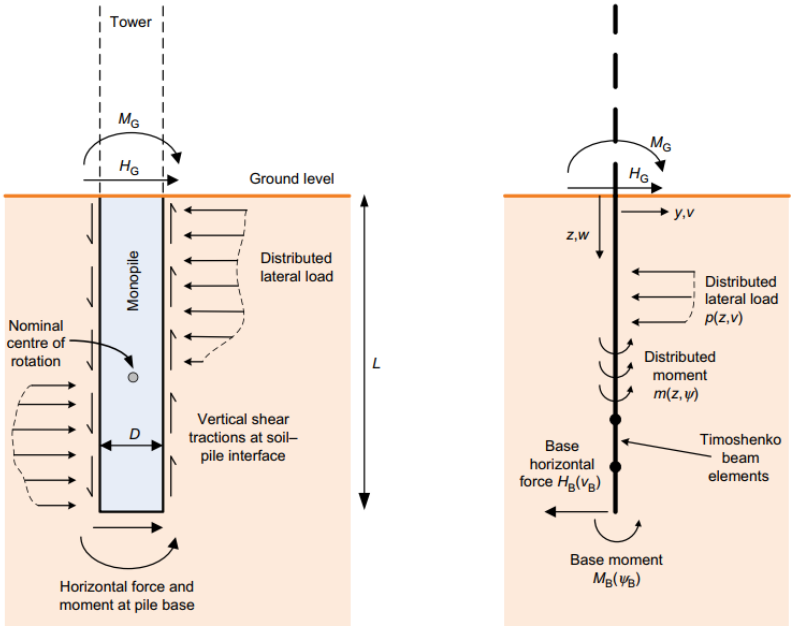
Monopile foundations subjected to lateral loads are typically designed using the *p*-*y* method originally developed for the offshore oil and gas industry (Matlock, 1970; Reese et al., 1974). This method treats the pile as a beam supported by non-linear independent springs along its length, where the spring force per unit length (p) is described as a function of the local lateral deflection (y). However, current forms of the method (i.e. as specified in DNVGL(2016) and API (2011)) are considered to have significant limitations when applied to OWT monopiles which generally have low L/D (< 6) ratios (Byrne et al., 2017).

The combined action of dynamic loads can cause OWT monopile foundations to accumulate rotations and lateral displacement, affecting the strength and stiffness of the surrounding soil due to accumulation of pore water pressures, which may not have enough

time to dissipate during a loading cycle. Current industry practice such as that set out in Appendix F.2 in DNVGL(2016) or 8.5 in BS EN ISO 19901-4:2016 (i.e. the UK implementation of API (2011)) addresses cyclic loading by presenting modified *p-y* curves with a reduced soil resistance at a given displacement using empirical factors.

1.4.2 PISA method

The PISA project was a joint industry study aimed at developing a new design method for monopile foundations under monotonic lateral loading. The project consisted of field testing and site characterisation, 3D finite-element modelling and 1D model development (Byrne et al., 2015; Burd et al., 2017; Byrne et al., 2020; Zdravković et al., 2020). The PISA method builds on the simplicity of the *p-y* method in the form of a new 1D beam model with additional components (i.e. a distributed moment *m* along the length of the pile, a horizontal force H_B and a moment M_B acting on the pile base – illustrated in Figure 1-5) to improve its performance.



(*a*) (*b*)

Figure 1-5: PISA design model: (a) idealisation of the soil reaction components acting on the pile (b) 1D finite-element implementation of the model showing the soil reactions acting on the pile Source: (Byrne et al., 2020)

A conic function is used to define the soil reaction curves within the PISA design model, whereby the parameters in the function are calibrated using site-specific 3D finite element models to accommodate different soil conditions. The calibrated 1D model shown in Figure 1-5(b) allows for an improved prediction of the ultimate monotonic response over the conventional *p-y* method (Byrne et al., 2020). The PISA project recognised the importance of establishing the monotonic response correctly before any progress on cyclic loading could be made. Following the success of PISA, a new project (next section) is currently underway to extend the model to accommodate cyclic loading.

1.5 PICASO Project

The research described in this thesis forms part of a greater framework of work undertaken at the University of Oxford through the Pile Cyclic Analysis (PICASO) project, a collaborative project between Ørsted and Oxford to develop new geotechnical design methods for offshore wind turbine foundations, with a specific focus on the cyclic lateral loading of monopiles (Byrne et al., 2020). The project aims to advance the design of OWT monopile foundations through model tests, theoretical developments, laboratory testing and advanced foundation modelling, with a specific focus on cyclic loading, Figure 1-6(a). The project follows on from the successful PISA project, which has led to significant cost savings for installed OWTs (Ørsted, 2019).

The PICASO project has involved field testing of medium-scale monopiles at a clay site with a high water table to simulate the conditions and loads relevant to a full-scale OWT monopile. The project consists of five main work packages highlighted in Figure 1-6(a). The research presented here falls under the work package “Calibration methods” and involves improving current design methods by linking mathematical or numerical models to soil element and medium-scale field tests. The laboratory work in this project is used to characterise the clay site, provide soil strength parameters for advanced foundation

modelling, and to serve as an input for the field-testing predictions. As a result, the project deliverables include a database of element tests (Figure 1-6(b)), and a calibrated soil constitutive model capable of capturing cyclic loading behaviours at soil element level.

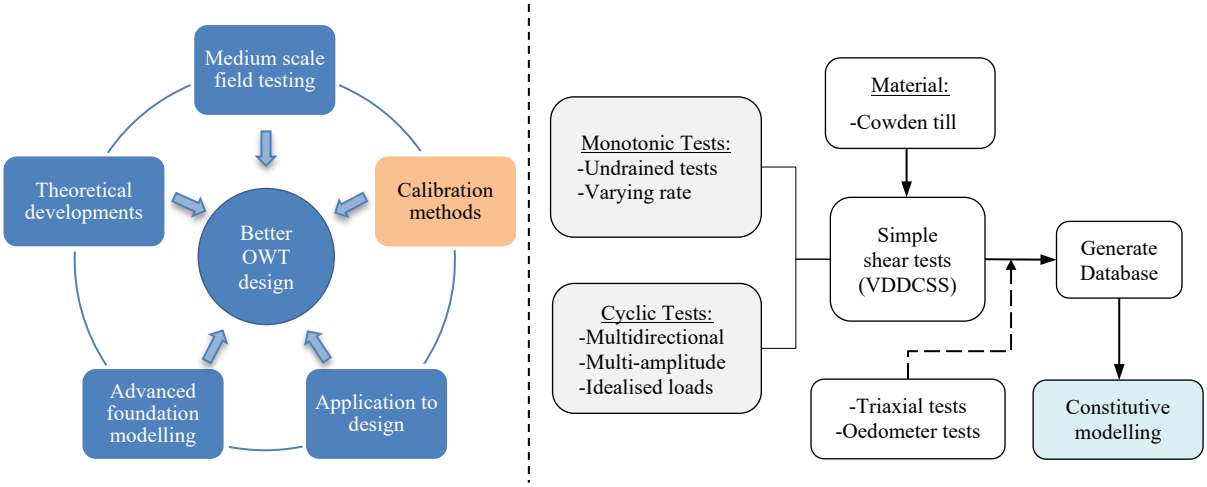


Figure 1-6: (a) Outline of work within the PICASO project and (b) overview of research

1.6 Research objectives

The experimental programme set out in this thesis aims to predict the behaviour of monopiles subjected to complex cyclic loading through the interpretation of advanced soil element testing. The work makes use of a Variable Direction Dynamic Cyclic Simple Shear (VDDCSS) testing system, specially manufactured by GDS Instruments for the University of Oxford. The device is used to generate an extensive test database to calibrate and validate an advanced soil constitutive model. The model is assessed according to its performance in capturing the following behaviour:

1) The elastic-plastic behaviour of soils during short and long-term cyclic loading;
2) Cyclic behaviours due to multidirectional and multi-amplitude loading and;
3) Rate effects.

The outcome of this work will allow for better design of OWT foundations, where the behaviour captured using the constitutive model will apply or be scalable to typical monopile geometries. Several databases of unidirectional cyclic element tests exist in the literature, but few include irregular multidirectional tests.

1.7 Thesis outline

The thesis is made up of eight chapters as follows:

Chapter 1 - Introduction to the research project, PICASO project, details on current offshore wind turbine (OWT) developments, loading and design methods for OWT monopile foundations, objectives and how the research fills the knowledge gap.

Chapter 2 - The literature review covers the fundamentals of soil mechanics for clays, looking into monotonic stress-strain behaviour, cyclic loading, and soil constitutive modelling. The chapter also covers the development of the direct simple shear test and its interpretation using current standards and best practice.

Chapter 3 - The novel variable direction dynamic cyclic simple shear (VDDCSS) device is introduced. The chapter covers the commissioning, specifications, modifications and test procedures following best practice. Furthermore, procedures and specifications for supplementary element tests are also covered.

Chapter 4 – This section covers the field test site details, the tested material (i.e. Cowden till) and preliminary site investigation works.

Chapter 5 - This chapter looks at the mechanical behaviour of Cowden till through advanced element testing. The tests focus on the key soil behaviours which include (*a*) rate effects, (*b*) anisotropy, (*c*) changes in OCR, (*d*) changes in stiffness, (*e*) stress dependency, and (*f*) 1-D compression behaviour. The tests are used to determine the undrained shear strength profile of the Cowden site, characterising the increase in strength with depth and variability of the tested tills.

Chapter 6 - This chapter explores unidirectional cyclic simple shear tests and more complex multidirectional and multi-amplitude cyclic tests. Realistic storm loading is also investigated. The behaviour of the specimens is analysed in terms of stiffness change and accumulated strains, while paying close attention to the load bias and stress reversal. The selected tests provide a comprehensive understanding of the cyclic simple shear behaviour of Cowden till, which is used to calibrate the constitutive model implemented in Chapter 7.

Chapter 7 - This chapter presents the implementation, validation, calibration and predictions of a multi-axial soil constitutive model formulated in the hyperplasticity framework. The model is used in a single-element context and is used to perform predictions of the key cyclic behaviours. In some cases, appropriate modifications are suggested to improve the model.

Chapter 8 - Conclusions and recommendations.

Chapter 2

Literature review

2.1 Introduction

Understanding the monotonic and cyclic response of fine-grained ‘cohesive’ soils is essential for the design of cost-effective offshore monopile foundations. For soils such as glacial tills, the geotechnical properties depend on their transport and sedimentation history, which are reflected in their structure. This chapter reviews various aspects of the behaviour of cohesive soils, such as their failure states, stiffness changes, associated modelling frameworks, and behaviour under cyclic loading. The chapter finishes with a brief review of the literature relevant to the hyperplastic constitutive model implemented in Chapter 7.

2.2 Monotonic loading

2.2.1 Framework for clay behaviour

Soils are complicated materials with behaviour dependent on their drainage conditions. For example, pronounced volume changes can occur under drained loading, but in undrained loading, volume changes are restricted, and excess pore pressures may develop. In the former, stress-dilatancy has a fundamental role in determining strength. The concept of dilatancy of granular materials was first described by Reynolds (1885).

Dilatancy provides a reasonable explanation of the relationship between the magnitudes of friction and dilation angles, allowing researchers such as Taylor (1948) and Terzaghi and Peck (1948) to explain the frictional and dilational components of strength for the angle of friction derived from the Coulomb theory. A further important contribution was made by Rowe (1962). One of the most popular stress-dilatancy relationships for clays is that adopted in the Cam-Clay model by Schofield and Wroth (1968). The original Cam-Clay model or modified Cam-Clay model are elastic-plastic strain hardening models based on the critical state concept and demonstrate how soils can deform and fail by different mechanisms, depending on the water content and the applied stresses.

An essential design parameter is the soil's undrained shear strength s_u, used during an undrained loading analysis to assess short-term stability. This is because the behaviour of cohesive fine-grained soils depends on the loading rate, where quick stress changes are typically modelled as undrained, while slow changes are assumed to be drained. Furthermore, the large-strain behaviour of clays is highly dependent on their stress history and clay content. This is evident in high OCR clays under undrained shearing. Clays with a low plasticity index (PI) demonstrate unstable shearing, whereas high *PI* clays undergo sliding to large strains and form shear bands (Jardine et al., 2004). For undrained compression triaxial tests on Cowden till, which has a high OCR and low *PI*, a well-defined deviator stress plateau occurs at strains of about 15-25% axial strain; bulging occurs but without any formation of shear bands (Ushev, 2017).

2.2.2 Critical state concept

When sheared to failure, all soils eventually tend to an ultimate condition in which plastic shearing continues indefinitely without changes in volume or effective stress. This phenomenon, known as the critical state (CS), was first discovered by Casagrande (1936) before it was developed into the well-known classical critical state framework (Roscoe et

al., 1963; Roscoe and Burland, 1968; Schofield and Wroth, 1968). The development of the framework was first intended for research on reconstituted ductile soils. Nevertheless, as seen in the work of Ushev (2017) and Lau (1988), natural soils with ductile properties, such as Cowden till, may still conform to the CS framework.

Casagrande (1938) introduced the concept of a critical void ratio *e* (or specific volume *v* = 1+e) during his studies on the liquefaction of granular soils, where the ratio follows the principles of CS such that when the change of volume remains constant, a critical void ratio is reached (Figure 2-1). This follows the tenet that a unique locus called the state boundary surface (SBS) is reached after large changes in strain. Within the classical framework, deformations within this locus can involve a combination of elastic and plastic behaviour, and the specific behaviour depends on the soil and loading conditions.

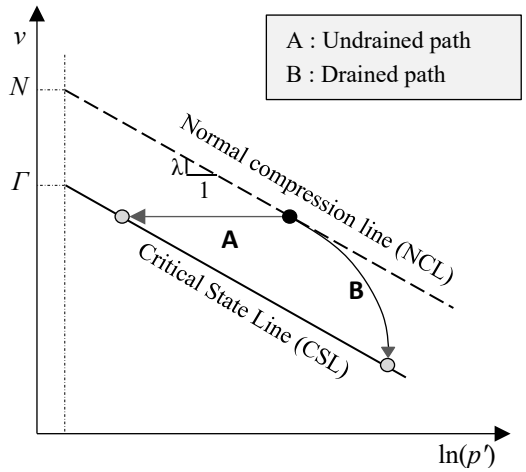


Figure 2-1: Illustration of critical void ratio in *v* – log (*p′*) space

The critical state model for isotropically compressed triaxial samples has been described in detail by Atkinson and Bransby (1978) and Wood (1990). Based on the 2D triaxial space, the framework for CS is defined in *v*-ln(*p′)* and *q*-*p′* spaces, where a critical state line (CSL) is formed. In the former space, the normal compression line (NCL) and CSL are presented as classical straight lines using:

$$NCL: v = N - \lambda \ln p' \quad (2\text{-}1)$$

$$CSL: v_{cs} = \Gamma - \lambda \ln p' \quad (2\text{-}2)$$

where N and Γ are the relevant specific volumes at $p' = 1$ kPa and λ is the slope. The CSL is observed as linear for cohesive soils, as shown in Figure 2-1 (Roscoe and Burland, 1968; Schofield and Wroth, 1968).

The critical state theory has seen many further developments since its inception, such as the state parameter framework by Been and Jefferies (1985). These continuous developments serve to enhance the robustness and precision of critical state models, positioning them as essential tools in geotechnical engineering for the comprehensive analysis of soil behaviour under diverse conditions.

2.2.3 Stress-strain behaviour in direct simple shear apparatus

Laboratory element tests are conducted on soil samples to determine their intrinsic behaviour and strength parameters. Under specific testing conditions (i.e. drained or undrained), measured values of stresses and strains are recorded, processed and used for geotechnical design. One of the most commonly used devices in the industry today is the direct simple shear (DSS) apparatus, due to its ease of use, small sample size, and short test durations.

The stresses in the soil around an OWT monopile foundation are complicated, and various stress paths can be followed. DSS tests are needed as they cover some of these paths, as shown in the simplified illustration in Figure 2-2(a). While only two instances of DSS conditions are depicted, the mechanism can manifest at different areas around the monopile, depending on the loading conditions. The simple shear device is an enhancement of the conventional direct shear box system. The latter device is one of the oldest forms of investigating the shearing resistance of soils. However, it has several disadvantages. These include shearing the sample along a predetermined failure plane, the unknown stress distribution within the box and the change in soil-on-soil contact area during shearing (Knappett and Craig, 2012).

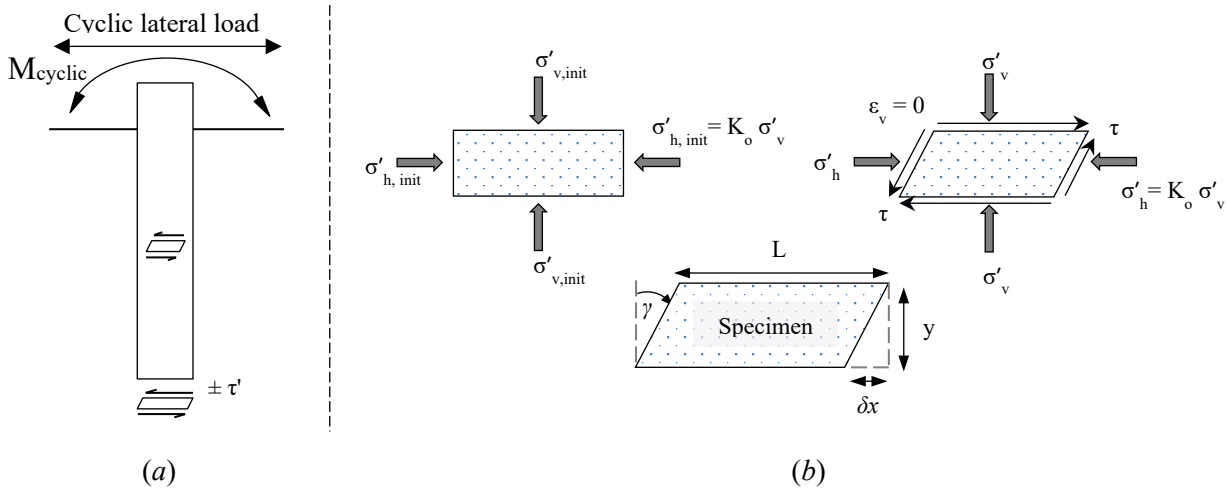


Figure 2-2: (*a*) DSS condition along monopile base and side (*b*) Stresses applied to DSS specimen

One of the earliest attempts at modifying the direct shear box into a simple shear apparatus was carried out by the Swedish Geotechnical Institute (SGI) in 1936 (Kjellman, 1951). In addition to the SGI device, a simple shear apparatus was developed by Roscoe (1953) at the University of Cambridge. The apparatus, later modified by Stroud (1971), consisted of metal flaps to provide lateral restraint and was connected to the top and bottom caps through hinges. Moreover, bespoke force-measuring instruments measured horizontal and vertical loads on the specimen, facilitating lateral stress measurement within the metal flaps. The instruments yielded precise readings, especially in the sample's central region, where stresses were assumed to be uniform (Li, 2018).

A third apparatus, developed by the Norwegian Geotechnical Institute (NGI), had similar attributes to the SGI apparatus but differed in terms of its confinement technique. Here, the sample was confined using a wire-reinforced rubber membrane to maintain a constant volume instead of a stack of rings (Airey and Wood, 1987). The DSS was developed to simulate plane strain conditions, where the element deforms only in one direction under a constant volume constraint (Bjerrum et al., 1966). During deformation, the sides of the specimen elongate whilst the height can be constrained to remain constant, thus maintaining constant-volume conditions. Unlike the triaxial device, the simple shear device

is typically not backpressure saturated and the pore pressures developed during shearing are not measured. Therefore, the excess pore pressures Δu for undrained conditions are generally inferred from changes in vertical stress $\Delta\sigma'_v$ during drained shearing at constant volume, as described in the work of Dyvik et al. (1987) and Bjerrum et al. (1966), where the approach was found to be valid for both granular materials and normally consolidated clays. While there is little information on how this relationship holds for overconsolidated soils, some evidence suggests that it may also be applicable (Andersen, 2015; Thian and Lee, 2017). Figure 2-2(b) shows the stresses acting on a simple shear specimen in at-rest and shear conditions. Since the sample is confined in the radial direction, the specimen is assumed to be subjected to K_o consolidation with the application of a vertical stress σ'_v. The shear stress τ and shear strain γ are given as:

$$\tau = \frac{F_{shear}}{A} \; ; \; \gamma = \frac{\delta_x}{y} \tag{2-3}$$

where F_{shear} is the measured shear force and A is the cross-sectional area. Various applied corrections, specific to the testing apparatus, are excluded in the formulae above but are addressed in Chapter 3.

2.2.4 Stress distribution

The purpose of a DSS test is to apply a pure shear strain deformation to a sample. However, the ideal pure shear strain (and hence pure stress) condition in a simple shear apparatus is rarely achieved due to boundary inconsistencies. These inconsistencies are attributed to the eccentricities developed between the top and bottom normal forces acting on the specimen, and the inability of current devices to provide complementary shear stresses at the vertical sides normal to the deformation plane. The imposed nonuniformities for both NGI and Cambridge-type apparatuses suggest that only the middle third of the sample demonstrates ideal pure shear state stress conditions, as illustrated in Figure 2-3 (Cole, 1967; Stroud, 1971; Airey, 1984; Budhu, 1984; Grognet, 2011; Li, 2016). Non-uniformities in DSS specimens

usually exist due to near-frictionless vertical boundaries that cannot develop complementary shear stresses (Wai et al., 2021). Ideally, the stresses and strains of the middle third core should be measured. However, DSS devices employed today only measure the responses from the boundaries of the specimen. From a practical standpoint, the specimen is assumed to be close enough to the pure shear stress state to justify the interpretation of results in the later chapters.

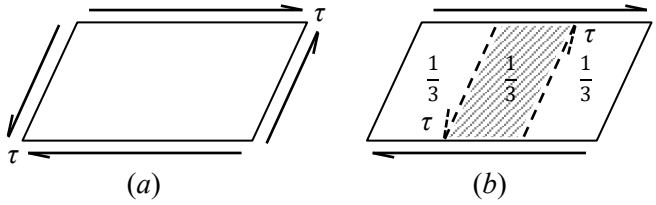


Figure 2-3: (*a*) Ideal simple shear state of stress (*b*) Determined simple shear stress state

Analytical methods have attempted to approximate the actual stress and strain fields in the past. For example, Roscoe (1953) conducted a mathematical analysis assuming a linear elastic material. His findings apply in the first stages of deformation but may also be used as a guide for behaviours at larger strains. Based on the stress state given in Figure 2-4, the stress distribution across an element of soil in a direct simple shear device can be interpreted, where *s* is the average shear stress applied to the sample.

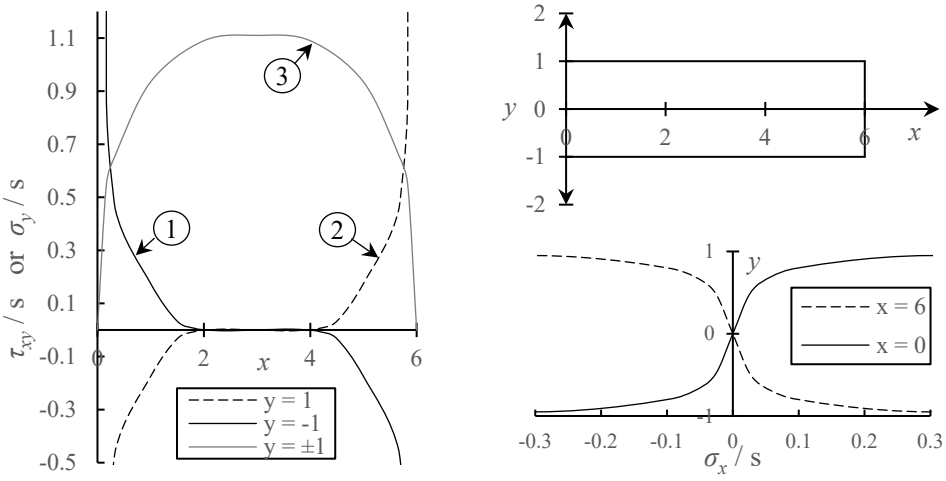
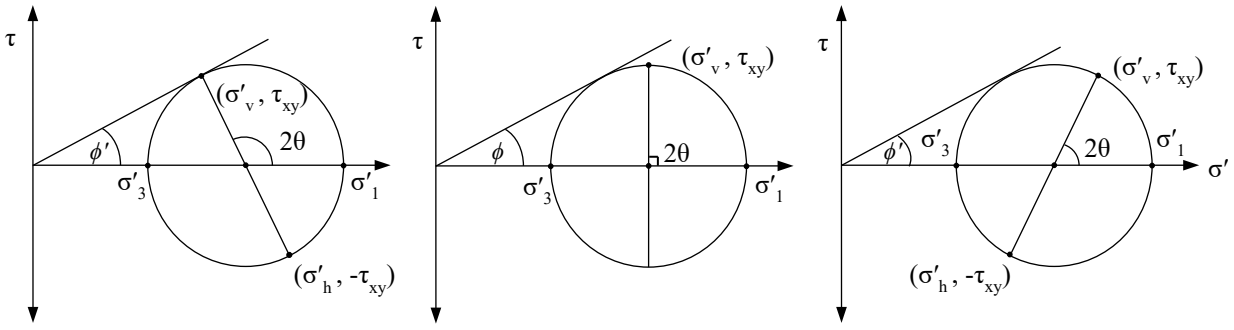


Figure 2-4: (*left*) Vertical (①+②) stresses and shear (③) stresses on upper and lower faces of sample (*top right*), sample boundary conditions and (*bottom right*) stresses on ends of the sample Modified from (Roscoe, 1953)

2.2.5 Failure states in direct simple shear

Determining the entire stress state of a specimen in a DSS apparatus is a widely debated topic. Conventional DSS systems provide the vertical effective stress σ'_v and shear stresses τ applied to the sample's surface. However, horizontal effective stresses are rarely measured in these systems as they require local sample instrumentation. Earlier studies using a Cambridge-type simple shear apparatus demonstrated how the complete stress state of a sample could be measured using instrumented load cells on the boundaries of the specimen (Roscoe, 1953; Cole, 1967; Stroud, 1971). Other authors who have made attempts at measuring lateral stress include Budhu (1979), Airey (1984) and Airey and Wood (1987). While these methods yield acceptable results, assuming that the maximum shear stress occurs on the horizontal plane due to stress non-uniformities along the sample boundaries, the solutions described by many authors do not satisfy equilibrium of boundary forces and moments, leading to different correction procedures to achieve equilibrium (Wood et al., 1979). Three different types of failure modes are generally considered for DSS-type devices. This includes:

1. The horizontal plane is the plane of maximum stress obliquity - Figure 2-5(a);
2. The horizontal plane is the plane of maximum shear stress - Figure 2-5(b);
3. The principal axes of stress coincide with the principal axis of strain, where the vertical plane is the plane of maximum stress obliquity - Figure 2-5(c).



(*a*) (*b*) (*c*)

Figure 2-5: Interpreted failure modes for direct simple shear test
Modified from (de Josselin de Jong, 1971)

The three failure mechanisms are assumed to be possible, and the selected mode is the one with the path of least resistance (de Josselin de Jong, 1971; Budhu, 1988). The failure mode in Figure 2-5(a) is commonly used as it provides conservative design parameters. However, the values of s_u can be misinterpreted in industry, and confused with the rare failure mode seen in Figure 2-5(b) due to a lack of local instrumentation. However, it can also be argued that the selection of Figure 2-5(b) provides a reasonable approximation of s_u. Furthermore, from the geometry of the failure modes, the shear stress measured from constant volume tests can be related to the undrained shear strength by:

$$\text{a: } s_u = \frac{\tau_{xy}}{\cos(2\theta - 90^\circ)} = \frac{\tau_{xy}}{\sin(2\theta)} \qquad \text{b: } s_u = \tau_{xy} \qquad \text{c: } s_u = \frac{\tau_{xy}}{\sin(2\theta)} \tag{2-4}$$

Alternatively, various theoretical and empirical methods have been proposed for estimating the stress state. These methods are briefly described and their application to overconsolidated soils such as Cowden till is discussed. Oda and Konishi (1974) performed simple shear tests on granular materials and observed the relationship:

$$\frac{\tau}{\sigma_v'} = k \tan\theta \tag{2-5}$$

where k is a material constant determined by the interparticle friction angle and θ is the inclination of the principal stress σ'_1 with the vertical axis. The method follows the distribution law of contact forces used to obtain the relations between the stress ratio $\frac{\tau}{\sigma_v'}$, the granular fabric and the orientation of the principal stress axes. This behaviour was confirmed by Wood et al. (1979), who performed constant volume DSS tests on Leighton Buzzard sand (LBS) at different initial void ratios and stress states. There is also evidence that Equation (2-5) may apply to normally consolidated soils, as suggested by Airey (1984). However, there is limited data on whether this method applies to overconsolidated soils. Combining Figure 2-5 and Equation (2-5), the principal stresses and horizontal stress can be formulated from the Mohr circle:

$$\sigma_1' = \frac{k\sigma_v'^2 + \tau^2}{k\sigma_v'} \tag{2-6}$$

$$\sigma_3' = (1-k)\sigma_v' \tag{2-7}$$

$$\sigma_h' = \frac{\tau^2}{k\sigma_v'} + (1-k)\sigma_v' \tag{2-8}$$

$$\sin\phi' = \frac{k^2 + \left(\frac{\tau}{\sigma_v'}\right)^2}{k(2-k) + \left(\frac{\tau}{\sigma_v'}\right)^2} \tag{2-9}$$

As stated by many authors, the physical definition of k is unclear (Oda et al., 1974; Budhu, 1979; Lau, 1988; Li et al., 2020). Ideally, the value of k would be determined for any material through an instrumented simple shear apparatus. However, in past practice, this was not possible and required other means of determining k. A method proposed by Ochiai (1975), assuming no volume change at critical state, suggests that the major principal stress σ'_1 is inclined at an angle θ = 45° to the vertical (Figure 2-6). Combining this assumption with Equation (2-5) gives

$$k = \frac{\tau}{\sigma_v'} = \frac{(\sigma_1' - \sigma_3')}{(\sigma_1' + \sigma_3')} = \sin\phi_{cv}' \tag{2-10}$$

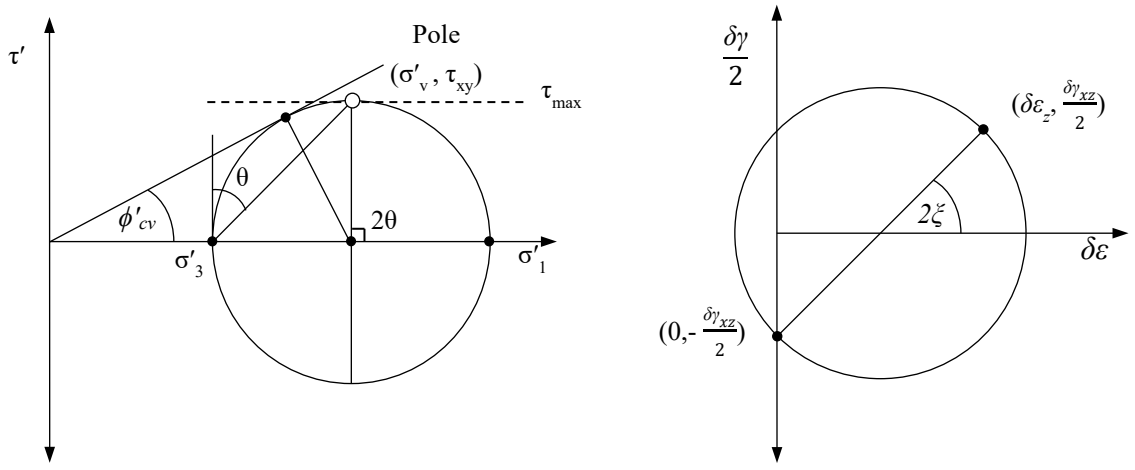
where ϕ'_{cv} is residual friction angle under constant volume conditions. While Cole (1967) found similar agreements using LBS in the Cambridge-type simple shear apparatus, Airey (1984) demonstrated that it underpredicts the value of k. Airey (1984) used both radial stress measurements and Equation (2-5) to determine the complete stress state of kaolin clay during shearing in a constant volume test. While radial stress measurements can be used to provide a reasonable estimate of the stress state, it must be noted that the measured radial stress σ'_r is not the same as the intermediate principal stress σ'_2 or horizontal stress σ'_h during shearing (Budhu, 1979).

An alternative to the method by Ochiai (1975), Budhu (1979) proposed a method of determining k through a drained type simple shear test (i.e. constant vertical stress). Assuming the principal axes of the stress increment coincide with the principal axes of the strain increment at the maximum normalised shear stress, k can be calculated as

$$k = \left| \frac{\tau_{max}}{\sigma'_{vc}} \cot \xi \right| \tag{2-11}$$

where ξ is the angle of rotation of the principal strain axes for a given increment. From Mohr's circle in Figure 2-6(b), the value of ξ can be determined. In a similar way to the previous method, Equation (2-11) was found to show good agreement for granular materials such as LBS (Li et al., 2020), but there is limited evidence of its use for overconsolidated clays, most likely due to the extensive testing durations required for drained tests on clay. Nevertheless, the relationship between k and ϕ'_{cs} was found to apply to most soils, as suggested by Lau (1988). This is supported by the work carried out by Airey (1984) for sands and kaolin, as seen in Figure 2-7. Equation (2-10), which was found to underpredict values of k, is also plotted. For this purpose, the use of Equation (2-5) would be preferred for this research.

In standard direct simple shear tests, the undrained strength s_u or failure shear stress τ_f is interpreted as the peak shear stress for cases with strain softening (Airey et al., 1987). The shear stress corresponding to some prescribed 'large' shear strain is reported for cases where no clear peak is observed. This strain is generally defined as a shear strain of 15% (Andersen, 2015), similar to the findings by Airey et al. (1987), where shear distortions were found to occur at 11% in constant volume tests for clay samples. However, Cowden till is a much more ductile material, exhibiting axial strain failures $\varepsilon_{a,f}$ in the triaxial apparatus at approximately ~17%, which corresponds to a shear strain at failure γ_f of 25% in the DSS, where for an undrained test $\gamma = 1.5\varepsilon_a$ (Erten and Maher, 1995). These findings are based on completed laboratory tests, where $\gamma_f = 25\%$ is adopted in Chapter 5.



(*a*) (*b*)

Figure 2-6: (*a*) Interpreted value of *k* based on constant volume DSS (*b*) Value of ξ from strain increment
Modified from (Lau, 1988)

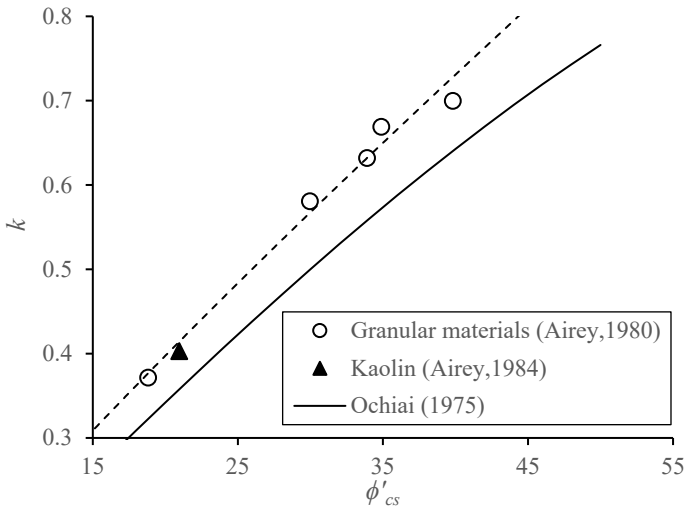


Figure 2-7: Relationship between *k* and ϕ'_{cs}

2.2.6 Rate effects in cohesive soils

The presence of rate effects in the straining or loading of soils has been known for more than 160 years. Early accounts of this behaviour, stretching from 1846-1959, have been summarised by Housel (1960). Past researchers investigated this effect for various purposes, including the effect of transient loads on structures imposed by earthquakes, explosions and traffic, or for the calibration of constitutive models (Seed and Lundgren, 1954; Tatsuoka et al., 2008). However, few have considered rate effects in analysing OWT monopiles subjected to pseudo-random loads. The s_u of cohesive soils typically increases with

increasing strain rate at approximately 6-15% per order of magnitude of strain rate (Kulhawy and Mayne, 1990; Mitchell and Soga, 2005; Mun et al., 2016). In contrast, the s_u of cohesionless soils is considerably less influenced by strain rate (Tatsuoka et al., 2008). Similarly, the effects of the shearing rate have been found to decrease with increasing overconsolidation ratio (OCR) for clays, as postulated in the research by Hight (1983) and Sheahan et al. (1996). For additional information on rate effects, refer to Wu's study (2022), which involved model piles tests on Cowden till.

2.3 Cyclic loading

In past studies, cyclic loading tests on soil samples have mainly been carried out using a triaxial apparatus to investigate the fundamental factors influencing liquefaction, a phenomenon often associated with seismic activity (Sha'al, 1972; Boulanger and Seed, 1995; Ghionna and Porcino, 2006). However, in the context of this project, cyclic loading is investigated in a simple shear device to understand the cyclic behaviour of the soil around an OWT foundation due to dynamic loads induced by wind and wave action.

2.3.1 Cyclic loading framework for simple shear tests

Cyclic loading is defined as the repeated application of stresses or strains to a structural component or element of material. Soil elements follow various stress paths depending on their location and are exposed to different combinations of average shear stress τ_{av} and cyclic shear stress $\tau_{cyc,}$ as defined in Figure 2-8(a). For realistic (pseudo-random cyclic) loading situations, the magnitude of the loading and period varies continuously from one cycle to another, thus varying the cyclic shear stress with each cycle (Andersen, 2015). The impact of cyclic loading on offshore foundations largely depends on the number of cycles experienced during storms and over the structure's operational life. The number of cycles can extend into the millions depending on the origin of the cyclic load, such as the case of nacelle rotor actions applied to wind turbine foundations (Jardine and Standing, 2012).

Like DSS tests, cyclic simple shear (CSS) tests generally employ either stress- or strain-controlled conditions, often normalised by the maximum undrained shear strength obtained from DSS tests. While offshore cyclic loads are generally irregular in nature, most cyclic soil element tests are restricted to shorter time frames and frequencies slow enough to allow precise control and data acquisition. Therefore, standard CSS tests employ regular sinusoidal loads at fixed frequencies. The loading is typically applied under undrained conditions, which is often considered to be the most critical case for offshore foundations (Ushev, 2017).

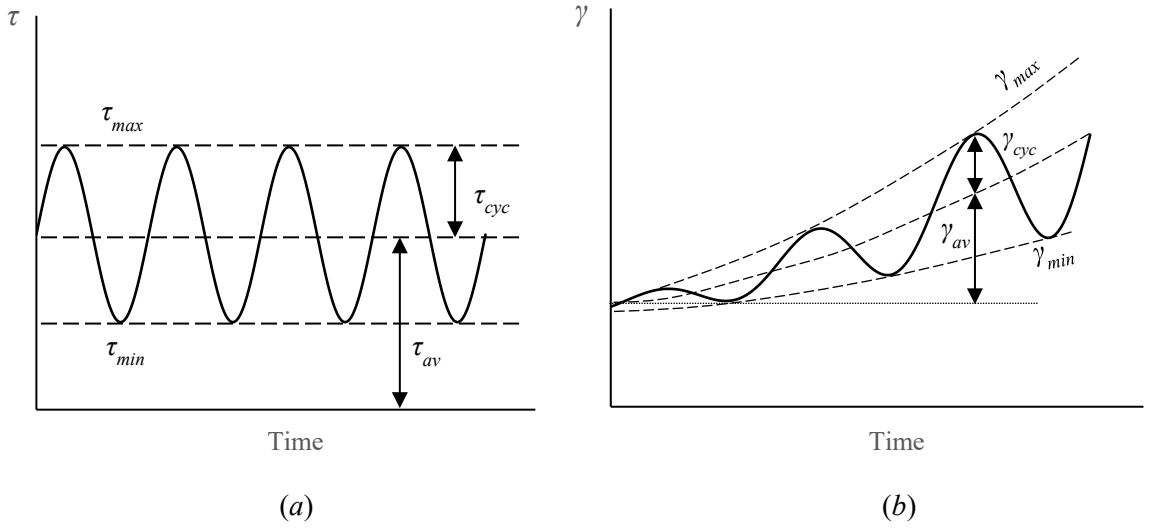


Figure 2-8: (*a*) Cyclic loading parameters (stress-controlled) (*b*) Cyclic stiffness estimation

Cyclic triaxial and cyclic simple shear tests are widely used in design for practical reasons and generally enforce reasonable approximations of the stress conditions determined from site (API, 2011; Andersen, 2015; DNVGL-ST-0126, 2016). The simple shear framework defines τ_{max} and τ_{min} as the maximum and minimum absolute loads. τ_{cyc} is defined as the cyclic amplitude. τ_{av} is the offset of the cycle from $\tau = 0$ kPa, indicating the magnitude of the load bias. τ_{max} and τ_{min} can be defined in terms of τ_{av} and τ_{cyc} as follows:

$$\begin{aligned} \tau_{max} &= \tau_{av} + \tau_{cyc} \\ \tau_{min} &= \tau_{av} - \tau_{cyc} \end{aligned} \tag{2-12}$$

From this definition, the load characterisation relationships as follows are often employed (LeBlanc et al., 2010; Abadie, 2015; Richards, 2019):

$$\zeta_b = \frac{\tau_{max}}{\sigma_{REF}} \quad , \quad \zeta_c = \frac{\tau_{min}}{\tau_{max}} \tag{2-13}$$

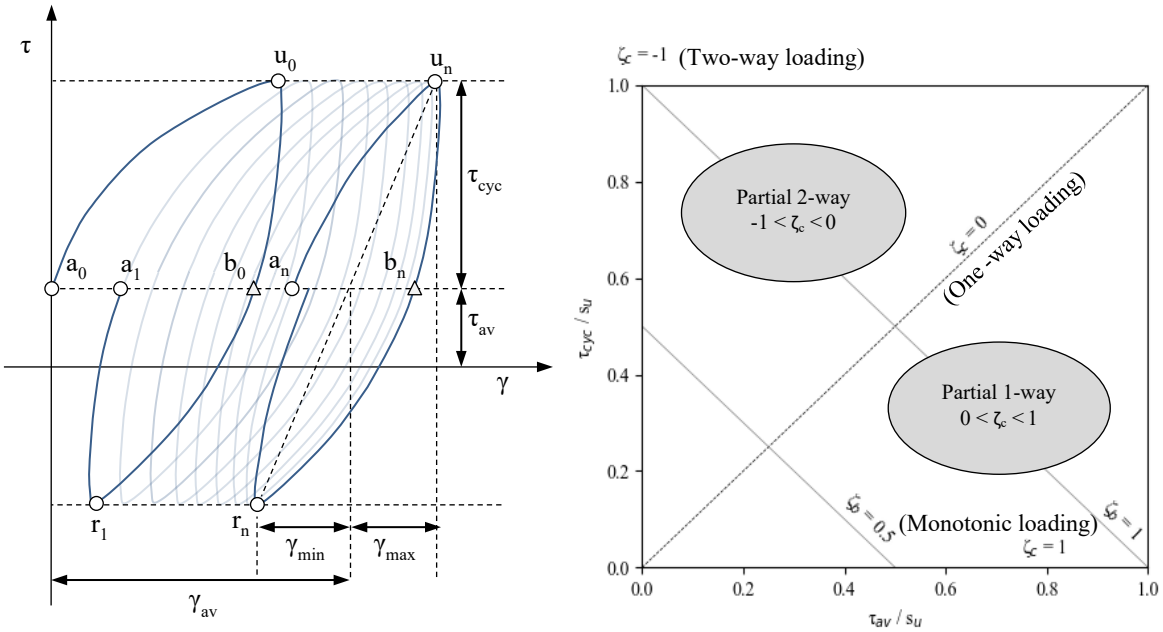
$$\tau_{cyc} = \frac{\tau_{max} - \tau_{min}}{2} \quad , \quad \tau_{av} = \frac{\tau_{max} + \tau_{min}}{2} \tag{2-14}$$

ζ_c indicates the degree of load reversal or loading symmetry, and ζ_b indicates the magnitude of the load applied. With these definitions, ζ_c is well-defined ($-1 \leq \zeta_c \leq 1$) and is independent of load direction, where it takes the value 1 for a static test, 0 for a one-way test and -1 for a two-way loading test (LeBlanc et al., 2010). The reference stress σ_{REF} can either be the monotonic undrained strength s_u or the pre-consolidation pressure of the sample σ'_{vc}, depending on the type of test performed. Cyclic loading tests can be divided into four categories: two-way, partial two-way, one-way and partial one-way, as labelled in the NGI style contour diagram (Andersen, 2015) in Figure 2-9(b). Examples of some of these loadings are shown in Figure 2-10.

Except for the case of two-way loading, permanent strain or ratcheting may develop under cyclic loading, as shown in Figure 2-9(a). In element testing, this strain accumulation is defined from the average strain γ_{av} measured mid-way between the maximum and minimum cyclic strains. However, while γ_{av} may decouple the ratcheting behaviour from changes in stiffness, the accumulated strain is not well defined. Therefore, based on the cyclic framework proposed by Balaam (2021), an alternative definition for ratcheting is used. Following Figure 2-9(a):

$$\gamma_{av,n} = \frac{1}{2}\left(\gamma(a_{n+1}) + \gamma(b_n)\right) \tag{2-15}$$

The above equation is preferred as γ is the average strain developed at τ_{av} on unloading and reloading. The definition also minimises the coupling of the change in hysteresis loop shape (i.e. stiffness) with ratcheting. Furthermore, ratcheting is taken to occur in the direction of the extreme load τ_{max}, except for the case of two-way loading, where $|\tau_{max}| = |\tau_{min}|$ (when this occurs, τ_{max} is defined in the direction of the initial loading).



(*a*) (*b*)

Figure 2-9: (*a*) Ratcheting definition (*b*) Cyclic loading characterisation
Modified from (Balaam, 2021)

2.3.2 Factors affecting cyclic behaviour

For undrained cyclic simple shear tests, the cyclic behaviour depends on both τ_{av} and τ_{cyc}, as evident in the three different types of failure for Dogger Bank sand shown in Figure 2-10 (Andersen, 2015). In the first test, cyclic shear strains developed with minor changes in permanent shear strains. As the shear stress passes through zero, the sand tends towards a liquefied state where the effective stresses are essentially zero. As a result, when the shear stress is increased, the shear strain increases significantly. The next test, with higher average shear stress (τ_{av} = 140 kPa), experiences a gradual increase in permanent strain, also known as ratcheting, while the cyclic strain shows no change. The final test, with τ_{av} = -140 kPa, behaves similarly to the previous test but on the extension side.

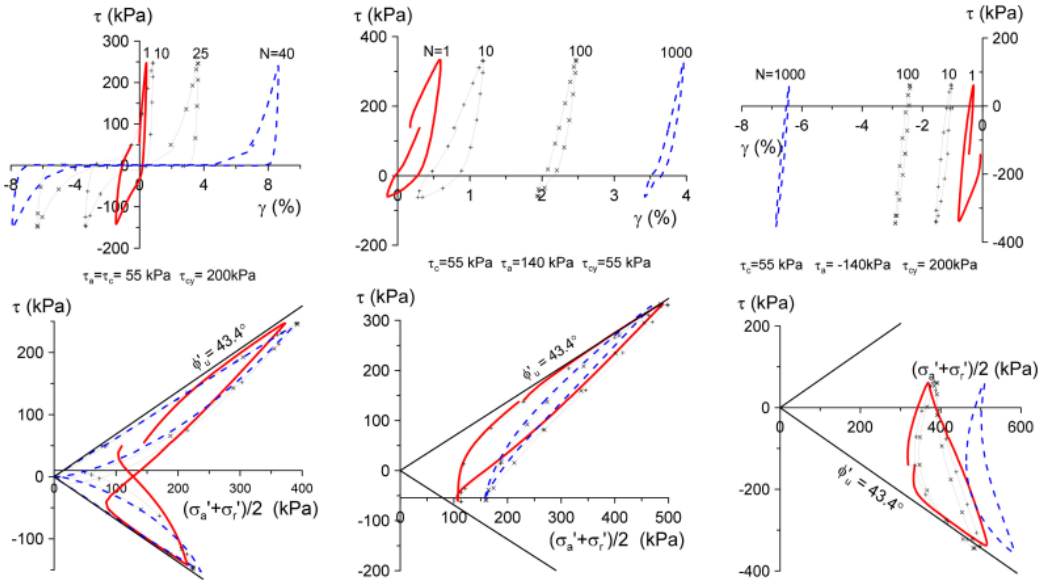


Figure 2-10: Stress-strain behaviour of dense Dogger Bank sand in DSS tests
Source: (Andersen, 2015)

Although not as apparent from the plots above, softening behaviour occurs as the number of cycles increases. This is better illustrated by the commonly used strain-contour plots for Drammen clay (Andersen, 2015), as given in Figure 2-11. An obvious observation is a decrease in the area enclosed by the plots with higher number of cycles. This is because the contours are constructed using static and cyclic test data at different ratios of τ_{av} and τ_{cyc}. In addition to the parameters above, cyclic loading behaviour in triaxial and simple shear tests is affected by various interacting factors. This includes the type of soil being tested, confining stress σ'_v, void ratio e, plasticity index (PI), degree of saturation (S), overconsolidation ratio (OCR), temperature, the number of cycles applied, creep duration and rate of loading.

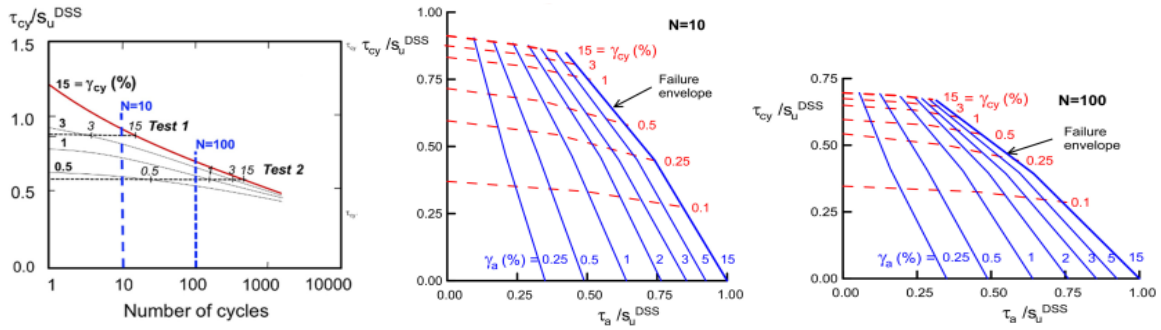


Figure 2-11: Softening behaviour of Drammen clay shown in cyclic contour plot
Source: (Andersen, 2015)

2.3.3 Stiffness and energy loss factor

The secant stiffness k_{sec} for a given cycle is generally defined using the loading stiffness k_l or unloading stiffness k_u, as illustrated in Figure 2-12(a). While this is well-defined for closed hysteresis loops (see Figure 2-12(b)), it is less so for cycles that experience ratcheting, where it is often coupled with stiffness change. Referring to Figure 2-12(a), terms such as the loading stiffness k_l (reloading point r_1 to unloading point u_1) or unloading stiffness k_u (unloading point u_1 to reloading point r_2) are commonly used to monitor the evolution of the secant stiffness with cycle number (Abadie, 2015; LeBlanc et al., 2010). A central cycle stiffness k_{sec} can be used to minimise the coupling between ratcheting and stiffness. The stiffness k_{sec} is defined as the inverse mean of k_l and k_u and was adopted from the definitions developed by Richards (2019) and Balaam (2021) to develop a consistent cyclic loading framework:

$$k_{sec} = 2\left(\frac{k_l k_u}{k_l + k_u}\right) \tag{2-16}$$

As the number of cycles increases, the mean stiffness k_{sec} may change; it generally increases for sands and often decreases for clays (Andersen, 2015; Beuckelaers, 2017; Richards, 2019). The behaviour directly affects the amount of stored elastic energy E_E per cycle, which in turn is used to quantify the amount of cyclic energy dissipation, quantified by a metric proportional to the ratio of hysteretic energy loss E_H to maximum stored elastic energy. For a closed hysteresis loop, the parameters are represented by the enclosed areas in Figure 2-12(b).

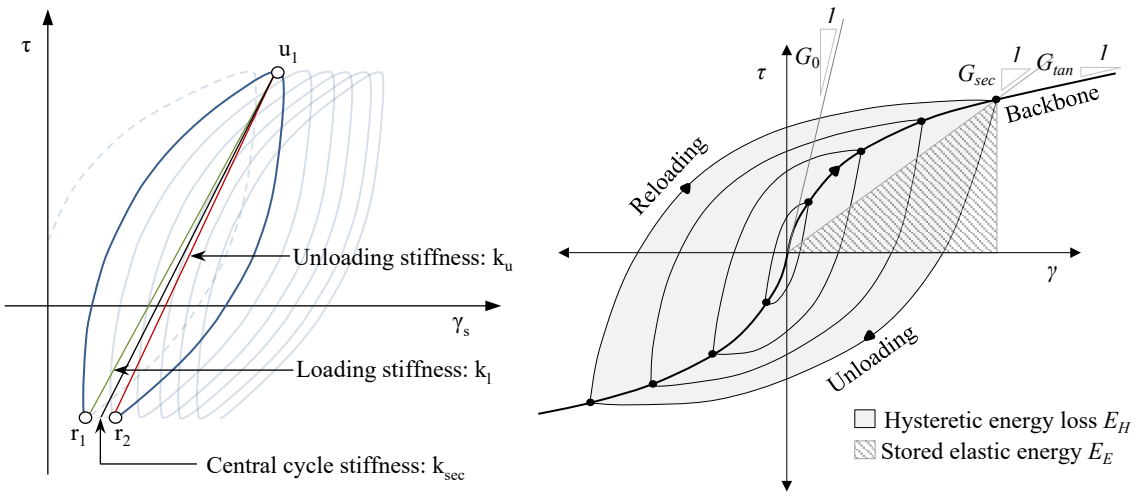


Figure 2-12: (*a*) Central cycle stiffness definition for open hysteresis (*b*) Stiffness definition for closed hysteresis loops

Energy dissipation in soil is often characterised by a 'damping ratio' ξ, which is often confused with the definition given in structural dynamics (i.e. ratio of viscous damping to critical damping). To avoid this and to be consistent with the literature, an alternative term known as the 'energy loss factor' η is used instead, given as (Inman, 2014; Balaam, 2021):

$$\eta = \frac{1}{2\pi}\frac{E_H}{E_E} \tag{2-17}$$

For 2-way cycling, the elastic energy (E_E) is defined as (see Figure 2-12(b)):

$$E_E = \frac{1}{2}\tau_{max}\gamma_{cyc} = \frac{(\tau_{max})^2}{2k_{sec}} \tag{2-18}$$

However, Equation (2-18) needs to be generalised for cases other than 2-way cycling, which can be done as follows (see Richards (2019)):

$$E_E = \frac{(\tau_{cyc})^2}{2k_{sec}} = \frac{(\tau_{max} - \tau_{min})^2}{8k_{sec}} \tag{2-19}$$

Many definitions for E_H are only valid for constant amplitude and one-way loading, reducing their applicability in this research project (Abadie, 2015). Balaam (2021) suggests the use of a more rigorous method by integrating the cycle response from reloading points r_n to r_{n+1} for cycle n to obtain the hysteretic energy loss E_H as:

$$E_H = \int_{r_i}^{u_i} \sigma d\varepsilon + \int_{u_i}^{r_{i+1}} \sigma d\varepsilon \tag{2-20}$$

such that a new energy loss factor η_I can be defined as:

$$\eta_I = \frac{1}{2\pi}\frac{E_H}{E_E} = \frac{4k_{sec}}{\pi(\tau_{max} - \tau_{min})^2}\left(\int_{r_i}^{u_i} \sigma d\varepsilon + \int_{u_i}^{r_{i+1}} \sigma d\varepsilon\right) \tag{2-21}$$

The definition η_I is the preferred method used in this project as it is the only definition consistent with the rigorous definition of hysteretic energy loss E_H for all general variations of non-closing loops. Further detail on the variation and the various definitions available can be found in Taborda et al. (2016) and Balaam (2021).

2.3.4 Multidirectional and multi-amplitude loading

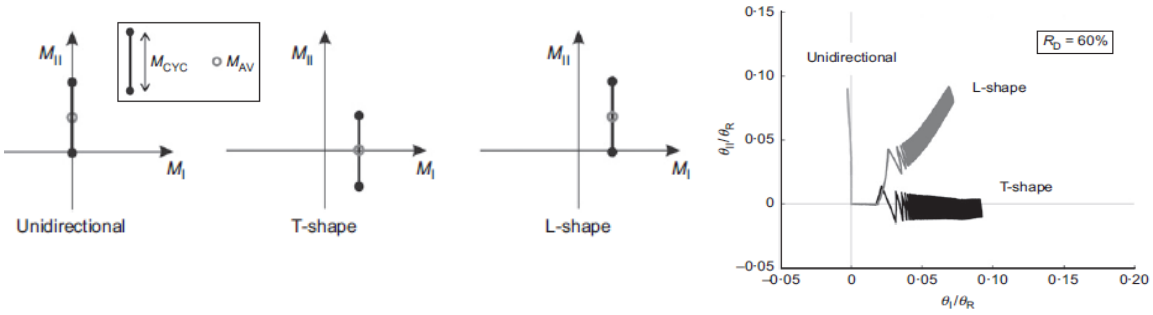
Pyke et al. (1975) introduced the first apparatus for multidirectional loading of soil samples. A series of multidirectional shaking table tests on dry sand was conducted to evaluate the material's resistance to liquefaction. They discovered a 15% decrease in liquefaction resistance for a sample under a gyratory shear stress condition compared to unidirectional loading. Ishihara and Yamazaki (1980) performed multidirectional simple shear tests on saturated sand to investigate changes in cyclic stress ratios at 5% shear strain. Their findings showed that samples under multidirectional loading with equal cyclic strain amplitude were, on average, 70% lower in strength than the unidirectional tests. Based on these discoveries, it is common practice to account for multidirectional loading as a strength reduction factor (Pyke et al., 1975; Kammerer et al., 2002). Several studies involving multidirectional simple shear apparatuses have investigated the effects of multidirectional loading. However, few have succeeded in adequately controlling the boundary conditions of the tested sample. As encountered by Ishihara and Yamazaki (1980), some notable issues include rocking and pinching problems. Table 2-1 summarises some previous work conducted with multidirectional loading in the simple shear apparatus.

Table 2-1: Previous work done on multidirectional simple shear testing

Author	Year	Sample	Findings
Ishihara et al.	1980 / 1988	Fuji river sand	Rocking behaviour observed during constant vertical stress conditions. Decrease in cyclic stress ratio as secondary shear stress increases. Load irregularity influenced by the density of sand.
Boulanger et al.	1995	Modified Sacramento river sand	Decrease in cyclic loading resistance for perpendicular bi-directional loading is attributed to differences in shear stress reversal and principal stress rotations
Kammerer	2002	Monterey #30 sand	Tests performed with initial static driving stress to replicate in-situ loading conditions for sloping ground. Reduction factors typically used for liquefaction differs for multidirectional loading.
Matsuda et al.	2011	Toyoura sand	At high cyclic amplitudes, there is little influence from the direction of loading on the decrease in effective stress. Under the same cumulative shear strain, there is little influence of the cyclic phase difference on the axial strain.
Rutherford	2012	Gulf of Mexico clay	Undrained shear strength increases with increases in initial shear stress. Build-up of excess pore water pressure is affected by stress reversal.
Li et al.	2017 / 2018	Leighton Buzzard sand	Shear behaviour is affected by the magnitude and direction of the consolidation shear stress ratio. Under monotonic loading, the angle between the two horizontal shear stress components can lead to either brittle or ductile responses.
Nhan et al.	2017	Kaolinite clay, Tokyo clay, Kitakyushu clay	Under multidirectional loading, pore water accumulation and post-cyclic settlement increase considerably more compared to uni-directional tests. This behaviour may differ for saturated sands.
Sun and Biscontin	2019	Hostun sand	Stress-controlled undrained cyclic multidirectional simple shear tests. Oval and circular load paths were compared to unidirectional CSS tests. Shear strain in perpendicular direction was limited when the static shear stress is sufficiently high to eliminate stress reversal.

However, in the framework of this project, the investigation of multidirectional loading is aimed at the stresses and strains experienced by the soil around an OWT foundation. Furthermore, it is known that wave and wind loads acting on the turbine are irregular in direction and magnitude. Therefore, a Variable Direction Dynamic Cyclic Simple Shear (VDDCSS) device acquired by Oxford from manufacturer GDS has explicitly been modified and improved to simulate realistic loading conditions relevant to an OWT foundation. With this apparatus, random cyclic loads can be applied using a pair of identical load actuators arranged in two perpendicular horizontal directions, but it is necessary to decide what stress/strain paths should be applied in the testing programme.

The behaviour of monopiles subject to complex multidirectional loading should therefore be considered. Richards et al. (2019) investigated the rotational response of a laboratory-scale monopile in sand under constant and variable amplitude, unidirectional and multidirectional cyclic loading. Perpendicular cyclic loading tests, shown in Figure 2-13, provided insight into the effect of load direction, whereby ratcheting was observed to occur in the direction of the average load M_{AV}, regardless of the direction of the cyclic load M_{CYC}. The subscripts I and II refer to the perpendicular directions normal to the monopile's vertical axis.



(*a*) (*b*)

Figure 2-13: (*a*) Schematic of perpendicular tests (*b*) Rotational response of perpendicular tests
Source: (Richards et al., 2019)

Moreover, the magnitude of ratcheting was found to be independent of the cyclic loading and the average load direction. These observations provide important insight when assessing constitutive models for multidirectional cyclic loading. Multidirectional loading effects can also be interpreted through a monopile's post-cyclic response, whereby an increase or decrease in post-cyclic capacity can be observed following the monotonic response. Rudolph et al. (2014) established that multidirectional loading induces significant accumulated pile displacement. Similar findings were made by Richards et al. (2019) and Boulanger et al. (1995), where decreases in cyclic loading resistances were observed. For irregular cyclic loads, the amount of pile displacement or rotation is dominated by the largest loading events in the time history (Richards, 2019). Additionally, the pile response follows the monotonic 'backbone' response when loads exceed those previously applied.

In the case of multi-amplitude loading where real storm loads are irregular, the consistent framework used for constant amplitude loading can be extended here to interpret the pseudo-random cyclic response. For each cycle, the response is defined in load and unload half-cycles (Figure 2-14), starting and ending at reloading points (i.e. points r_1 and r_2). Then, based on the amplitude for each cycle, a sensible tolerance *TOL* is introduced to discount cycles regarded as noise. The cycle counting process closely follows the method implemented by NGI (Norén-Cosgriff et al., 2015).

Unlike constant-amplitude tests, the average shear stress τ_{av} and cyclic amplitude τ_{cyc} are defined for each half-cycle instead of the mean value for the whole cycle. Similarly, the loading stiffness k_l and unloading stiffness k_u are calculated for each half-cycle, and both are reported instead of taking the central cycle stiffness k_{sec} (Equation (2-16)). It is not appropriate to take the average of the calculated values as these do not accurately represent the whole cycle behaviour.

OWT foundations typically experience tens of millions of irregular cycles over their lifetime (25 to 30 years), making it impractical to apply the same number of irregular cycles to element tests or FEA models due to increased complexity and time constraints. Instead, irregular cyclic load histories are transformed into parcels or packages of constant cyclic load amplitude and corresponding average load, and arranged in ascending order. It is generally accepted that applying loads in this order gives the most conservative result for capacity and permanent strain (Andersen, 2015). However, for soil stiffness, a different arrangement may be more critical.

In design, the effect of cyclic loading is usually considered by determining the equivalent number of cycles N_{eq} of the maximum load that would reproduce the cyclic degradation incurred during the actual cyclic load history (Andersen, 2015). By applying the packaged cyclic loads, N_{eq} can be determined using the pore pressure or strain accumulation

procedure. The latter is preferred as it is more suited for clay, since accurate laboratory measurement of pore pressure is more challenging to perform for clays than sands (Andersen, 2009). For the strain accumulation procedure, the cyclic strain serves as a memory of the cyclic behaviour by keeping track of the cyclic shear strain over the entire cyclic load history, as shown in Figure 2-14(b). Here, a soil element undergoes 100 cycles at τ_{cyc} = 36 kPa, moving from point A to B. The cyclic shear strain at B is γ_{cyc} = 0.75%. When τ_{cyc} is increased to 41 kPa, the soil follows the γ_{cyc} = 0.75% contour to Point C. With a subsequent increase in cyclic shear stress, the cyclic shear strain rises by approximately 0.1% to γ_{cyc} = 0.85% at Point D (N = 35). After 40 cycles at τ_{cyc} = 41 kPa, the soil reaches N_{eq} = 75 (Point E). With N_{eq} known, the contour diagrams (e.g. Figure 2-11) can be used directly to determine the cyclic shear strength and deformation characteristics for a given load history. However, the cyclic shear strain accumulation procedure only gives good predictions when the packaged loads are arranged in ascending order (Andersen, 2015).

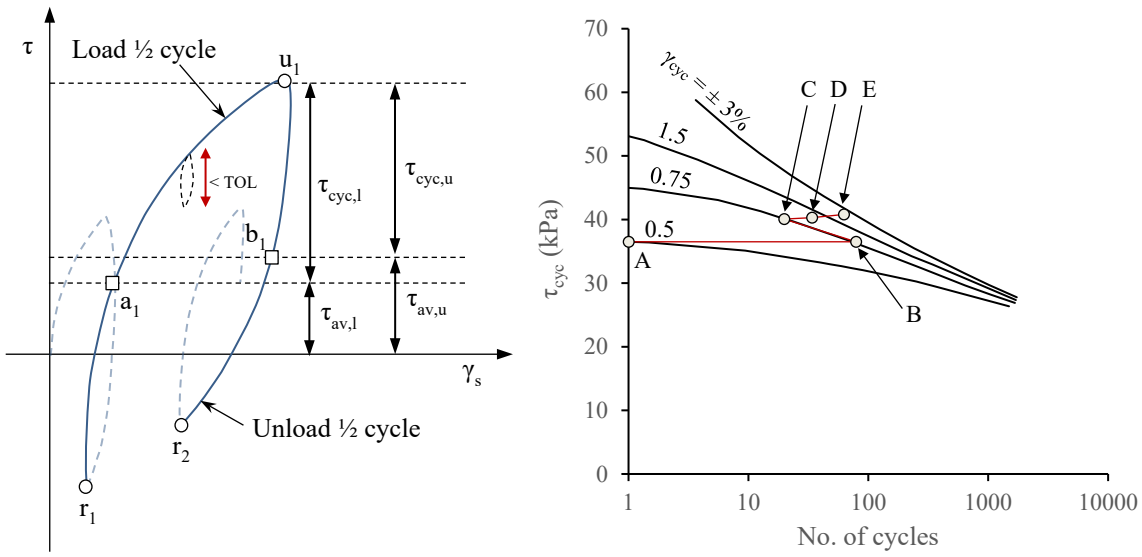


Figure 2-14: (*a*) Definitions for multi-amplitude loading (*b*) Cyclic shear strain accumulation Modified from (*a*) Balaam (2021) and (*b*) Andersen (2015)

2.3.5 Realistic storm loading at element scale

The analysis of cyclic loading for offshore foundations is generally focused on (1) the type of loading (defined by the combination of τ_{av} and τ_{cyc} or loading characterisation parameters ζ_b and ζ_c), (2) the number of imposed cycles, (3) stiffness degradation with cycle number, (4) loading magnitude, (5) development of permanent deformations and (6) pore pressure development. Realistic loading at the element level enables scalability the key cyclic components. An example is the load magnitude comparison between the measured shear stress τ in simple shear tests and the lateral pressure p measured from typical offshore monopile foundations. When normalised by an appropriate reference stress (i.e. undrained shear strength s_u for simple shear and ultimate lateral resistance p_u for the monopile), it may be assumed that $\tau/s_u \approx p/p_u$ as postulated by Zhang et al. (2017). This relationship facilitates convenient load magnitude comparison within a normalised cyclic stress space framework, as illustrated in Figure 2-15, with tests normalised by their respective reference stresses, as given in the legend. The realistic storm load history is taken from the work of Richards (2019) based on the experimental study of a scaled-down monopile subjected to a 9-hour storm history, representing a 100-year return period storm from the North Sea.

Figure 2-15 shows that typical storm loads generally occur at $\zeta_b < 0.5$ and are either partial one-way ($0 < \zeta_c < 1$) or partial two-way ($-1 < \zeta_c < 0$). The element tests shown in this example involve normalised load magnitudes far higher than those experienced by OWT foundations during a severe storm load, as pointed out by both White (2020) and Balaam (2021). While it is true that element tests at low amplitudes contribute little to the overall strain development, such tests are necessary to avoid over-conservatism in design. Large strain and high amplitude tests are fundamental in understanding the complete behaviour of a particular soil, but more element tests should be concentrated at the working cyclic stress levels expected in soil. This enables the accurate calibration of constitutive models to account for cyclic loading components at realistic load intensities.

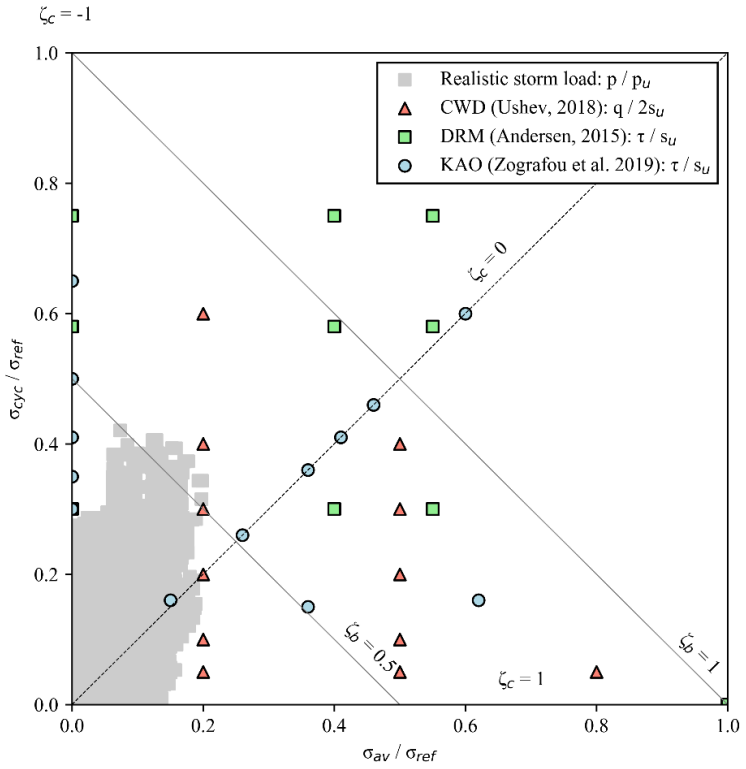


Figure 2-15: Load magnitude comparison between realistic storm loads and those in element tests

2.4 Soil constitutive model

Using soil constitutive models has become a core part of the design of OWT foundations. The available models range in complexity and are developed to predict the key cyclic loading characteristics commonly observed in the cyclic element testing of cohesive soils. In this research, only a single model is explored, based on its applicability to multidirectional loading and its potential for accurate prediction as documented in the literature. The model is a multi-surface kinematic hardening model formulated in the Hyperplasticity framework.

2.4.1 Hyperplasticity framework

Hyperplasticty is a rigorous mathematical framework for developing plasticity models that conform to the laws of thermodynamics. The framework facilitates the development of new constitutive models and allows the comparison of other competing material models. The concept was first introduced by Ziegler (1977) before being further developed by Houlsby (1981) and Collins and Houlsby (1997). The method has proven successful in describing

many engineering materials, particularly soil materials in geotechnical engineering. Houlsby and Puzrin (2006) give comprehensive examples of these models, highlighting their ability to describe the unique non-linear behaviour of soil materials and their applicability to both rate-independent and rate-dependent materials or systems. The three main advantages of Hyperplasticity over other standard plasticity models include:

1) The framework guarantees developed models obey the Laws of Thermodynamics;
2) The framework ensures a compact model and allows the systematic development of new material models;
3) The constitutive material behaviour can be fully specified using just two potential functions, where one describes the stored energy and the other the dissipation.

Here, the stored energy may be either described using the Helmholtz free energy $f(\varepsilon,\alpha)$ or the Gibbs free energy $g(\varepsilon,\alpha)$ function. For rate-independent behaviour, the dissipation may be defined using a dissipation function of the $d(\varepsilon,\alpha,\dot{\alpha})$ form or a yield function of the form $y(\varepsilon,\alpha,\chi)$. For rate-dependent behaviour, the dissipation potential may be written in the form of the force potential z or the flow potential w (Houlsby and Puzrin, 2006). The f and g, as well as w and z functions, are related through a Legendre transform, while the d and y functions are related through a degenerate Legendre transform (see Houlsby and Puzrin (2006) for details). Moreover, dissipation potentials d and z are related by:

$$d = \frac{\partial z}{\partial \dot{\alpha}} . \dot{\alpha} \tag{2-22}$$

Here, d is said to be equivalent to z and rate-independent when d is a homogenous and first-order tensor in $\dot{\alpha}$. The model introduced here follows closely the Hyperplasticity models already developed by Abadie (2015), Beuckelaers (2017), Houlsby et al. (2017), Richards (2019) and Balaam (2021). Typically, the constitutive and incremental behaviour of the

model can be derived from the potentials using standardised procedures. For example, the behaviour of the model can be derived from the following:

$$\varepsilon = -\frac{\partial g}{\partial \sigma} \qquad \bar{\chi} = -\frac{\partial g}{\partial \alpha} \qquad \chi = -\frac{\partial d}{\partial \dot{\alpha}} \qquad \bar{\chi} = \chi \tag{2-23}$$

where, $\bar{\chi}$ is the generalised stress, χ the dissipative generalised stress and α the internal conjugate variable. Based on the second law of thermodynamics, $(\bar{\chi} - \chi)\dot{\alpha} = 0$ is implied. However, the Hyperplasticity framework presented by Houlsby and Puzrin (2006) makes use of a much stronger condition, where $\bar{\chi} = \chi$. This statement, also known as the orthogonality expression presented by Ziegler (1977), is more restrictive and central to the framework. The principle applies to a number of materials and behaviours and is fully capable of capturing the constitutive relation without any additional assumptions. The dissipation potential can be augmented using a Lagrange multiplier Λ by applying kinematic constraints to the internal variable where $c(\dot{\alpha}) = 0$:

$$d^* = d(\varepsilon, \alpha, \dot{\alpha}) + \Lambda c(\dot{\alpha}) \tag{2-24}$$

The dissipative generalised stress is then derived from the augmented dissipation function $\left(\chi = \frac{\partial d^*}{\partial \dot{\alpha}}\right)$, where the $c(\dot{\alpha}) = 0$ constraint eliminates the Lagrange multiplier Λ.

The above formulations for *g* and *d* are for a rate-independent model and need to be modified to capture rate-dependent behaviour. Houlsby and Puzrin (2006) show that the energy function remains unchanged when accounting for rate effects, while the dissipation function no longer applies as potentials for the generalised stress χ must be replaced using either the force potential *z* or flow potential *w* function, which is related to the dissipation function such that $d = z + w$.

2.4.2 Evolution of multi-surface kinematic hardening model

The hierarchy of kinematic hardening models is based on the development of plasticity models, which adhere to the extended Masing rules (Masing, 1926; Pyke, 1979). Instead of the expected expansion or contraction of the yield surface upon yielding, the extended Masing type behaviour refers to the translational movement of the yield surface. These models, also known as Iwan models (Iwan, 1967), are able to capture the hysteretic response of soils in cyclic element tests (Pyke, 1979; Balaam, 2021).

Figure 2-16(a) illustrates a mechanical analogue for the simplified kinematic hardening model in a parallel configuration. The model consists of elements in parallel, each consisting of spring H_n and slider k_n components. The springs provide the kinematic hardening behaviour, while the sliders represent the stress at which yield occurs for each yield surface. The models are described globally by conjugate variables, stress σ and strain ε, and employ internal variables α_n, $n = 1 \ldots N_s$ for the plastic strain. The model can capture the smooth elastic-plastic transition of a material with adequate accuracy by increasing the number of surfaces (N_s). Accuracy in this instance refers to the non-linearity, where an increase in N_S increases the non-linearity but at the cost of increased computational time. Balaam (2021) found that by employing 40 yield surfaces, an error of less than 0.1% is observed when comparing the area beneath a fitted curve to the area reproduced by the kinematic hardening model. A rate-dependent multi-surface model with a ratcheting element is explored following the model by Balaam et al. (2020) to account for rate effects and ratcheting behaviour. Figure 2-16(b) to (c) highlights the inclusion of these mechanisms, starting with a viscous damper μ (as a dashpot) and then the addition of the ratcheting element R. The kinematic hardening models presented here are expressed within the Hyperplasticity framework but can also be described using conventional plasticity theory. A complete representation of the framework for rate-dependent models can be found in Puzrin and Houlsby (2001) and Houlsby and Puzrin (2006).

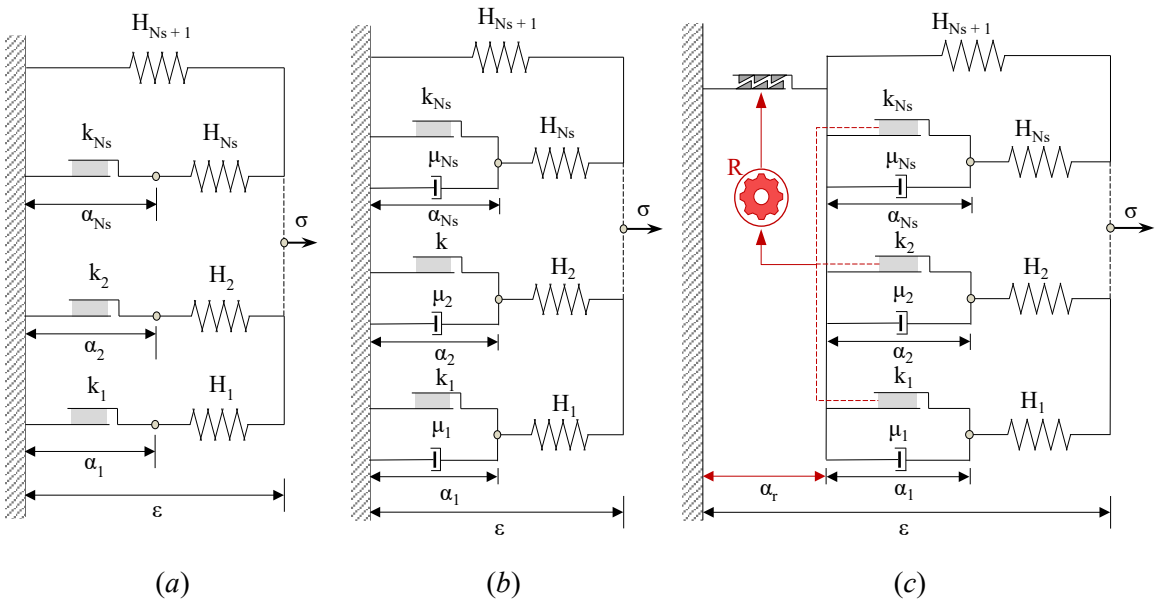


Figure 2-16: Rate-independent multi-surface kinematic hardening model: (a) Standard model, (b) standard model with viscous damper, and (c) standard model with viscous damper and ratcheting

Table 2-2 shows the evolution of the Gibbs free energy function and dissipation function for a parallel configuration:

Table 2-2: Evolution of Kinematic hardening model

Model	Energy function	Dissipation function
Rate independent	$g = -\frac{\left(\sigma + \sum_{n=1}^{N_s} H_n \alpha_n\right)^2}{2E_0} + \sum_{n=1}^{N_s} \frac{H_n}{2} \alpha_n^2$	$d = \sum_{i=1}^{N_s} k_n \lvert\dot{\alpha}_n\rvert$
Rate dependent (Rate Process Theory)		$d = \sum_{i=1}^{N_s} k_n \lvert\dot{\alpha}_n\rvert + \frac{\mu_n}{t_{ref}} \dot{\alpha}_n \sinh^{-1}\left(\lvert\dot{\alpha}_n\rvert t_{ref}\right)$
Rate + ratcheting	$g = -\frac{\left(\sigma + \sum_{n=1}^{N_s} H_n \alpha_n\right)^2}{2E_0} - \sigma\alpha_r + \sum_{n=1}^{N_s} \frac{H_n}{2} \alpha_n^2$	$d = \sum_{i=1}^{N_s} k_n \lvert\dot{\alpha}_n\rvert + \frac{\mu_n}{t_{ref}} \dot{\alpha}_n \sinh^{-1}\left(\lvert\dot{\alpha}_n\rvert t_{ref}\right) + \sigma\dot{\alpha}_r$

Notes:

E_0 = Initial stiffness based on bender element or resonant column tests (for a parallel model: $E_0 = \sum_{n=1}^{N_s+1} H_n$)

μ_n = Viscous term defined as $\mu_n = k_n t_{ref} \eta$

t_{ref} = Time taken as inverse of local reference strain rate (Rate typically assumed to be very slow~1000 hrs to failure)

η = Viscous constant defined as $\eta = \frac{\eta_{10}}{\ln(10)}$, where η_{10} represents increase in σ per order magnitude increase in rate

One of the main contributions in this thesis is to extend the current unidirectional load models to bi-directional loading. The model closely follows the version of the bi-directional model presented by Houlsby et al. (2017) and Richards (2019). The main difference between past and current models is the introduction of rate effects within a parallel configuration. As a result, the implemented model combines elements from Richards (2019) and Balaam (2021). The ratcheting and rate effect elements are both addressed, and the entire stress-strain behaviour of the material can be captured using two functions, the Gibbs energy function of the form

$$g = -\frac{1}{2E_0}\left(\left(\sigma_x + \sum_{n=1}^{N_s} H_n\alpha_{nx}\right)^2 + \left(\sigma_y + \sum_{n=1}^{N_s} H_n\alpha_{ny}\right)^2\right) - \sigma_x\alpha_{rx} - \sigma_y\alpha_{ry} + \sum_{n=1}^{N_s}\frac{H_n}{2}\left(\alpha_{nx}^2 + \alpha_{ny}^2\right) \tag{2-25}$$

and flow potential w, knowing $d = \chi\dot{a}$, $dz/\dot{a} = \chi$ and $w = d - z$:

$$w = \sum_{n=1}^{N_s}\frac{k_n\eta}{t_{ref}}\left(\cosh\left(\frac{\langle\sqrt{{\chi_{nx}}^2 + {\chi_{ny}}^2} - k_n + R_n\left(\sqrt{{\chi_{rx}}^2 + {\chi_{ry}}^2} - \sqrt{{\sigma_x}^2 + {\sigma_y}^2}\right)\rangle}{k_n\eta}\right) - 1\right) \tag{2-26}$$

In these equations, subscripts x and y denote the direction, η is the viscous constant (also defined as $\eta_{10} = \ln(10)\eta$), t_{ref} is the reference time (i.e. the inverse of the local reference quasi-static strain rate $\dot{a}_{qs}$, defined as $t_{ref} = 1/\dot{a}_{qs}$), and α_r is the internal variable accounting for ratcheting. It can be easily seen that the above equation reduces to the unidirectional case when either $\sigma_x = 0$ or $\sigma_y = 0$. It can be further shown that the multidirectional model is isotropic, which means that the unidirectional response is the same irrespective of the loading direction (Houlsby et al., 2017). The softening and ratcheting elements included in the model are discussed in further detail in Chapter 7, highlighting the function selection and calibration procedure.

2.5 Summary

Historically, cyclic element testing has been focused on constant amplitude cyclic loading tests of high magnitude and a relatively low number of cycles. However, such tests do not represent the types of cyclic loads typically experienced by OWT foundations. Furthermore, as these structures become more efficient, understanding their behaviour for more realistic cyclic loads becomes more relevant. As a result, there is a need to establish a consistent framework for both monotonic and cyclic loading to ensure the measured outputs at the element scale can be evaluated and that the defined variables can be extended to more complex cyclic loading tests (i.e. multidirectional and multi-amplitude loading).

There is often confusion with the measured parameters for direct simple shear testing and how they relate to other element tests. This chapter addresses these concerns by clarifying the stress-strain behaviour and stress distribution experienced by a soil element under simple shear. Furthermore, different failure states were also considered while highlighting the impact of the shearing rate for cohesive soils.

For cyclic element testing, tests are generally performed at load intensities far higher than those experienced by an OWT foundation. There is a need for a high-cycle cyclic element test database undertaken at representative stress levels so that cyclic load characteristics can be comparable to foundations subjected to realistic histories of working and storm loads. In addition, one of the novel elements in this research is the multidirectional simple shear testing of a soil specimen, hence the need to understand the key cyclic loading characteristics reported in the literature and how these effects are typically accounted for in design. From the database of element tests, a bi-directional kinematic-hardening multi-surface type model will be implemented and evaluated in terms of its ability to capture the key characteristics observed.

Chapter 3

Apparatus description

3.1 Introduction

This chapter provides an overview of the element testing systems used. A detailed description of each device is given, followed by the sample setup and testing procedures. The majority of the research is performed using the simple shear apparatus. Therefore, relevant corrections and modifications to this apparatus are also considered here.

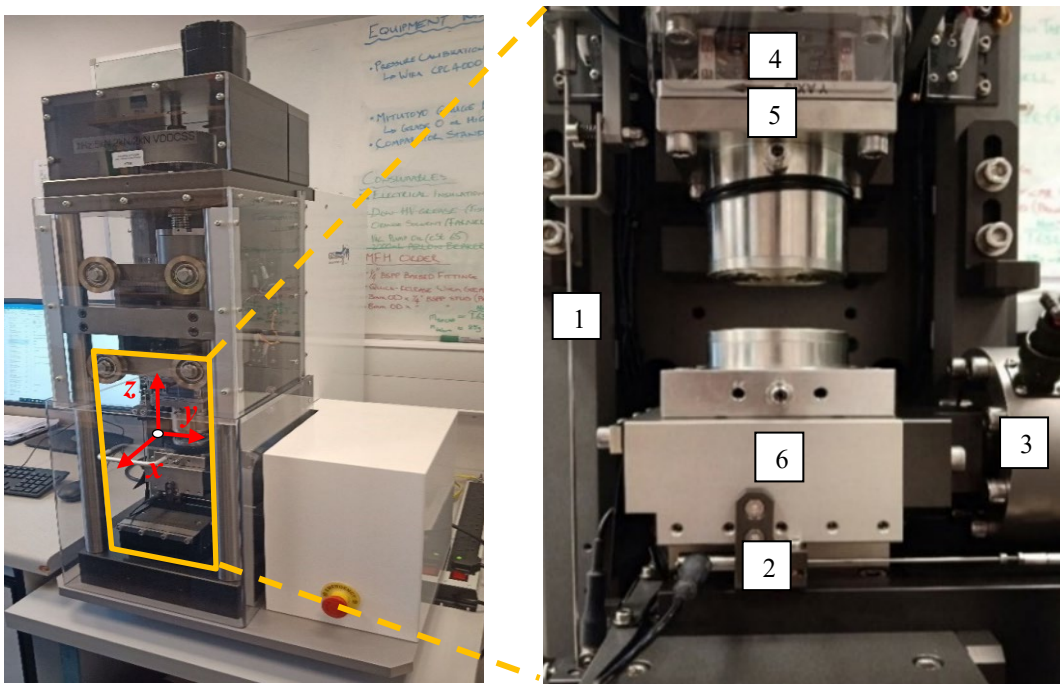
3.2 Variable direction dynamic cyclic simple shear apparatus (VDDCSS)

3.2.1 Equipment overview

The VDDCSS is a simple shear device designed and manufactured by Global Digital Systems Instruments Ltd, UK (GDS). The apparatus allows a soil specimen to be sheared in two directions through two orthogonal electro-mechanical high-accuracy actuators on the *x*-*y* plane (Figure 3-1), each with a 2 kN capacity. It is the first commercially available multidirectional cyclic simple shear device capable of performing custom stress or strain paths on the shearing plane. In addition, a third actuator on the *z*-axis has a 5 kN capacity and is used to apply vertical (normal) stress to the cylindrical soil specimen.

All three actuators are controlled via three synchronised entry-level dynamic control system (ELDCS) units with a control loop running at 500 Hz. The actuators can be independently controlled using displacement or load control commands. The former is carried out using voltage (motor rotational velocity) based PID (proportional-integral-derivative) control, while the latter is carried out using current (motor torque) based PID control.

Additionally, a 'pancake' load cell is located at each actuator to measure the loads, coupled with servo motor encoders to measure the displacements. The displacements have a ±10 mm range in the shear axes and a ±25 mm range in the normal axis. The system also includes an additional 2 kN two-axis platform-type shear load cell to measure the horizontal loads in the *x*-*y* plane. For high accuracy and short-range displacement measurements (±2.5 mm), vertical and horizontal Linear Variable Differential Transformers (LVDT) are used.



1. Axial LVDT
2. Horizontal LVDT (*y*-axis)
3. Load cell (*y*-axis)
4. Shear load cell (*z*-axis)
5. Top platen
6. Sliding carriage

Figure 3-1: VDDCSS apparatus

Table 3-1 summarises the accuracy and resolution of each of the mechanical components. The values were taken under standard laboratory testing conditions following ASTM D6528-17 (2017). The transducers function using an excitation voltage and return outputs in millivolts directly proportional to the measured parameter. Data is processed by a 23-bit analogue input module for both load and displacement transducers. While this produces high resolutions, the software interface (GDS Lab) only permits readings to four decimal places, which allows for realistic control and viewing of data.

Table 3-1: Accuracy and resolution of VDDCSS transducers

Transducer	Units	Unit range	Sensitivity	Noise amplitude*	Resolution
Vertical load cell (x)	N	± 5000	2.5933 mV/V	0.2 N	1.38E-03 N
Horizontal load cell (x & y)	N	± 2000	2.3608 mV/V	0.4 N	7.57E-04 N
x-y shear load cell	N	± 2000	2.3750 mV/V	0.5 N	6.95E-05 N
Long-range encoders (x & y)	mm	0 - 18	6.104E-05 mm/count	0.8 µm	0.0060 µm
Long-range encoder (z)	mm	0 - 25	3.052E-05 mm/count	0.8 µm	0.0060 µm
LVDT transducer	mm	0 - 5	0.2562 mm/mV	0.4 µm	0.0003 µm

*These values were calculated based on one standard deviation

3.2.2 Sample size and preparation for DSS tests

The ASTM D6528 standard recommends a maximum H/D ratio of 0.4 with a minimum diameter and height of 45 mm and 12 mm, respectively. However, several past and current researchers have adopted H/D ratios lower than that set by the standard to improve the stress distribution within the sample. Some different ratios and dimensions used by various researchers are provided in Table 3-2.

Table 3-2: Different dimensions of simple shear specimens used

Author	Year	Type of test	Specimen diameter, D (mm)	Specimen height, H (mm)	H/D ratio
Roscoe, K.H.	1953	Cambridge: Undrained	60 (length)	20	0.333
Bjerrum, L. & Landva, A.	1966	NGI: Drained + Undrained	80	10	0.125
Peacock et al.	1968	Cambridge: Undrained	60 (length)	20	0.333
Dyvik et al.	1987	NGI: Undrained	80	16	0.200
Porcino et al.	2008	NGI: Undrained	80	20	0.250
Vucetic, M. & Mortezaie, A.	2015	NGI: Undrained	67	19	0.284
Li et al.	2017	VDDCSS-SGI: Undrained	70	17	0.243

Much criticism has been raised about the stress distribution within a simple shear sample, where uniform normal stresses and shear stresses are not adequately imposed. However, as shown by Boulanger and Seed (1995) and Rutherford (2012), the uniformity of the sample can be improved by decreasing the H/D ratio (< 0.4) of the specimen.

For this project, a 70 mm diameter cylindrical sample with a 20 mm shear height was used (H/D ~0.29). These dimensions were adopted as they are commonly used in industry and are the default size provided by GDS Instruments. A stack of 1 mm high low-friction Teflon rings surrounds the membrane-enclosed specimen as illustrated in Figure 3-2. This ensures that the specimen volume is kept constant, thus enforcing K_0 conditions with the height unchanged during the shearing stage. Drainage lines are connected to the top platen and base pedestal to allow for drainage of the specimen during consolidation.

The test programme for the Cowden till involved two phases, a preliminary and a final testing phase. The preliminary phase consisted of mostly monotonic tests, conducted on approximately 100 mm diameter rotary core samples. The samples were trimmed to the appropriate dimensions and then used to characterise the testing site using the VDDCSS, triaxial apparatus, and oedometer.

The final testing phase (involving cyclic tests) focused on specimens obtained from the Cowden block samples, which had dimensions 310 mm x 310 mm x 310 mm and an approximate weight of 80 kg. Moisture contents were measured immediately for each of the block samples to check that they had not dried out during procurement (i.e. trimming, packaging, waxing, etc.) and transportation. The block samples were preferred for the cyclic tests in this research, mainly due to minimised variability with sample depth, similar stress history, and improved soil quality.

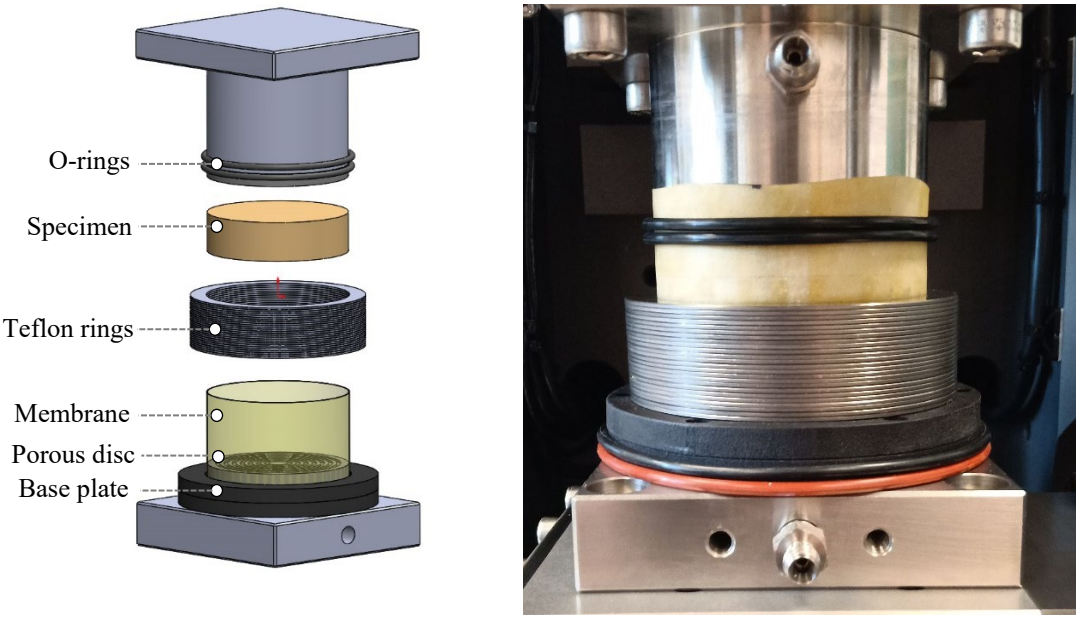


Figure 3-2: VDDCSS sample assembly

3.3 Test procedure

The test method described below covers the unidirectional monotonic testing of soils in the VDDCSS. The procedure follows best practice according to ASTM D6528-17 and incorporates some of the techniques followed by commercial laboratories. The Cowden till material was stony, making it challenging to prepare, where trimming the sample took approximately 30-60 minutes. With the aid of the thick rings (discussed in Section 3.4.1.3), smooth porous discs were used as this was found to cause the least disturbance to the sample's surface.

3.3.1 Setup

Specimens for the VDDCSS apparatus were set up using the following steps:

1) Carefully trim the sample to its required dimensions, 70 mm diameter and 30 mm height (10 mm added to accommodate thick rings - see Figure 3-3 or Figure 3-6), using a cylindrical core cutter, and take the moisture content from the trimmings. Measure the mass of the specimen.
2) Place top and bottom porous stones in a beaker containing water. Deair porous stones in a vacuum desiccator under -1 bar.
3) Place the corresponding porous stone and platens back into VDDCSS and zero the reading for the axial displacement transducer using a stainless-steel block of known height. This allows for the height of the sample to be accurately monitored throughout the test. Note: platens are flushed with de-aired water before attaching the porous stones.
4) Remove the bottom platen and then place the trimmed specimen on top of it.
5) Place a lightweight cylindrical block (70 mm in diameter) on top of the specimen before enclosing the specimen in a latex membrane using a membrane stretcher.
6) Using an o-ring extender, place two o-rings over the sample and onto the bottom platen, followed by two base plates.
7) Similarly, place two o-rings on the top platen.
8) Install lateral pressure sensor on latex membrane (see Section 3.4.2).
9) Place thick rings and Teflon-coated thin rings over the sample. The height of the thin ring stack is recorded.
10) Fold membrane over rings and place the entire bottom platen assembly back into the device.
11) Following ASTM D6528-17 (2017), a minor normal seating stress of approximately 5 kPa is applied to the specimen using load control. This value is large enough such that no seating displacement errors are induced but small enough such that premature consolidation does not take place.
12) Measure the height of the sample using a displacement encoder and connect drainage lines to platens.
13) Adjust the LVDT armature such that it is measuring the correct voltage range.
14) Cover the VDDCSS apparatus in insulation to minimise temperature effects (see Section 3.4.1.4).
15) Set all transducers in the *x*-*y* plane to zero.

3.3.2 Saturation

For granular soils, saturation of the sample is not necessary as constant volume conditions can be assured by shearing at constant height, but saturation is preferred to simulate conditions for offshore wind turbines (Peacock et al., 1968). In contrast, for clay samples, water was only connected to the specimen during the consolidation stage. Access to water was prevented during preparation as the sample is likely to swell if exposed to water. The sample is assumed to be fully saturated at the time of preparation.

3.3.3 Consolidation

Since a stack of Teflon rings confined the membrane-enclosed specimen, K_0 consolidation conditions were enforced (Figure 3-3(a)). This implied that no horizontal deformations were permitted when a vertical stress was applied to the top of the specimen. The specimens were loaded to a vertical effective stress matching the estimated in-situ stress conditions in a single step at a rate of 100 kPa/hour. Afterwards, the sample was left to either consolidate for 12 (sand) or 24 (clay) hours, depending on the type of material, or when creep strain rates diminished to less than 0.005 %/day (Zdravković et al., 2020). This allowed excess pore pressures to dissipate, making further changes in sample height negligible.

To limit the suction of water from the porous discs (due to sample's swelling potential), the drainage lines were only opened once the specimen reached its in-situ stress conditions. In this research, specimens were either normally loaded (NL) to a targeted stress level or overloaded (OL) to a value based on the preconsolidation stress σ'_{vc} and then unloaded back to the in-situ vertical effective stress σ'_v. Further details on the consolidation approach can be found in Section 5.2.

3.3.4 Static shear

As illustrated in Figure 3-3(b), the samples can be sheared under either constant volume conditions or constant vertical stress conditions. In the former, the height and diameter of the specimen were maintained constant during shear, thus enforcing zero volumetric strain. Changes in vertical stress were assumed to be equivalent to the negative of the excess pore water pressure that would be developed in a true undrained test, as proven by Dyvik et al. (1987). In a constant vertical stress test, a constant normal load was applied to the top of the specimen, and the height is allowed to change. The targeted height or load was kept constant through a feedback control loop using either the displacement actuator or the load cell.

The specimens were sheared at an appropriate fixed strain rate such that drained shearing was slow enough to allow excess pore pressures to dissipate ($\Delta u_w = 0$) and undrained shearing was slow enough to allow for the equalisation of excess pore pressures. For DSS tests, specimens are usually sheared to 20% shear strain γ or when the shear stress τ drops 20% below the maximum value (ASTM D6528-17, 2017). However, the specimens exhibited ductile behaviours at large strains based on preliminary DSS tests on Cowden till. As a result, specimens were sheared to 50% shear strain instead.

While the selection of a suitable strain rate depends on the type of soil and its permeability, it is widely accepted that the selected strain rate should result in the time to specimen failure exceeding double the time needed to achieve 90% consolidation. Consequently, ASTM D6528-17 recommends a shear strain rate of 5% per hour for clayey soils. Alternatively, BS 1377-7:1990 and BS EN ISO 17892-10:2018 recommends the maximum displacement rate to be based on the minimum time of failure t_f determined from a consolidation test. Therefore, a conservative but widely used shear strain rate of 3% per hour was selected for this project, and was checked against the t_f obtained during the consolidation stage.

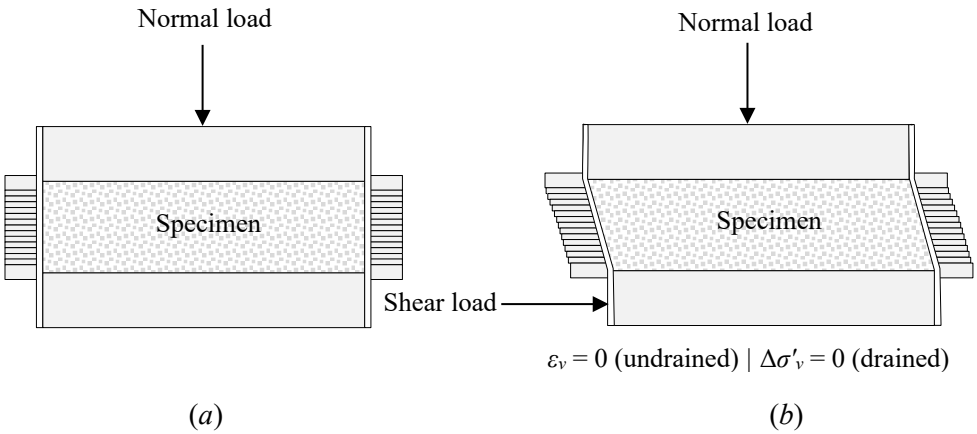


Figure 3-3: (*a*) K_0 consolidation stage (*b*) shear stage

3.3.5 Cyclic stage

The cyclic loading test programme for the VDDCSS included undrained cyclic tests aimed at calibrating the implemented constitutive model, as well as tests used to explore the key cyclic behaviours associated with Cowden till under a range of complex loads. Following the saturation and consolidation procedures, the specimens were loaded at constant volume to the specified τ_{av} and allowed to rest for another 60 minutes. After the rest period, a stress-controlled sinusoidal shear stress variation at a frequency of 0.1 Hz was applied to the specimen. The tests were generally carried out to at least 3000 cycles unless failure occurred. Failure was deemed to be reached when γ_{av} or γ_{cy} reached 15% shear strain. Furthermore, a post-cyclic static shear stage was introduced for tests that did not reach failure.

3.4 Commissioning of VDDCSS

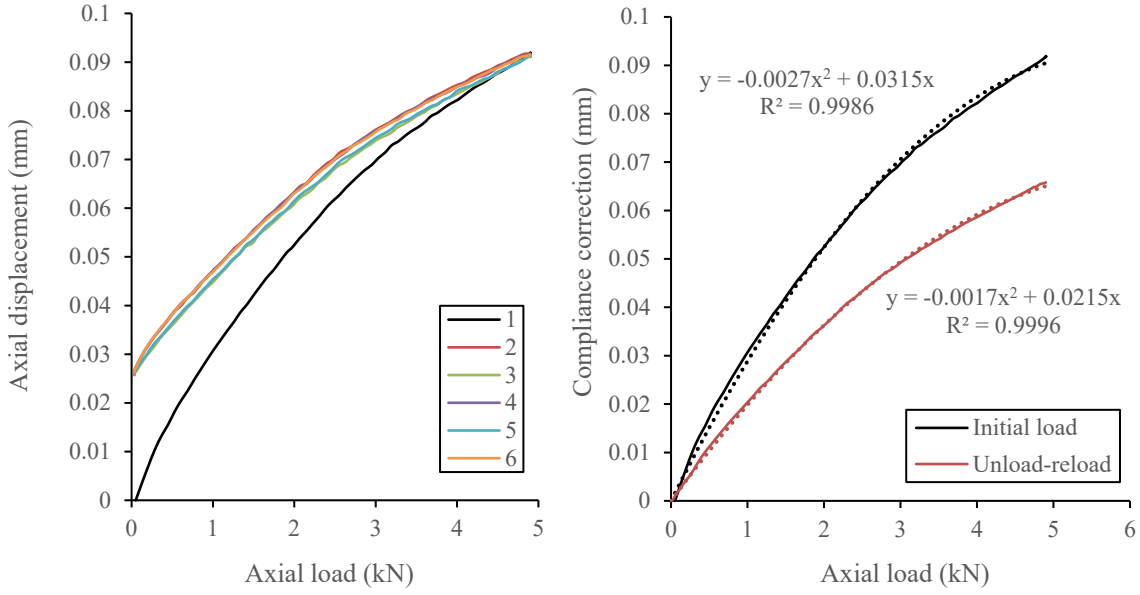
To improve the performance and functionality of the VDDCSS apparatus, several issues were addressed. This included corrections due to system compliance and friction, employment of lateral stress measurement techniques, and overall system control. The commissioning of the apparatus was further assessed using comparable equipment in a different laboratory.

3.4.1 System corrections

3.4.1.1 System compliance

The VDDCSS consists of an assembly of machined parts, equipped with load and displacement transducers. Most of these parts are made of high-strength stainless steel to withstand the applied loads from the actuators. However, when an apparatus such as the VDDCSS is subjected to a force, the assembly (i.e. frame, load cell, couplings, etc.) experiences a degree of deformation, referred to as the system's compliance. To determine the displacement of the specimen solely, the system's compliance must be removed from the recorded displacement measurements. Recognising this, ASTM D6528-07 states that the axial displacement must be corrected when the apparatus deformation exceeds 0.05% of the specimen height.

The compliance in the system was evaluated by using a steel disk as the specimen and measuring the axial displacement as the vertical force increased from the seating value to close to its maximum load (~4.9 kN). Additional unload-reload loops were added to the sequence to evaluate changes in compliance. Figure 3-4(a) depicts a stark difference in compliance between the initial loading curve (No. 1) and the following unload-reload curves (No. 2 to 6). This is likely attributed to the compliance inherent in the top and bottom platens of the VDDCSS when they are removed and placed back in for each test. To account for this, two separate compliance corrections are given as second-order polynomials (Figure 3-4(b)). While the unload-reload compliance may not be required in a standard monotonic test, the secondary compliance correction is necessary for an overconsolidated sample with two loading stages. The VDDCSS apparatus employs active height control and a fixed compliance correction to ensure constant volume conditions during the shearing stage. However, one of the limitations of the apparatus is that it fails to apply a real-time compliance adjustment during shearing, where under constant vertical stress conditions, the measured axial strain for a dilative specimen may be incorrect (Wai et al., 2021).



(*a*) (*b*)

Figure 3-4: Compliance correction for VDDCSS system- (*a*) raw and (*b*) processed data

3.4.1.2 Friction corrections

During shear, the membrane and the Teflon-coated rings exert a frictional force against the sample. To measure the force arising from the application of the boundary conditions, the empty specimen was filled with water and sheared to the limits of the apparatus (i.e. positive 10 mm and negative 10 mm). The water itself is assumed to be frictionless during shear, thus isolating the stiffness and friction contributions from the membrane and rings. The water-filled samples were tested under a pressure of 20 kPa. Low pressure was used as it was difficult to prevent leakages during the shearing stage.

The test was carried out three times and yielded similar results, showing slight variation. Consequently, the curves were approximated using a single function. The horizontal force F_H was assumed to be a function of displacement x and was captured using the exponential expression $F_H = 0.0016x^{0.61}$ (Figure 3-5). Other frictional errors generally considered in the simple shear testing device include the bottom carriage's track bearing friction. However, since the shear load cell was located directly above the sample in the VDDCSS, track-bearing friction was already eliminated from the measurements.

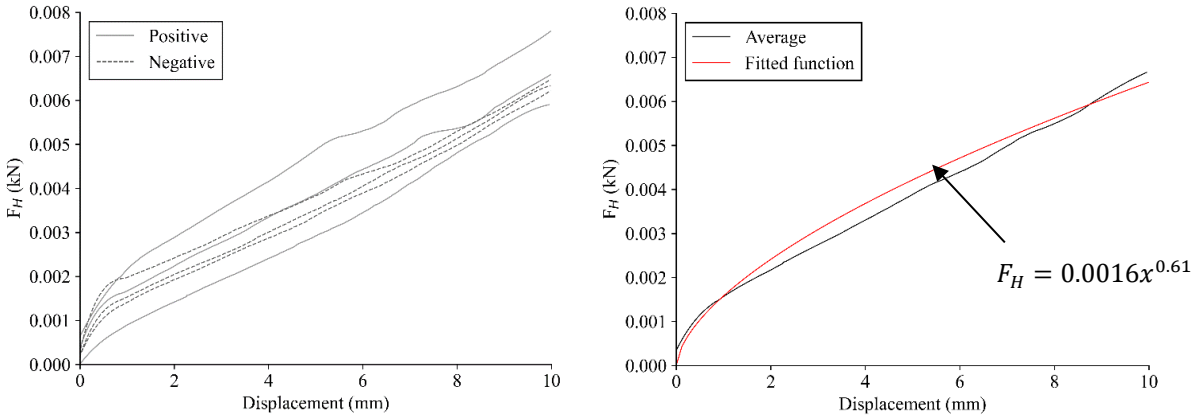
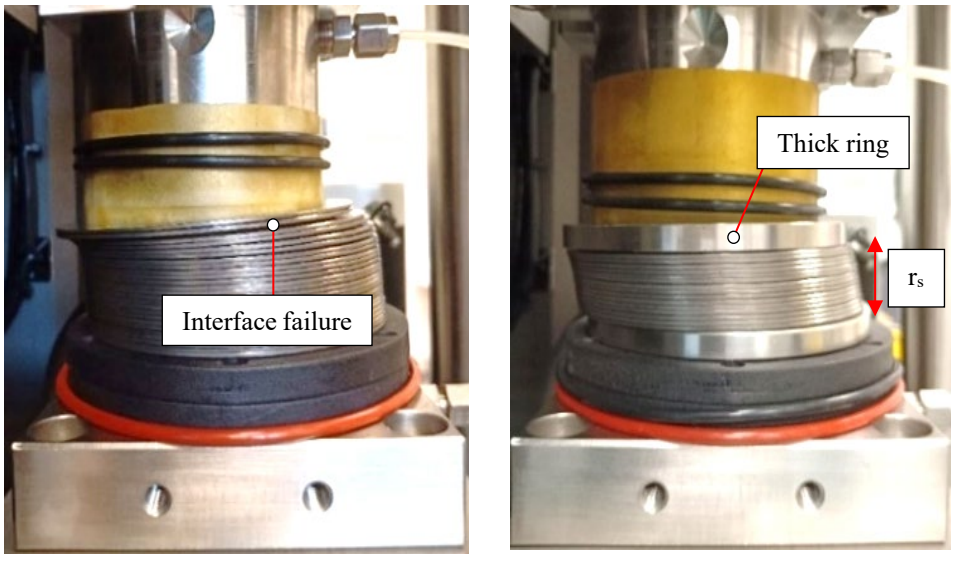


Figure 3-5: Ring friction and membrane correction - (*a*) raw and (*b*) processed data

3.4.1.3 Shear interface

As pictured in Figure 3-6, thick stainless-steel rings were introduced along with smooth porous discs to avoid shear-box-like failures (i.e. failure occurring on a specific shear plane near the disc and specimen interface). The specimen is seated in the middle of the thick rings, which prevents premature failure and allows for an even stress distribution (Figure 3-6(b)). For these reasons, grooved or pinned interfaces were not favoured when testing stiff glacial tills. The advantages also included an accurate determination of the sample height with the use of a smooth interface. However, it subsequently restricted the sample's shear height to the height of the confining ring stack r_s.



(*a*) (*b*)

Figure 3-6: (*a*) Shear failure using Teflon coated rings (*b*) Replacing interface with thick rings

3.4.1.4 Temperature fluctuations

ASTM D6528-17 states that laboratory tests should be conducted in an environment where temperatures do not fluctuate by more than 2°C. With temperature-sensitive measuring equipment, such as the axial LVDT, fluctuations can lead to significant inaccuracies within the readings. This is mainly attributed to the thermal expansion of the armature, made of stainless steel (grade 316), as pictured in Figure 3-7(a). Moreover, it can potentially disrupt the sample if the LVDT controls the axial displacement (i.e. strain control). Under constant-volume conditions, an unintentional cyclic load can be applied to the sample when temperature fluctuations occur.

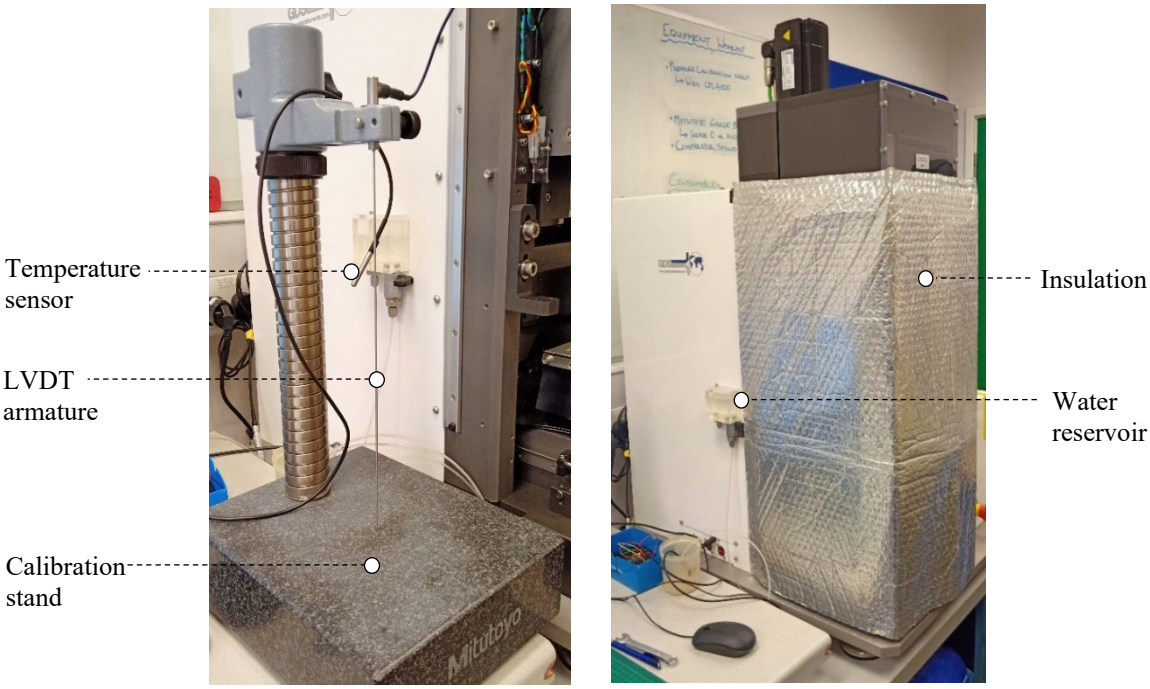


Figure 3-7: (*a*) Temperature fluctuation monitoring of LVDT (*b*) Insulation cover for VDDCSS

Several measures were put in place to address the effects of temperature. This included minimising contact time with the apparatus during testing, covering the apparatus with a protective insulation layer (see Figure 3-7(b): equivalent to a 55 mm thick polystyrene cover), and replacing the stainless steel armature with a material that was less temperature-sensitive. The armature was replaced with a nickel-iron (FeNi36) alloy called 'invar', known

for its low coefficient of thermal expansion. Changing the material of the armature proved to be effective. This was demonstrated by monitoring the change in LVDT readings over 24 hours for both armature variants on a comparator stand. From the data below, it was clear that the new armature gave improved readings, with changes < 0.01% over the measured range compared to the old armature which had changes > 0.05%, exceeding the prescribed limits in ASTM D6528-17.

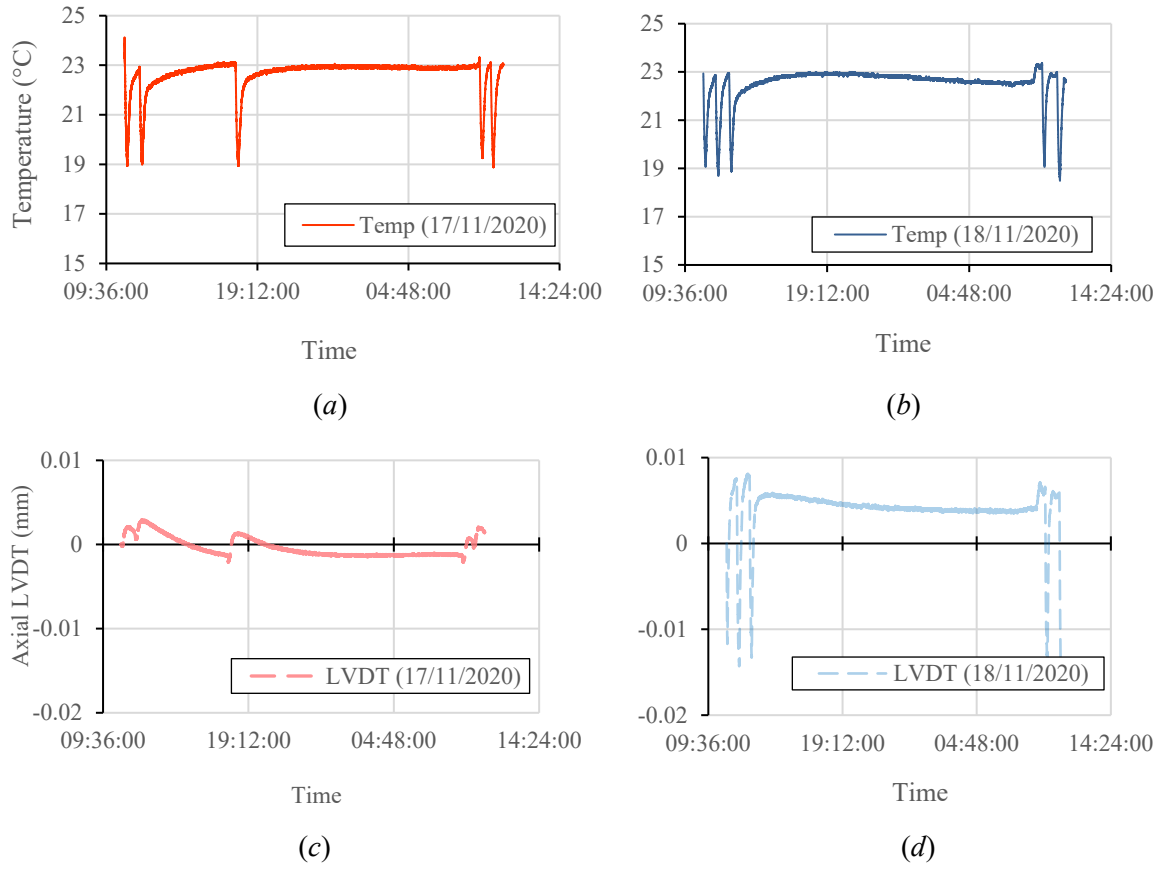


Figure 3-8: Temperature and displacement monitoring of (*a*)+(*c*) new LVDT armature and (*b*)+(*d*) old LVDT armature

3.4.2 Lateral stress measurement

To draw comparisons with the triaxial apparatus and understand the true stress state of the sample, the lateral stress σ_h on the specimen must be measured. A thin, flexible piezoresistive force sensor (i.e. FlexiForce A201) produced by Tekscan Ltd was used to obtain these measurements (Figure 3-9(b)). The sensor is non-intrusive, making it ideal for measuring the pressure on the sample. The sensor was calibrated hydraulically to simulate testing

conditions using a bespoke calibration kit, as seen in Figure 3-9(a). The design used a steel casing lined with a latex membrane that was sealed off with pipe blockers on either end to ensure a water-tight seal. A dual pressure-volume controller, intended for the triaxial device, was used to pressurise the chamber.

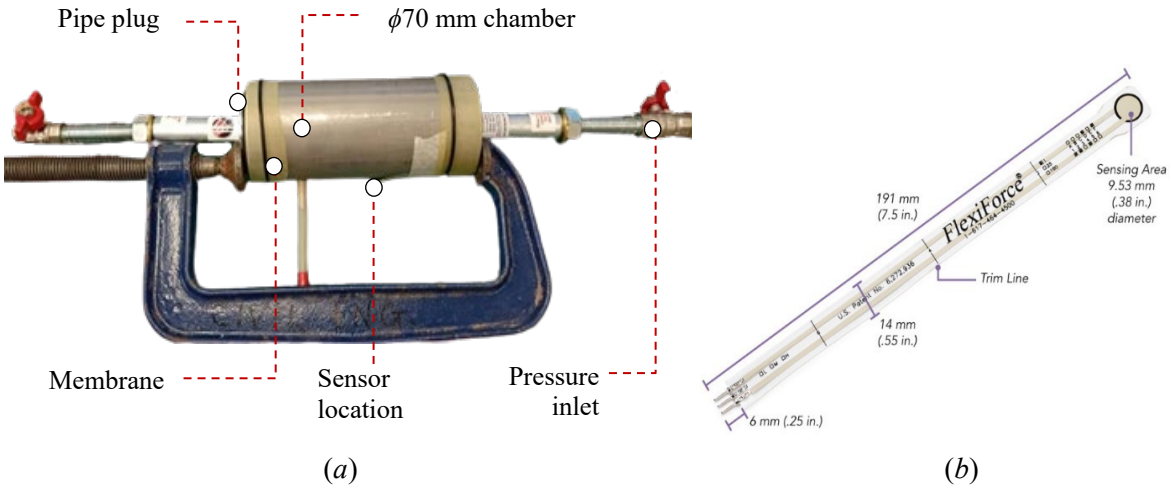


Figure 3-9: (*a*) Calibration chamber (*b*) Flexiforce A201 sensor

The sensor has a force range of 0-111N (Pressure: 0 to 1556 kPa) with a linearity error of < ±3% over its full scale. One of the notable drawbacks of the sensor was the amount of cumulative drift throughout a typical test. Drift is the change in the sensor's output caused by applying a constant force, which causes the sensor's resistance to decrease continually. While the drift is claimed by Tekscan to be < 5 %/logarithmic time, it was necessary to evaluate it as this varied from sensor to sensor.

The drift was minimised according to the calibration curves in Figure 3-10(a). The plot illustrates the pressure drift associated with the sensor under different applied loads. When plotted on a semilogarithmic plot, as given in Figure 3-10(b), a linear function can be fitted to the data. The drift gradient m_{drift} for each of the curves was used to approximate the amount of generated drift per logarithmic time, resulting in a drift correction σ_{drift} of the form: $\sigma_{drift} = m_{drift}\,[ln(t)] + \sigma_{applied}$, where σ is the stress component in kPa and t is time in seconds.

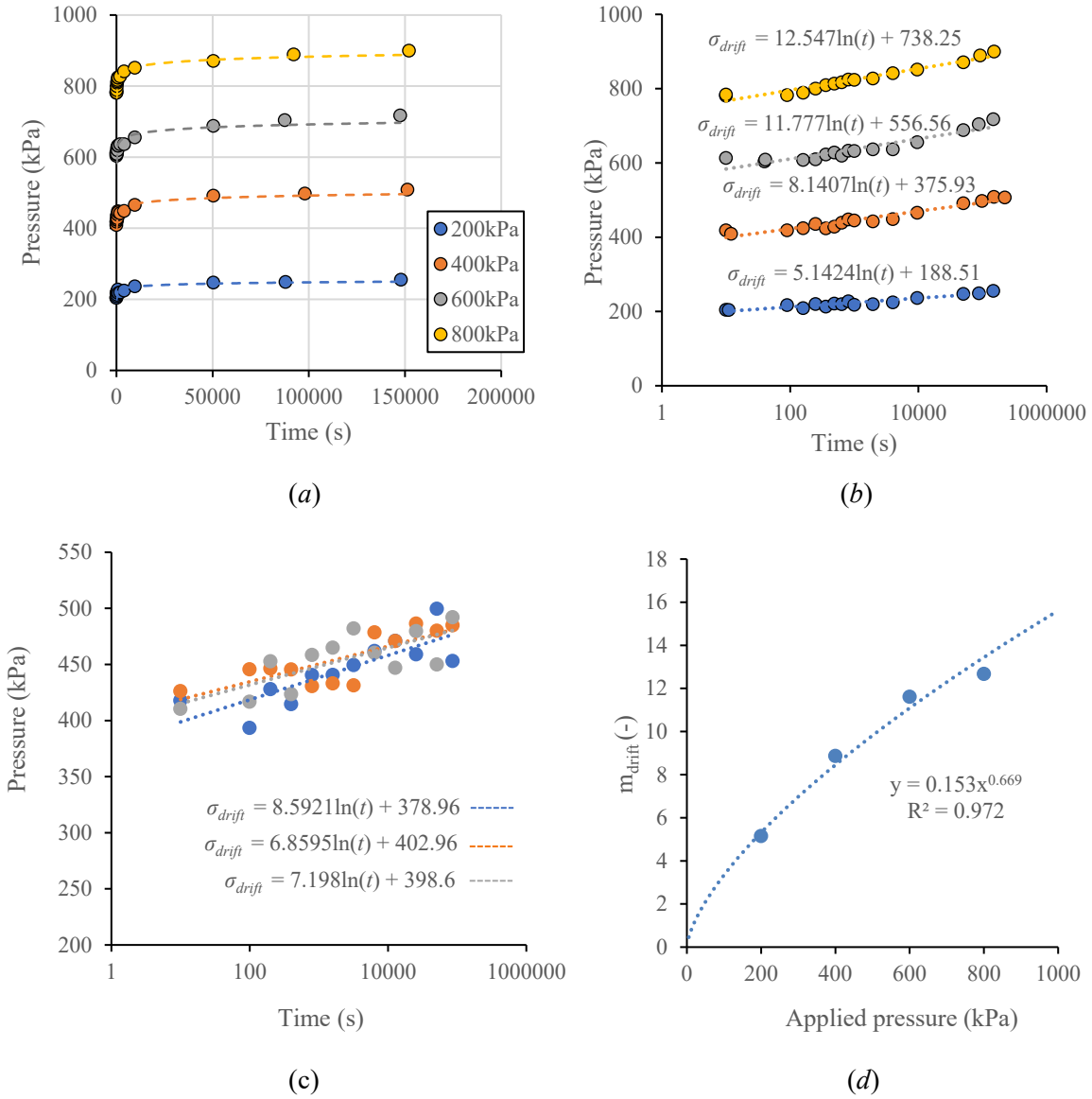


Figure 3-10: (*a*) Pressure drift under different applied loads (*b*) Drift per logarithmic time (*c*) Sensor repeatability (*d*) Drift ratio versus applied pressure

In addition to the calibration process discussed, the sensor shows good repeatability, as evident in Figure 3-10(c). The sensor was subjected to 400 kPa pressure over 24 hours and repeated three times, giving a mean drift ratio of 7.55. Considering the linearity of the sensor, the ratio is in close agreement with the drift gradient of 8.141 (~93%) determined in Figure 3-10(b). Figure 3-10(d) provides an overview of the drift ratios used in the correction for the sensor. Once calibrated, the sensor was installed in between the membrane and the confining rings, as illustrated in Figure 3-11.

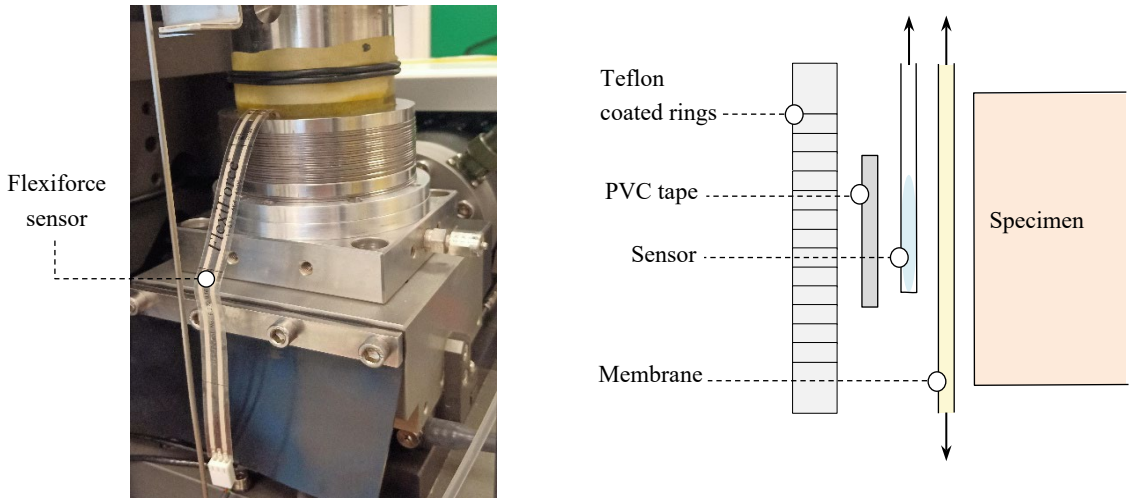


Figure 3-11: (*a*) Sensor in VDDCSS (*b*) Installation of sensor on sample

3.4.3 Wired reinforced membrane

A comparison was made between two different confinement techniques commonly used in practice, a wired reinforced membrane and Teflon-coated rings. The findings are discussed later in Section 5.5.4. The wired reinforced membranes (WRM) were supplied by NGI and designed to be stiffer to withstand the large stress magnitudes and strains associated with a stiff overconsolidated glacial till. Similar to the correction applied for the friction arising from the stack of rings, the membrane resistance was determined by filling up the membrane with water, followed by a shearing stage. A function was then fitted to the results and used as part of the correction procedure for WRM tests.

3.4.4 VDDCSS cyclic control

The VDDCSS has two horizontal actuators, allowing it to apply complex stress or strain paths. As part of the commissioning process, various multidirectional load paths (i.e. circular, figure 8, and spiral loops) were prescribed via the GDS Lab software interface, producing the displacement paths shown in Figure 3-12. The GDS Lab control and acquisition software can be used to define distinct testing stages. In addition to the standard module for consolidation and monotonic shear stages, the dynamic cyclic loading module can apply dynamic loads of a specific frequency, angle, and waveform. Custom load or

displacement paths in the form of a .csv file (e.g. 3 columns: Time, load in x-axis (F_x) and load in y-axis (F_y)) can be uploaded into the device, giving the user freedom to explore load paths such as pseudo-random cyclic tests. The arbitrary load path tests in Figure 3-12 were performed on a rotary core Cowden till sample that had already been tested and reconsolidated to its estimated in-situ vertical effective stress. The VDDCSS demonstrates the adequate control of the actuators at low stress levels and forms a valuable basis for applying more realistic storm loading histories. The actuators are highly accurate, encoder-controlled and can be used for both displacement and load controlled tests.

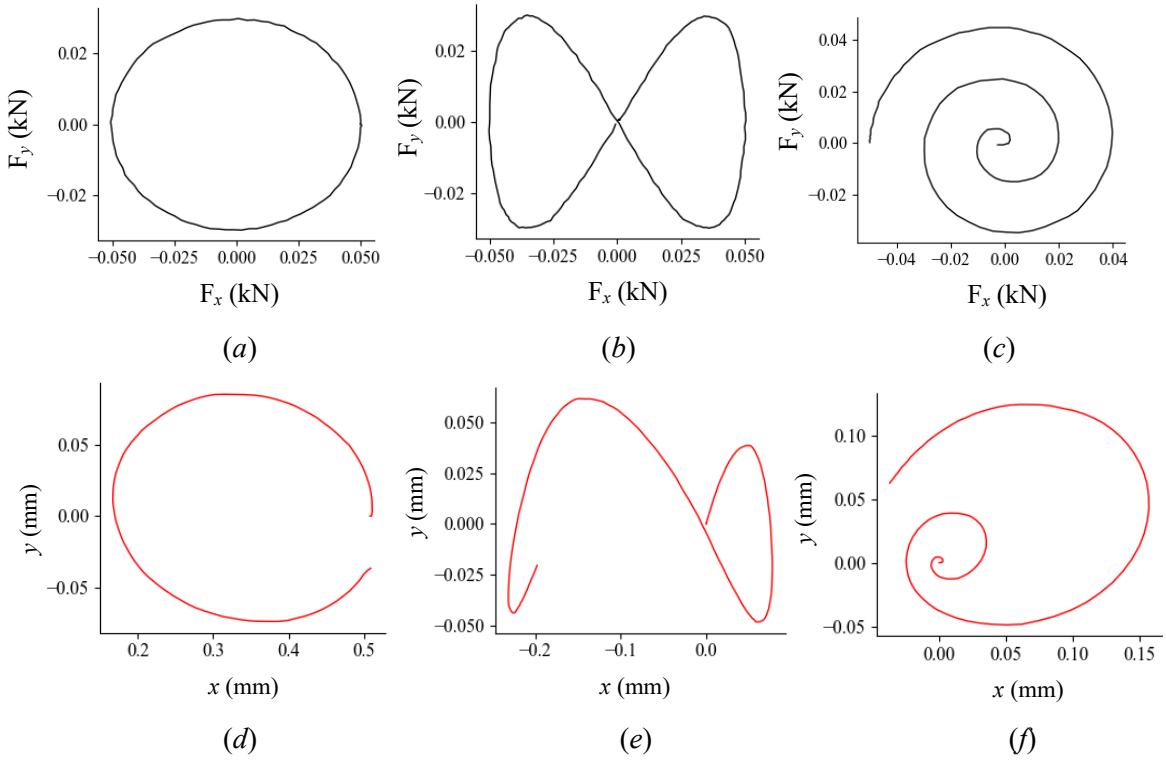


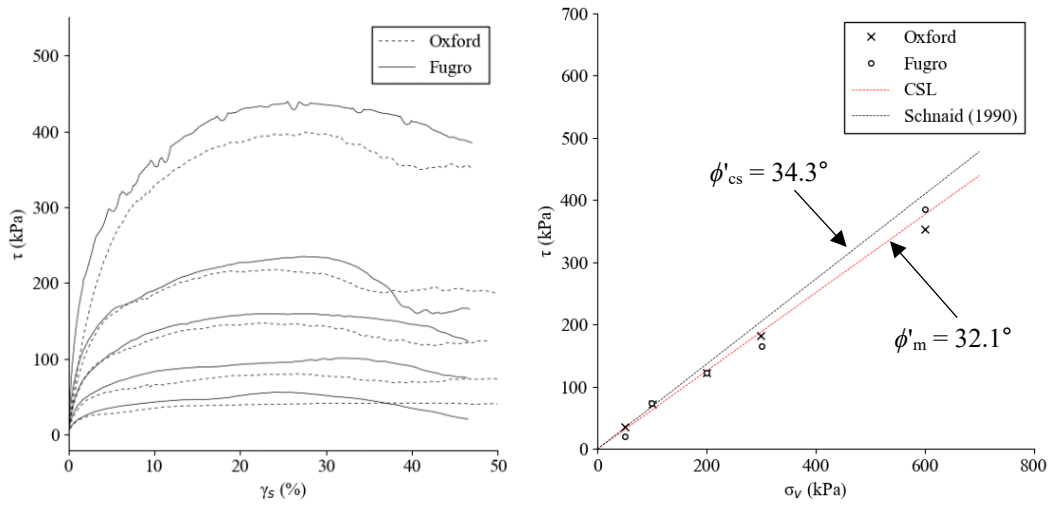
Figure 3-12: Load and displacement path for (*a*)+(*d*) circular loop, (*b*)+(*e*) figure 8 loop and (*c*)+(*f*) spiral loop test

3.4.5 Validation and repeatability

To fully commission the VDDCSS device, the performance of the hardware and control systems must be checked. Therefore, two main sets of commissioning tests were carried out. The first verified the performance of the VDDCSS by comparison with a simple shear device in a commercial laboratory, and the second involved verifying the repeatability of the tests.

All tests were carried out under constant vertical stress conditions using Fraction B (14/25) Leighton Buzzard sand (LBS) and consolidated to various confining pressures (50-600 kPa).

As part of the first round of commissioning, direct simple shear (DSS) tests were conducted at Fugro GB Marine Ltd, located in Wallingford, UK, using their unidirectional simple shear devices. The tests conducted at Oxford replicated the results at Fugro. Though different sample heights were used, the measurements of mobilised friction angle ϕ'_m agreed closely with their Fugro counterparts (Figure 3-13(b)). However, the Oxford tests presented peak stresses slightly lower than the Fugro peak stresses. Accounting for specimen variability, the sample preparation method may have caused a slight difference in the targeted relative density (>80%), with the height of the compacted layers at Fugro not as closely monitored. Most samples exhibit a hardening and then softening behaviour before reaching steady-state conditions. Overall, the behaviour of LBS between the two different sets of tests was quite similar. The measured joint data determined a mobilised friction angle of ϕ'_m= 32.1°. While a similar friction angle was measured by Schnaid (1990) for LBS in a direct shear box (ϕ'_{cs} = 34.3°), the angles are not directly comparable due to differences in principal axis rotations. However, the value provides a close approximation to a DSS test.



(*a*) (*b*)

Figure 3-13: (*a*) Stress-strain plots for LBS tests at σ'_v = 50, 100, 200, 300 and 600 kPa (*b*) Comparison of results at steady state

The second set of commissioning tests focused on the repeatability of the DSS tests. Three identical tests were performed, two on the *x*-axis and one on the *y*-axis. The tests should yield consistent results if the transducers and load cells have been correctly calibrated and consistent sample preparation has been followed. Figure 3-14 and Table 3-3 demonstrated this to be the case. As a result, the VDDCSS was concluded to be fully commissioned.

Table 3-3: Repeatability test outputs for LBS

Variable	Symbol	Units	Test 1	Test 2	Test 3
Vertical effective stress	σ'_v	kPa	50	50	50
Relative density	R_d	%	80.63	83.02	82.48
Peak shear stress	τ_{peak}	kPa	42.26	43.18	42.80
Strain at peak stress	$\gamma_{s,peak}$	%	37.81	23.16	30.00
Critical shear stress	$\tau_{critical}$	kPa	39.55	39.11	39.28
Initial void ratio	$e_{initial}$	-	0.599	0.593	0.594
Final void ratio	e_{final}	-	0.671	0.670	0.654

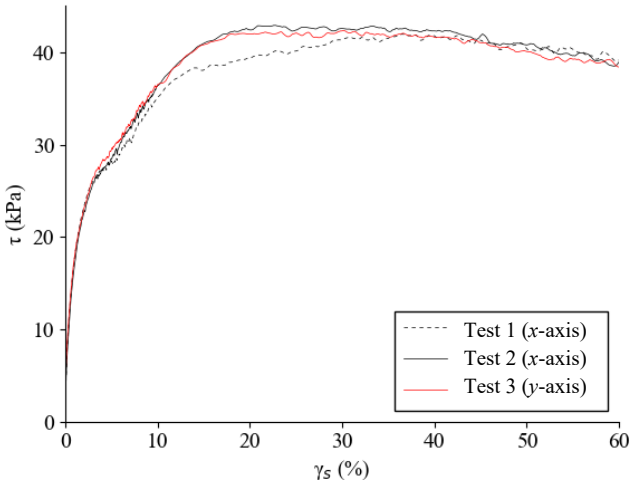


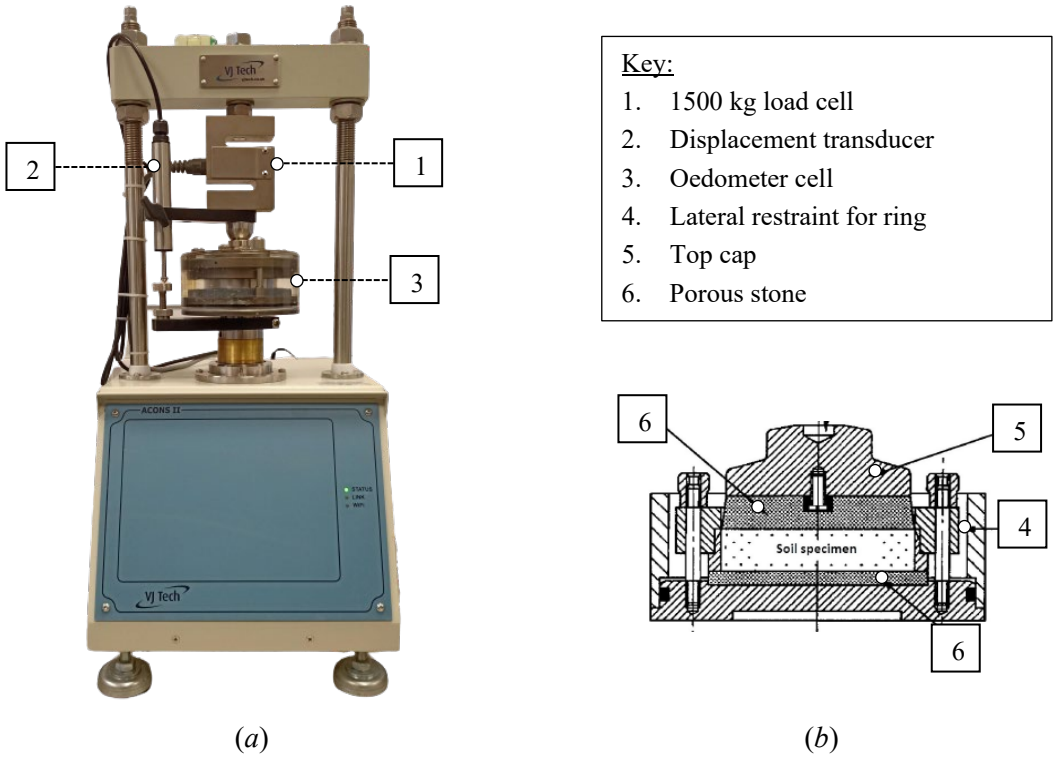
Figure 3-14: Repeatability of LBS tests in VDDCSS

3.5 Supplementary element tests

Supplementary oedometer and triaxial tests were carried out to understand further aspects of the soil's behaviour. The former was used to investigate one-dimensional compression and swelling behaviour, while the latter was used as a benchmark for the DSS tests. The resolution and accuracy of the two systems are summarised at the end of this section.

3.5.1 Oedometer apparatus

The oedometer used in this research is shown in Figure 3-15. It was manufactured by VJ Tech and could apply a maximum load of 14.7 kN, offering a maximum pressure of 7.5 MPa for a 50 mm diameter specimen. The oedometer cell, as seen below, consists of a stainless steel confining ring fitted into the restraining frame via bolts through the base of the cell. The cell consists of two porous stones placed at the ends of the soil specimen, along with filter paper to prevent the stones from clogging. The cell assembly was submerged in water to prevent the sample from drying during testing. For all oedometer tests, a 50 mm specimen with a 20 mm height was used (D/H = 2.5). The vertical displacements and applied loads were measured by a displacement transducer and load cell, respectively, and logged using the CLISP Studio software. The transducer had a resolution of 0.001 mm with no noticeable drift due to temperature. Like the VDDCSS, the oedometer measurements were also corrected for compliance.



(*a*) (*b*)

Figure 3-15: (*a*) VJ Tech oedometer apparatus (*b*) Details of typical oedometer cell
Source: (BS 1377:1990)

After the sample preparation and water content measurement, the procedure followed closely the guidelines set out in the BS EN ISO 17892-5:2017 standard. The loading sequence consisted of multiple loading stages, with each stage increasing in load by a factor of two. Due to the nature of Cowden till (i.e. heavily overconsolidated), specimens were loaded to a maximum of 6.4 MPa, with each increment given a hold period of 24 hours.

Given the magnitude of the loads, a degree of compliance was expected in the apparatus. Based on an initial compliance check through the loading of an empty cell, a correction of the form $y = 0.079ln(x)-0.203$ was used, where y is the compliance correction in mm and x is the axial load in kN. One of the main outputs from an oedometer test is the preconsolidation pressure σ'_{vc}, defined as the maximum vertical effective overburden stress the sample has experienced in its history. Estimation tools such as the standard Casagrande bisection method are often used to determine σ'_{vc}. However, such techniques rely on determining the point of maximum curvature on a semilogarithmic plot. Without a rigorous approach, such an estimation is prone to highly variable values of σ'_{vc}. To avoid such discrepancies, a curvature function κ was used (Gregory et al., 2006; Keller et al., 2011).

$$\kappa = \frac{\frac{d^2e}{d(log\sigma)^2}}{\left[1+\left(\frac{de}{d(log\sigma)}\right)^2\right]^{\frac{3}{2}}} \tag{3-1}$$

where e is a fourth-order polynomial curve fitted to the oedometer data. The point of maximum curvature is where $\frac{d\kappa}{d(log\sigma)} = 0$.

3.5.2 Triaxial apparatus

Monotonic triaxial tests were undertaken using the TriScan-100 Pro triaxial apparatus manufactured by VJ Tech, shown in Figure 3-16. The apparatus is identical to that used by White (2020) for investigating sand behaviour at low confining stresses. An internal submersible load cell (ISLC) with a 10 kN capacity was used for the tests presented in this

thesis. Due to sample recovery limitations (see Section 4.3) and the quality of tests required, a specimen 70 mm in diameter and 140 mm in height (H/D = 2) was used. A bespoke base pedestal and top cap were machined to accommodate these dimensions in the large triaxial cell measuring approximately 230 mm in diameter and 410 mm in length. The selected specimen dimensions allowed on-sample LVDTs, a mid-height pore water pressure probe, and horizontal bender elements to be attached.

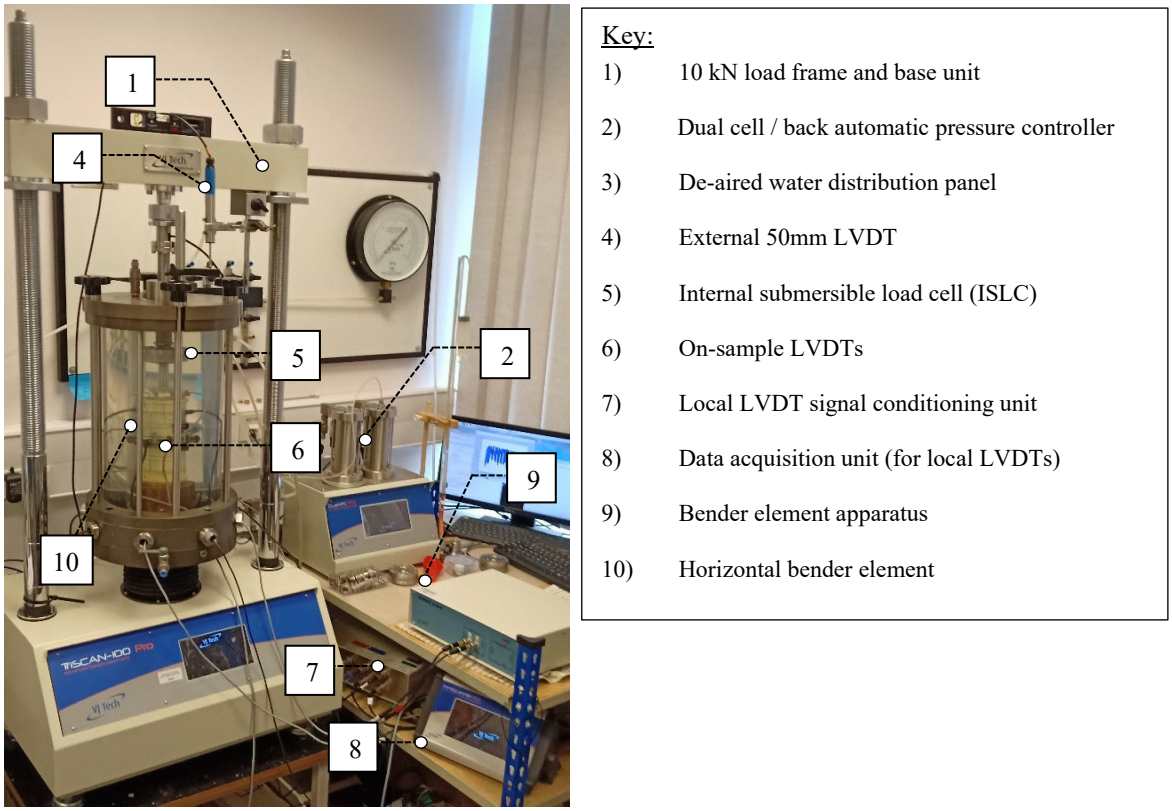


Figure 3-16: TriScan-100 Pro triaxial apparatus
Source: (White, 2020)

The test procedure followed for undrained compression and extension tests was based on the guidelines given by Lade (2016) and the approach adopted by Ushev (2017). For comparative purposes, saturation ramps, creep duration, and shearing rates were based on the latter as he produced a comparable database of high-quality triaxial tests on Cowden till. Various corrections were applied to the measured quantities, which included corrections for membrane resistance, cross-sectional area deformation, filter drains, and system compliance. The corrections follow those recommended by Lade (2016).

Test procedure:

3.5.2.1 Test set-up:

After trimming the sample to its desired dimensions, a latex membrane with appropriate incisions to accommodate the bender elements and a mid-height probe was prepared. The incisions are later sealed with silicone sealant. This was followed by de-airing the porous stones and all the water supply/drainage lines. The sample was placed on top of the base pedestal with porous stones and circular filter drains at each end. Vertical filter drains were installed on the specimen surface before placing the top cap. Using membrane stretchers, the sample was enclosed with the latex membrane and then sealed off using o-rings. To ensure water-tightness, a layer of high-vacuum silicon grease was placed on the sides of the base pedestal and top cap, thus forming a better seal with the membrane. All local instrumentation was then mounted onto the sample (i.e. LVDTs, bender element, and mid-height probe) and the displacement transducers were set to their correct voltage range. The cell was then assembled, and flooded with water and the submerged load cell, which is connected to the triaxial cell's crossbeam via a load ram, was zeroed using the Clisp Studio software. This initial reading does not account for the weight of the top cap and was suitably offset in the processing stage.

The next stage involved manually docking the ISLC with the top cap. This was done with extreme care by lowering the threaded connection of the ISLC into the centre of the top cap, making sure not to over-torque and disturb the sample. Once connected, using the stepper motor's displacement and load control commands, the pedestal was raised until it reached the crossbeam connection and then screwed together. This process involved entering a small target axial force value into the control software (i.e. 5N) to carefully screw the crossbeam to load the ram connection until it was fully secured. Once docked, the cell pressure and back pressure were increased to 10 kPa and 0 kPa, respectively, whilst maintaining a zero axial load.

3.5.2.2 Saturation:

For undrained compression and extension tests, the specimens were saturated by applying cell pressure and back pressure in stages at a rate of 20 kPa/h. The specimen was presumed to be fully saturated once the saturation check B value, given by Equation (3-2), was > 0.95.

$$B = \frac{\Delta u}{\Delta \sigma_c} \tag{3-2}$$

where Δu is the change in pore pressure and $\Delta \sigma_c$ the change in cell pressure. This criterion was generally reached at a cell pressure between 400-500 kPa. At the end of this stage, the mean effective stress $p'_{initial}$ was recorded.

3.5.2.3 Consolidation:

Like the DSS tests, the samples were either overloaded under drained conditions to 80% of σ'_{vc} before unloading to the estimated in-situ mean effective stress (Figure 3-17(b)) or reconsolidated directly to the in-situ stress (Figure 3-17(a)). The tests were carried out assuming the K_0 profile given in Section 4.8. A consolidation rate of 1 kPa/h was used and this was deemed slow enough to prevent the build-up of excess pore pressures. This was achieved by ensuring good agreement between the mid-height probe and the base pore pressure transducer. Furthermore, the excess pore-water pressure was checked not to exceed 5% of the mean effective stress (Fugro, 2020). After the consolidation stage, the soil was given sufficient time to rest until a creep rate 1000 times lower than the shearing rate was reached (typically 24-48 hours).

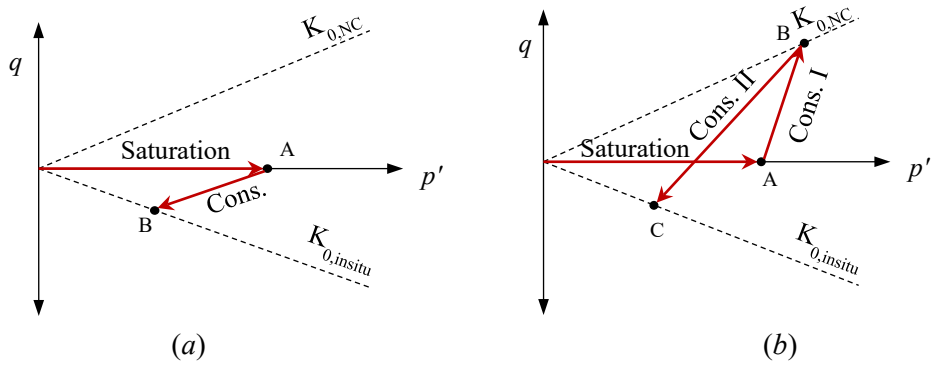


Figure 3-17: (*a*) Standard K_0 consolidation (*b*) Overloaded consolidation

3.5.2.4 Monotonic shear:

Before shearing, the horizontal and vertical stiffnesses of the sample were captured using bender elements. Then, strain-controlled undrained compression or extension tests were performed at the standard rate of 5% axial strain per day (Ushev, 2017). Based on the preliminary DSS tests, the Cowden till samples exhibited high plastic strains. As a result, the triaxial compression tests were usually continued to ~30% axial strain.

3.5.3 Equipment specification

For both the oedometer and triaxial apparatus, load cells and displacement transducers were calibrated approximately every six months to an accuracy of ±1N and ±0.001 mm, respectively. Below is a summary of the accuracy and resolution of the supplementary equipment used in this research.

Table 3.4: Accuracy and resolution of triaxial and oedometer transducers

Transducer	Units	Unit range	Sensitivity	Noise amplitude*	Resolution
Oedometer apparatus					
Load cell (15kN)	N	±15 000	2.1074 mV/V	1.1	0.320
Displacement transducer	mm	0-25	7.072 mV/V	0.02	0.001
Triaxial apparatus					
Load cell (10kN)	N	±10 000	2.2091 mV/V	0.8	0.270
Volume controller	cm^3	0-250	-	0.006	0.001
Pressure transducer	kPa	0-1000	-	0.13	0.012
LVDT	mm	0-5	-0.0002863 mm/mV	0.0013	0.001
Displacement transducer	mm	0-50	7.798 mV/V	0.006	0.003

*These values were calculated based on one standard deviation

3.6 Summary

This chapter has provided details on the equipment used throughout this research project, which included the VDDCSS, triaxial, and oedometer apparatus. The VDDCSS is the main hardware used and is controlled via firmware and software written by GDS Instruments. The commissioning of the simple shear testing device included devising corrections for mechanical friction (membrane and Teflon-coated rings) and systematic errors (vertical compliance). This allowed the removal of unwanted effects in the device so that improved simple shear tests could be performed. Some modifications were also made. These included replacing the LVDT armature with one made out of 'invar' alloy to combat temperature effects, the use of thick rings to improve interface contact, and the use of a lateral pressure sensor to measure lateral stresses on the sample.

Evaluations of the VDDCSS also included repeatability tests and the accuracy of the stress/strain control when using the advanced cyclic control module. Based on the tests performed and corrections applied, the apparatus was suitably commissioned for high-quality element testing, along with the oedometer and triaxial devices. Relevant corrections were also applied to the supplementary element test kits, ensuring accuracy and confidence in the results. All procedures outlined in this chapter follow best practice to generate a high-quality database of experimental tests.

Chapter 4

Site description and soil characterisation

4.1 Introduction

The Cowden test site was selected as part of the PICASO project to represent a clay profile of the type typically encountered for offshore wind turbine monopile foundations in the North Sea. As a result, the soil profile needed to be uniform with sufficient thickness to accommodate the embedded length (~7.5m) of the largest piles for the medium-scale field testing. Furthermore, the water table needed to be close to the finished ground level to ensure complete soil saturation (Martin, 2023). This section covers the formation of Cowden till clay, also known as 'boulder clay', and its geotechnical properties identified through site investigation works and those documented in the literature. Further details about the site and the field testing programme can be found in Martin (2023).

4.2 Cowden till formation

The Cowden test site is in the North-East of England as pointed out in Figure 4-1. Due to the similarities between the PICASO and PISA projects (Byrne et al., 2015, 2017; Zdravković et al., 2019), and their proximity to one another, the locations of both sites are shown in Figure 4-2. The PICASO site can draw valuable knowledge from the PISA site, which includes an extensive database of soil characterisation and laboratory tests (Ushev,

2017), supplemented with historical data from the Building Research Establishment (BRE) test site neighbouring it (Powell and Butcher, 2003). These sites fall in the same geological unit, thus adding site-specific data for the PICASO site.



Figure 4-1: Location of PICASO Cowden test site
Source: (www.google.co.uk/maps)



Figure 4-2: Satellite image of PICASO, BRE and PISA test sites
Source: (www.google.co.uk/maps)

A site investigation was carried out to build on the historical data provided by Powell et al. (2003) and the PISA field tests (Zdravković et al., 2015). Six Geobore-S triple barrel wireline boreholes were used for logging the stratigraphy and obtaining samples for laboratory testing. The boreholes were advanced to depths between 11.25m and 20m below ground level (BGL). The ground conditions within these depths consisted mainly of overconsolidated glacial till overlying Cretaceous chalk. Additionally, the glacial till layer had traces of sandy silt bands of approximately 1m to 3m thickness. The till material,

henceforth known as Cowden till, is described as a weathered or unweathered firm to stiff stony brown clay, as highlighted by the site's stratigraphy in Table 4-1. A more in-depth analysis of the site stratigraphy is covered by Martin (2023).

Research by Davies et al. (2011) indicates that Cowden is located within the Bolders Bank Formation, suggesting a subglacial till origin, where the soil is subjected to intense deformation at high pressure in a confined saturated environment. Upon inspection, the samples generally consist of a stiff dark brown silty-clay matrix with gravel-sized clasts and occasional chalk traces. This observation is typical of the Bolders Bank Formation created during the Devensian and Wolstonian glaciation periods, as described by Davies et al. (2011).

Beyond the depths of interest, the clay till can be expected to be underlain by chalk at approximately 40m depth (Powell et al., 2003). The site was excavated to a reduced level (RL) of 10.8 mAOD (i.e. metres above ordinance datum) for the medium-scale field testing, which took place after the in-situ testing. This corresponded to approximately 1.7m to 3.2m of excavation across the test area.

Table 4-1: Stratigraphy of PICASO Cowden site

Reduced level (mAOD)	Depth (mBGL)	Material	Description
10.8 to 4.0	0 to 6.8	Withernsea till	Unweathered brown stiff stony clay till with fissures
4.0 to -29.2	6.8 to 40	Skipsea till	Unweathered dark brown stiff stony clay till with bands of silty sand, most notably between 4 to 1 mAOD
< -29.2	> 40	Chalk	-

Based on the piezometers installed during the in-situ testing, the groundwater level is estimated to be just below the finished surface level (~0.5m). The PICASO piezometer measurements in Figure 4-3 indicate a potentially under-drained pore water pressure distribution occurring at the silty sand layer, similar to behaviours documented by Zdravković et al. (2019) and Powell and Butcher (2003) in similar regions.

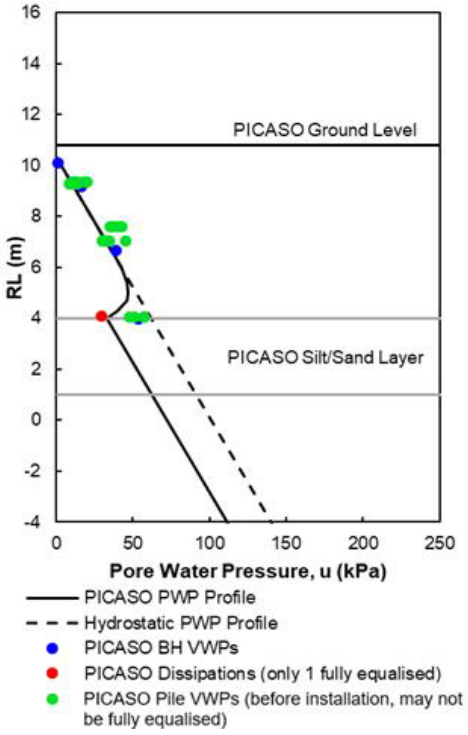


Figure 4-3: Pore water pressure measurements at PICASO Cowden site
Source: (Martın, 2023)

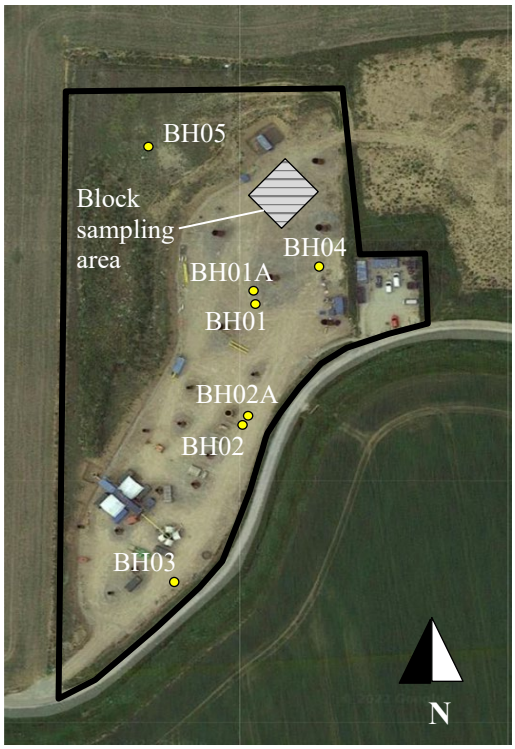


Figure 4-4: Location of boreholes and block sampling area

4.3 Soil sampling

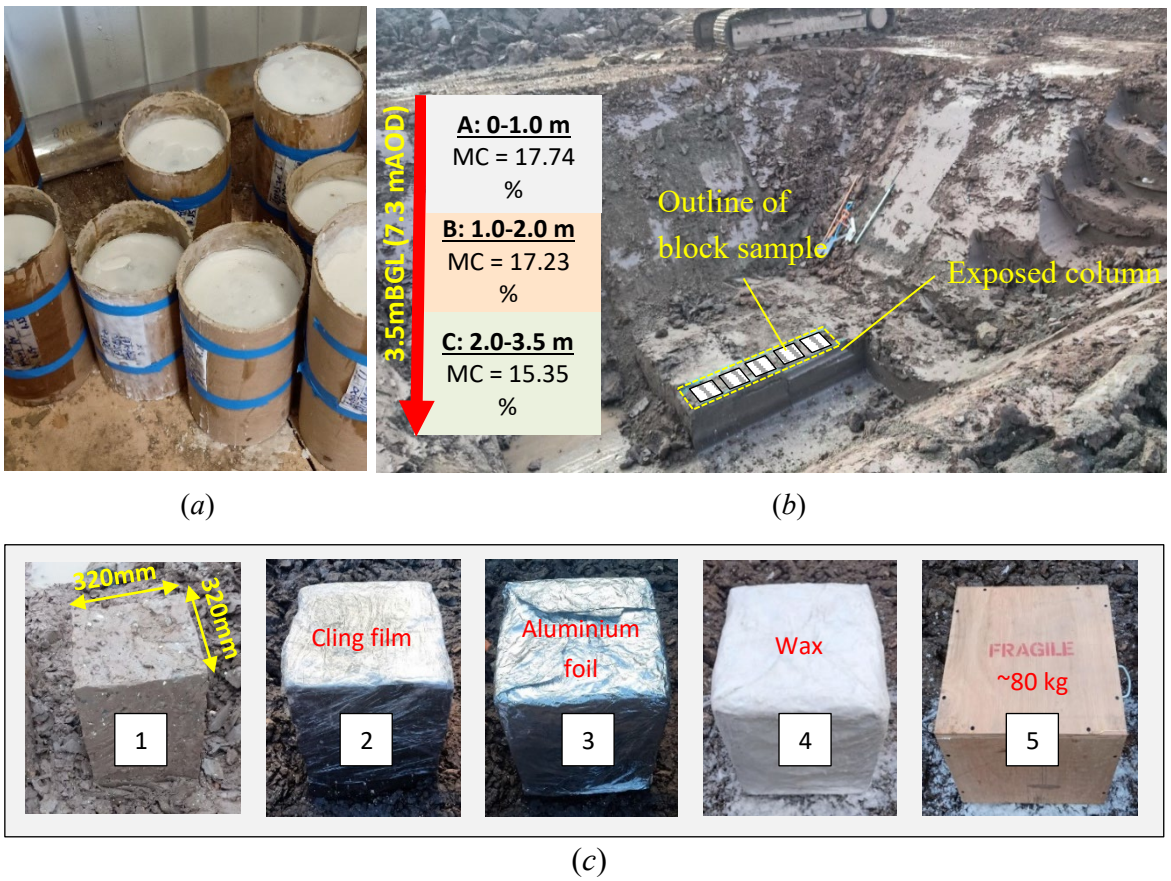
Two different types of samples were extracted from the Cowden site: (a) rotary core (RC) and (b) block samples (BS). RC samples were taken from the site in 2019 from the 23rd of September to the 3rd of October, employing rotary coring at six locations (BH01 to BH04), as shown in Figure 4-4 and Table 4-2, before the installation of the PICASO test piles. Supplementary core samples (BH05) were taken from the site in 2021 (23rd - 25th February) to provide further insight into the quality of the samples (Figure 4-5(a)). After the medium-scale field testing, the block samples were collected from a mechanically excavated trial pit positioned between BH04 and BH05 from the 24th of January to the 5th of February 2022.

Table 4-2: Coordinates of boreholes at PICASO Cowden test site

Borehole No.	Latitude	Longitude	Ground level (RL: mAOD)
1	53° 50' 27.28" N	0° 7' 9.58" W	12.709
1A	53° 50' 27.37" N	0° 7' 9.61" W	12.687
2	53° 50' 25.91" N	0° 7' 9.98" W	12.496
2A	53° 50' 26.01" N	0° 7' 9.90" W	12.509
3	53° 50' 24.25" N	0° 7' 11.14" W	12.633
4	53° 50' 28.57"N	0° 7' 8.74" W	12.771
5	53° 50' 29.19" N	0° 7' 11.33" W	15.080

In total, 21 block samples from three different horizons (seven in each) were taken, reaching a depth of 3.5 mBGL (7.3 mAOD) (see Figure 4-5 (b)). An excavator was used to remove the piling mat from the work area and soil down to the middle of the first horizon (A:0-1 mBGL). The excavator then created a 0.5m wide and 2m in length central column of soil by excavating the soil adjacent to the bottom of the horizon before battering it for safe entry.

The samples were then shaped into 320 mm by 320 mm blocks using sharp spades. The samples were then preserved using two layers of cling film, aluminium foil and ozokerite wax (Figure 4-5 (c)). Next, an extra layer of the same arrangement was applied for additional protection, followed by lining the plywood box with expanding foam and placing it over the block. Once the block was detached from the ground and sealed, the process was repeated for each block in each horizon. The samples were then safely transported back to Oxford and stored.



(*a*) (*b*)

(*c*)

Figure 4-5: (*a*) Preserved rotary core sample from BH05 (*b*) Excavated pit down to 3.5 mBGL with exposed column of soil (*c*) Procedure for preservation of block samples

4.4 Sample quality

This research focused on the high-quality element testing of Cowden till. Therefore, samples retrieved from the site needed to be carefully handled and stored before testing. However, some of the samples from BH01 to BH04, unfortunately, did not meet the quality standards set out for this campaign. While they were cautiously handled, sample disturbance was unavoidable due to the limitations of the rotary coring system and heavy rainfall. As covered by Dahl et al. (2010), the effects of sample disturbance can be attributed to the many events experienced by the sample from extraction to testing (see Figure 4-6). Each event induces a certain amount of shear strain and loss in vertical effective stress σ'_v, meaning recompression to the same in-situ σ'_v may not establish the same mean effective stress p', as the developed horizontal stresses may be lower than the in-situ value (Dahl et al., 2010).

For overconsolidated soils, sample disturbance generally causes a decrease in the undrained shear strength. However, the effects can be minimised by following the modified recompression technique proposed by Ladd and Degroot (2003), where DSS specimens are preloaded (also referred to as overloading) to 80% of the estimated in-situ preconsolidation stress σ'_{vc} and then unloaded to the in-situ σ'_v before shearing. This allows the sample to replicate a portion of its stress history, provided a reasonable estimate of the σ'_{vc} is made. In contrast, loading the specimen to the in-situ stress alone will give smaller K_0 values in the DSS device compared to the in-situ K_0, leading to a softer and weaker response from the specimen (ASTM D8296-19, 2019).

The sample quality can be assessed using different techniques; (a) the amount of volumetric strain ε_v induced during reconsolidation (Terzaghi et al., 1996), (b) the change in void ratio relative to the initial void ratio ($\Delta e/e_0$) as proposed by Lunne et al. (1997), (c) the measurement of the oedometer stiffness ratio (M_0/M_L) as used by Karlsrud and Hernandez-Martinez (2013), and (d) initial suction measurements, which can be determined using the "filter paper" method (Chandler et al., 1986; Bicalho et al., 2006) or with a tensiometer

(Poirier et al., 2005; Donohue and Long, 2009). All four techniques employed in this research have shown the quality of the sample to be primarily affected by the extraction method. For advanced element testing, block samples are preferred as they provide the highest quality samples available for onshore practice (Lunne et al., 2011).

As observed by Ushev (2017) and Liu (2018), the initial effective stresses developed in the Cowden till samples were susceptible to the specimens' state during field sampling and test preparation. As a result, due to drying and sample disturbance, the suction measurements using the techniques described could not offer any reliable information regarding in-situ conditions. From the preliminary tests, samples from BH01 to BH05 were generally graded as "very poor" to "poor" (covered further in Section 5.9). Apart from the damage caused by drilling, it was suspected that the samples may have swelled due to prolonged exposure to water. Nonetheless, samples were layered in cellophane and aluminium foil, placed in cardboard tubes and submerged in ozokerite wax to preserve the samples in their as-extracted state. One of the main concerns with the testing of Cowden till was the unforeseen clusters of boulders and gravels in the specimen matrix. Zdravković et al. (2019) states, "Despite the till's stony nature, its finer matrix dominates its mechanical properties". This statement is supported by research on reconstituted and remoulded tests performed by various researchers (Lau, 1988; Atkinson et al., 1991; Ushev, 2017).

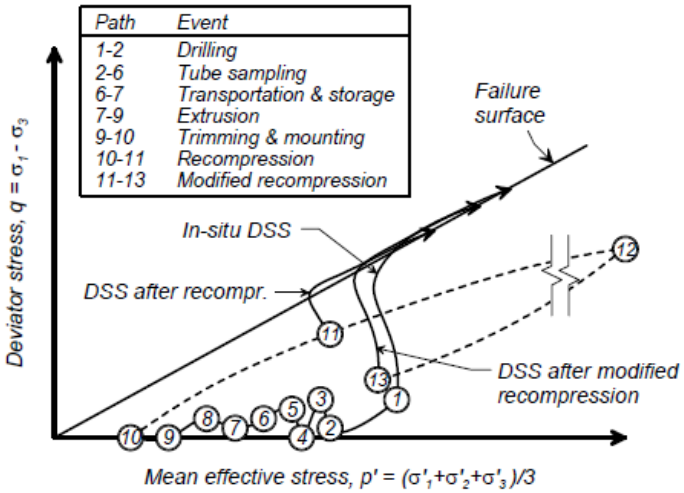


Figure 4-6: Effect of sample disturbance
Source: (Dahl et al., 2010)

4.5 Index properties of test material

A summary of the index properties (i.e. water content w, specific gravity G_s, plasticity index PI, and bulk density ρ) for Cowden till is given in Table 4-3. The variations of these properties with depth are shown in Figure 4-7, alongside the index properties measured during the PISA project (Zdravković et al., 2020). The measurements are relatively consistent from 2 to 18m below ground level (BGL), with more significant variability present at the surface. The depths reported in Figure 4-7 reflect pre-excavation levels; the final ground level sits at ~2 mBGL or at a reduced level (RL) of 10.8 mAOD.

Table 4-3: Summary of Cowden till parameters

	Water content, w (%)	**Bulk density, ρ (Mg/m^3)**	**Specific gravity, G_s**	**Liquid limit, LL**	**Plastic limit, PL**	**Plasticity index, PI**	**%Fines**
	12-31	2.04 – 2.23	2.66 – 2.71	28 – 53	15 – 24	13 – 29	53 – 96
Mean:	18	2.16	2.68	37	18	19.1	-

The different soil characterisation tests followed the procedures described in the relevant British Standard (BS 1377-2: 1990). In addition to index tests carried out in the laboratory, tests performed by Socotech UK Ltd on 14 different specimens were also included, covering the soil profile of interest (0 to 20 mBGL (10.8 to -9.2 mAOD)). This proved useful for comparison and quality control. Figure 4-7 (a) to (d) shows that the PICASO material has similar index soil properties to those measured for PISA (Ushev, 2017). The figures are not presented against the reduced level (i.e. mAOD) as the PISA site is at an elevation ~5m above the PICASO site.

Figure 4-7 (a) presents the natural water content distribution with depth for the PICASO site. The water content in the top 2m is approximately 20% higher than the consistent values for the rest of the depth. It is probably affected by seasonal variations and drainage infrastructure in the area. The measurements were taken from the laboratory's rotary core trimmings and some on-site measurements during the block sampling. While the shape of the profile shows good agreement with the PISA values, the RC samples tended to

have water contents 1-2% higher than the block samples, due to possible water intake during Geobor-S sampling and heavy rainfall. For depths lower than 2 mBGL (8.8 mAOD), the water content ranges from 15-18%. In cases where moisture contents were recorded in the upper range (>18%), this may be due to the presence of a sand layer in the region where the clay has been allowed to swell.

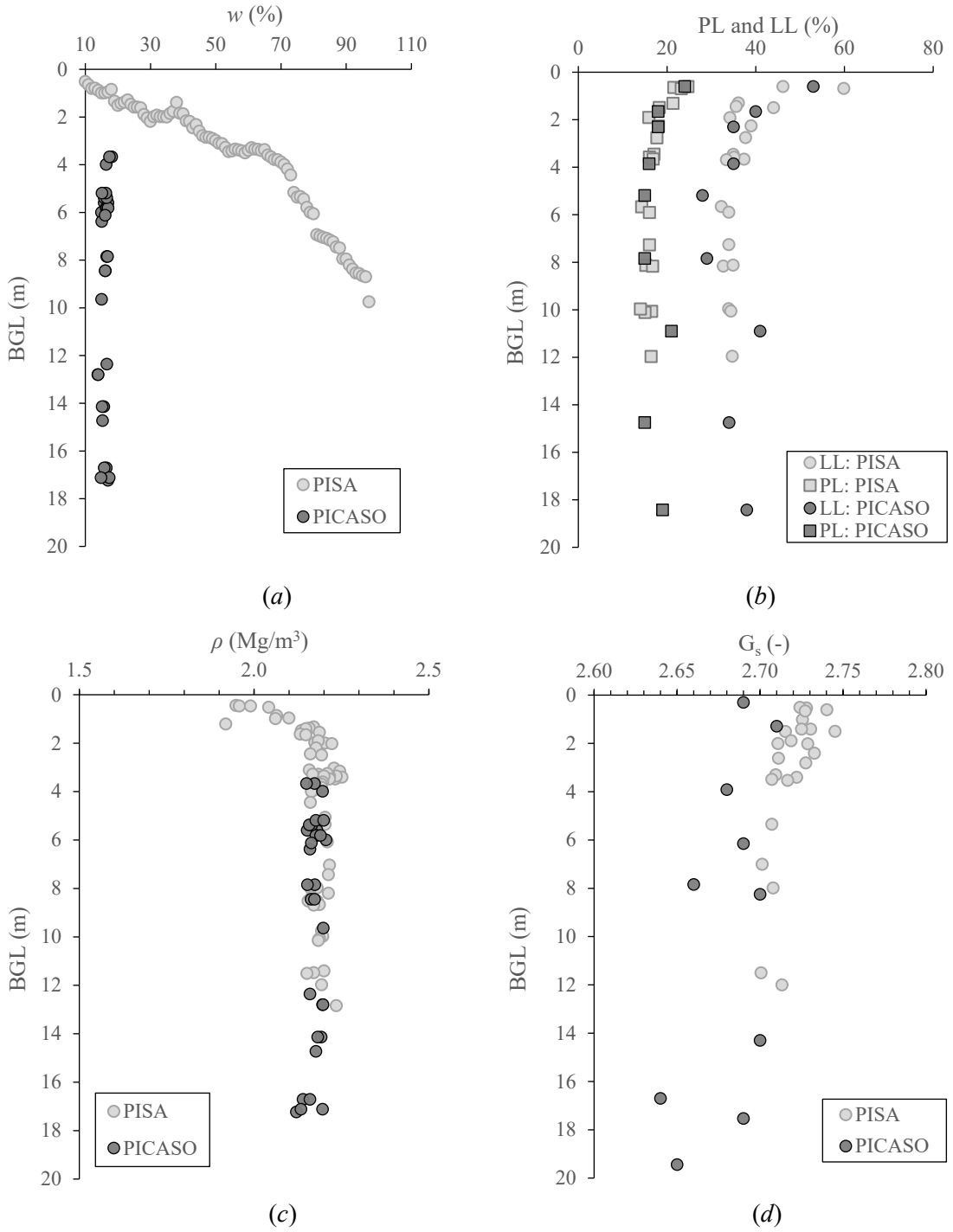


Figure 4-7: Index properties of Cowden till with depth: (*a*) water content, (*b*) plasticity, (*c*) bulk density and (*d*) specific gravity

The average unit weight of the RC samples ranged from 20.0 to 21.9 kN/m^3, with a mean of 21.2 kN/m^3. The values lie close to the range of unit weights of 18.8 to 22.1 kN/m^3 obtained for the PISA project (Ushev, 2017). The specific gravity of the RC samples was measured using the small pyknometer method (BS 1377:1990). Each point represents an average of two readings, varying between 2.62 to 2.72 and an average of 2.68. The lower range values likely reflect regions with higher silt and sand content.

The LL and PL from the PICASO project follow a similar trend to the PISA profile, decreasing rapidly in the top 1.0m, moving from 50% to 30% and 25% to 16%, respectively (Lehane, 1992; Powell et al., 2003; Ushev, 2017). The Casagrande plasticity chart in Figure 4-8 classifies Cowden till as a low to intermediate plasticity clay (CL to CI) with depth.

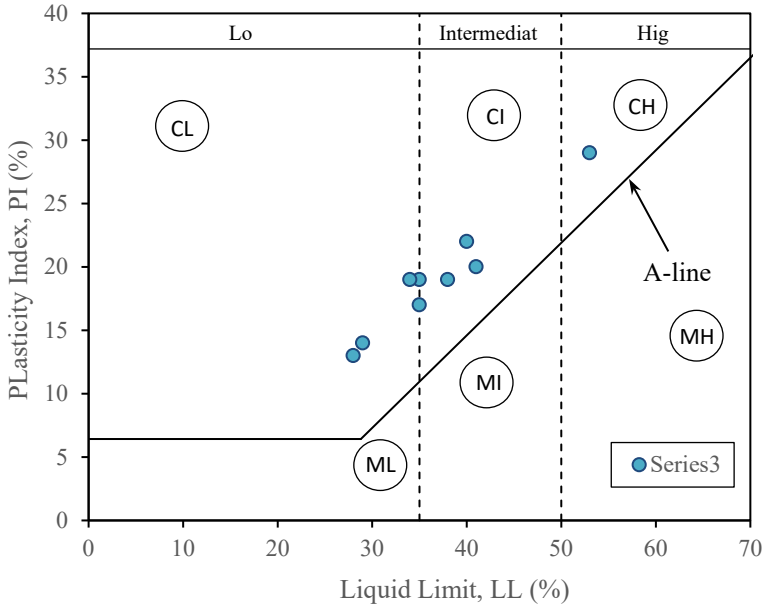


Figure 4-8: Casagrande plasticity chart for PICASO CWD samples

4.6 Grading and composition

Previous studies have shown Cowden till to be well-graded and uniform (Lehane, 1992; Powell et al., 2003; Ushev, 2017). Figure 4-9 shows that the Cowden material recovered for PICASO has similar grading characteristics to those reported previously. The particle size distribution (PSD) for the till is mainly similar for most of the profile, indicating contents of approximately 30-40% clay, 40-50% silt, 20-30% sand and 10-20% gravel. The granular

fraction primarily consists of chalk (>50%), with the remainder including flint, sandstone, limestone and quartzite. These findings are consistent with those of Powell et al. (2003) and Lehane (1992). Layers of sand are apparent in the profile but are not included in the grading analysis.

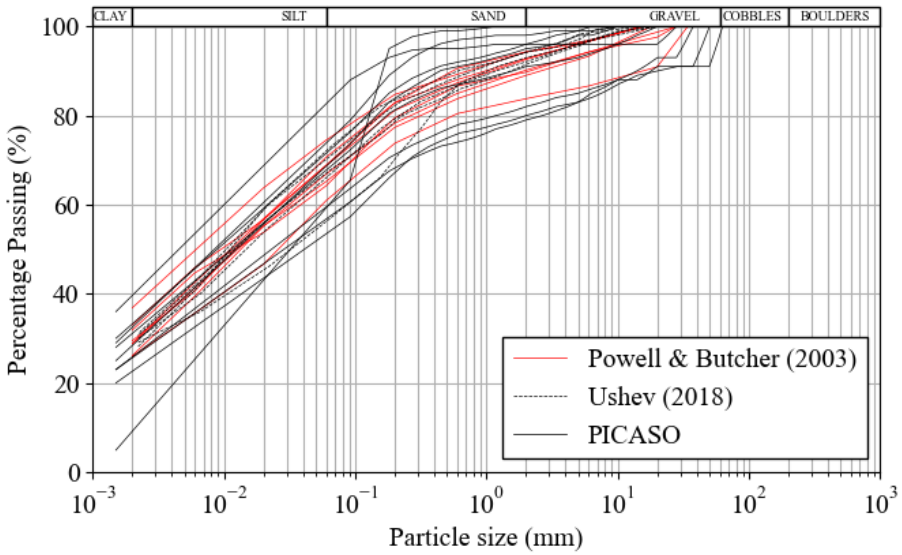


Figure 4-9: Particle size distribution (PSD) of Cowden till

4.7 CPT profiles

The site investigation included 23 cone penetration tests (CPT), including three seismic CPTs. For this strand of research, the cone resistance profiles of five CPTs corresponding to the relevant boreholes are presented in Figure 4-10. The CPTs are based on the final site level of 10.8 mAOD, which is approximately 2 mBGL. Each CPT measures the cone tip resistance q_t, sleeve friction f_s, and pore pressure u. The plots generally follow a consistent trend apart from discrete peaks observed in the cone resistance (>10 MPa) and sleeve friction (>0.2 MPa) measurements at various depths, corresponding to the silty sand layer observed in the boreholes. The silty sand layer, which is consistent across the site has been marked by shading on the plot. Outside of this zone, values for q_t are typically between 2-5 MPa and for f_s between 0.05-0.1 MPa. Unlike the profile from the BRE or PISA sites, where the first sand layer was located at 12.5 mBGL (~3.7 mAOD) (Lehane, 1992; Powell et al., 2003), the layer at PICASO is encountered at greater depth.

The pore pressure profile is relatively consistent from 10.8 to 1.0 mAOD, with values ranging from -0.06 to 0.04 MPa. A more significant scatter is observed past this depth, with measurements reaching as high as 1 MPa.

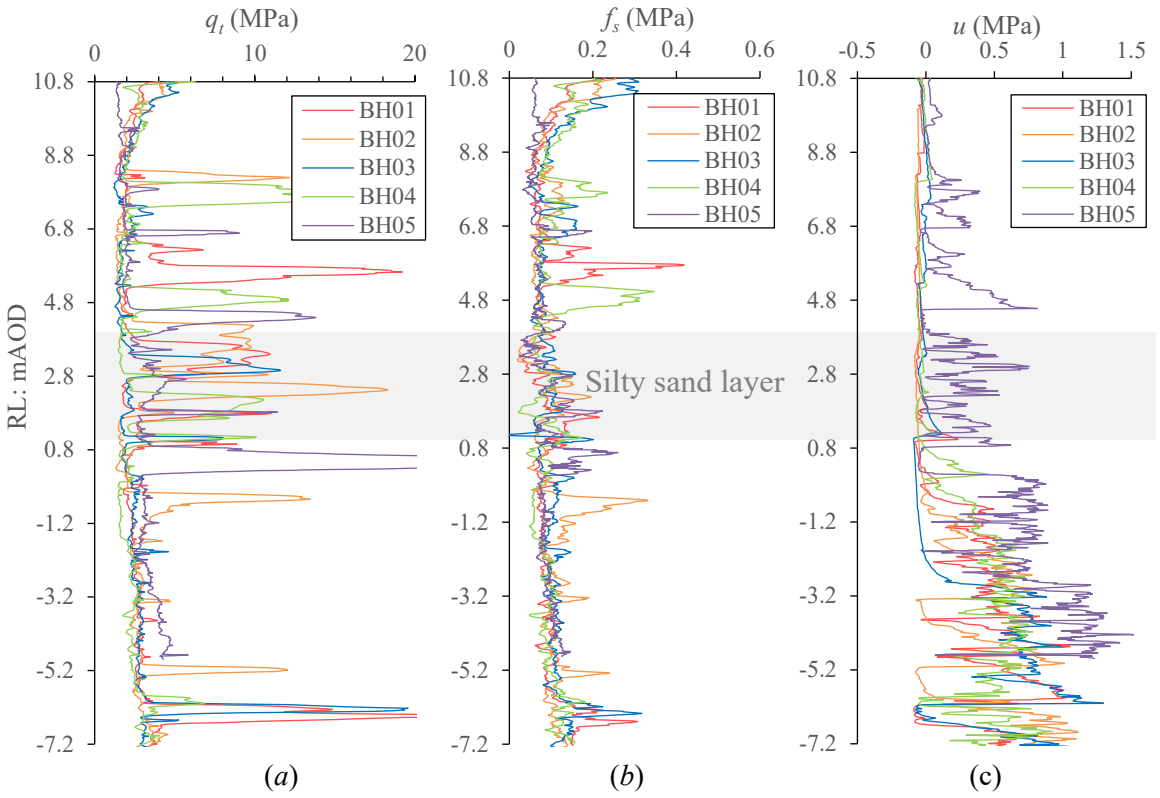


Figure 4-10: CPT measurements profiles for (*a*) cone resistance q_t, (*b*) sleeve friction f_s and (c) pore-water pressure u

4.8 Estimate of undrained shear strength, K_0 and OCR

The site characterisation includes approximating the profile of undrained shear strength s_u. This is done by correlating s_u with the CPT results through an empirical cone factor N_{kt}. Historically, N_{kt} = 14 to 16 and N_{kt} = 19 were used on the PISA site (Zdravković et al., 2020) and the BRE site (Lehane, 1992), respectively. However, based on a detailed N_{kt} assessment for the PICASO site (further details in Section 5.9), a value of 18 was adopted for use in

$$s_u = \frac{(q_t - \sigma_v)}{N_{kt}} \tag{4-1}$$

where s_u is the undrained shear strength, q_t is the cone penetration resistance, and σ_v is the total vertical stress. The groundwater level (GWL) was assumed to be 2m below the surface (pre-excavation), and a soil unit weight γ of 21.2 kN/m^3 was used to calculate the vertical

stress. Figure 4-11(a) illustrates the mean CPT-derived s_u readings from the PICASO site alongside eight preliminary CIU triaxial (TX) tests performed by Socotech UK and the s_u profile from the PISA site. The triaxial results within the top 5m (10.8 to 5.8 mAOD) are underestimates of the actual s_u as there was no attempt to establish an equivalent mean effective stress p' to account for the higher K_0 (~1.5) near the surface. Additionally, the lower values may be attributed to sampling quality.

Figure 4-11 (c) shows the variation of OCR with depth for both the PISA and PICASO sites. The OCR was obtained from oedometer tests and correlations with CPTs using an N_{kt} factor of 16 for PISA and 18 for PICASO. The correlation follows the expression proposed by Jardine et al. (2005) and Ladd and Foott (1974):

$$\frac{s_u}{\sigma'_{v0}} = A[OCR]^b \tag{4-2}$$

where A and b are fitted parameters calibrated as 0.28 and 0.75, respectively, according to triaxial compression tests for PISA by Ushev (2017). At both the PISA and PICASO sites, the OCR can be seen to reduce from values of more than 20 at the surface to values close to 2 at depth. While the 1-D compression tests by Lehane (1992) indicate some problems interpreting yield points for Cowden till using conventional e-log(σ'_v) axes, oedometer tests by Ushev (2017) suggest otherwise. Similar findings were made in this research, covered later in Section 5.3. Despite these different interpretation methods, there is reasonable agreement between the CPT correlation and oedometer results. With a known representative OCR profile along with the effective angle of shearing resistance ϕ', values for K_0 can be determined using the equation by Mayne and Kulhawy (1990):

$$K_0 = (1 - sin\emptyset')OCR^{sin\emptyset'} \tag{4-3}$$

Based on triaxial compression tests by Ushev (2017), a preliminary value of $\phi' = 27°$ was used and was found to be similar to the value measured in Section 5.7.3. While Equation (4-3) may be unsuited for clays such as Cowden till, which have undergone multiple reload-unload glacial cycles, it demonstrates how the K_0 profile can be expected to decrease with

depth. A similar profile was adopted for the PISA project, based on reported in-situ lateral stress measurements obtained from total stress spade cells, oedometer tests, suction measurements and pressuremeter tests (Lehane, 1992; Powell et al., 2003; Ushev, 2017). While the PICASO site is close to the PISA site (~1000m away), there is limited historical information on the site to assist with the estimation of K_0. However, Figure 4-11(b) suggests that a similar trend is likely to exist, with K_0 above 1 in the upper layers and $K_0 \rightarrow 1$ at deeper depths. Alternative methods for determining K_0 are covered in Section 5.6, showing similar trends to those predicted. As a starting point, the upper layers (up to 4.8 mBGL or 6.5 mAOD) were limited to $K_0 = 1.5$ as it is argued that stiff marine clays that have experienced weathering and many glacial cycles are unlikely to impose K_0 ratios as high as those suggested by Powell et al. (2003) and the PICASO CPT readings (Brosse et al., 2017; Zdravković et al., 2020).

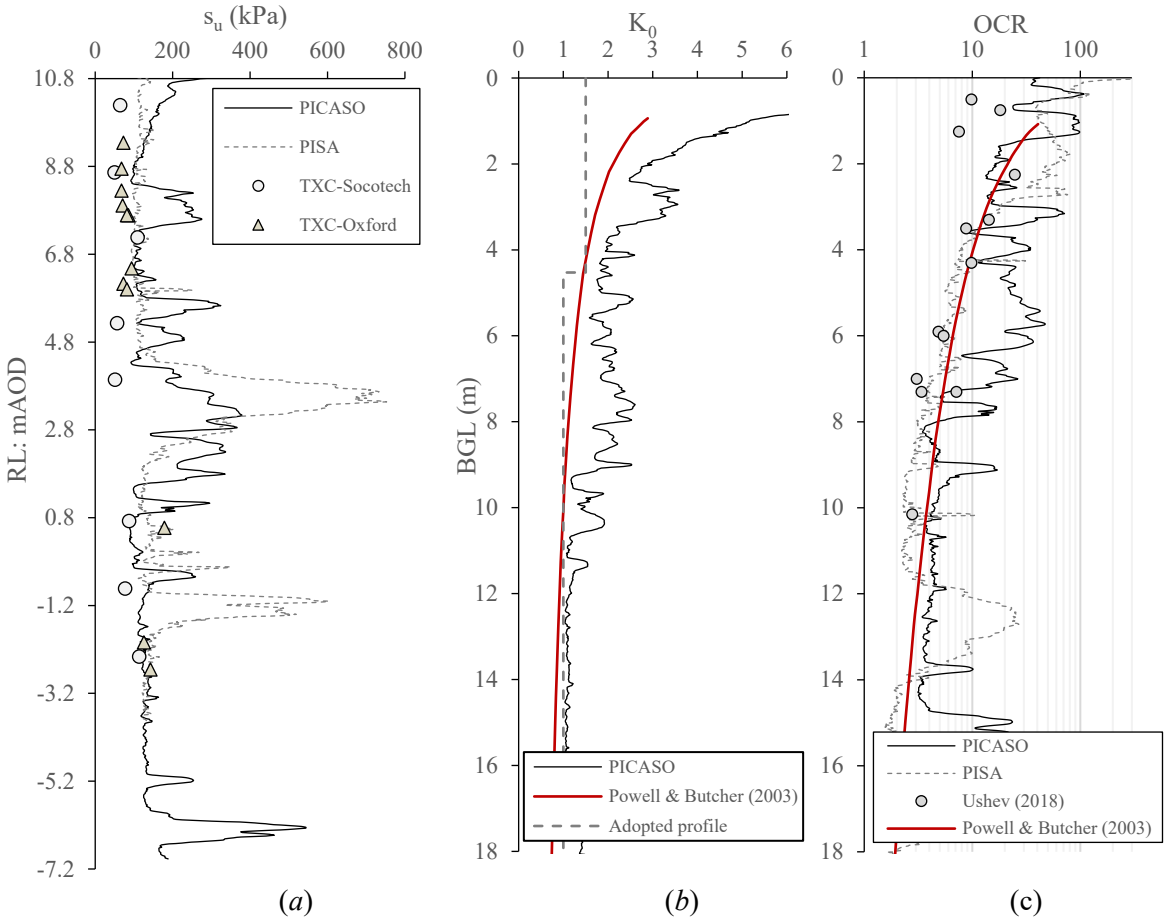


Figure 4-11: Depth profile for (*a*) undrained shear strength s_u, (*b*) estimated K_0, and (c) overconsolidation ratio *OCR*

4.9 Soil sensitivity

The sensitivity (S_t) of a particular clay is defined as the ratio between the undisturbed undrained shear strength s_u to the remoulded undrained shear strength $s_{u,rem}$ at the same void ratio (Terzaghi, 1944). Cowden till has historically been classified as a soil of low sensitivity (Lehane, 1992; Ushev, 2017), meaning the soil should not experience significant strength losses when disrupted. While no remoulded element tests were carried out in this research, Robertson (2009) suggests that the sensitivity of most fine-grained soils can be determined following the relation given by:

$$S_t = \frac{s_u}{s_{u,rem}} = \frac{q_t - \sigma_v}{N_{kt}}\left(\frac{1}{f_s}\right) \tag{4-4}$$

where f_s is the sleeve resistance. From Figure 4-12, the soil appears to have a sensitivity only slightly greater than 1, suggesting an insensitive soil. The regions giving values > 2 correspond to the silty sand layers. While a sand layer has been identified at 4 to 1 mAOD, there likely also exists another at 8.5 to 7.5 mAOD but it is only present in some of the boreholes.

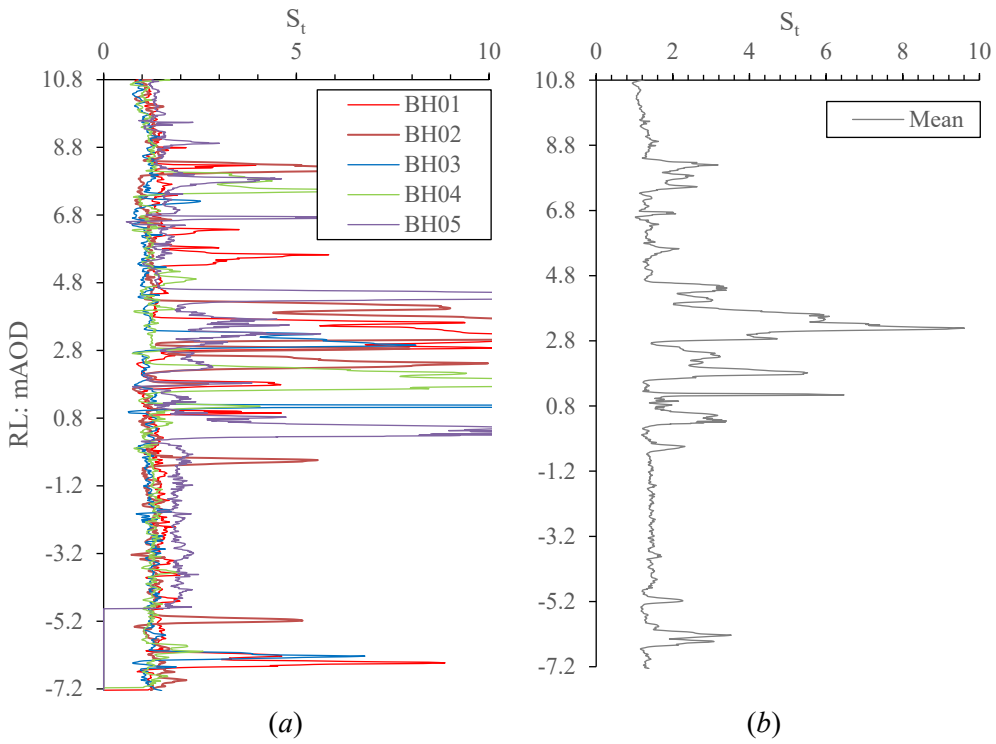


Figure 4-12: Sensitivity measurement for (*a*) each borehole and (*b*) mean value

4.10 Summary

A description of the PICASO clay site is presented in this chapter along with the in-situ testing results and index property tests, which were used to characterise the soil profile for the Cowden till site. The site investigation results were interpreted and formed the basis for the medium-scale field testing reported in detail by Martin (2023). The findings likewise formed a necessary input to the work detailed in Chapters 5 (Monotonic testing) and 6 (Cyclic testing). Cowden till material was extracted from the site via a rotary core drilling method and through manual excavation to obtain higher-quality block samples.

From the index property tests, Cowden till is classified as a low plasticity, heavily overconsolidated glacial till with traces of cobbles throughout. The material has properties similar to those measured from the PISA project, which is not surprising considering the proximity of the two sites. The properties of the material included a mean water content w = 18%, a bulk density ρ = 2.16 Mg/m^3, a specific gravity G_s = 2.68, and a plasticity index PI = 19.1%. Throughout the profile, there were traces of silty sand layers, most notably at depths 4.0 to 1.0 mAOD.

The key profiles (s_u, K_0 and OCR) derived from the CPT tests and preliminary experiments give similar correlations to the PISA CPT outputs, highlighting again the similarity between the two sites. K_0 appears to be limited to a value of 1.5 for depths up to 4.8 mBGL and then unity for the rest of the profile. The OCR profile has values ranging from > 20 at the surface to values of around 2 at the deeper depths.

Chapter 5

Monotonic testing of Cowden till

5.1 Introduction

This chapter focuses on the monotonic testing of natural Cowden till obtained for the PICASO project, exploring the mechanical behaviour at both small and large strains. One of the aims of the test programme was to characterise the undrained shear strength profile of the PICASO Cowden till site, which involved performing constant volume tests under a stacked ring configuration in the variable direction dynamic cyclic simple shear (VDDCSS) device on samples from a range of depths. CPT profiles, oedometer tests, and triaxial experiments were used to study the soil, evaluating its strength characteristics and compressibility. Rate effects, critical state parameters, and stiffness were also reviewed.

An extensive database of reliable element tests was created, which was used to calibrate an advanced soil constitutive model as described in Chapter 7. While many triaxial compression and extension tests have been undertaken on Cowden till and reported in the literature (Ushev, 2017), freely available test data using the direct simple shear device is extremely limited. Therefore, the chapter starts by introducing the 1-D compression results, then direct simple shear results, triaxial results, and finally, an overview of the undrained shear strength profile of the PICASO Cowden site.

5.2 Testing programme

The test schedule was generated according to the samples' quality, the testing objective, and the time at which the samples were procured from site. In order of suspected sample quality (poor to excellent), the specimens were obtained from rotary core (RC) samples and block samples (BS). The main research objectives left BS for more advanced cyclic testing, while the RC samples were used to characterise the strength of the Cowden site and investigate the monotonic behaviour of Cowden till.

An attempt was made to reconsolidate the RC specimens to their in-situ stress conditions, approximated using bulk density measurements covered in Section 4.5 and an assumed water table level. However, as most of these samples were graded as "poor" following the evaluation criteria proposed by Lunne et al. (2006), discussed in Section 5.9, a modified recompression technique was used to minimise the effects of sample disturbance on selected samples.

The technique closely follows the method proposed by Ladd and Degroot (2003), where they recommend preloading direct simple shear (DSS) specimens to 80% of the estimated preconsolidation stress σ'_{vc} and then swelling them back to their in-situ vertical effective stress σ'_{v0} before undrained shearing. The present testing programme provides invaluable data on the effectiveness of this technique when compared to the normally loaded approach over large sets of element tests for a low plasticity overconsolidated glacial till. The technique differs from the SHANSEP procedure developed by MIT (Ladd et al., 1974), where specimens are consolidated beyond σ'_{vc}. The σ'_{vc} was estimated following the method in Section 4.8 through interpreted CPT data. The parameters used in the equation were later verified using DSS and triaxial compression (TXC) test data in Section 5.7.4. An example of the determination of σ'_{vc} is given below.

Example (CWD_BS_DSS_CU_OL35)

Known parameters and assumptions:

Reduced level: 7.69 mAOD (BH04)

Groundwater level: 2 mBGL (pre-excavation)

Pre-excavation depth: 4.91 mBGL

Soil bulk unit weight: γ = 21.2 kN/m^3

Post-excavation depth: 3.11 mBGL

q_t = 1.87 MPa (Section 4.7)

N_{kt} = 18 (from Section 5.9); A = 0.28, b = 0.75

$$N_{kt} = \frac{q_t - \sigma_{v0}}{s_{u,TXC}} \rightarrow 18 = \frac{1.87 \times 10^3 - (21.2 \times 4.91)}{s_{u,TXC}}$$

$$s_{u,TXC} = 98.11\ kPa$$

$$\frac{s_u}{\sigma'_{v0}} = A[OCR]^b \rightarrow \frac{(98.11)}{(2\ (21.2) + 2.91(21.2 - 9.81))} = (0.28)[OCR]^{(0.75)}$$

$$OCR = 7.735$$

$$OCR = \frac{\sigma'_{vc}}{\sigma'_{v0}} \rightarrow 7.735 = \frac{\sigma'_{vc}}{(2\ (21.2) + 2.91(21.2 - 9.81))} = \frac{\sigma'_{vc}}{75.5}$$

$$\sigma'_{vc} = 584.3\ kPa$$

$$\therefore 0.8\sigma'_{vc} = 467.4\ kPa$$

All tests were either normally loaded (NL) to their estimated in-situ stress or overloaded (OL) following the modified recompression technique. A comparison of these approaches is made and is discussed in Section 5.4. For the latter approach, the estimated σ'_{vc} was based on pre-excavation levels, in line with the time when the CPTs were taken. In some cases where the corresponding CPT measurements were found to be in a suspected sandy silt layer, the interpreted OCR profile based on CPT readings and available oedometer tests was used instead. The interpreted OCR profile is covered in Section 5.3.1. The application of $0.8\sigma'_{vc}$ for the experiments ensured that realistic stress-strain-strength data was measured, and the sample could sustain the applied vertical load without damaging its structure (Ladd, 1991). Due to the different testing conditions, a 'Test type ID' was set up to distinguish each test, as given in Table 5-1. The tests on RC samples were numbered in no particular order but tested for a range of depths to determine the complete undrained shear strength profile. Unfortunately, core recovery in the suspected silty sand layer zones (Reduced level, RL: 4

to 1.0 mAOD) was poor and is reflected in most plots, with notable gaps in the data at those depths. The nomenclature for each key is described below:

CWD_RC_DSS_CU_NL100 - notes
a b c d e f

Table 5-1: Nomenclature used for key ID

Key	Description	Nomenclature
a	Sample type	CWD: Cowden till
b	Material extraction method	RC: Rotary core sample BS: Block sample
c	Test apparatus	OED: Oedometer DSS: Direct simple shear TX: Triaxial
d	Test condition (Not applicable to OED ∴ omitted)	Direct simple shear (DSS) CU: Consolidated undrained (Constant volume) Triaxial (TX) CIUc: Consolidated isotropic undrained compression CAUc: Consolidated anisotropic undrained compression CIUe: Consolidated isotropic undrained extension
e	Loading type (Not applicable to OED ∴ omitted)	NL: Normally loaded OL: Overloaded
f	Effective confining stress (Initial vertical effective stress for DSS & OED)	xxxx: Numerical value in kN/m^2
-	Notes	WRM: Wired-reinforced membrane

The research aims to investigate several key behaviours associated with Cowden till. As a result, the monotonic test programme was split into four categories. This includes tests for:

i. Apparatus commissioning,
ii. Site characterisation,
iii. Soil constitutive model calibration,
iv. Rate effects.

A summary of all monotonic tests carried out in this research project is given in Table 5-2. The tests were performed using one of three test apparatuses, which include the oedometer (OED), the direct simple shear apparatus (DSS), and the triaxial device (TX).

Table 5-2: Summary of monotonic test programme

Reduced level (mAOD)	Target Profile	Sample type (-)	Test apparatus			Purpose of test (-)
			OED	DSS	TX	
10.8 to 6.0	Upper layer	RC	18	49	11	i, ii, iii
10.8 to 7.5	Block sample layer	BS	1	6	3	i, ii, iii, iv
		Total no. of tests:	19	55	14	
		Testing time (days):	266	165	168	

Ushev (2017) performed 13 ring shear tests, 13 oedometer tests, and 46 triaxial tests for the PISA project. Considering the research objectives around direct simple shear testing, the monotonic test programme carried out in this research is believed to be just as comprehensive as that carried out for PISA. Furthermore, the number of undrained monotonic DSS tests is comparable to the number typically performed for an OWT site investigation, estimated to be around 50 DSS tests (White, 2021).

5.3 1-D compression results

5.3.1 Oedometer test programme

1-D compression tests were carried out for samples over the entire depth of the investigated Cowden till profile. A total of 19 oedometer tests were carried out on the intact RC samples using a high-load motorised oedometer described in Section 3.5.1 and summarised in Table 5-3. Each test took 12 days to complete, based on loading and unloading increments, holding each increment for 24 hours. The tests are assessed against the empirically calculated OCR values derived from the PICASO CPT readings (see Section 4.8), as shown in Figure 5-1.

The OCR reduces with depth, with values ranging from 4 to > 10 from the surface to 4 mAOD and values between 2 and 4 for the rest of the profile. The measured values appear to agree with those inferred from the CPT profile, showing improved correlation with increasing depth. Some of the underpredictions may be attributed to the sandy layers

encountered in the profile, most notably at depths 4 to 1 mAOD, explaining the discrepancy seen for the test conducted at 2.94 mAOD as observed in Figure 5-1. The preconsolidation pressure σ'_{vc} for each test was estimated following the Casagrande construction, shown in Figure 5-2, and based on a maximum curvature determined through a fourth-order polynomial (see Section 3.5.1).

Table 5-3: Summary of Oedometer test results

No	Test ID	RL (m)	BGL (m)	σ'_{v0} (kPa)	σ'_{vc} (kPa)	OCR (-)	w (%)	e_i (-)	C_c (-)	C_s (-)	λ (-)	κ (-)
1	CWD_RC_OED_12	9.78	1.02	12	538	44.8	15.8	0.426	0.141	0.030	0.080	0.022
2	CWD_RC_OED_18	9.18	1.62	18	332	18.4	16.4	0.449	0.151	0.028	0.070	0.018
3	CWD_RC_OED_21	8.93	1.87	21	143	6.8	17.3	0.471	0.119	0.050	0.068	0.021
4	CWD_RC_OED_21	8.93	1.87	21	215	10.2	18.4	0.517	0.161	0.032	0.057	0.016
5	CWD_BS_OED_35	7.85	2.95	35	484	13.8	18.5	0.485	0.158	0.036	0.069	0.016
6	CWD_RC_OED_39	7.41	3.39	39	316	8.1	15.4	0.444	0.142	0.029	0.053	0.012
7	CWD_RC_OED_42	7.09	3.71	42	343	8.2	16.5	0.448	0.134	0.038	0.059	0.013
8	CWD_RC_OED_47	6.7	4.1	47	228	4.9	16.5	0.444	0.127	0.091	0.064	0.017
9	CWD_RC_OED_65	5.04	5.76	65	445	6.8	17.4	0.467	0.162	0.033	0.110	0.039
10	CWD_RC_OED_73	4.41	6.39	73	317	4.3	16.6	0.467	0.133	0.042	0.058	0.013
11	CWD_RC_OED_75	4.15	6.65	75	826	11.0	16.0	0.440	0.135	0.048	0.058	0.014
12	CWD_RC_OED_76	4.09	6.71	76	520	6.8	26.3	0.743	0.252	0.039	0.070	0.018
13	CWD_RC_OED_90	2.94	7.86	90	238	2.6	15.3	0.438	0.147	0.031	0.055	0.013
14	CWD_RC_OED_121	0.22	10.58	121	340	2.8	14.1	0.412	0.137	0.042	0.058	0.014
15	CWD_RC_OED_124	-0.11	10.91	124	389	3.1	13.7	0.366	0.122	0.033	0.062	0.014
16	CWD_RC_OED_153	-2.62	13.42	153	379	2.5	14.4	0.399	0.131	0.043	0.070	0.019
17	CWD_RC_OED_155	-2.77	13.57	155	319	2.1	15.6	0.455	0.156	0.031	0.052	0.011
18	CWD_RC_OED_176	-4.63	15.43	176	315	1.8	17.9	0.500	0.162	0.037	0.065	0.017
19	CWD_RC_OED_179	-4.89	15.69	179	643	3.6	17.6	0.494	0.183	0.024	0.061	0.014
	Average (Upper - RL: 10.8 to 6.0m)					=	16.8	0.460	0.142	0.042	0.070	0.020
	Average (Lower - RL: 6.0 to -5.0m)					=	16.8	0.471	0.156	0.037	0.062	0.015

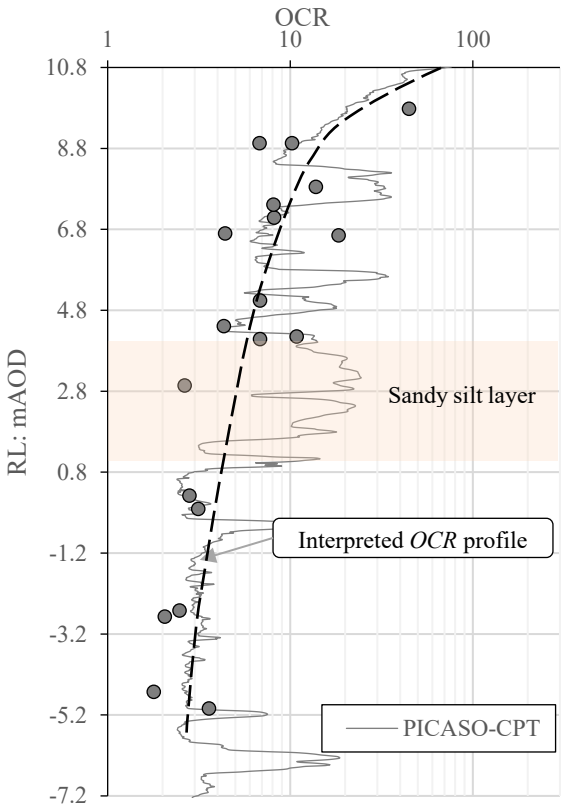


Figure 5-1: Estimated OCR from oedometer plotted with depth

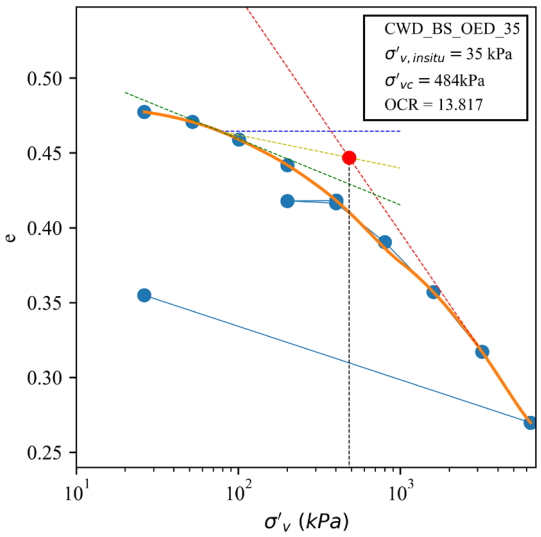


Figure 5-2: Example of Casagrande construction method

5.3.2 Behaviour of Cowden till in 1D compression

As shown in Figure 5-3, the one-dimensional behaviour for all oedometer tests is closely comparable except for test CWD_RC_OED_76, which possesses an initial void ratio almost twice as high as the rest of the profile, reflected also in its naturally higher water content (Table 5-3). The specimens were loaded to vertical effective stresses up to 6.4 MPa, following the procedures described in ASTM: D2435/D2345M-11 (2011). However, this allowed the samples to yield gradually, making it difficult to identify any sharp yielding points. For all samples (excluding CWD_RC_OED_76) normally compressed to 6.4 MPa, a scatter in the final void ratio before unloading was recorded between 0.202 and 0.288. The scatter in the data is mainly due to the variable nature of the undisturbed clay samples across the site, particularly in the upper layers. The scatter is less evident in the PISA oedometer results or historically derived values as their tests focussed on reconstituted samples (Lau, 1988; Ushev, 2017).

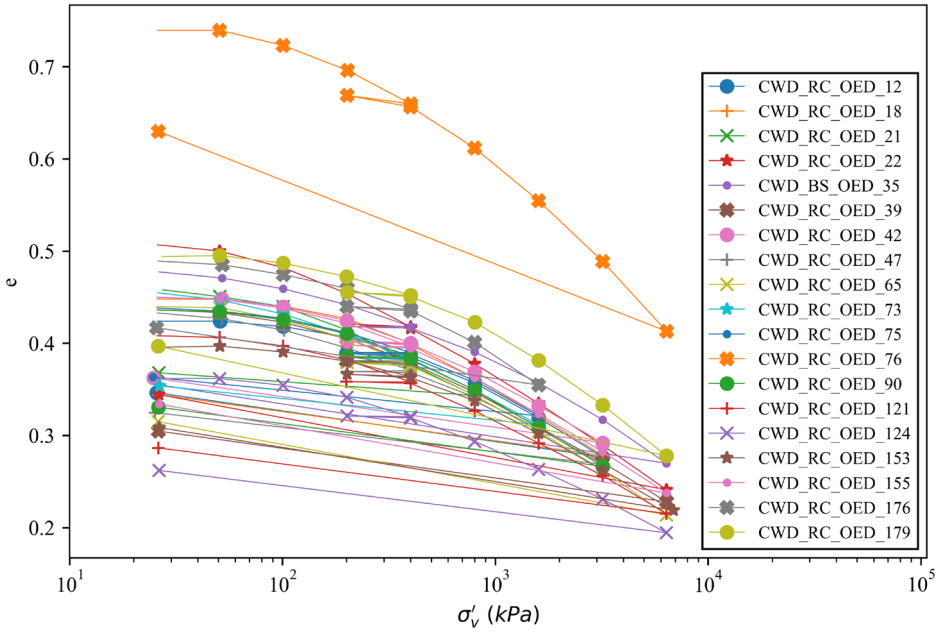


Figure 5-3: 1-D compression results in oedometer

For tests with similar initial void ratios (e.g. CWD_RC_OED_42 and CWD_RC_OED_90), their curves converge towards a similar path with increasing vertical effective stress, and values for the compression index C_c were found to differ by no more than 0.017 (i.e. one standard deviation) and for the swelling index C_s by 0.015. The values of C_c and C_s can be directly related to λ and κ as follows (Schofield and Wroth, 1968):

$$\lambda = \frac{C_c}{2.303} \; ; \; \kappa = \frac{C_s}{2.303} \tag{5-1}$$

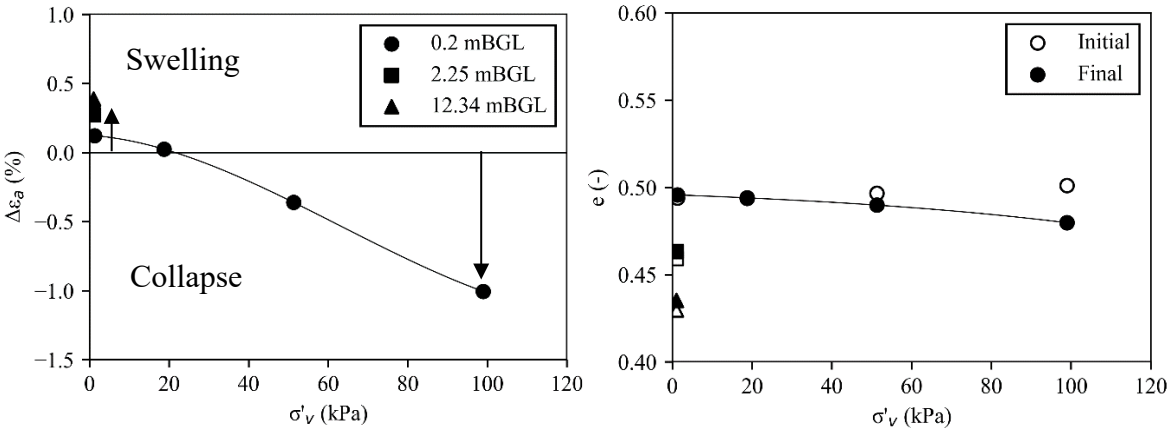
Therefore, excluding CWD_RC_OED_76, the average λ was equal to 0.070, and κ was equal to 0.020 for depths ranging from 10.8 to 6.0 mAOD (upper). Similarly, for the lower depths between 6.0 to -5.0 mAOD, the values were 0.060 and 0.014, respectively, demonstrating a slight decrease in C_c (or λ) and C_s (or κ) with depth. The parameters are consistent with those measured for PISA, where λ = 0.062 and κ = 0.012 for the lower part of their soil profile (Zdravković et al., 2020). From the results, the parameters λ and κ for the upper and lower layers only differ slightly, which is similar to the findings made by Lau (1988). In terms of soil constitutive model implementation, these measured parameters are for 1D compression and must be used with caution if used as inputs in a model such as Cam-Clay, which assumes isotropic compression and swelling.

5.3.3 Swelling sensitivity

The research was carried out solely on natural Cowden till samples. As a result, comparisons with its intrinsic compression and swelling behaviour were not possible as this requires testing reconstituted samples. However, as covered in Section 4.9, the material's natural insensitivity suggests that the natural soil's compression behaviour is not too dissimilar to that of a reconstituted sample, as reported by Ushev (2017) and Zdravković et al. (2019).

Swelling tests according to ASTM D4546-08 were performed on selected Cowden till samples at three different depths. The method measures one-dimensional wetting-induced swelling or collapse, where four identical specimens are subjected to different loads. Each is given access to water until primary swelling or collapse is reached under constant vertical total stress. The deformations and relevant water contents are then recorded. The method is also valid for a single intact specimen, but this only gives information about the induced strain under the selected vertical stress.

Out of six tests, four were close to the surface at ~0.2 mBGL (10.6 mAOD), one at 2.25 mBGL (8.55 mAOD) and one at 12.34 mBGL (-1.54 mAOD). The surface samples were push samples obtained by Wu (2022), while the other two were from RC samples. Figure 5-4(a) shows greater swelling tendencies for deeper samples when inundated with water, with swelling strains as high as 0.39%. Conversely, under a pressure of 1 kPa, the surface sample showed little swelling (~0.12%). This is unexpected, considering that 2m of soil was excavated in 2019 to reach the current surface level. However, the site was located in an area of heavy rainfall, recording approximately 875 mm of precipitation in 2020 (World Weather Online, 2021). This means the surface push samples may have swelled significantly by the time they were procured in May 2021. Figure 5-4(b) highlights the final void ratio after swelling/collapse.



(*a*) (*b*)

Figure 5-4: (*a*) Stress versus wetting-induced swelling/collapse strain (*b*) Initial and final void ratio due to swelling/collapse strain

5.3.4 Coefficients of compressibility, consolidation, and permeability

When performing oedometer tests, coefficients of compressibility m_v, consolidation $c_{v,}$ and permeability k were obtained at each load increment. The determination of these coefficients is standard and can be found in ASTM D2435/D2345M-11 (2011) and BS EN ISO 17892-5 (2017). At σ'_v = 400 kPa, the samples were unloaded to 200 kPa to analyse for swelling. In Figure 5-5(a), the m_v curves peak at σ'_v = 100 kPa but start to decrease sharply with higher stresses before converging at around σ'_v = 400 kPa. Generally, the deeper samples are less compressible, with m_v < 0.0015 m^2/kN, showing gradual decreases in m_v with increasing σ'_v. Based on these values, Cowden till has very low to medium compressibility, a classification common for heavily overconsolidated clays (Das, 2011).

For the coefficient of consolidation, the values for c_v were similar across all depths, as pictured in Figure 5-5(b). The samples converged towards a mean value of c_v = 0.6 x 10^{-6} m^2/s at σ'_v = 100-200 kPa before converging to ~0.2 x 10^{-6} m^2/s at σ'_v = 6.4 MPa. The values are higher than those measured for the PISA project, which gave c_v = 1 x 10^{-7} m^2/s at σ'_v = 250-500 kPa (Ushev, 2017). There is also a noticeable jump in c_v at σ'_v = 0.8 MPa, which corresponds to the segment after the sample has been unloaded and reloaded, where swelling likely aided the samples in becoming more compressible.

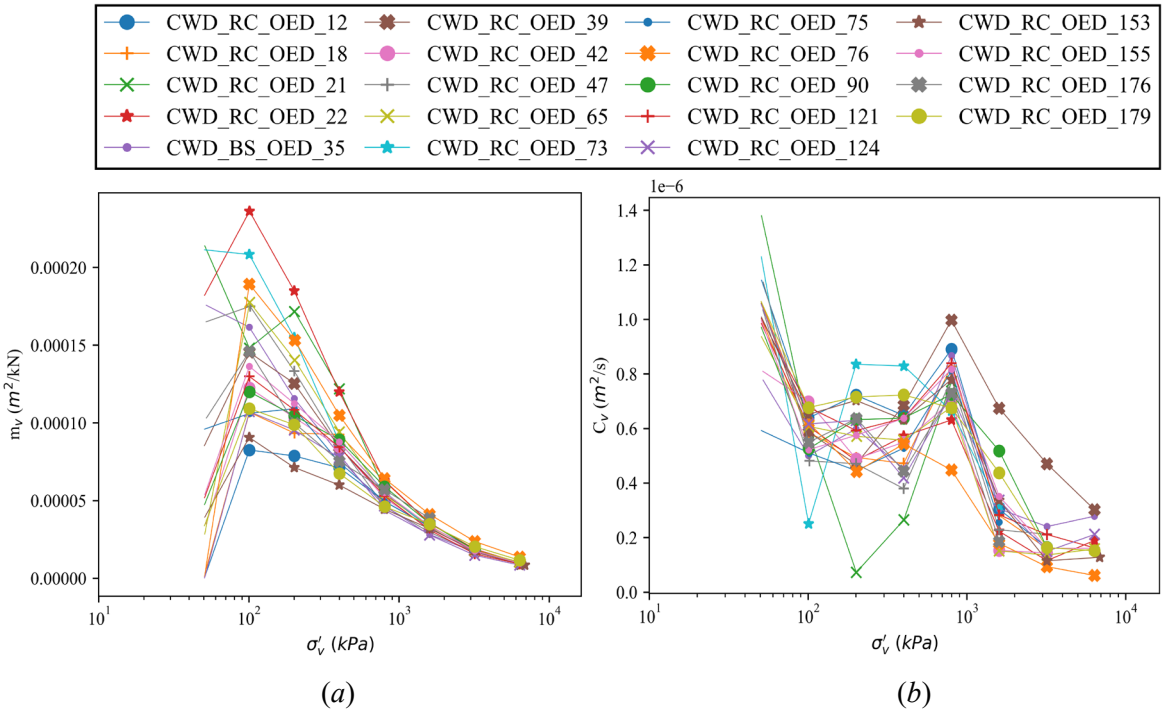


Figure 5-5: (*a*) Coefficient of compressibility m_v of Cowden till and (*b*) Coefficient of consolidation c_v of natural Cowden till

Figure 5-6 shows the deduced variations in permeability k with increasing vertical effective stress. The samples in the upper layers generally have a higher permeability than those in the deeper profile portions. It was also noted that permeability k converged to a value of 1.5×10^{-11} m/s at 6.4 MPa, which is consistent with the findings by Ushev (2017) at similar pressures.

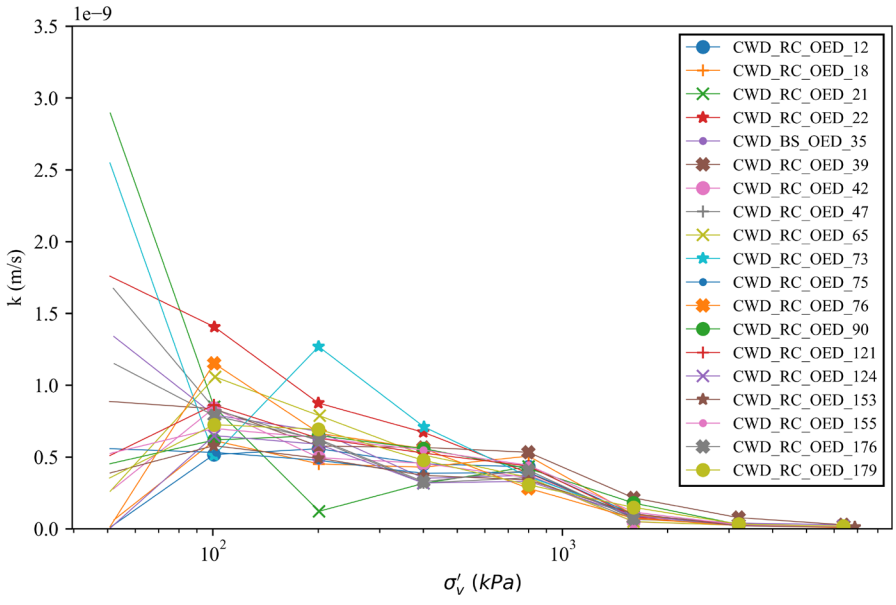


Figure 5-6: Permeability of Cowden till determined from oedometer test

5.4 DSS test results

This section covers the stress-strain behaviour of Cowden till under monotonic loading in the DSS apparatus. All tests were performed under constant volume conditions using the VDDCSS apparatus described in Chapter 3 and confined using a stack of Teflon coated rings. All tests were conducted at a shear strain rate $\dot{\gamma}$ = 3 %/hour, unless stated otherwise. This was considered to be sufficiently slow, so generated pore pressures could be taken as zero (Lau, 1988; Atkinson et al., 1991).

The samples were consolidated under either NL or OL conditions and sheared to failure, where failure occurs when the shear stress reaches a peak or plateau (Airey et al., 1987). The two different loading approaches were evaluated over two depth ranges (Upper: RL = 10.8 to 6.0m and Lower: RL = 6.0 to -5.0m) from Section 5.4.1 to 5.4.4. The OL approach was found to be the preferred method, with higher measured soil strength and reassurance of elevated stress for an overconsolidated condition.

In some cases, a lateral force sensor (LFS) was used during a test in an attempt to map the principal stresses acting on the specimen. The application and calibration of the LFS can be found in Chapter 3, and the results are discussed in Section 5.6. The lateral stress results support the claim for an OL approach, where the measured NL values for K_0 are substantially lower than the CPT-derived values for the in-situ soil. The recommended procedure has only recently been introduced into practice (ASTM D8296-19, 2019). Finally, the stress-strain response at small strains was measured using local LVDT instrumentation, while the long-range encoders were used for larger strains.

The test results are summarised in Table 5-4 and shown in Figure 5-7 to Figure 5-10, which contain plots of normalised shear stress τ/s_u versus shear strain γ, vertical effective stress σ'_v versus shear strain γ, shear stress τ versus σ'_v, and inferred shear-induced pore pressure Δu_w versus γ. From the normalised shear stress plots, it is evident that normalisation by s_u gives a more consistent pre-failure response when compared to normalisation by σ'_v. This is observed in Figure 5-7(a) and Figure 5-8(a), where normalisation by σ'_v is given in grey and shows no convergence to any unique curve. The curves are scattered, and as a result, only normalisation by s_u is considered hereafter.

In total, only 45 DSS tests out of 120 performed were presented in this section. Several tests were disregarded as they were either subjected to incorrect loads, affected by temperature fluctuations or had large stones/pebbles present within the sample. On average, it took approximately a week to complete two DSS tests in the VDDCSS, equating to a total testing time of 23 weeks for the tests selected. For ease of analysis, the results are split into four groups according to loading condition and RL, ranging from 10.8 to -5.0 mAOD. The results in each part are briefly discussed, highlighting prominent trends and expected behaviours, followed by a more in-depth discussion in Section 5.5, focussing on the stress-strain behaviour and pore pressure response across all four groups.

Table 5-4: Summary of monotonic DSS test programme and results

No	Test ID	RL (m)	BGL (m)	σ'_{v0} (kPa)	$0.8\sigma'_{vc}$ (kPa)	w (%)	ρ (Mg/m^3)	e_i (-)	e_f (-)	s_u (kPa)	γ_f (%)
1	CWD_RC_DSS_CU_NL21	8.93	1.87	21	21	18.1	2.173	0.483	0.466	25	46
2	CWD_RC_DSS_CU_OL21	8.93	1.87	21	218	17.4	2.15	0.448	0.409	60	43
3	CWD_RC_DSS_CU_NL23	8.75	2.05	23	23	17.1	2.138	0.468	0.448	17*	50
4	CWD_RC_DSS_CU_NL26	8.55	2.25	26	26	17.1	2.18	0.44	0.426	20*	50
5	CWD_RC_DSS_CU_OL26	8.55	2.25	26	74	16.7	2.169	0.442	0.412	32*	50
6	CWD_RC_DSS_CU_OL29	8.25	2.55	29	119	18.3	2.129	0.489	0.452	49*	50
7	CWD_RC_DSS_CU_NL33	7.91	2.89	33	33	16.6	2.176	0.435	0.418	41*	50
8	CWD_RC_DSS_CU_OL33	7.91	2.89	33	107	16.6	2.157	0.448	0.416	48*	49
9	CWD_BS_DSS_CU_NL35	7.69	2.95	35	35	15.6	2.164	0.431	0.411	35*	50
10	CWD_BS_DSS_CU_OL35	7.69	2.95	35	467	16.4	2.189	0.425	0.369	86	40
11	CWD_BS_DSS_CU_OL35a	7.69	2.95	35	467	16.0	2.169	0.433	0.365	81	29
12	CWD_RC_DSS_CU_NL39	7.41	3.39	39	39	16.3	2.177	0.432	0.419	39*	50
13	CWD_RC_DSS_CU_OL39	7.41	3.39	39	193	15.2	2.199	0.403	0.373	75	36
14	CWD_RC_DSS_CU_NL40	7.31	3.49	40	40	15.8	2.165	0.434	0.418	31*	50
15	CWD_RC_DSS_CU_NL47	6.68	4.13	47	47	16.2	2.195	0.419	0.402	31*	50
16	CWD_RC_DSS_CU_OL47	6.68	4.13	47	164	17.3	2.17	0.448	0.404	57	43
17	CWD_RC_DSS_CU_OL49	6.48	4.32	49	225	16.1	2.164	0.439	0.394	63	33
18	CWD_RC_DSS_CU_OL53	6.13	4.67	53	170	15.1	2.16	0.428	0.386	51	33
19	CWD_RC_DSS_CU_NL55	6.00	4.8	55	55	17.4	2.156	0.459	0.428	32*	50
20	CWD_RC_DSS_CU_NL65	5.04	5.76	65	65	18.3	2.162	0.466	0.445	44	40
21	CWD_RC_DSS_CU_OL65	5.04	5.76	65	137	17.8	2.163	0.46	0.415	59	37
22	CWD_RC_DSS_CU_NL69	4.75	6.05	69	69	16.6	2.174	0.437	0.414	43	47
23	CWD_RC_DSS_CU_OL69	4.75	6.05	69	269	16.8	2.153	0.454	0.407	56	30
24	CWD_RC_DSS_CU_NL76	4.09	6.71	76	76	25.9	2.015	0.674	0.656	37	42
25	CWD_RC_DSS_CU_OL76	4.09	6.71	76	304	29.5	2.015	0.77	0.707	48	21
26	CWD_RC_DSS_CU_NL117	0.57	10.23	117	117	12.4	2.295	0.313	0.294	65*	50
27	CWD_RC_DSS_CU_OL117	0.57	10.23	117	288	13.1	2.231	0.358	0.301	92*	50
28	CWD_RC_DSS_CU_NL124	-0.11	10.91	124	124	13.9	2.196	0.389	0.355	67	35
29	CWD_RC_DSS_CU_OL124	-0.11	10.91	124	268	14	2.197	0.39	0.346	82	26
30	CWD_RC_DSS_CU_NL144	-1.84	12.64	144	144	16	2.175	0.429	0.39	68	41
31	CWD_RC_DSS_CU_NL144_WRM	-1.84	12.64	144	144	15.6	2.238	0.384	0.346	53	15
32	CWD_RC_DSS_CU_OL144	-1.84	12.64	144	415	16.6	2.183	0.432	0.368	112	29
33	CWD_RC_DSS_CU_OL144_WRM	-1.84	12.64	144	415	16	2.184	0.423	0.366	88	13
34	CWD_RC_DSS_CU_OL146	-2.04	12.84	146	471	15.3	2.177	0.42	0.347	107	25
35	CWD_RC_DSS_CU_NL153	-2.62	13.42	153	153	14.5	2.181	0.407	0.372	66	30
36	CWD_RC_DSS_CU_OL153	-2.62	13.42	153	360	14.6	2.181	0.408	0.353	106	26
37	CWD_RC_DSS_CU_NL164	-3.56	14.36	164	164	16.4	2.151	0.451	0.408	66	30
38	CWD_RC_DSS_CU_OL164	-3.56	14.36	164	406	16.4	2.142	0.456	0.39	106	29
39	CWD_RC_DSS_CU_NL170	-4.11	14.91	170	170	16.5	2.14	0.459	0.412	73	21
40	CWD_RC_DSS_CU_OL170	-4.11	14.91	170	389	15.8	2.16	0.437	0.376	116	26
41	CWD_RC_DSS_CU_NL173	-4.43	15.23	173	173	17.4	2.134	0.473	0.418	74	27
42	CWD_RC_DSS_CU_OL173	-4.43	15.23	173	400	14.8	2.196	0.402	0.353	122	21
43	CWD_RC_DSS_CU_NL175	-4.59	15.39	175	175	17.2	2.15	0.461	0.423	69	27
44	CWD_RC_DSS_CU_NL179	-4.89	15.69	179	179	17.5	2.174	0.425	0.396	73	22
45	CWD_RC_DSS_CU_OL179	-4.89	15.69	179	537	15	2.156	0.429	0.363	126	28

Notes:

RL = Reduced level or metres above ordnance datum (mAOD)

BGL = Below ground level post-excavation

e_i = Initial void ratio

e_f = Final void ratio at the end of shearing

γ_f = Failure shear strain typically reported at peak τ

* = Shear strains denoted by a * indicate no clear peak was reached, thus the τ at $\gamma = 25\%$ was reported for s_u

5.4.1 Constant volume NL tests in upper soil (RL: 10.8 to 6.0m)

For specimens at lower confining stresses, it was noted that they failed to reach a plateau at large strain. As a result, the value of s_u at $\gamma = 0.25$ was reported, corresponding to the mean failure axial strain measured from the triaxial experiments, where ε_a (= 0.165) = γ/1.5. The plots below highlight the trends for specimens recompressed directly to their estimated in-situ stress and then sheared under constant volume conditions. In addition, a failure envelope of $\phi'_{cv,upper}$ = 35° was measured for the NL tests in the upper layer, which is higher than expected compared to the PISA project findings (discussed further in Section 5.5.1).

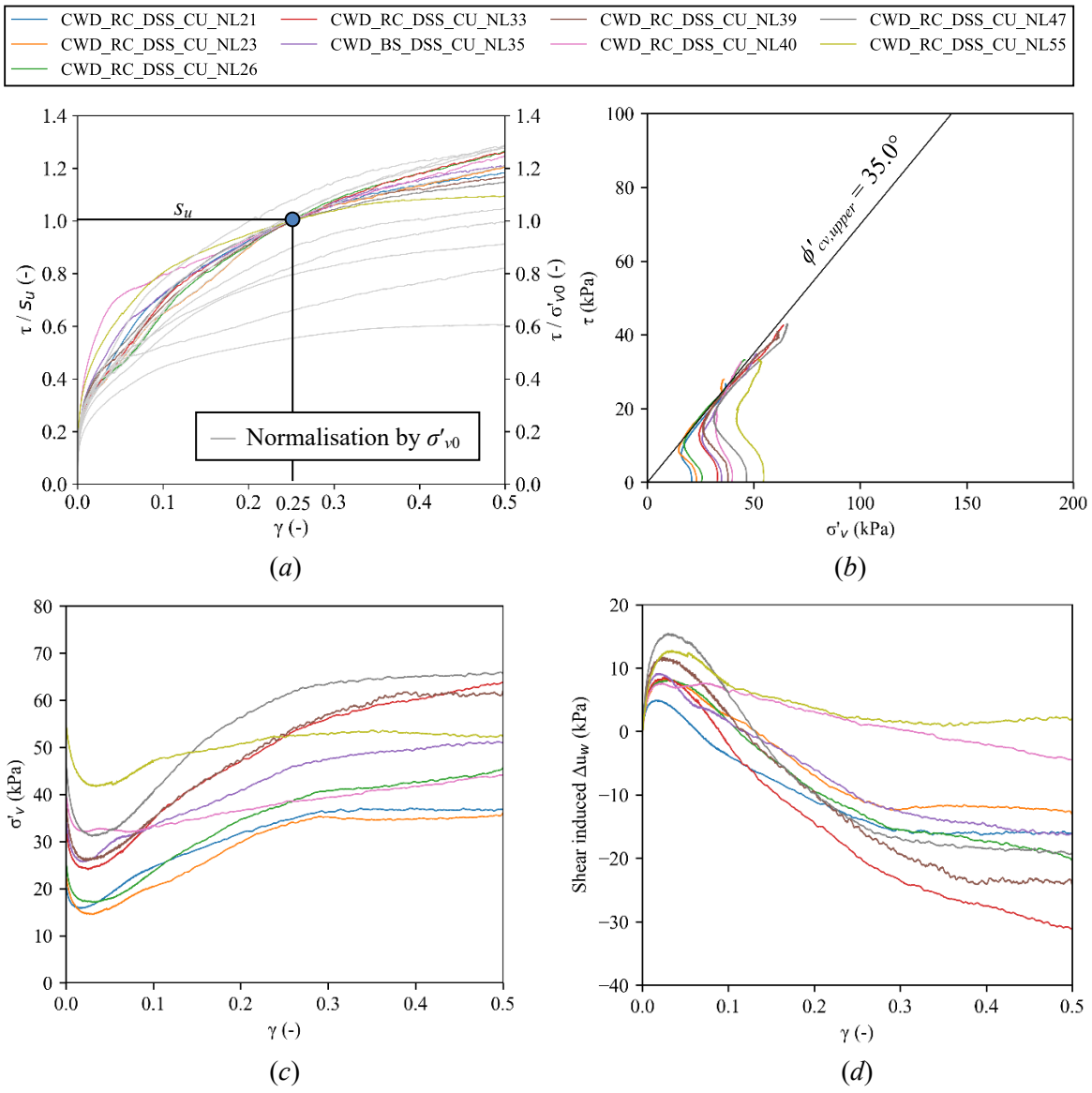


Figure 5-7: Summary of normally loaded DSS outputs from 10.8 to 6.0 mAOD - (*a*) Normalised shear stress versus shear strain, (*b*) DSS stress path, (*c*) normal stress versus shear strain, and (*d*) inferred pore pressure change versus shear strain

5.4.2 Constant volume OL tests in upper soil (RL: 10.8 to 6.0m)

The shallower OL specimens show signs of peak or failure at $\gamma_f \approx 0.38$. A failure envelope of $\phi'_{cv,upper} = 31.1°$ was measured for the OL samples, ~4° lower than that measured for the NL tests. The difference is likely caused by the NL samples not fully reaching failure conditions before the end of the test, as discussed further in Section 5.5. The specimens also show a more dilative response when compared to the NL specimens, where inferred pore pressure changes are seen to be purely negative and continually increasing before plateauing at points corresponding to γ_f.

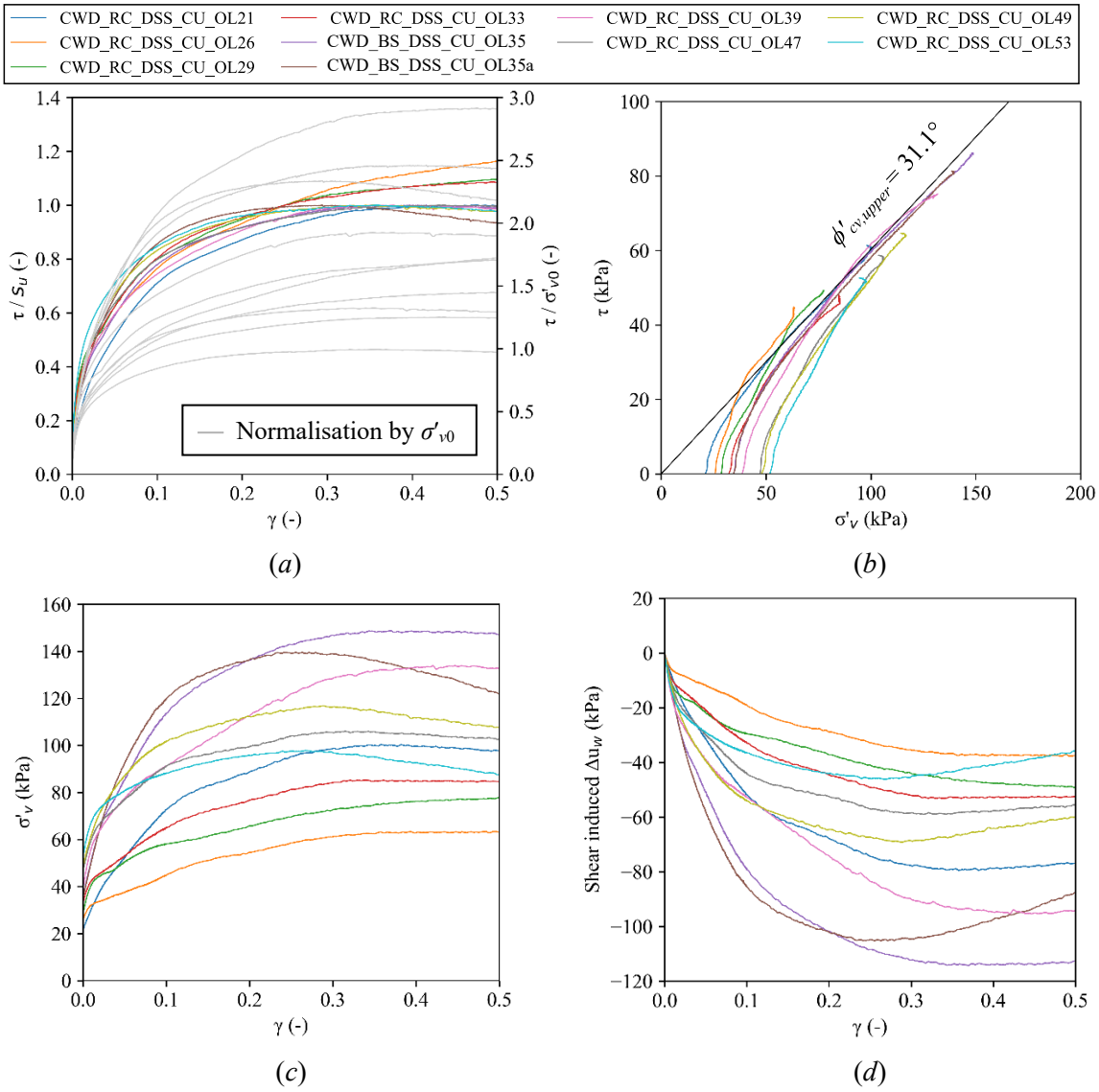


Figure 5-8: Summary of overloaded DSS outputs from 10.8 to 6.0 mAOD - (*a*) Normalised shear stress versus shear strain, (*b*) DSS stress path, (*c*) normal stress versus shear strain, and (*d*) inferred pore pressure change versus shear strain

5.4.3 Constant volume NL tests in lower soil (RL: 6.0 to -5.0m)

For specimens at higher confining stresses, all but one of the tests reached a clear peak before the end of the test. An average failure shear strain of $\gamma_f \approx 0.33$ was recorded for the tested specimens in this depth range. In terms of the stress path and changes in vertical effective stress, the behaviour is primarily consistent with what was observed for the NL specimens in the upper layers, apart from the inferred changes in pore pressure, which appear to be changing at large shear strains. A mean failure friction angle of 28.7° was measured, significantly lower than that measured in the upper layer.

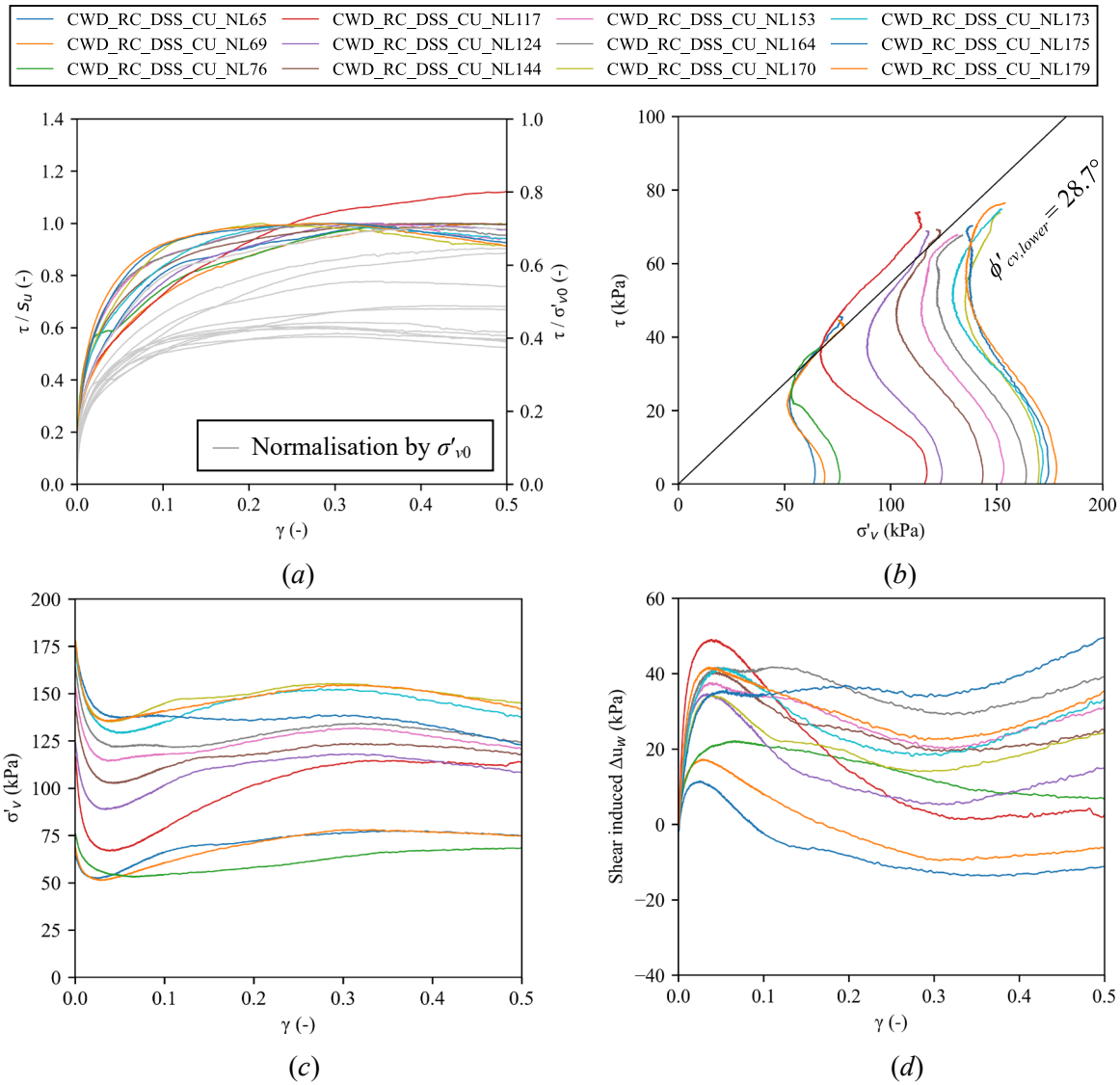


Figure 5-9: Summary of normally loaded DSS outputs from 6.0 to -5.0 mAOD - (*a*) Normalised shear stress versus shear strain, (*b*) DSS stress path, (*c*) normal stress versus shear strain, and (*d*) inferred pore pressure change versus shear strain

5.4.4 Constant volume OL tests in lower soil (RL: 6.0 to -5.0m)

The OL specimens at this depth gave γ_f values even lower than their NL counterparts, with an average of around $\gamma_f \approx 0.28$. The tests converge towards a unique failure envelope inclined at $\phi'_{cv,lower} = 26.4°$. This is only ~2° lower than that obtained for the corresponding NL tests, which is not as significant a difference as observed for the upper layers. The changes in inferred pore pressure also follow similar trends, with the specimens showing a more dilative response.

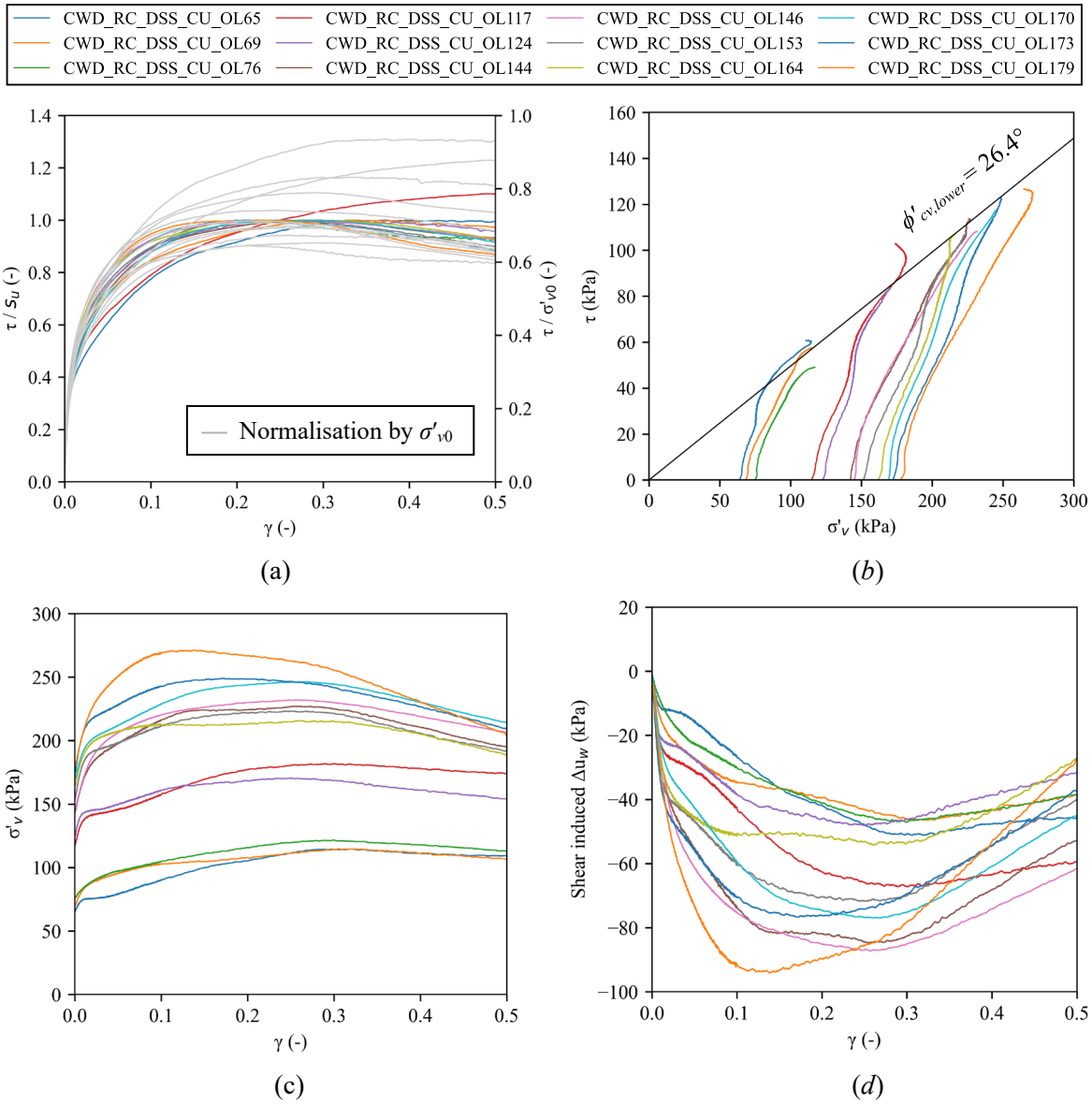


Figure 5-10: Summary of overloaded DSS outputs from 6.0 to -5.0 mAOD - (*a*) Normalised shear stress versus shear strain, (*b*) DSS stress path, (*c*) normal stress versus shear strain, and (*d*) inferred pore pressure change versus shear strain

5.5 General observations of DSS tests across depth profile

5.5.1 Stress-strain behaviour and the effect of confining stress

Many of the specimens in the upper layers failed to reach a peak or show plateau of shear stress. While Cowden till is characterised as a ductile material (Zdravković et al., 2020) with PI = 19%, no peak strength was reached for some samples at shear strains up to 50%. However, this is not unusual, as seen in the research by McKinlay et al. (1974), who made similar observations for a comparable glacial till. For selected tests where $\gamma_f > 0.5$, the s_u at $\gamma = 0.25$ was reported as shown in Figure 5-7(a). This is relatively uncommon as most researchers report s_u values at $\gamma = 0.15$ for clays, as seen in the work by Lau (1988) and Andersen (2015). However, based on the axial failure strains ($\varepsilon_{a,f} \approx 16.5\%$) observed in the undrained triaxial compression tests described in Section 5.7, the reporting of s_u at $\gamma = 0.25$ was deemed to be more appropriate. The adjustment was generally used for shallower samples with low confining stresses.

The tests were conducted from in-situ effective stress conditions following one of the two loading methods discussed in Section 5.2. This series of experiments underline the importance of overloading the samples to correct for sample disturbance. There were noticeable differences in the strain developments between the methods, with failure shear strains γ_f being lower when using the OL approach, as seen when comparing Figure 5-9(a) to Figure 5-10(a), where γ_f drops from a mean of 0.33 to 0.28. The measured failure shear strains agree with the results documented by both Lau (1988) and Ushev (2017). Furthermore, the stress paths between the two methods are distinct, with OL giving a more dilative and stiffer response and NL giving a more contractive and softer response before undergoing a phase transformation. From the stress paths, the tests appear to approach a well-defined critical state line. Examining the stress path was preferred as it is unclear whether the samples have reached a critical state when evaluating conventional shear stress-

strain curves (Atkinson et al., 1991). While not the same as the critical state friction angle ϕ'_{cs} measured in a triaxial or direct shear box apparatus (Bishop, 1972), due to the shear orientation, the differences are small for clays (Duncan and Seed, 1966; Atkinson et al., 1991).

Nonetheless, the till approaches an average critical state friction angle $\phi'_{cv,upper} = 33.0°$ for the upper layer and $\phi'_{cv,lower} = 27.6°$ for the lower layer. The angle for the upper layer is unusually high for clay and is greater than the values reported in literature for Cowden till. The PISA project reported a value of $\phi'_{cs,PISA} = 27.5°$ (Zdravković et al., 2020) and Atkinson et al. (1991) reported a value of $\phi'_{cs} = 30°$. The higher friction angle in the upper layers may be due to samples not fully reaching critical state conditions, or non-uniformity of samples at high strain.

Specimen CWD_RC_DSS_CU_NL117 and its OL pair, shown in Figure 5-9 and Figure 5-10, respectively, were considered outliers, exhibiting a higher normalised shear strength and more significant changes in vertical effective stress during shear. This behaviour might reflect the depositional changes of one of the sandy silt layers encountered around a depth of 1.0 mAOD. This is also supported by the comparatively low moisture content and low bulk density recorded for these specimens in Table 5-4. Other notable tests included CWD_RC_DSS_CU_NL76NL and CWD_RC_DSS_CU_OL76, giving similar trends but higher moisture content. Initial observations suggest that these specimens differed from the other tested tills, with no clear cobbles and stones in the clay matrix (Figure 5-11). It appears that the matrix dictates a large part of the soil's mechanical behaviour, which is analogous to the findings made by Zdravković et al. (2019). This also raises issues surrounding the representative elementary volume (REV) addressed in Chapter 3. Excluding the outliers, there was a slight trend of s_u increasing with decreasing initial void ratio e_i as shown in Figure 5-12, using a least squares regression fit.

There was a marked difference in mechanical behaviour for the upper layers (RL: 10.8 to 6.0m) compared to the lower profile (RL: 6.0 to -5.0m). As pointed out earlier, this includes higher failure shear strains and smaller changes in σ'_v as there was likely to be a more contractive response in the lower layers. Apart from the lower confining stress, the soil's behaviour at the top of the profile was also affected by its higher plasticity, water content, and OCR, comparable to the PISA findings discussed in Section 4.5. Cowden till is regarded as a heavily anisotropic material (Liu et al., 2020), which may have affected the measured outputs, where material variability was inevitably introduced by the till's erratic gravel particles and fissure systems.

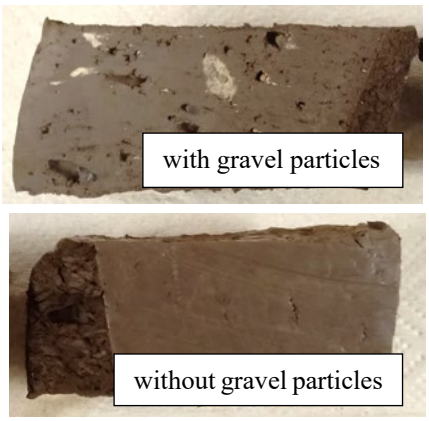


Figure 5-12: Cross-section of Cowden till specimens with and without gravel particles

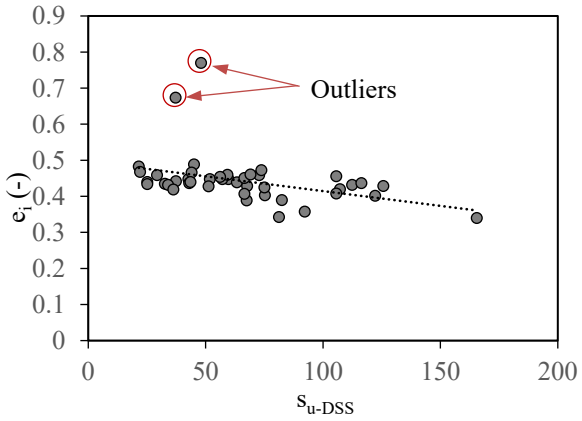


Figure 5-11: Correlation between initial (i.e. end of final consolidation stage) void ratio and measured s_u in DSS

5.5.2 Pore pressure response

The pore pressure response in a constant volume test using a simple shear apparatus is often inferred by assuming that the change in effective normal stress required to maintain constant volume is equal and opposite to the change in pore pressure that would have developed in a truly undrained test with the total vertical stress held constant, a method commonly employed for normally consolidated soils (Dyvik et al., 1987). However, some evidence suggests that it can also be applied for overconsolidated soils such as Cowden till (Thian and Lee, 2017; Jana et al., 2021). Standards such as ASTM D6528-17 (2017) apply this assumption for all fine-grained soils tested under constant volume DSS conditions.

After an initial contraction stage, the NL specimens tend to dilate, with the pore pressure initially increasing and then reducing, which is consistent with the findings by Thian and Lee (2018) on similar marine-type clays that have been heavily overconsolidated. Furthermore, based on triaxial tests (Section 5.7.2) using both loading approaches, it was discovered that changes in the measured u_w had similar progressions. However, this meant that suggesting the change in pore pressure can be inferred directly from the change in normal stress was not correct for the OL DSS tests, as the plots in Figure 5-8(d) and Figure 5-10(d) yield a purely negative change in pore pressure. This implies that the method proposed by (Dyvik et al., 1987) may not be suited for overconsolidated clays in this project.

5.5.3 Effect of shearing rate

The shearing rate impacts the measured undrained shear strength of cohesive soils, as many researchers have observed (Matešić and Vucetic, 2003; Watanabe and Kusakabe, 2013; Mun et al., 2016). For most rate effect tests on clays, the increase in s_u with strain rate is approximately 8% to 20% per log cycle. For this project, nine rate effect tests were performed and were found to exhibit a similar rate of increase.

Selected DSS tests were performed at three different rates under strain rate control conditions with $\dot{\gamma}$ = 3, 30, and 300 %/hour (see Table 5-5). This builds on the main body of 3 %/hour tests used to characterise the undrained shear strength of the PICASO site. In all cases, the samples were overloaded, meaning the inferred pore pressure response was not considered. For all plots in Figure 5-13, there was a clear increase in strength at faster shearing rates. For consistency, the ultimate strength or s_u was taken at γ = 25%. Although the six tests share some similarities, for moisture content, density and void ratio, the rate of increase in strength per log cycle, denoted by Λ_R, differed by large margins. Previous reports suggested the material to have a value of around 6 to 8% (Ushev, 2017), but most of the values recorded (summarised in Table 5-5) in this study were between 6 and 18%. Similar

findings have been made by Wu (2022), whose work involves investigating rate effects on monopile foundations in clay. A better approximation of Λ_R was determined by performing a multi-rate test (Le et al., 2022; Wu, 2022). This is illustrated in Figure 5-13(c), where the multi-rate test varied from a shear strain rate of 3 to 300 %/hour at set increments. Here the backbone for the two tests is approximated using a hyperbolic tangent curve (Jeanjean et al., 2017), showing a 9.3% increase in strength per log cycle. A representative Λ_R is likely to lie closer to this value as both rates were carried out on a single sample, thus mitigating the high variability associated with this type of soil.

Table 5-5: Rate effect results for Cowden till

No.	Test ID	RL (m)	BGL (m)	w_{avg} (%)	ρ_{avg} (Mg/m^3)	$e_{f,avg}$ (-)	$s_{u,\dot{\gamma}=3\%/hr}$ (kPa)	$s_{u,\dot{\gamma}=30\%/hr}$ (kPa)	$s_{u,\dot{\gamma}=300\%/hr}$ (kPa)	Λ_R (%)
1	CWD_BS_DSS_CU_OL35	8.55	2.25	16.4	2.192	0.404	82	93	99	10.1
2	*CWD_BS_DSS_CU_OL35a	8.55	2.25	16.4	2.192	0.404	86	–	94	9.3
3	CWD_ RC_DSS_CU_OL65	5.04	5.76	17.6	2.164	0.416	58	66	-	12.9
4	CWD_ RC_DSS_CU_OL124	-0.11	10.91	13.7	2.124	0.368	83	110	115	18.1
5	CWD_ RC_DSS_CU_OL164	-3.56	14.36	16.3	2.165	0.380	106	113	120	6.4

Notes:

Λ_R = Percentage increase in shear strength per log cycle of shear strain rate
$\dot{\gamma}$ = Shear strain rate applied to corresponding DSS test
w_{avg} = Average moisture content taken over all tests
$e_{f,avg}$ = The average void ratio at failure for all tests
* = Multi-rate test ranging from $\dot{\gamma}$ = 3 %/hr to 300 %/hr

Selected specimens from Section 5.4 had one or two corresponding rate effect tests. The number of tests performed was restricted by the number of usable samples obtained from the preserved cores within specific depth ranges. Assuming a log-linear increase in strength, as suggested earlier, the following equation was fitted to each data set shown in Figure 5-14.

$$s_u = B \log_{10}(\dot{\gamma}) + C \tag{5-2}$$

where $\dot{\boldsymbol{\gamma}}$ is the shear strain rate, and B and C are the slope and intercept values of the semi-logarithmic relationship. The fitted curves uncover a lack of consistency with the results, where no clear trend was evident, which is likely to be attributed to the variability of the soil. Interestingly, inconsistencies were also reported in the PISA results, with increases as large as 22.7%. Considering all the tests, a mean increase of ~12% in s_u per log cycle of

strain rate was calculated. A standard deviation of ± 4.5% was measured, highlighting the variability of the soil. Here the slopes of the fitted curves relate to the increase in actual shear strength (in kPa) per log cycle of strain rate and not percentage increase, thus should not be confused with the values denoted by Λ_R.

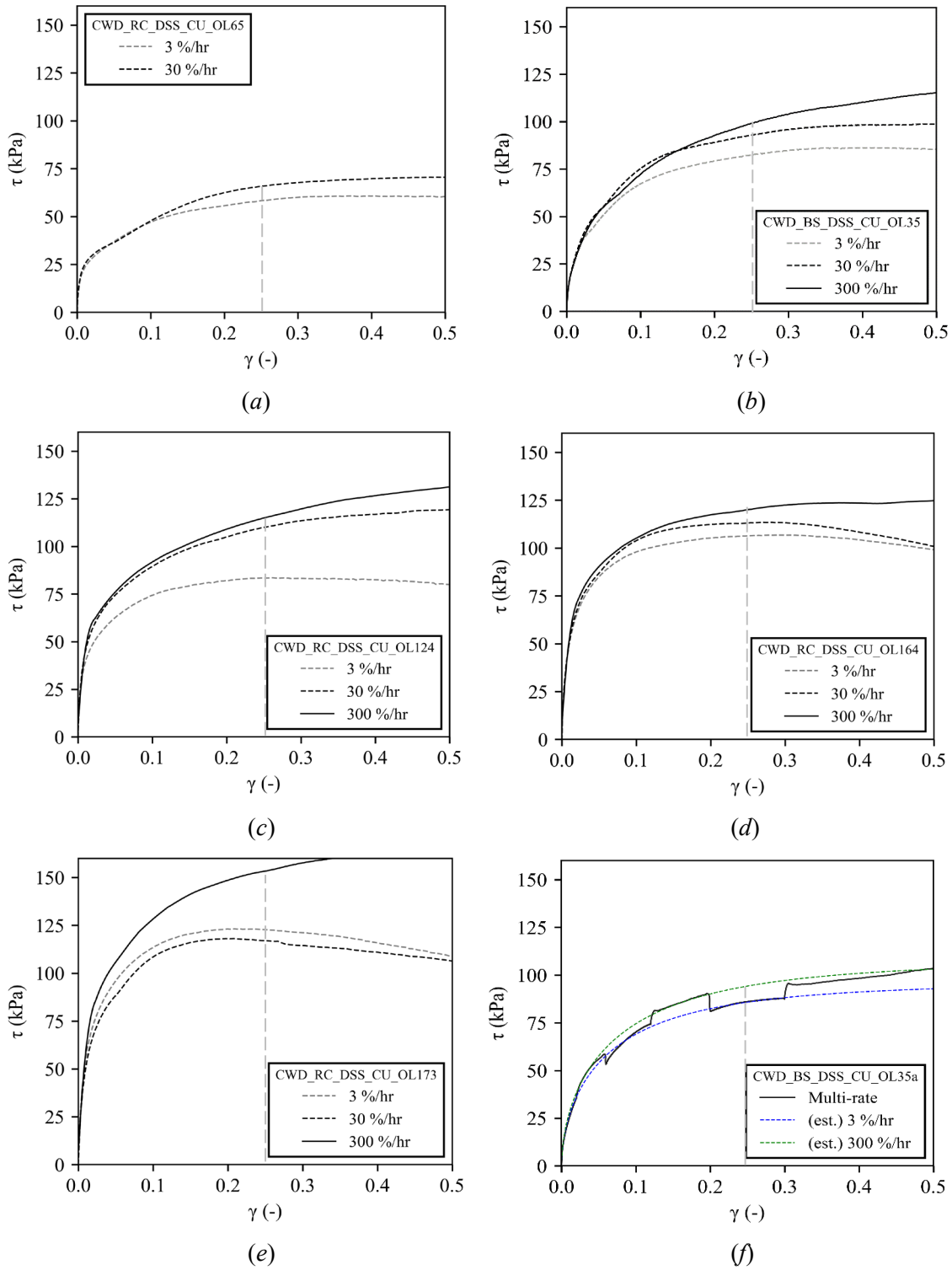


Figure 5-13: Comparison of s_u for samples under different rates of shear strain $\dot{\gamma}$

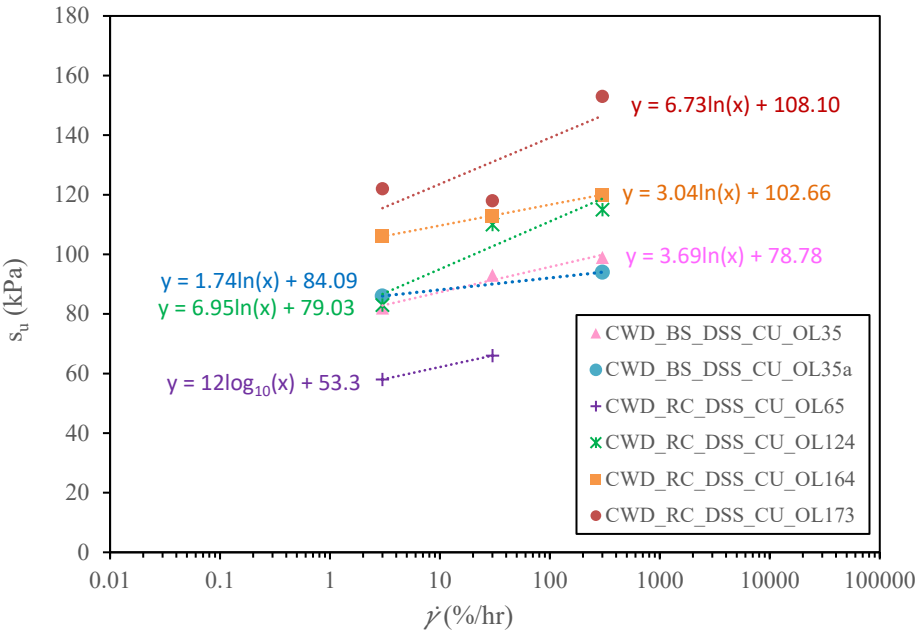


Figure 5-14: Undrained shear strength s_u of specimens plotted as a function of shear strain rate

5.5.4 Effect of sample confinement method

While not all confinement methods were explored in this research, there was felt to be merit in investigating the use of both a wire-reinforced membrane (WRM) and a stack of confining rings to better understand the discrepancies between the two approaches. It was initially assumed that using a WRM on stiff clay samples would not be feasible as the membrane may prevent the sample from deforming uniformly. This was investigated by increasing the wire stiffness and the number of wire windings. The WRMs were supplied by the Norwegian Geotechnical Institute (NGI) to compare the two different confinement methods and whether they applied to the current research project.

WRMs were used for tests CWD_RC_DSS_CU_NL144_WRM and CWD_RC_DSS_CU_OL144_WRM; their results are plotted in Figure 5-15 and Figure 5-16, alongside the corresponding tests utilising confining rings. For both loading approaches, the tests with WRMs deliver lower bound s_u values combined with low γ_f values, registering s_u values of 53 kPa for NL and 88 kPa for OL. This equates to a 22% reduction in strength when using a WRM. Equally, the failure shear strains γ_f were recorded as 0.13 and 0.15, significantly lower than the original DSS tests (γ_f = 0.29 and 0.41) and slightly less than the

mean axial strains ($\varepsilon_{a,f}$ = 16.5%) measured from the triaxial tests. These observations differ from the findings by McGuire (2011) and Baxter et al. (2010), who both contended that the two confinement systems gave comparable stress-strain results. While the ultimate shear strengths were similar, the failure strains were underestimated compared with the results obtained with confining rings. However, the progression of strain-softening at large strains was consistent with the above authors. While the use of WRMs would not be an issue for most soils since they reach peak strengths at strains of less than ~5% (Baxter et al., 2010), the extremely ductile nature of the stiff glacial till at Cowden means that the confinement technique has a relatively large influence on the measured peak strength.

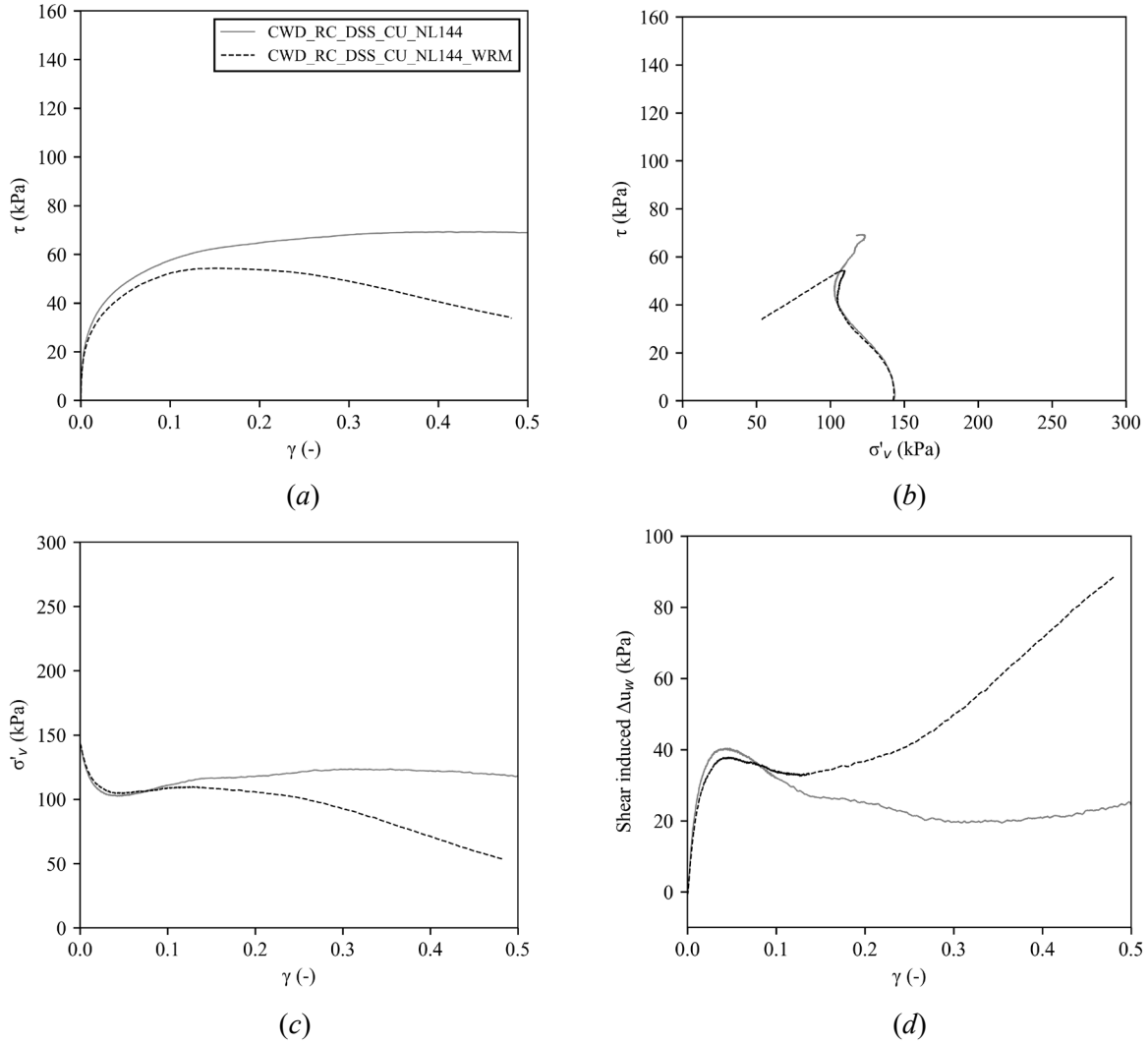


Figure 5-15: Comparison of confinement techniques for NL DSS tests

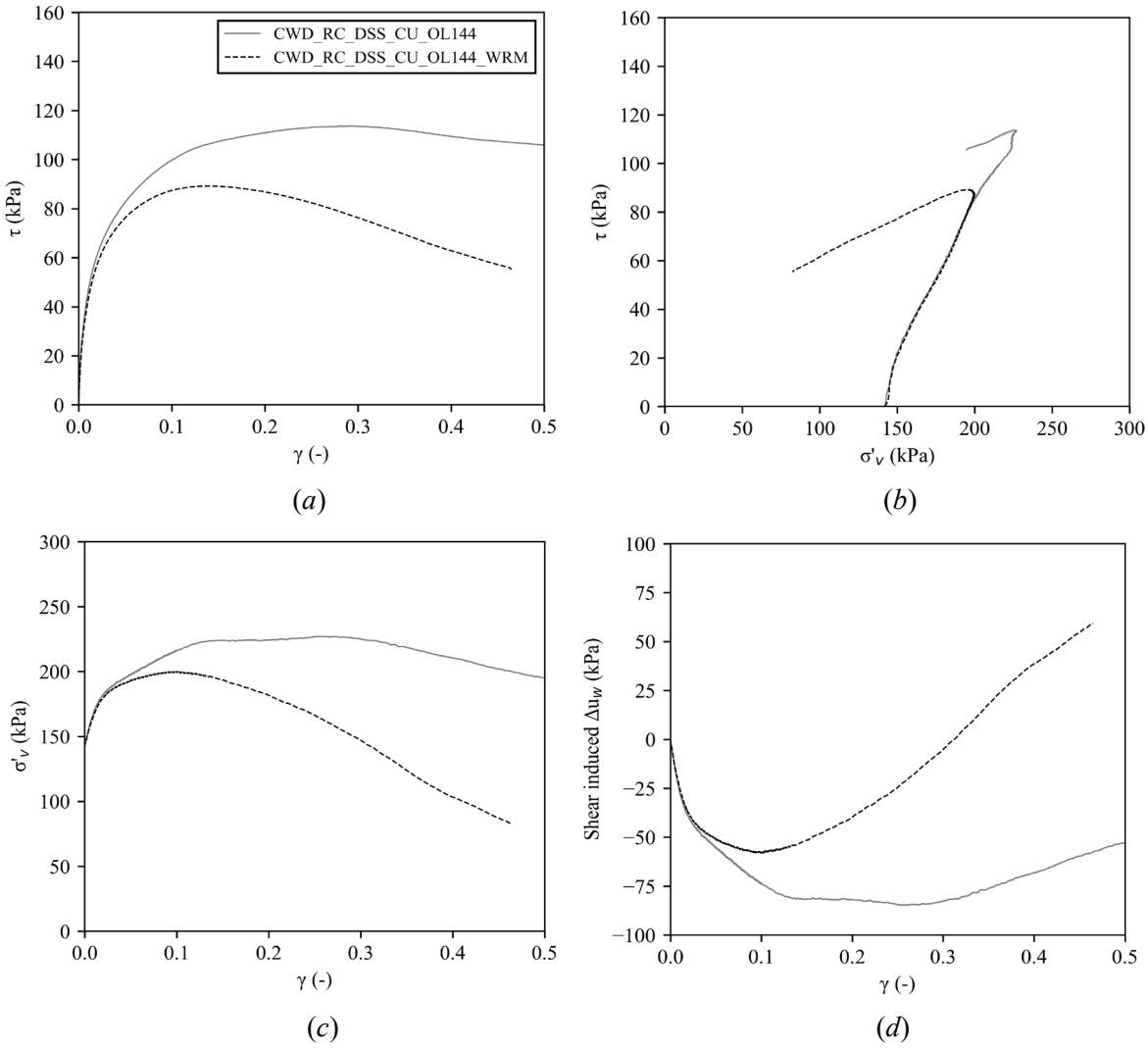


Figure 5-16: Comparison of confinement techniques for OL DSS tests

Presumably, at high strains $\gamma > 0.05$, the non-uniform stress conditions induced by the WRM reduce the amount of vertical stress acting on the specimen (Figure 5-15(c) and Figure 5-16(c)), which in turn results in a corresponding decrease in shear stress, explaining the softening behaviour seen in most tests using WRMs (Degroot et al., 1994). The non-uniformity refers to the DSS system's inability to impose complementary shear stresses on the sides of the specimen due to their near-frictionless vertical boundaries (Wai et al., 2021). This is less evident at small strains as the bulk of the specimen volume reaches simple shear conditions, as confirmed by Airey et al. (1985) and Budhu (1984). This is shown in both Figure 5-15 and Figure 5-16, where the responses for both confinement methods are identical at the start, but those equipped with WRMs decrease in σ'_v and τ more rapidly.

5.6 Stress distribution and lateral stress estimation in DSS tests

Rarely is the complete state of stress in a DSS sample known during a test. This is due to the lack of horizontal stress measurements in most modern DSS apparatus (Baxter et al., 2010; Rutherford, 2012; Acharya and Airey, 2017; Li et al., 2017), with the exception of the Cambridge-type device (Wroth and Bassett, 1965; Stroud, 1971) and some that have employed sensors or a pressure confinement system (Airey, 1984; Le Meil et al., 2016; Klar et al., 2019; Zwanenburg et al., 2019). However, in this research, piezoresistive force sensors detailed in Section 3.4.2 aided the overall analysis, allowing estimation of the complete stress state and comparing it with other commonly used empirical methods. As shown in Figure 5-17, the installed sensors measured the intermediate principal stress $\sigma'_2 = \sigma'_h$ acting perpendicular to the plane of shearing. This may not be the same as the horizontal stress $\sigma'_3 = \sigma'_h$ acting in the plane of shearing (Budhu, 1979), but σ'_2 was used instead to prevent possible damage to the sensor while also providing a reasonable estimate of the lateral stress during both the consolidation and shearing stage.

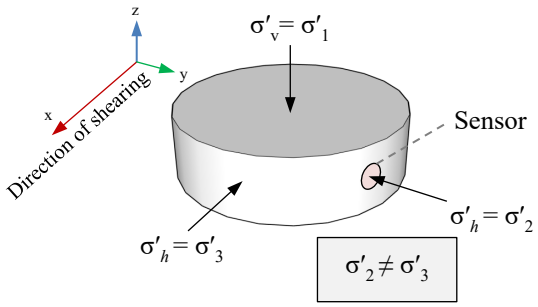


Figure 5-17: Orientation of principal stresses acting on DSS sample

From the lateral stress measurements, the at-rest earth pressure coefficient at the end of the consolidation stage $K_{0,con}$ can be determined by dividing the lateral stress reading by the applied vertical effective stress σ'_v ($= \sigma'_{v0}$). Figure 5-18(a) reveals a good match between the sensor-derived $K_{0,con}$ values and the PICASO project's adopted K_0 profile, discussed in Section 4.8. The findings are also consistent with the K_0 values used for the PISA project (Liu et al., 2020). The OL values give better approximations since in the NL tests the

extruded specimens may not be fully mobilised with the sensor due to insufficient contact between the confining rings and the sample. When considering solely the OL tests, mean values of $K_{0,con}$ = 1.28 from 10.8 to 4.0 mAOD and $K_{0,con}$ = 0.93 from 4.0 to -5.0 mAOD were determined. The lower part of the profile was found to be a good fit with the OL-determined $K_{0,con}$, excluding test CWD_RC_DSS_CU_OL179. However, this was not the case for layers just below the surface, where greater deviations were seen. Apart from the sensor's limitations and measurement of the intermediate principal stress, the soil's erratic cobble content could also be a reason for the scattered readings in the upper layers. Additionally, swelling may have played a role, which is addressed in Section 5.3.3.

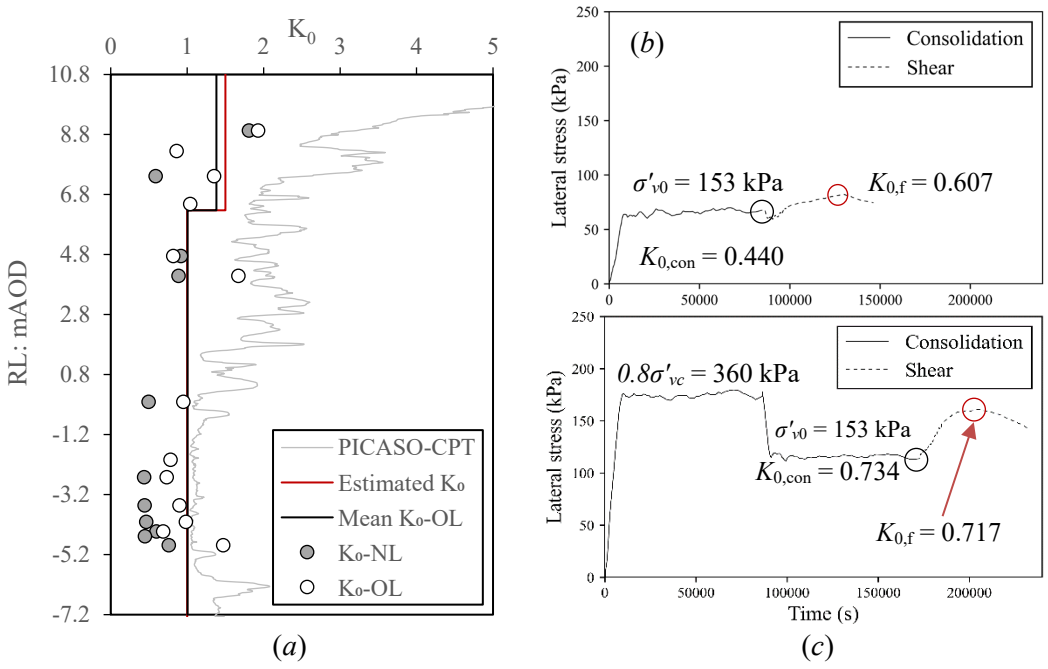


Figure 5-18: (*a*) Measured K_0 values with depth (b) Lateral stress measurements for tests CWD_RC_DSS_CU_NL153 and (c) CWD_RC_DSS_CU_OL153

Only a few researchers have recently attempted to measure the lateral stress in a DSS-type system (Klar et al., 2019; Zwanenburg et al., 2019). Therefore, the failure interpretation presented in Figure 5-19, previously covered in Section 2.2.5, was assumed to be the primary mode of failure in a DSS test. With this assumption, the true undrained shear strength $s_{u,true}$ can be determined following the expression (Lau, 1988):

$$s_{u,true} = \frac{s_u}{\sin 2\theta} \tag{5-3}$$

where θ is the rotation of the principal axes of stress as shown in Figure 5-19, which can be calculated from the measured stresses acting on the specimen (i.e. σ'_v, σ'_h, τ). The σ'_h was determined by measuring the lateral stress acting on the specimen at failure, which in turn provided the K_0 at failure (Figure 5-18(b) and (c)). While the use of such a sensor is novel, it must be stated that due to its noise and drift susceptibility, the measured values are regarded as approximations. More detail on the performance and applicability of the sensor can be found in Section 3.4.2. A summary of the K_0 measurements is given in Table 5-6, along with the adjusted $s_{u,true}$. For 50% of the tests, little difference (< 5%) was seen when adjusting for s_u. This adjustment is not common in standard practice as some may consider the differences negligible, or devices are not well equipped to measure the horizontal stresses acting on a sample. An example of the calculation of the adjusted $s_{u,true}$ is given below:

Example (CWD_RC_DSS_CU_OL153)

Known parameters and assumptions:	Lateral stress @ failure: σ'_h = 160 kPa
Reduced level: -2.62 mAOD	Vertical effective stress @ failure: σ'_v = 223 kPa
Post-excavation depth: 13.42 mBGL	K_0 at failure: $K_{0,f}$ = 0.717
Vertical effective stress: σ'_v = 153 kPa	Recorded undrained shear strength: s_u = 106 kPa

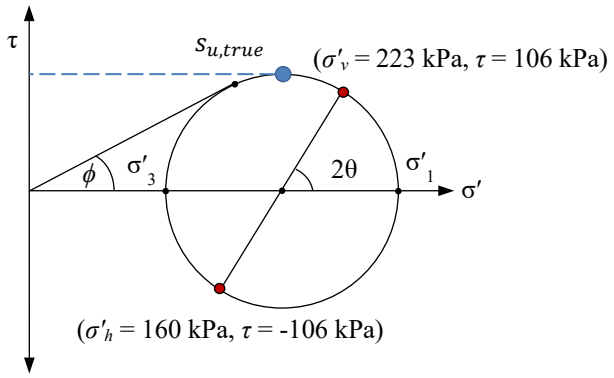


Figure 5-19: Assumed failure criterion in DSS

$$\sigma'_h = K_0\sigma'_v \quad \rightarrow \quad 160 = K_{0,f}(223)$$
$$K_{0,f} = 0.717$$

$$2\theta = \tan^{-1}\left(\frac{2\tau}{\sigma'_v - \sigma'_h}\right) \quad \rightarrow \quad 2\theta = \tan^{-1}\left(\frac{2(106)}{(223 - 159.9)}\right)$$
$$\theta = 36.7°$$

$$s_{u,true} = \frac{s_u}{\sin 2\theta} \quad \rightarrow \quad s_{u,true} = \frac{106}{\sin(2(36.7))}$$
$$s_{u,true} = 110\ kPa$$

Table 5-6: Measured K_0 based on lateral stress measurements in VDDCSS

No.	Test ID	RL (m)	BGL (m)	σ'_{v0} (kPa)	$\sigma'_{v,f}$ (kPa)	$K_{0,\ con}$	$K_{0f,\ shear}$	$s_{u,\ initial}$ (kPa)	$s_{u,\ true}$ (kPa)	%Δ
1	CWD_RC_DSS_CU_NL21	8.93	1.87	21	37	1.810	0.789	25.1	25.3	1.2
2	CWD_RC_DSS_CU_OL21	8.93	1.87	21	98	1.930	0.502	59.7	64.8	8.0
3	CWD_RC_DSS_CU_OL29	8.25	2.55	29	77	0.863	0.654	49.3	50.8	3.6
4	CWD_RC_DSS_CU_NL39	7.41	3.39	39	62	0.590	0.507	39.2	41.9	7.3
5	CWD_RC_DSS_CU_OL39	7.41	3.39	39	132	1.354	0.606	75.2	79.4	5.8
6	CWD_RC_DSS_CU_OL49	6.48	4.32	49	115	1.042	0.619	63.2	66.7	5.8
7	CWD_RC_DSS_CU_NL69	4.75	6.05	69	76	0.920	0.811	43.0	43.6	1.4
8	CWD_RC_DSS_CU_OL69	4.75	6.05	69	114	0.819	0.645	56.1	59.5	6.3
9	CWD_RC_DSS_CU_NL76	4.09	6.71	76	67	0.889	0.785	37.2	37.9	1.9
10	CWD_RC_DSS_CU_OL76	4.09	6.71	76	117	1.671	1.013	48.0	48.0	0.0
11	CWD_RC_DSS_CU_NL124	-0.11	10.91	124	117	0.497	0.812	67.4	67.9	1.3
12	CWD_RC_DSS_CU_OL124	-0.11	10.91	124	170	0.952	0.674	82.4	86.6	5.5
13	CWD_RC_DSS_CU_OL146	-2.04	12.84	146	232	0.785	0.573	107.1	117.9	10.2
14	CWD_RC_DSS_CU_NL153	-2.62	13.42	153	132	0.440	0.607	66.5	70.9	7.3
15	CWD_RC_DSS_CU_OL153	-2.62	13.42	153	223	0.734	0.717	105.6	110.3	4.1
16	CWD_RC_DSS_CU_NL164	-3.56	14.36	164	134	0.445	0.715	66.4	68.7	4.1
17	CWD_RC_DSS_CU_OL164	-3.56	14.36	164	215	0.902	0.709	105.6	110.5	4.3
18	CWD_RC_DSS_CU_NL170	-4.11	14.91	170	152	0.466	0.517	72.7	81.7	12.0
19	CWD_RC_DSS_CU_OL170	-4.11	14.91	170	246	0.986	0.621	116.2	125.0	7.7
20	CWD_RC_DSS_CU_NL173	-4.43	15.23	173	152	0.601	0.631	73.7	79.1	7.0
21	CWD_RC_DSS_CU_OL173	-4.43	15.23	173	248	0.688	0.576	122.2	132.8	8.9
22	CWD_RC_DSS_CU_NL175	-4.59	15.39	175	138	0.449	0.518	69.0	76.6	11.0
23	CWD_RC_DSS_CU_NL179	-4.89	15.69	179	179	0.761	0.971	73.1	73.0	0.1
24	CWD_RC_DSS_CU_OL179	-4.89	15.69	179	154	1.473	0.963	125.6	126.0	0.4

5.7 Triaxial test results

5.7.1 Triaxial test programme

A total of 11 triaxial compression tests and three extension tests, all with local instrumentation, were performed (see Table 5-7). This included anisotropic and isotropic compression tests using two different loading approaches similar to the DSS tests. The testing conditions were based on an estimated in-situ mean effective stress and a K_0 profile derived from CPT readings, as previously discussed in Section 4.8. The complete loading and shearing procedures for the triaxial tests can be found in Section 3.5.2. The tests have been used to characterise the undrained shear strength of the PICASO site and to aid in the interpretation and analysis of the DSS results.

5.7.2 Test results

The results for the triaxial compression and extension tests are presented in Figure 5-20 and Figure 5-21, containing plots of deviator stress q versus axial strain ε_a, q versus mean effective stress p', change in pore pressure versus ε_a, and normalised stress ratio q/p' versus ε_a. The OL triaxial compression tests followed a similar loading procedure to that given for the DSS example in Section 5.2. Furthermore, the anisotropic triaxial tests were based on the adopted K_0 profile covered in Section 4.8 (Figure 5-35) - (e.g. CWD_RC_TX_CAUc_NL31: K_0 = 1.5, σ'_v = 23.4 kPa, p'_0 = 31 kPa). The results from the tests are summarised in Table 5-7 and cover both BS and RC samples. Only two tests (one in compression and one in extension) on BS were carried out and were considered to be sufficient for comparison against the RC sample results. This was based on the similarities in sample quality observed between triaxial BS and RC tests covered in Section 5.9.

Table 5-7: Summary of monotonic Triaxial test programme

No.	Test ID	RL (m)	BGL (m)	p'_0 (kPa)	$0.8\sigma'_{vc}$ (kPa)	w (%)	ρ (Mg/m^3)	e_i (-)	e_f (-)	s_u (kPa)	$\varepsilon_{a,f}$ (%)
1	CWD_RC_TX_CAUc_OL29	9.34	1.46	29	298	16.5	2.165	0.442	0.426	73	16.5
2	CWD_RC_TX_CAUc_NL31	8.75	2.05	31	31	17.4	2.162	0.455	0.47	68	20.6
3	CWD_RC_TX_CAUc_OL39	8.25	2.55	39	119	18.9	2.126	0.5	0.482	68	18.7
4	CWD_RC_TX_CAUc_NL44	7.91	2.89	44	44	17.0	2.158	0.453	0.456	71	15.9
5	CWD_BS_TX_CAUc_NL47	7.69	2.95	47	47	14.2	2.211	0.384	0.388	113	17.8
6	CWD_BS_TX_CAUe_NL47	7.69	2.95	47	47	16.8	2.128	0.471	0.478	59	9.8
7	CWD_RC_TX_CIUc_OL65	6.48	4.32	65	225	15.8	2.165	0.434	0.434	94	14.3
8	CWD_RC_TX_CIUc_OL53	6.13	4.67	53	169	16.7	2.168	0.442	0.435	73	17.4
9	CWD_RC_TX_CIUc_NL55	6	4.80	55	55	17.4	2.158	0.458	0.463	82	19.1
10	CWD_RC_TX_CIUc_NL117	0.57	10.23	117	117	13.1	2.252	0.345	0.346	179	19.9
11	CWD_RC_TX_CIUc_OL146	-2.04	12.84	146	471	14.9	2.188	0.408	0.369	126	11.4
12	CWD_RC_TX_CIUc_NL153	-2.66	13.46	153	153	15.7	2.173	0.427	0.409	143	13
13	CWD_RC_TX_CIUe_NL175	-4.59	19.44	175	75	17.3	2.140	0.472	0.452	54	1.6
14	CWD_RC_TX_CIUe_NL187	-5.63	18.1	187	187	17.3	2.089	0.507	0.503	85	3.7

Notes:

p'_0 = Initial mean effective stress

$0.8\sigma'_{vc}$ = 80% of σ'_{vc} inferred from corresponding CPT readings

K_0 = Pre-shearing K_0 adopted from CPT results

$\varepsilon_{a,f}$ = Axial strain at failure

CAUc = Samples anisotropically loaded to a K_0 = 1.5

5.7.2.1 Triaxial compression tests

Like the DSS tests, the triaxial compression tests reveal an increase in undrained shear strength with consolidation to higher p'. Failure was defined as the point of peak deviator stress, around 16.5% axial strain ε_a for compression, compared with 25% measured in the PISA project (Ushev, 2017). The Cowden till is highly ductile and only exhibits slight post-peak softening in compressional shearing, with all specimens bulging as they approached failure. Under both loading conditions (NL and OL), there was a negligible difference between the results, giving a similar stress-strain response and pore pressure change Δu_w.

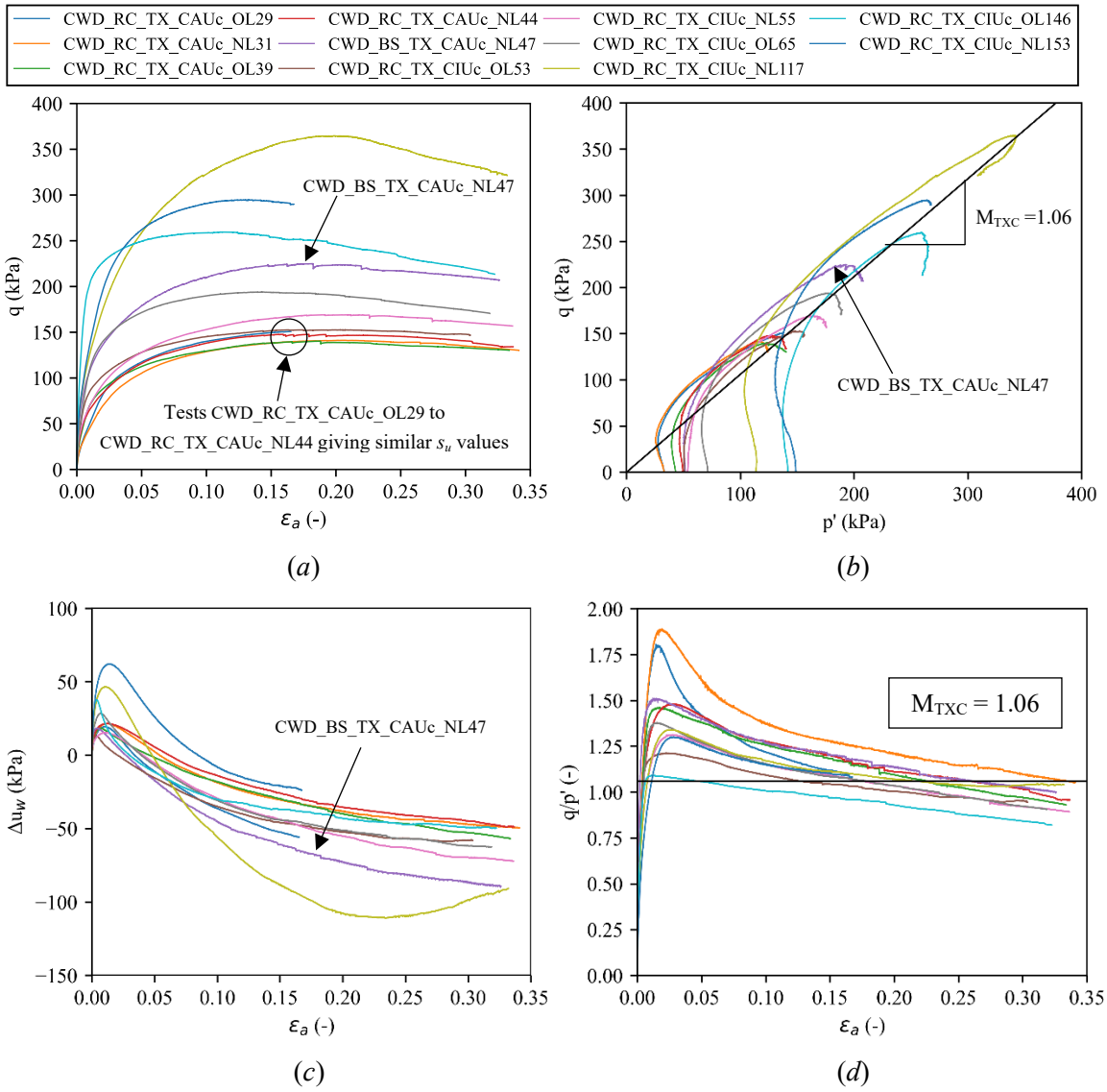


Figure 5-20: Triaxial compression tests - (*a*) Deviator stress versus axial strain (*b*) Effective stress path (*c*) Pore pressure versus axial strain (*d*) Normalised stress ratio versus axial strain

Although the experiments show a clear peak in q at failure, the measured Δu_w appears to be continually decreasing and hinting at semi-stable conditions when ε_a > 25%, similar to the triaxial compression tests carried out for PISA (Ushev, 2017; Zdravković et al., 2020). The pore pressure response was similar to the inferred values measured in the DSS NL tests, showing an initial contraction before a continuously dilative curve till failure. Furthermore, when comparing OL and NL triaxial tests such as CWD_RC_TX_CAUc_OL29 to CWD_RC_TX_CAUc_NL31 or CWD_RC_TX_CAUc_OL39 to CWD_RC_TX_CAUc_OL44, there was negligible or little difference in s_u (see Figure 5-20(a)). This was expected considering their similarities in sample quality (i.e. "good" to "excellent") outlined in Section 5.9. In contrast, there was a large difference between the NL and OL DSS tests. This is likely due to sample size, where the triaxial specimens give a more representative elementary volume and are less likely to be affected by the soil's erratic cobble content and interface disturbance.

5.7.2.2 Triaxial extension tests

Although there are limited data, the triaxial extension tests also reveal an increase in undrained shear strength with consolidation to higher mean effective stress. Failure occurred around ε_a = 6.8%, which is expected, considering it is similar to the PISA extension tests (Ushev, 2017). For the three triaxial extension tests shown, the specimens started to neck as they approached failure, which meant the tests were halted at strains less than 10% and did not progress fully to their critical states.

Test CWD_RC_TX_CIUe_NL175 was stopped prematurely as a leak in the membrane occurred, meaning the specimen did not reach its ultimate failure strength compared to CWD_ BS_TX_CAUe_NL47 and CWD_ RC_TX_CIUe_NL187. For the latter two specimens, the deviator stress dropped rapidly after peak and continued to drop as necking progressed. Before the onset of necking, the pore pressure response suggests dilative behaviour.

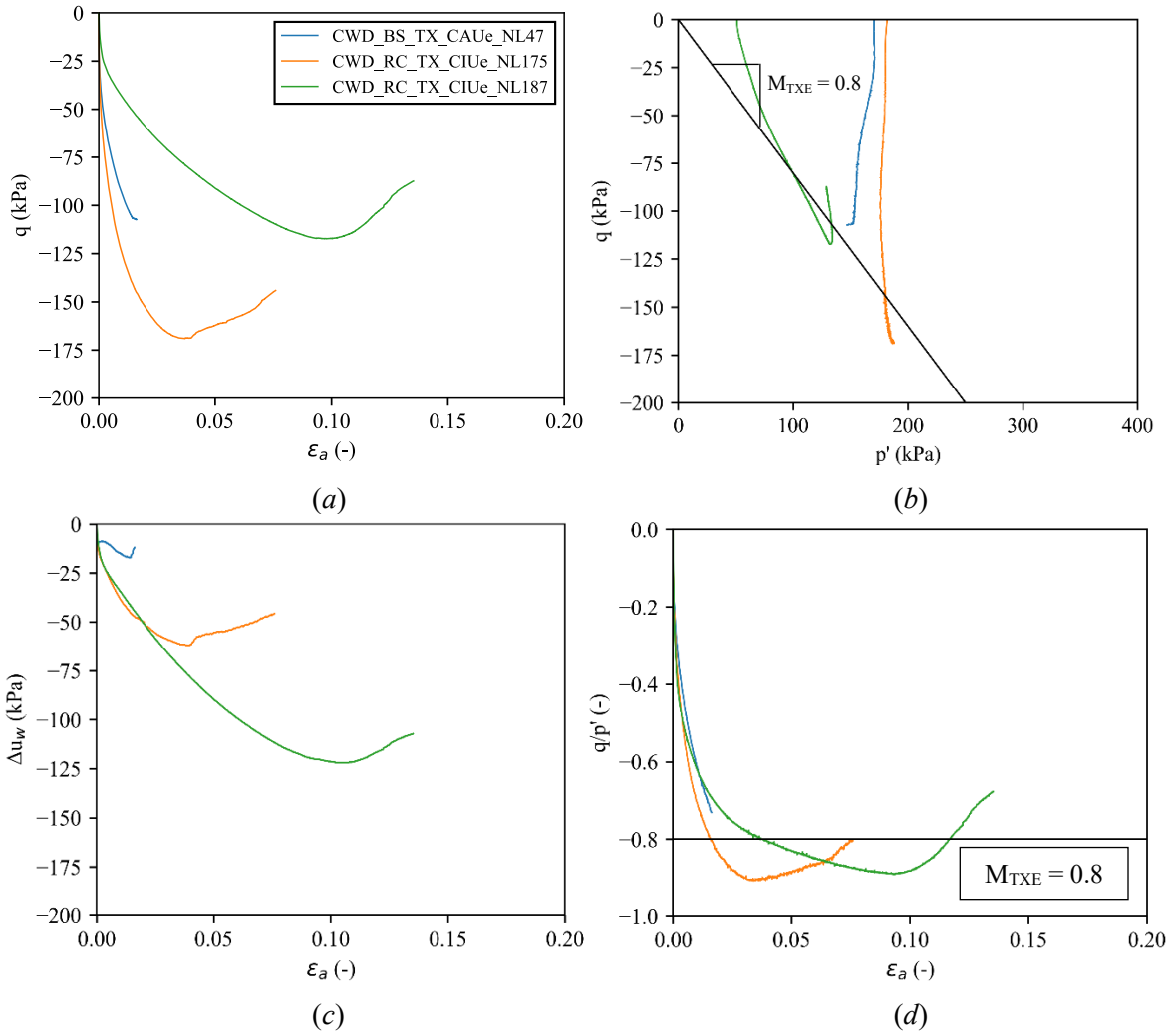


Figure 5-21: Triaxial extension tests - (*a*) Deviator stress versus axial strain (*b*) Effective stress path (*c*) Pore pressure versus axial strain (*d*) Normalised stress ratio versus axial strain

5.7.3 General observations

Evaluating Figure 5-20(b) and (d) shows how the stress ratio develops with axial strain for all 10 compression tests carried out from in-situ conditions. While CWD_RC_TX_CIUc_NL117 appears to be an outlier based on its stress-strain and pore pressure responses, it follows a similar stress path to the other tests, with a mean trend for the ultimate failure stress ratio q/p', M_{TXC} = 1.06. This lies within the range of 1.01 to 1.09 measured for the PISA tests (Ushev, 2017; Zdravković et al., 2020) and lies close to the average ultimate stress ratio, $M_{TXC,PISA}$ = 1.07 (Zdravković et al., 2020). The PICASO stress ratio M_{TXC} = 1.06, this corresponds to a critical state angle of shearing resistance, $\phi'_{cs,TXC}$ = 26.8°, which is smaller

than the values ($\phi'_{cv,upper}$ = 33° and $\phi'_{cv,lower}$ = 27.6°) measured in the DSS device. The finding is surprising considering that Atkinson et al. (1991) reported the opposite from tests on similar material, where triaxial measurements generally gave higher values.

For the extension tests in Figure 5-21(b) and (d), an ultimate stress ratio, M_{TXE} = 0.8, was determined based on CWD_ BS_TX_CAUe_NL47 and CWD_RC_TX_CIUe_NL187, which equates to a critical state angle of $\phi'_{cs,TXE}$ = 27.5°. The result was lower than that measured for PISA, where $M_{TXE,PISA}$ = 0.9 (Zdravković et al., 2020). Figure 5-22 outlines the TXC and TXE critical state lines based on the triaxial tests carried out.

The pore pressure measurements were verified by comparing and investigating the readings at the top, base, and mid-height of the samples. Figure 5-23 shows an example (CWD_RC_TX_CIUc_NL117) of the measured pore pressures at the standard shear rate of 5 %/day as covered in Section 3.5.2, showing almost identical responses. This confirms that the tests were sheared sufficiently slowly to allow for equalisation of generated pore pressures.

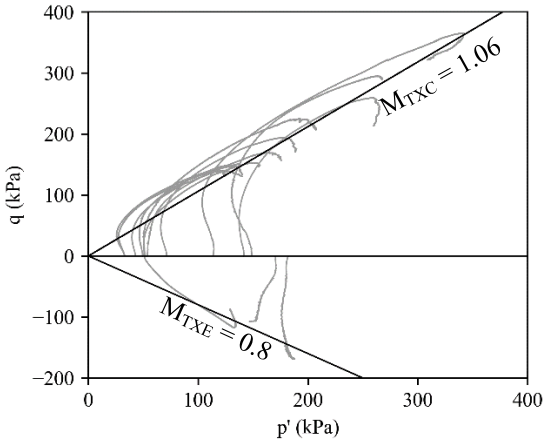


Figure 5-22: Summary of stress paths measured for TXC and TXE tests

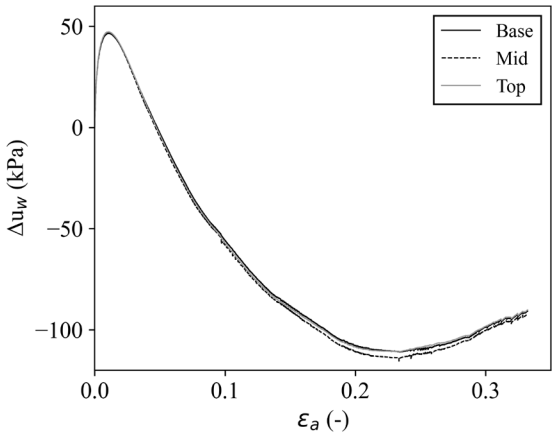


Figure 5-23: Pore pressure measurements in typical triaxial test (CWD_RC_TX_CIUc_NL117)

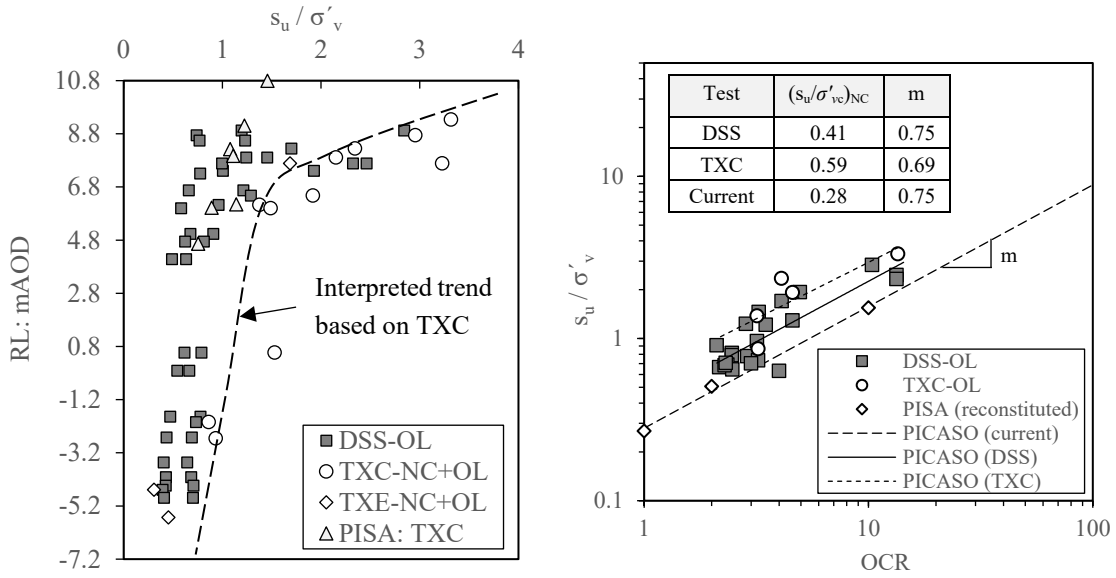
5.7.4 Comparison with DSS results

A necessary step in this research involved comparing triaxial results with DSS results. Performing standard undrained triaxial tests on stiff glacial tills is well documented (Lehane, 1992; Powell et al., 2003; Ushev, 2017), and the principal stresses acting on the specimen are known at all stages of the test. However, the DSS apparatus used in this research had no back-pressure control and no on-sample instrumentation, making it difficult to monitor the stresses acting on the specimen at each stage. As a result, attempts were made to measure the lateral stress acting on the specimens to determine the unknown principal stresses by using lateral force sensors (LFS), as discussed in Section 5.6.

The undrained shear strengths (s_u) obtained in the different shearing modes can be compared to one another, as portrayed in Figure 5-24. As pointed out in much of the literature (Mayne, 1985; Ladd et al., 2003), DSS strength outputs generally sit between the strengths obtained from triaxial compression and extension tests. This is clear in Figure 5-24(a), where the normalised s_u decreases with increasing depth. The PISA triaxial compression tests are plotted alongside the PICASO tests, but the PISA tests involved higher in-situ vertical effective stresses. This is because the PISA site ground level is at a higher elevation meaning the results are from depths greater than 5.5 mBGL, where a $K_0 = 1$ was applied (Ushev, 2017). However, this allowed the PISA data points to be plotted over the PICASO RL range of interest.

Figure 5-24(b) shows a similar relationship between the different shearing modes for tests recompressed to an estimated preconsolidation pressure. However, there is an insufficient number of triaxial extension (TXE) tests to establish a reliable correlation between s_u and OCR. However, for DSS and triaxial compression tests (TXC), their respective slopes m encapsulate the previous exponent used for the initial predictions of OCR carried out in Section 4.8, where $(s_u/\sigma'_v)_{NL} = 0.28$ and $m = 0.75$, labelled as 'PICASO (current)' in the plot. Based on the intercepts of the fitted power curves, the estimated OCR

values used for the DSS OL tests may have been overestimated and would seem to be more suited if corrected using the fitted parameters (e.g., (s_u/σ'_v) = 0.41 and m = 0.75). However, since the OL samples were only loaded to a fraction (0.8) of σ'_{vc}, it may suggest that some of the points depicted in the plot would slightly shift to the right if samples were loaded to their full σ'_{vc}. Nonetheless, the preliminary coefficients based on the PISA reconstituted triaxial specimens are considered sensible estimates for the PICASO material considering the similarity of the slopes m. Likewise, the TX and DSS tests provide a reasonable approximation of the fitting parameters, provided the material is assumed to be of low sensitivity (S_t) as interpreted in Section 4.9.



(*a*) (*b*)

Figure 5-24: (*a*) PICASO s_u/σ'_v ratio profile (*b*) Variation of s_u/σ'_v with OCR for OL TXC and DSS tests

Figure 5-25 shows that the TXC and DSS tests form a well-defined critical state line in v-ln(p') space with slopes λ_{TXC} = 0.109 and λ_{DSS} = 0.071. Additionally, their intercepts cross the p' = 1 kPa axis at Γ_{TXC} = 1.99 and Γ_{DSS} = 1.71. In theory, there should be little difference between the two datasets. However, it is likely due to the sensitivity of the sensor covered in Section 3.4.2 that differences are observed. For the DSS tests, p' is defined as ($p' = \frac{\sigma'_v+2\sigma'_h}{3}$), where $2\sigma'_h$ is obtained from the lateral stress sensor.

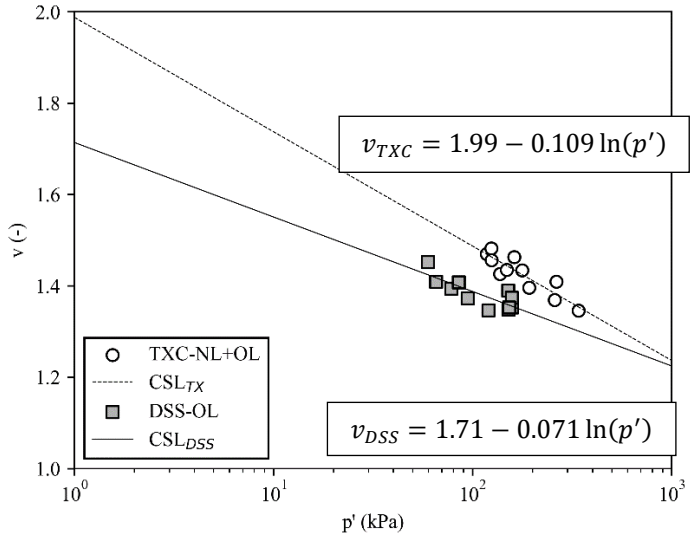


Figure 5-25: Critical state line for TXC tests and OL DSS tests equipped with lateral stress sensors

A feasible method for comparing the different shearing modes is to assess the data on the deviatoric π-plane with respect to Lode angle. The following assumptions are required:

- The measured horizontal stresses in the DSS apparatus are accurate and are equal to the intermediate principal stress σ'_2.
- Yield surfaces are based on the critical state friction angle obtained from TXC tests.
- Failure is defined once the shear stress reaches a peak. In the case of no pronounced peak, the critical state condition is assumed to be reached at the end of the test.

The construction of the Mohr-Coulomb and Matsuoka-Nakai yield surfaces in 3D stress space follows the convenient method proposed by Lagioia and Panteghini (2016) with reference to Davis and Selvadurai (2002), as presented in Figure 5-26. The Coulomb yield surface is one of the most widely used failure criteria for soils as it provides a good approximation of the yield locus in the π-plane. However, as pointed out by Davis and Selvadurai (2002) and Roscoe et al. (1963), the actual surface is similar to the hexagonal Coulomb surface but somewhat smoother. As a result, modified versions of the Mohr-Coulomb surface, such as Matsuoka-Nakai, were developed. The surfaces selected are plotted using an effective stress angle of shearing resistance obtained from triaxial compression tests, where $\phi'_{cs,TXC} = 26.8°$.

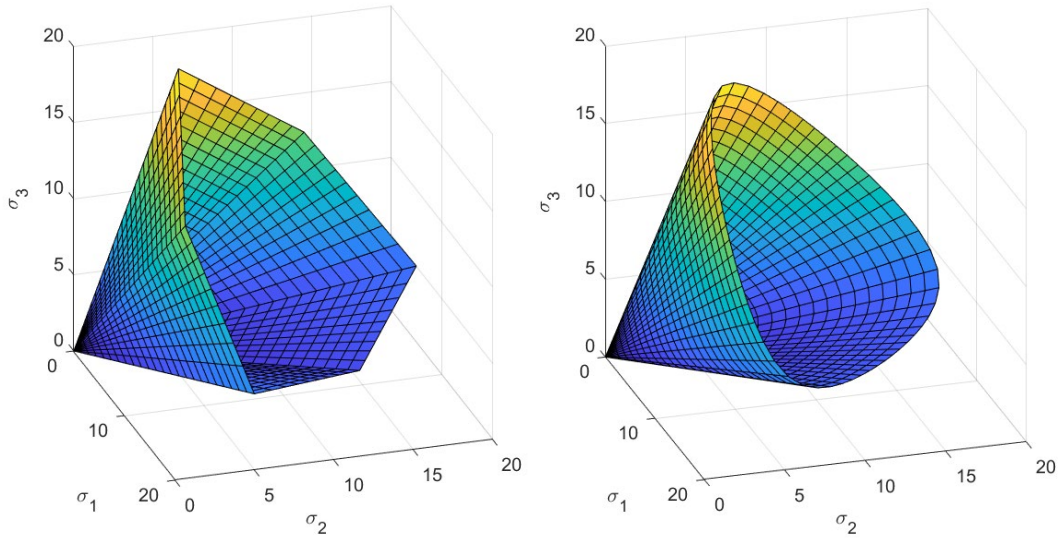
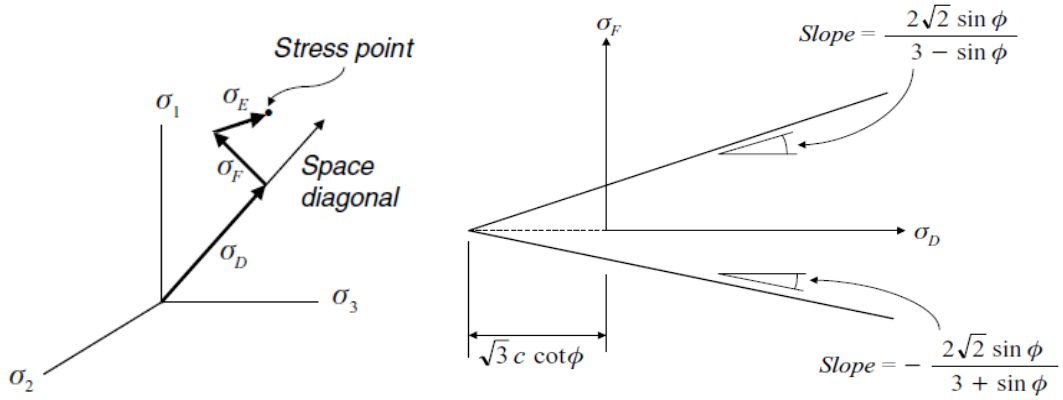


Figure 5-26: (*a*) Mohr-Coulomb failure envelope (*b*) Matsuoka-Nakai failure envelope

An alternative coordinate system was used for ease of interpretation on various π-planes along the space diagonal, where σ_E and σ_F are the stress components shown in Figure 5-27. The normalised cross-section of both yield surfaces along the space diagonal is shown in Figure 5-28(a).



$$\sigma_1' = \frac{\sigma_{xx}' + \sigma_{yy}'}{2} + \sqrt{\left(\frac{\sigma_{xx}' - \sigma_{yy}'}{2}\right)^2 + \tau_{xy}^2} \quad (5\text{-}4)$$

$$\sigma_E' = \frac{-\sigma_2' + \sigma_3'}{\sqrt{2}} \quad (5\text{-}5)$$

$$\sigma_2' = \sigma_{zz}' \quad (5\text{-}6)$$

$$\sigma_F' = \frac{2\sigma_1' - \sigma_2' - \sigma_3'}{\sqrt{6}} \quad (5\text{-}7)$$

$$\sigma_3' = \frac{\sigma_{xx}' + \sigma_{yy}'}{2} - \sqrt{\left(\frac{\sigma_{xx}' - \sigma_{yy}'}{2}\right)^2 + \tau_{xy}^2} \quad (5\text{-}8)$$

$$\sigma_D' = \frac{\sigma_1' + \sigma_2' + \sigma_3'}{\sqrt{3}} \quad (5\text{-}9)$$

Figure 5-27: Coordinate system in principal stress space along with cross-section through yield surface

Source: (Davis and Salvadurai, 2002)

The principal stresses from the triaxial and DSS experiments were determined and converted into the normalised π-plane coordinate system, shown in Figure 5-28(b). The OL DSS tests were found to lie well outside both criteria when using the lateral stress readings, labelled as DSS-OL. This is attributed to the actual effective stresses being unknown, given that the pore pressures are not measured. This suggests that the critical state line determined in Figure 5-25 for the DSS tests may not be representative, where the actual p' could be higher than that assumed when plotting the normalised stresses in Figure 5-28(b). Other reasons could be attributed to the accuracy of lateral stress sensor, variability of the soil, and DSS tests not reaching failure conditions before the end of the test. The latter applies even more to the samples closer to the surface, exhibiting more significant plastic strains.

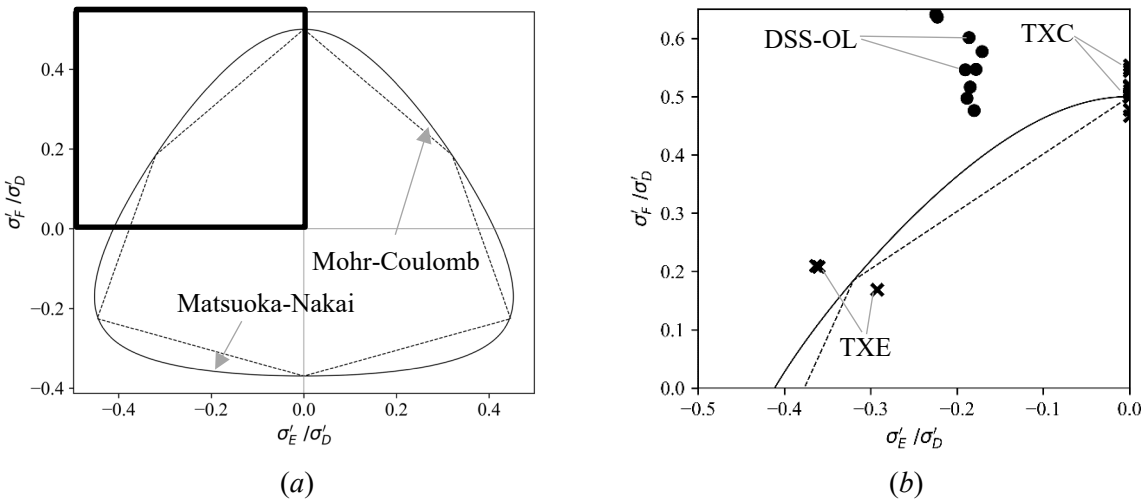


Figure 5-28: (*a*) Normalised Mohr-Coulomb and Matsuoka-Nakai yield loci in deviatoric plane (*b*) Close-up of quadrant with experimental outputs

5.8 Stiffness estimate

One notable characteristic of Cowden till is the degree of anisotropy in the shallower layers of the profile (Liu et al., 2020; Ushev and Jardine, 2020). To verify these findings, the stiffness of the Cowden specimens was interpreted through measurements using local instrumentation for both the DSS and triaxial tests, along with bender elements installed in the latter apparatus. The bender element tests were performed immediately before shearing and consisted of firing 12V single amplitude shear wave pulses through both the length (G_v)

and width (G_h) of the samples with frequencies from 5 to 10 kHz. This is appropriate for measuring the stiffness of stiff clays such as Cowden till (Hosseini Kamal, 2012). The shear modulus G was calculated based on the density ρ of the soil and the measured shear wave velocity v_s, with the relationship:

$$G_v \text{ or } G_h = \rho v_s^2 \tag{5-10}$$

where G_v is the shear modulus in the vertical plane and G_h is the shear modulus in the horizontal plane. The shear wave velocity v_s was calculated as:

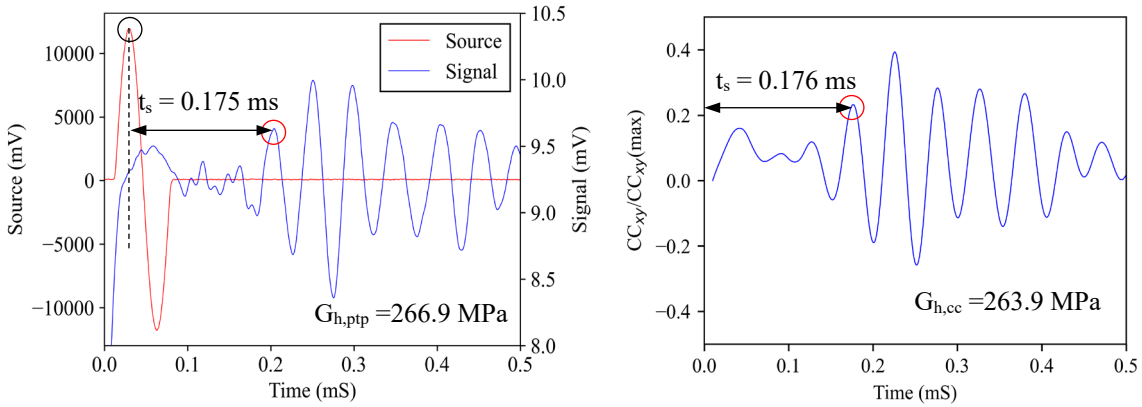
$$v_s = \frac{L}{t_{arrival}} \tag{5-11}$$

where L is the tip-to-tip distance between the bender elements and $t_{arrival}$ is the arrival time of the source shear wave at the receiver (Atkinson and Viggiani, 1995). Challenges arose with using bender elements as the stony nature of the tills occasionally prevented the detection of usable frequency signals. The arrival times $t_{arrival}$ were interpreted using both the peak-to-peak (preferred method) and cross-correlation methods, which are commonly reported in the literature (Atkinson and Viggiani, 1995; Lade, 2016).

The peak-to-peak method as based on the assumption that the received signal has a high resemblance to the source signal. In this case, the shear wave time $t_{arrival}$ is taken as the time lapse between the peak of the transmitted signal and the "first major peak" of the received signal. The signal peaks are visible in the example test shown in Figure 5-29(a). However, the signals for all tests were subjected to significant background noise, resulting in the determination of the first major peak being challenging. As a result, the cross-correlation method was used to provide an alternative means of determining the arrival time (Figure 5-29 (b)). While the peak-to-peak method requires subjectivity, the cross-correlation method measures the level of correspondence between the source and received signal as expressed by the cross-correlation coefficient CC_{xy} (Atkinson et al., 1995):

$$CC_{xy}(t_s) = \lim_{T\to\infty} \frac{1}{T} \int_0^T x(t)\, y(t + t_s) dt \tag{5-12}$$

where T is the recording time, $x(t)$ and $y(t)$ are the transmitted and received signals, and t_s is the time shift between the two signals. The full details of the cross-correlation method are provided by Atkinson and Viggiani (1995). In the method, the maximum peak should be used as reference. However, in this analysis, it was found the first peak yielded the most similar and consistent results with those measured using the peak-to-peak approach. Below in Figure 5-29 is an example of both interpretation methods for test ID: CWD_RC_TX_CAUc_OL39, giving similar values of G_h.



(*a*) (*b*)

Figure 5-29: Bender element interpretation techniques for G_h in test CWD_RC_TX_CAUc_OL39 - (*a*) Peak-to-peak and (b) cross-correlation method

For axial stiffness using local LVDT instrumentation, measurements down to strains of 10^{-3} % can be accurately captured, compared with bender elements which gave measurements down to strains of 10^{-4} %, as illustrated in Figure 5-30. This is based on the 5 mm working range and resolution of 0.001 mm of the LVDTs used. The axial stiffness was measured using a least-squares method up to strains of 0.002%, presumed to be the end of the linear range as seen in Figure 5-31, where E_{v0} is the initial Young's modulus.

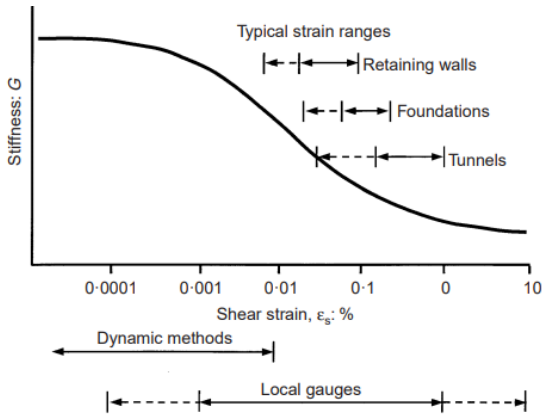


Figure 5-30: Schematic stiffness degradation curve for soils (Source: Atkinson (2000))

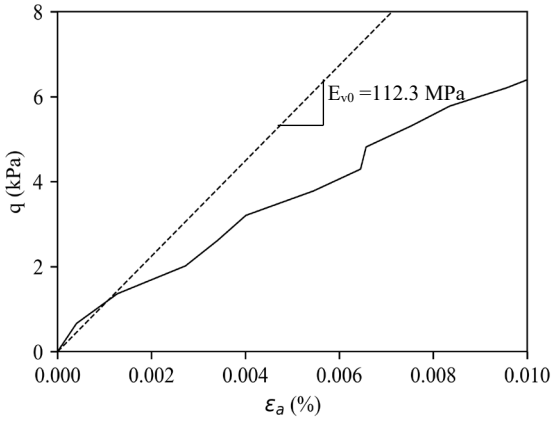
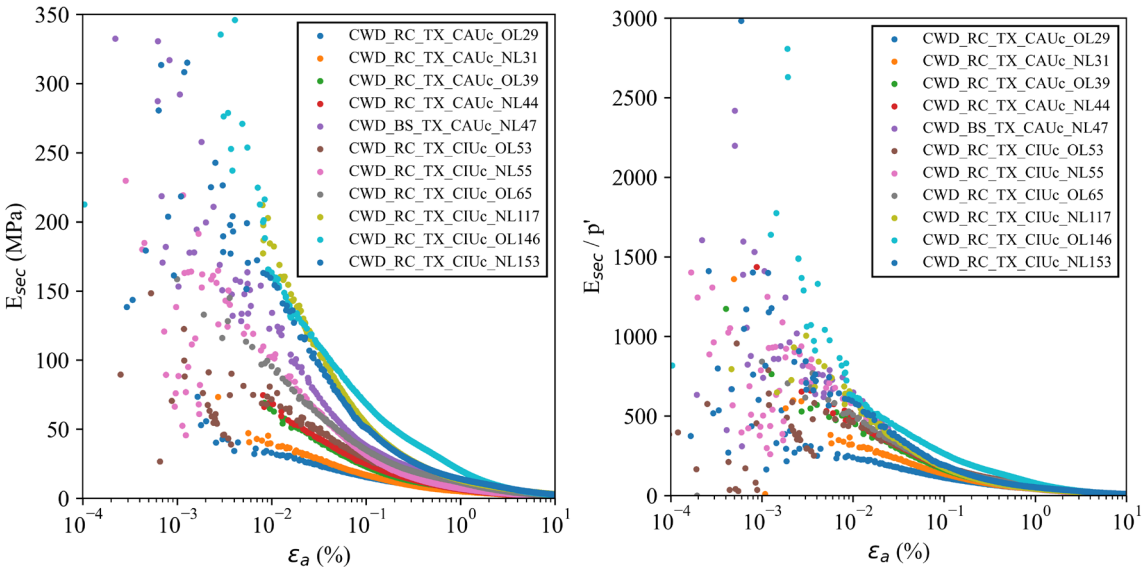


Figure 5-31: Local instrumentation estimation of E_{v0} (CWD_RC_TX_CAUc_OL39)

The local axial stiffness measurements are given in Figure 5-32, which shows the variation of the secant Young's modulus E_{sec} with axial strain. The curves of E_{sec} normalised by p' brings the E_{sec} trends closer together and it shows values increasing with depth. Alternatively, the E_{sec} can be normalised as $(E_{sec}/p'_{ref})/(p'/p'_{ref})^{0.5}$ but this is not explored here.



(*a*) (*b*)

Figure 5-32: Stiffness degradation curves from local LVDT instrumentation - (*a*) Secant stiffness versus axial strain and (*b*) normalised secant stiffness

A summary of the triaxial tests containing all stiffness measurements is presented in Table 5-8. Interestingly, CWD_BS_TX_CAUc_NL47 has an initial axial stiffness E_{v0} considerably higher than the rest of the samples within a similar stress level range. This is attributed to the sample being of higher quality which is discussed in Section 5.9.

Table 5-8: Summary of stiffness measurements in triaxial apparatus and corresponding SCPT

No.	Test ID	G_v (MPa)	G_h (MPa)	E_{v0} (MPa)	$G_{vh,SCPT}$ (MPa)	$G_v / G_{vh,SCPT}$	$G_h / G_{vh,SCPT}$
1	CWD_RC_TX_CAUc_OL29	90.1	-	52.8	118.9	0.76	-
2	CWD_RC_TX_CAUc_NL31	-	77.0	74.7	179.2	-	0.43
3	CWD_RC_TX_CAUc_OL39	-	266.9	112.3	236.5	-	1.13
4	CWD_RC_TX_CAUc_NL44	160.5	-	89.1	268.7	0.60	-
5	CWD_BS_TX_CAUc_NL47	-	-	160.8	-	-	-
6	CWD_RC_TX_CAUc_OL65	-	-	116.3	160.4	-	-
7	CWD_RC_TX_CIUc_OL53	68.3	34.4	121.1	90.6	0.75	0.38
8	CWD_RC_TX_CIUc_NL55	-	203.6	177.0	157.2	-	1.30
9	CWD_RC_TX_CIUc_NL117	188.1	149.7	258.1	272.8	0.69	0.55
10	CWD_RC_TX_CIUc_OL146	-	134.7	354.2	387.6	-	0.35
11	CWD_RC_TX_CIUc_NL153	402.5	243.41	314.2	314.5	1.28	0.77

Notes:

E_{v0} = Initial axial stiffness of sample measured using local LVDT instrumentation

$G_{vh,SCPT}$ = Shear modulus measurements at the relevant SCPT test location

In Figure 5-33, when comparing the results, the values for G_v and G_h from the bender elements far exceeded the $E_{v0}/3$ values by 3.2 and 2.0-fold, respectively. This reflects the anisotropy in the sample, as previously noted. Moreover, misinterpretation of the elastic range and sample disturbance may have played a role. A summary of the soil stiffness results with depth across the site is given in Figure 5-34. Considering the erratic nature of tills, the magnitudes measured from the bender elements were broadly in line with those captured from the seismic CPT measurements undertaken for the PICASO project. While there were clear signs of anisotropy within the samples tested, there was limited usable data to provide conclusive anisotropic values associated with this type of material, particularly from the bender element triaxial readings. The estimated bender element stiffness values were evaluated against the on-sample stiffness measurements $E_{v0}/3$. The division by 3 corresponds to a value of Poisson's ratio of 0.5 for an undrained test on isotropic saturated soil (Lade, 2016). However, whilst such a simplification is not usually valid for anisotropic soils such as those of Cowden till, it is adopted here to provide an approximation of the relationship and magnitudes expected from the bender elements. For a more in-depth assessment of the suspected anisotropic nature of this material, refer to Liu et al. (2020).

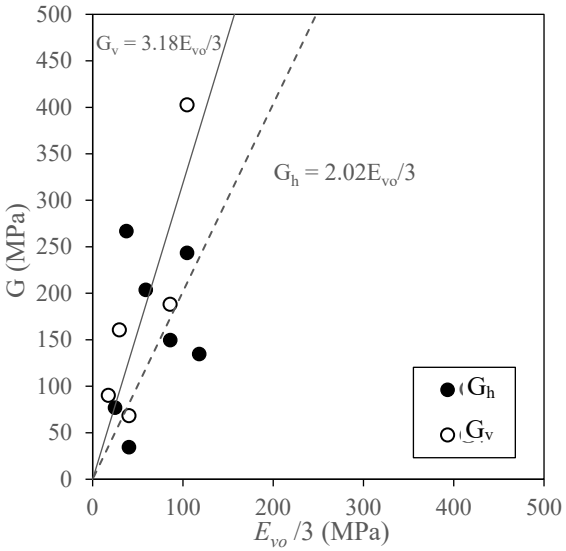


Figure 5-33: G versus $E_{v0}/3$ plot for triaxial tests at selected depths

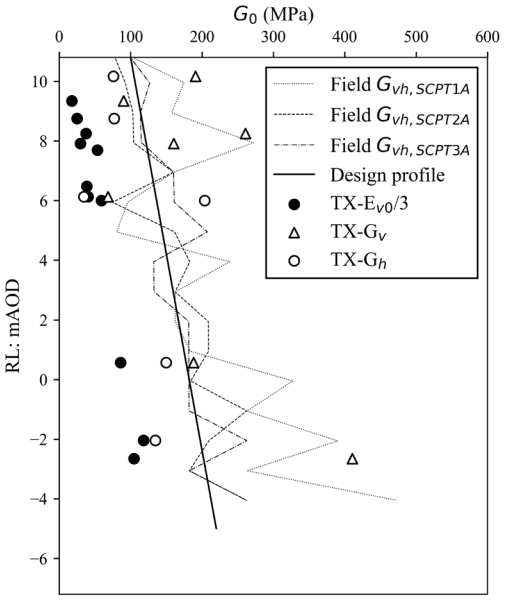


Figure 5-34: Overview of measured shear modulus with depth for PICASO

5.9 Undrained shear strength profile of PICASO Cowden site

The undrained shear strength profile of the PICASO site was determined by performing constant volume DSS tests on Cowden till specimens consolidated under different estimated in-situ vertical effective stresses. The stresses were based on the post-excavation ground level, bulk density measurements and an assumed water table level. The reported value of s_u corresponds to the peak shear stress measured during the shearing stage. However, in the cases where no peak was observed, the strength corresponding to 25% shear strain γ was reported. The variation of $s_{u,DSS}$ with depth is plotted in Figure 5-35, alongside comparative tests performed in the triaxial apparatus (i.e. $s_{u,TXC}$). As mentioned in Section 5.7.2, the NL and OL consolidation approaches showed little difference for the triaxial tests. This is different from the DSS tests, where a large contributor to their difference was related to sample size, such that soil disturbance at the interface was likely to have a greater effect on the smaller DSS specimens (i.e. DSS: D = 70 mm and H = 30 mm, Triaxial: D = 70 mm and H = 140 mm). Therefore, the triaxial NL and OL results were combined to avoid confusion. Henceforth, any mention of NL or OL refers only to the consolidation procedures applied to the DSS specimens.

For the DSS tests, the points for NL and OL are shown separately, highlighting the strength discrepancy between the two consolidation approaches. For the heavily overconsolidated Cowden till samples, the OL approach was preferred as it minimised the adverse effects of sample disturbance (see Chapter 3). The OL method produced an improved response from the poor-quality samples, giving strengths close to those predicted from the CPT. The s_u values from the DSS tests are generally lower than expected when compared to the CPT readings. Similarly, triaxial s_u values in the upper layers (RL: 10.8 to 6.0m) lie on or below the lower bound of the CPT profile.

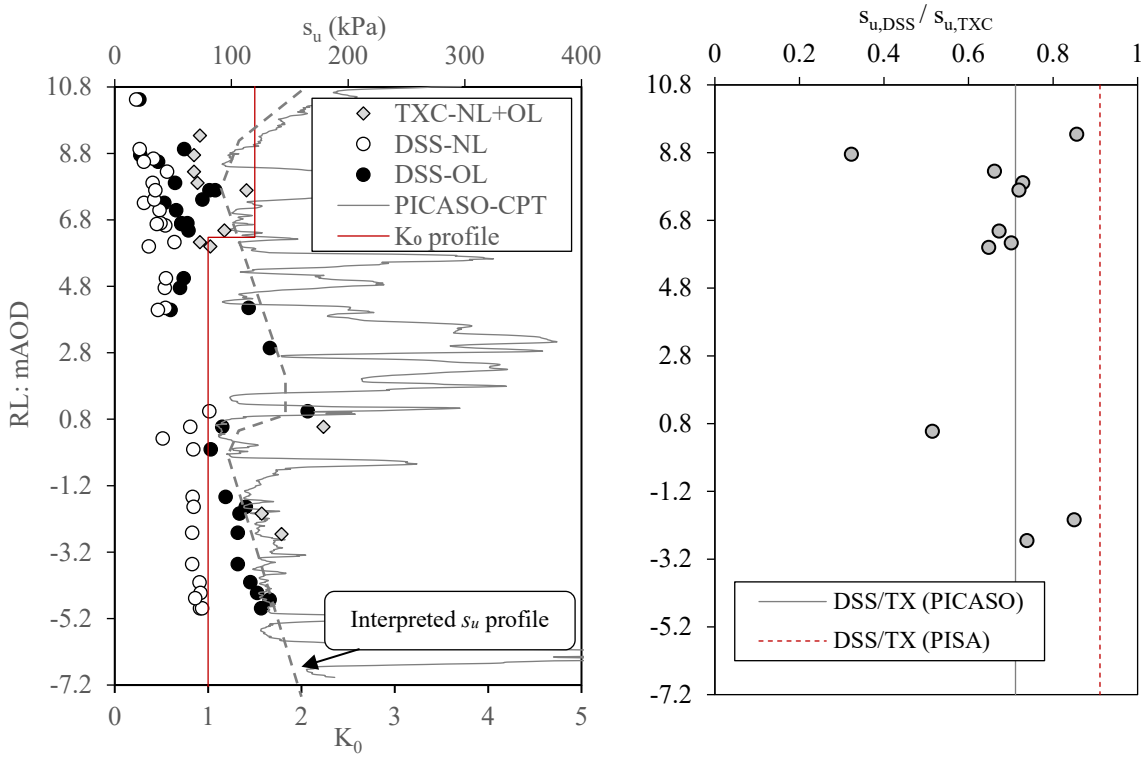


Figure 5-35: (*a*) Undrained shear strength profile of PICASO Cowden till site (*b*) Anisotropic ratio between DSS and TXC tests at selected depths

TXC tests and corresponding DSS tests were performed at selected depths to estimate the anisotropy ratio $s_{u,DSS}/s_{u,TXC}$ between the two shearing modes. There is significant scatter in the results seen in Figure 5-35(b), showing ratios ranging from 0.32 to 0.86. The tests yield a mean anisotropy factor of 0.711, excluding the outlier at 0.32. All of the data points from this study sit well below the ratio of 0.911 previously used in the PISA FEA modelling,

based on hollow cylinder experiments (Liu, 2018; Martin, 2023). For the PICASO tests, obvious outliers were not included in the analysis, with errors attributed to sandy layers or poor-quality samples. The anisotropy factor may be underestimated, but it is consistent with the ratios typically encountered for heavily overconsolidated clay (Mayne, 1985; Andersen, 2015). Mayne (1985) reviewed undrained strength data from 50 different clays in both simple shear and triaxial devices and found that the average value of s_u from simple shear tests was ~0.7 of the s_u from TXC tests, with Andersen (2015) making similar findings for Drammen clay (~0.74). N_{kt} = 18 was used for the CPT profile plotted in Figure 5-35(a). This value was determined by performing a back analysis using the equation:

$$N_{kt} = \frac{q_t - \sigma_{v0}}{s_{u,TXC}} = \frac{q_{net}}{s_{u,TXC}} \tag{5-13}$$

where q_{net} is the cone resistance q_t minus the total overburden pressure σ_{v0} and $s_{u,TXC}$ is the measured shear strength from triaxial compression tests. The cone resistance was interpreted from the nearest CPT at each borehole location. Before the selection of N_{kt} = 18, an N_{kt} factor of 20.6 was calculated from Figure 5-36(a) alongside shaded regions indicating 95% confidence levels, giving $N_{kt} \approx 20.6 \pm 2.1$. This value is considerably higher than the value of N_{kt} = 16 that was interpreted for the PISA project, which is unexpected considering the similarity of the two sites. The value is also unusually high by comparison with recommendations in the literature, with Lunne et al. (1997) recommending a maximum of 20 for clays.

It is suspected that the higher N_{kt} values were due to the amount of anisotropy in the upper till layers and the testing of lower-quality RC samples. This is evident in Figure 5-36(b), where points closest to the surface give N_{kt} values as high as 39. These were taken as outliers and not included in the analysis since, excluding these points, a trend hovering around a mean of N_{kt} = 18.9 was observed. The PISA project avoided the problem in the

upper till layers by using block samples instead, thus avoiding the need to use RC samples for N_{kt} selection in the upper layers (Ushev, 2017). To prevent the overestimation of the undrained shear strength profile, N_{kt} = 18 has been adopted for the PICASO project. This encompasses most of the points from 6.8 mAOD downwards with a 95% confidence interval, as shown in Figure 5-36(b).

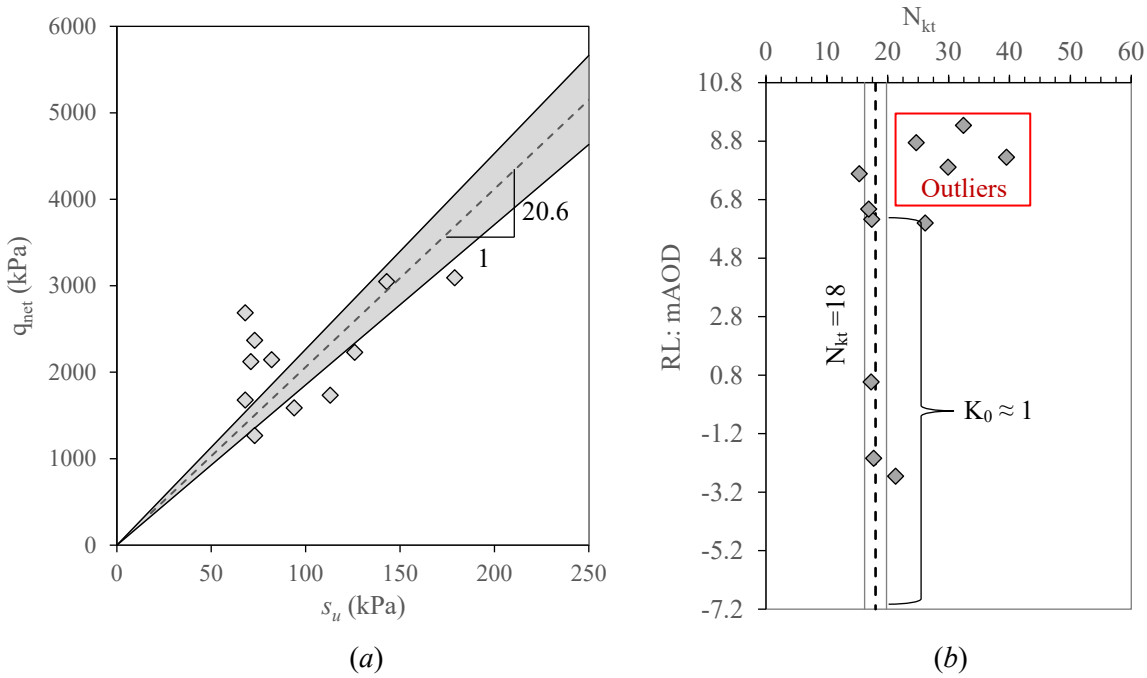


Figure 5-36: (*a*) $q_{net} = q_t - \sigma_{v0}$ versus $s_{u,TXC}$ based on q_t from CPT readings (*b*) Selection of N_{kt} factor along with 95% confidence intervals

According to Dahl et al. (2010), loading specimens of overconsolidated clay to their in-situ vertical effective stress alone would generally produce lower lateral stresses than those present in-situ, thus leading to specimens exhibiting a softer and weaker response than would be expected. Therefore, it was assumed that the two loading procedures (NL and OL) for a higher-quality sample would yield less difference in mechanical behaviour than for a poor-quality sample. Consequently, the quality of the samples was assessed quantitatively following the evaluation criteria (based on $\Delta e/e_0$) proposed by Lunne et al. (1997), where Δe is the change in void ratio when loading to the vertical effective in-situ stress and e_0 is the initial void ratio. The results of the assessment are presented in Figure 5-37, and the sample quality criteria are given in Table 5-9.

Table 5-9: Sample quality criteria for overconsolidated clays

Sample quality	Ratio $\Delta e/e_0$
Very good to excellent	0-0.03
Good to fair	0.03-0.05
Poor	0.05-0.1
Very poor	> 0.1

The samples appear to have a significant spread, grading from "very good to excellent" to "very poor", with DSS tests grading lower than TX tests overall. This was presumably due to the sample size (i.e. DSS: D = 70 mm and H = 30 mm, Triaxial: D = 70 mm and H = 140 mm), where disturbances at the interface caused by specimen preparation were greatly reflected in the quality evaluation ($\Delta e/e_0$) for the smaller DSS samples. From a practical point of view, the use of confining rings meant achieving the desired lateral stress during consolidation for a natural overconsolidated sample is rarely achieved due to insufficient interface contact between the membrane-enclosed sample and rings. Due to poor ring contact, samples need to deform before making adequate contact, hence the large axial strain deformations during consolidation for all DSS samples. Many OL DSS samples were graded as 'very poor' since recompressing the sample restricted the recoverable deformations when allowed to swell, thus increasing Δe. However, a 50% increase in the measured s_u was observed when using the OL consolidation approach and is the preferred approach as recommended by ASTM D8296-19 (2019). The quality of the samples used for triaxial testing was comparable to that for the PISA project triaxial tests (see Figure 5-37).

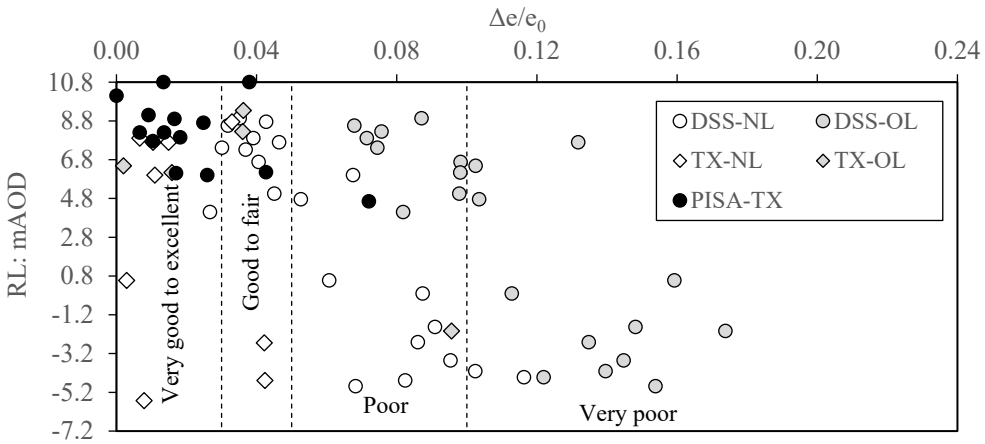


Figure 5-37: Sample quality evaluation of Cowden till DSS and TX samples

5.10 Summary

This chapter covers the mechanical behaviour of Cowden till through the interpretation of oedometer, direct simple shear, and triaxial experiments. Based on these experiments, the site was fully characterised by its mechanical strength properties. Two different loading procedures were used for the DSS and TX testing; these included either a normally loaded (NL) or overloaded (OL) recompression stage. OL was introduced to minimise the effects of sample disturbance and was found to give a 50% increase in $s_{u,DSS}$, while minimal differences between NL and OL were recorded for the TX tests. This is presumably due to the size of the samples, where disturbances caused by specimen preparation resulted in inferior quality evaluation (based on $\Delta e/e_0$) for the smaller-sized DSS samples. In addition, the samples demonstrated an extremely ductile behaviour for both DSS and TX tests, with mean failure strains at $\gamma_f = 33\%$ and $\varepsilon_{a,f} = 16.5\%$, respectively.

In the upper layers of the Cowden profile, 10.8 to 6.0 mAOD, a critical state friction angle $\phi'_{cv,upper} = 33.0°$ for DSS was determined, compared with $\phi'_{cv,lower} = 27.6°$ for the lower layer. When performing OL tests in the DSS, the inferred pore pressure readings showed similar trends but did not correlate quantitatively with the pore pressures measured directly in the OL TXC tests. It was found that rate effects also significantly impacted the outputs, with an increase of 10% per log cycle across the profile.

The triaxial tests recorded average critical state friction angles of $\phi'_{cs,TXC} = 26.8°$ for compression and $\phi'_{cs,TXE} = 27.5°$ for extension. The DSS and TX results were consistent with initial CPT estimates, as seen when comparing s_u/σ'_v with OCR or evaluating the undrained shear strength with depth. Furthermore, comparisons were made for DSS samples with lateral stress measurements, which showed that the DSS results plotted outside the failure criteria defined from the TX results. While the lateral sensors implemented may have caused these large discrepancies due to their signal noise, they provide a reasonable estimate of K_0 over each testing stage.

A summary of the strength parameters that can be used to calibrate conventional critical state type models is presented in Table 5-10. Where possible, values corresponding to both upper (RL:10.8 to 6.0m) and lower (RL:6.0 to -5.0m) portions of the profile are given. For the DSS parameters, values corresponding to the block sample level (RL = 7.69m) are also reported.

Table 5-10: Summary of Cowden till strength properties

Apparatus	Parameter	Variables	Value		
			Upper (RL:10.8 to 6.0m)	**Lower (RL:6.0 to -5.0m)**	**Mean or RL = 7.69m**
Oedometer	Compression index	Cc	0.142	0.156	-
	Swelling index	Cs	0.042	0.037	-
	Swelling slope	κ	0.020	0.015	-
	NCL slope	λ	0.070	0.062	-
Direct simple shear	Friction angle	ϕ'_{cv}	31.1°	26.4°	-
	Undrained shear strength	s_u	-	-	84 kPa
	Failure shear strain	γ_f	0.38	0.28	0.33
	s_u increase/log cycle (rate effect)	Λ_R	-	-	10%
	Coefficient of earth pressure	K_0	1.5	1	1.5
Triaxial	Undrained shear strength	s_u	-	-	113 kPa
	Failure strain	$\varepsilon_{a,f}$	-	-	0.165
	Stress ratio	M_{TXC} M_{TXE}	-	-	1.06 0.8
	Anisotropy ratio	$S_{u,DSS}$ / $S_{u,TXC}$	-	-	0.711
	CSL slope	λ	-	-	0.109

Chapter 6

Cyclic simple shear tests

6.1 Introduction

This chapter focuses on cyclic simple shear testing of natural Cowden till, exploring the stress-strain behaviour at both small and large numbers of cycles. All tests were conducted in the VDDCSS under constant volume cyclic loading conditions and the imposed shear stresses (i.e. τ_{av} and τ_{cyc}) were chosen relative to a reference s_u obtained from two monotonic tests (CWD-BS-DSS-CU-OL35 and CWD-BS-DSS-CU-OL35a) described in Chapter 5. The effects of cyclic loading on the shear strain, stiffness and damping behaviour are examined in detail. There is also a focus on the development of cyclic contour diagrams and the creation of a database of cyclic tests to calibrate and challenge a soil constitutive model (Chapter 7). The database also explores the effects of multidirectional, pseudorandom, and idealised undrained cyclic loading. Finally, comparisons are made between the cyclic element tests in the laboratory and the medium-scale pile tests performed at the Cowden site.

6.2 Test plan

All tests in this chapter were performed using block samples obtained in early 2022. The samples are from horizon C in Figure 4-5 (2 to 3.5 mBGL or 8.8 to 7.3 mAOD), such that they were overloaded to a $0.8\sigma'_{vc}$ of 584 kPa and then unloaded to an initial in-situ stress of σ'_v = 35 kPa.

This follows the same procedure used for overloaded tests in Section 5.2. Apart from the two-way cyclic tests, all tests were presheared to their desired average shear stress τ_{av} before undergoing cycling (see Section 3.3.5).

The samples were cycled at a frequency of 0.1 Hz, at varying mean and cyclic shear stresses under stress control conditions until failure was reached, defined as γ_{av} or $\gamma_{cyc} > 15\%$. Andersen (2009) and Le et al. (2014) employed a similar failure criterion for tests on offshore clay found in Norway. While this criterion differs from the failure shear strain $\gamma_f = 25\%$ defined for the DSS tests, it is preferred for comparison with the PISA triaxial tests (Ushev, 2017). The low cyclic frequency ensured adequate system control, while maintaining a balance between test duration and data acquisition, ensuring sufficient data points could be captured to evaluate small strain behaviour. Furthermore, this was consistent with the typical cyclic periods (i.e. 10 - 20s) that occur during storm wave loading (Andersen, 2009). For samples that did not reach failure, a post-cyclic monotonic shearing stage was introduced to investigate the effect of cyclic loading on the ultimate undrained strength.

Although OWT foundations typically experience 10^7 loading cycles over their lifetime (LeBlanc et al., 2010), it is recognised that for element tests under constant amplitude loading, cycle counts above 10^4 yield diminishing returns in understanding the evolution of accumulated strain, stiffness degradation and energy dissipation (Abadie, 2015; White, 2020). Therefore, tests that did not reach failure were stopped at 3000 cycles, balancing the need to capture behaviour at both small and large numbers of cycles. This limit is also comparable to testing carried out for the PISA project (Ushev, 2017).

The cyclic simple shear tests aimed to investigate the cyclic behaviours observed for Cowden till, with the schedule split into five test categories:

i. Standard unidirectional sinusoidal tests for calibration of soil constitutive models,
ii. Perpendicular cyclic loading tests to investigate the effects of load bias,
iii. Random cyclic loading tests to simulate offshore wind and wave loading conditions,
iv. Packaged cyclic tests derived from (iii), discretised into equivalent number of cycles,
v. Challenge cyclic tests used to evaluate the performance of a soil constitutive model.

All cyclic test samples were prepared and consolidated under similar loading conditions, using material from the block samples. A simplified test ID was used, as follows:

Table 6-1: Test ID and the total number of cyclic tests

No.	Test ID	Test type	No. of tests	Purpose
i	CSS	Cyclic simple shear	15	Cyclic analysis and model calibration
ii	PCSS	Perpendicular cyclic simple shear	13	Investigate cyclic loading direction
iii	RCSS	Random cyclic simple shear	3	Investigate random amplitude loading
iv	RPCSS	Random packaged cyclic simple shear	3	Investigate idealisation of RCSS load history
v	CCSS	Challenge cyclic simple shear	2	Model evaluation

6.3 Standard cyclic simple shear tests (CSS)

Fifteen undrained cyclic simple shear tests were performed from a common depth range (3.10 to 3.20 mBGL or 7.70 to 7.60 mAOD). The generation of cyclic contour plots, as well as the effects of cyclic loading on vertical effective stress, shear strain, stiffness and damping were examined.

6.3.1 Test programme

A summary of the unidirectional constant-amplitude tests for different combinations of average stress ratio (ASR = τ_{av} / s_u) and cyclic stress ratio (CSR = τ_{cyc} / s_u) are shown in Figure 6-1. The contour diagram framework developed by NGI (Andersen, 2015) proved to be a helpful basis for planning the cyclic simple shear testing campaign, where the allocated tests are normalised by the ultimate undrained strength obtained from Chapter 5 (CWD-BS-DSS-CU-OL35 and CWD-BS-DSS-CU-OL35a*:* s_u = 84 kPa). The tests have been assembled to cover the relevant loading space, most notably in areas where ζ_b (= ASR + CSR) < 1 and covering the entire ζ_c (= τ_{max} / τ_{min}) range from -1 to 1. This is important as behaviour differs depending on the loading regime, with the combination of ASR and CSR governing the type of cyclic mechanism observed due to load bias or stress reversal. Tests at lower magnitudes, where ζ_b < 0.5, are of particular interest as they are closer to the likely loads experienced by OWT foundations during severe storm conditions (see Balaam (2021)).

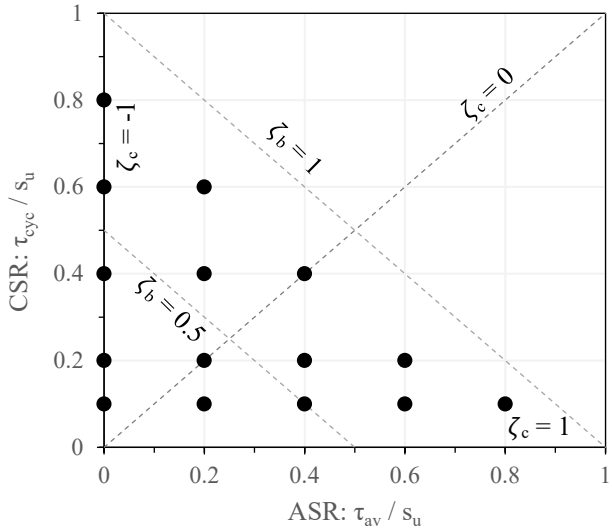


Figure 6-1: Normalised cyclic stress space showing tests performed

6.3.2 Test schedule results and general observations

Table 6-2 summarises the results of the 15 cyclic simple shear tests undertaken at various combinations of CSR and ASR. The stress-strain behaviour and stress paths for each test are presented in Figure 6-2 to Figure 6-16. The failure envelope (τ vs σ'_v) for DSS tests in the upper profile (RL: 10.8 to 6.0m) is included for reference. Cycles at N = 10, 100 and 1000

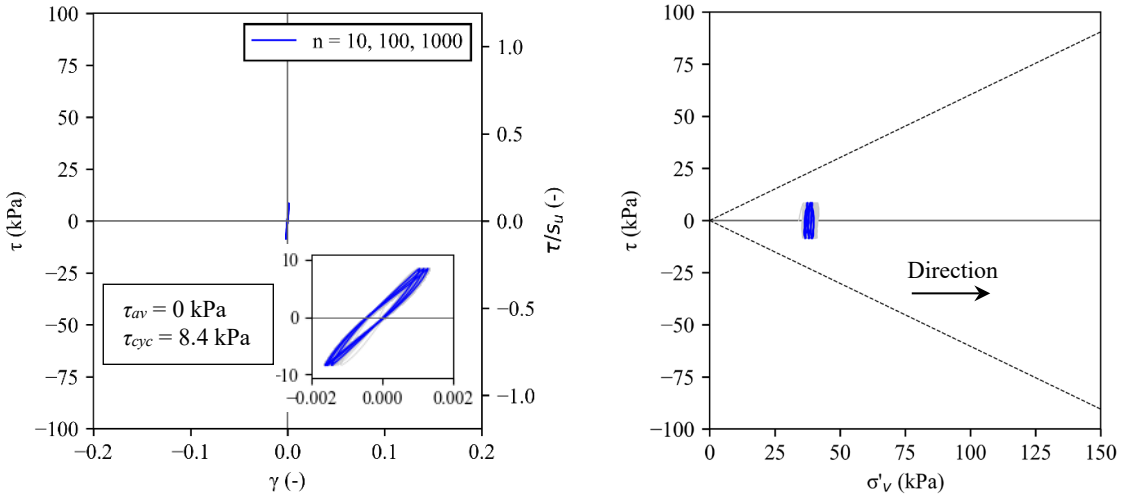
for each test are highlighted. The VDDCSS typically achieved a stress tolerance of ± 0.5 kPa. However, for two-way cyclic tests with high ζ_b, where samples tended to experience large degrees of strain or stiffness degradation, the system could not maintain the desired loading accurately. System compliance and pilot tests were performed to identify suitable control parameters for the loading system, though it was not possible to adjust these stiffness control parameters during the cyclic stages. If a sample experiences significant stiffness degradation, where it transitions from a very stiff to medium stiff sample, then the load actuators may fail to reach the prescribed loads. This is a common problem seen in stress-controlled cyclic tests (Guo et al., 2013; Le et al., 2014; Jin et al., 2022). To mitigate this effect, two-way cyclic tests CSS04 and CSS05 were conducted at lower frequencies (~ 0.05 Hz) to ensure that the user-defined CSR was reached.

Table 6-2: Summary of CSS results

Test ID	ASR	CSR	τ_{av} (kPa)	τ_{cyc} (kPa)	ζ_b (-)	ζ_e (-)	$\gamma_{av,10}$ (%)	$\gamma_{av,100}$ (%)	$\gamma_{av,1000}$ (%)	$\gamma_{cyc,10}$ (%)	$\gamma_{cyc,100}$ (%)	$\gamma_{cyc,1000}$ (%)	N_f (-)	$s_{u,post-cyclic}$ (kPa)
CSS01	0	0.1	0	8.4	0.1	-1	0.00	-0.02	-0.02	0.12	0.14	0.15	-	86.7
CSS02	0	0.2	0	16.8	0.2	-1	0.09	0.12	0.16	0.35	0.38	0.45	-	87.0
CSS03	0	0.4	0	33.6	0.4	-1	0.16	2.12	1.07	2.42	18.33	26.83	67	-
CSS04	0	0.6	0	50.4	0.6	-1	4.75	-	-	18.59	-	-	9	-
CSS05	0	0.8	0	67.2	0.8	-1	1.46	-	-	30.04	-	-	4	-
CSS06	0.2	0.1	16.8	8.4	0.3	0.3	0.26	0.26	0.28	0.07	0.07	0.07	-	-
CSS07	0.2	0.2	16.8	16.8	0.4	0	0.46	0.56	0.68	0.20	0.20	0.21	-	-
CSS08	0.2	0.4	16.8	33.6	0.6	-0.3	3.36	13.41	-	1.82	3.98	-	106	-
CSS09	0.2	0.6	16.8	50.4	0.8	-0.5	16.58	-	-	6.05	-	-	9	-
CSS10	0.4	0.1	33.6	8.4	0.5	0.6	2.13	2.44	2.72	0.10	0.10	0.09	-	98.3
CSS11	0.4	0.2	33.6	16.8	0.6	0.3	4.46	5.72	6.65	0.31	0.31	0.30	-	65.6*
CSS12	0.4	0.4	33.6	33.6	0.8	0	11.13	18.79	34.26	1.16	1.19	1.28	38	-
CSS13	0.6	0.1	50.4	8.4	0.7	0.7	4.76	5.67	6.49	0.08	0.08	0.08	-	94.1
CSS14	0.6	0.2	50.4	16.8	0.8	0.5	7.24	9.41	11.39	0.23	0.24	0.23	-	87.1
CSS15	0.8	0.1	67.2	8.4	0.9	0.8	11.03	14.01	18.25	0.11	0.08	0.09	174	-

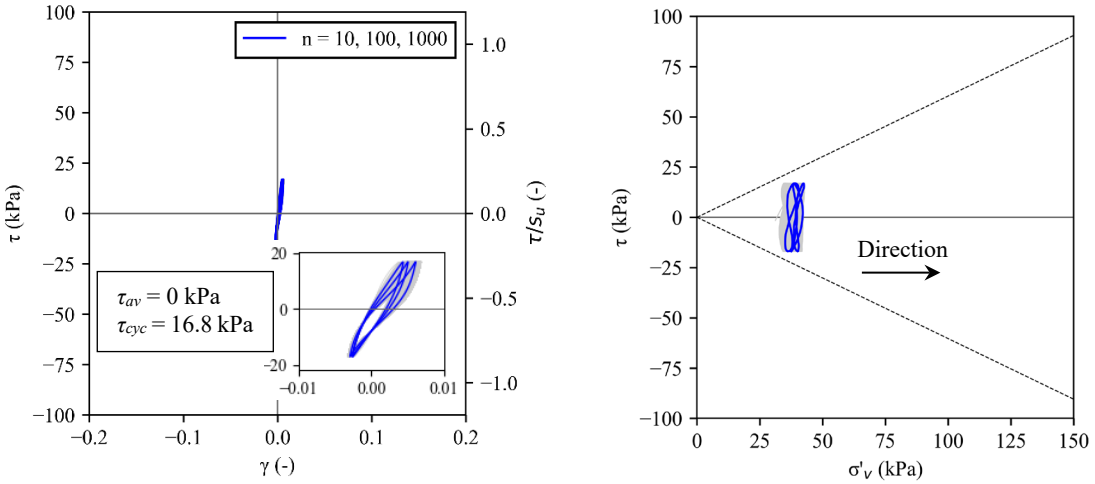
*Not included in the post-cyclic analysis as the test failed prematurely

6.3.2.1 Cyclic simple shear (ASR = 0, CSR = 0.1 to 0.8)



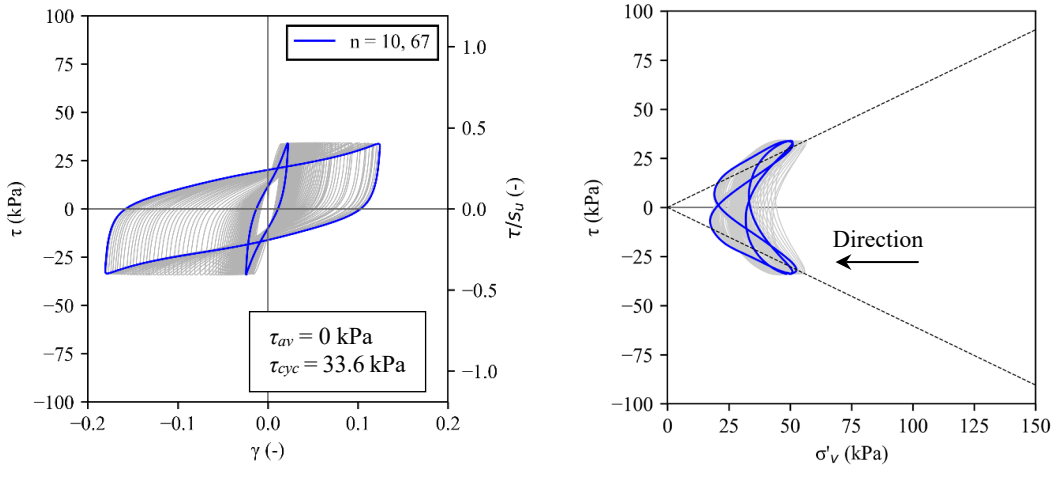
(*a*) (*b*)

Figure 6-2: Specimen-*CSS01* (*a*) Cyclic stress-strain behaviour (*b*) Cyclic effective stress path



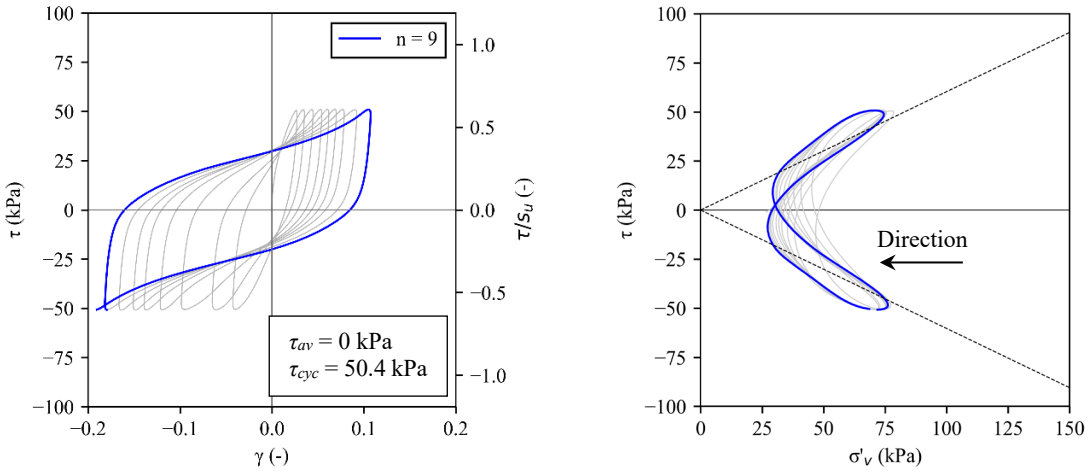
(*a*) (*b*)

Figure 6-3: Specimen-*CSS02* (*a*) Cyclic stress-strain behaviour (*b*) Cyclic effective stress path



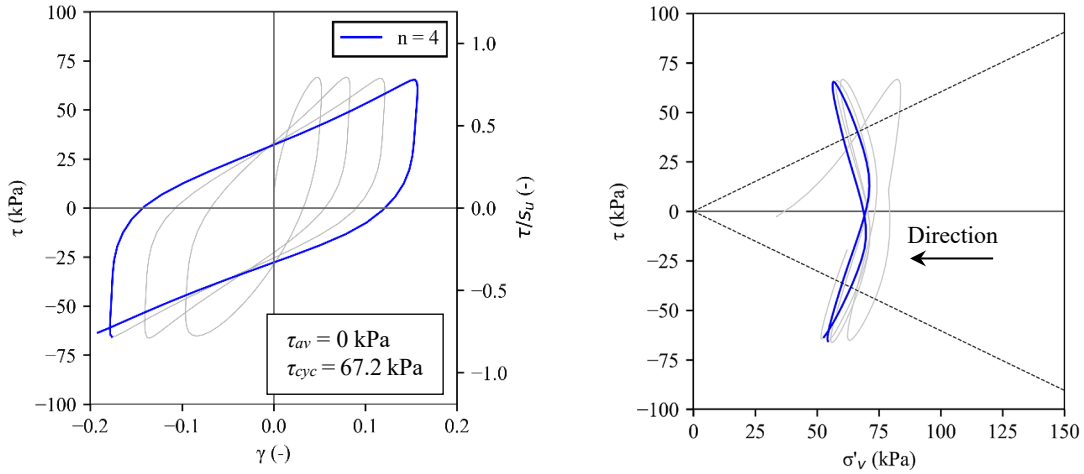
(*a*) (*b*)

Figure 6-4: Specimen-*CSS03* (*a*) Cyclic stress-strain behaviour (*b*) Cyclic effective stress path



(*a*) (*b*)

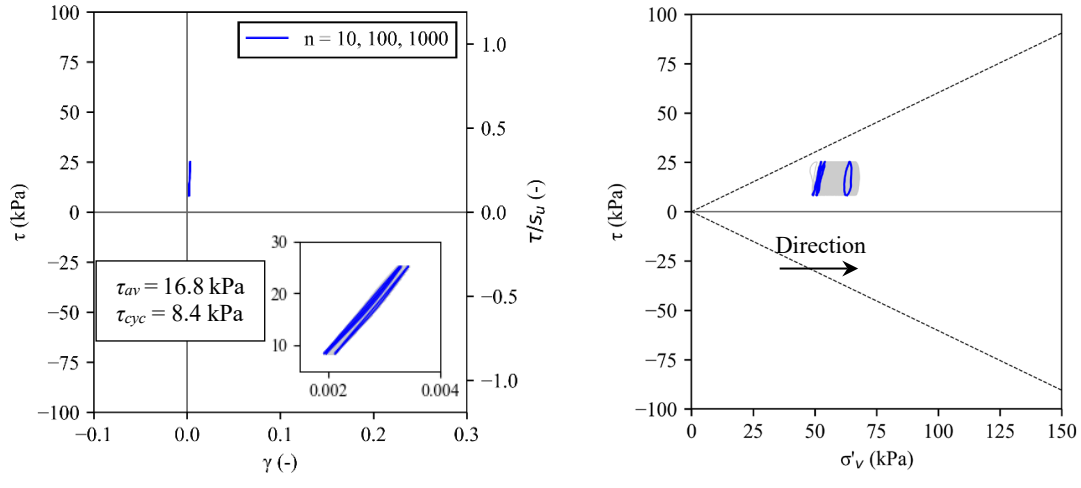
Figure 6-5: Specimen-*CSS04* (*a*) Cyclic stress-strain behaviour (*b*) Cyclic effective stress path



(*a*) (*b*)

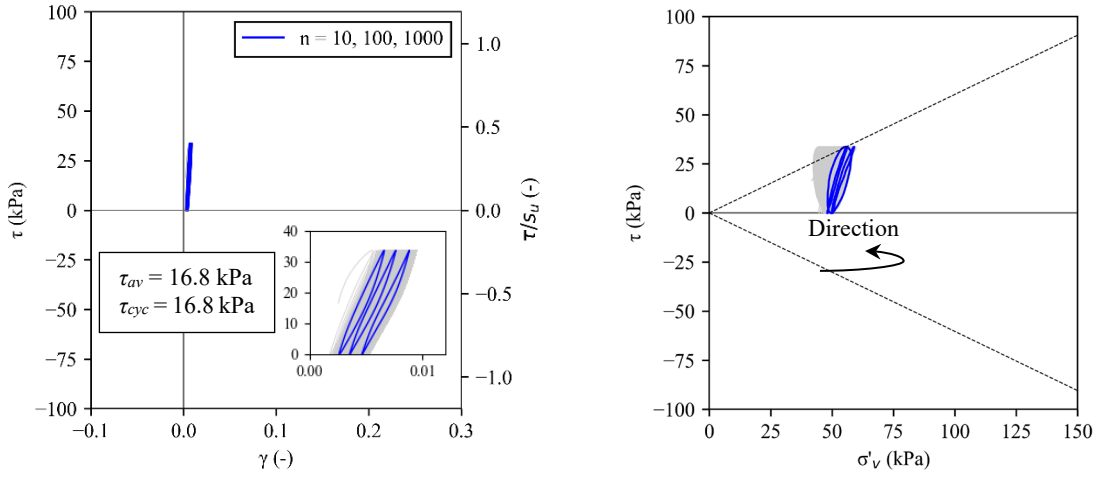
Figure 6-6: Specimen-*CSS05* (*a*) Cyclic stress-strain behaviour (*b*) Cyclic effective stress path

6.3.2.2 Cyclic simple shear (ASR = 0.2, CSR = 0.1 to 0.6)



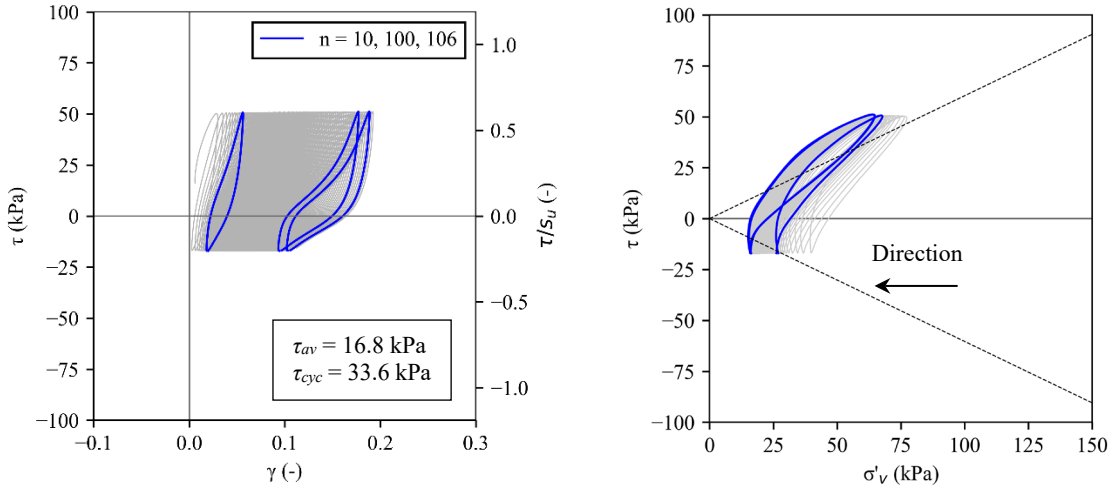
(*a*) (*b*)

Figure 6-7: Specimen-*CSS06* (*a*) Cyclic stress-strain behaviour (*b*) Cyclic effective stress path



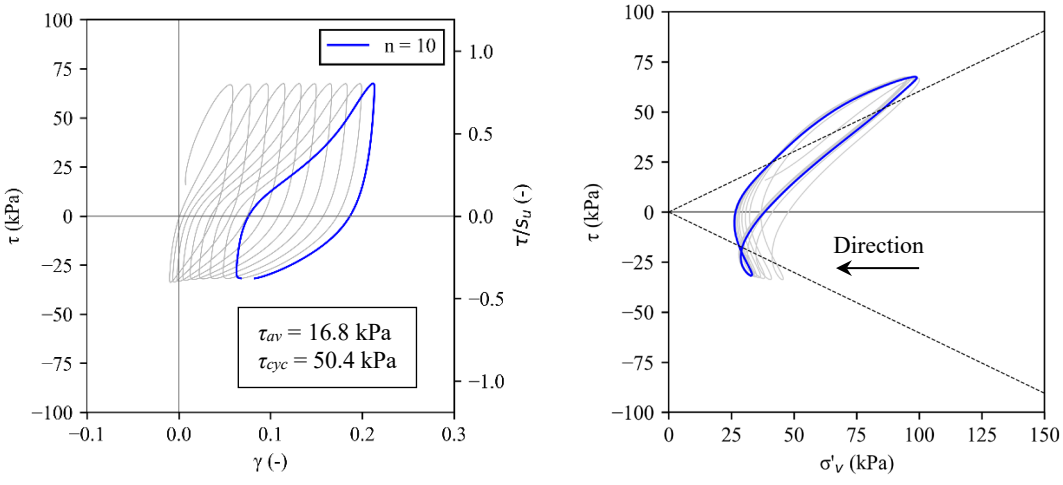
(*a*) (*b*)

Figure 6-8: Specimen-*CSS07* (*a*) Cyclic stress-strain behaviour (*b*) Cyclic effective stress path



(*a*) (*b*)

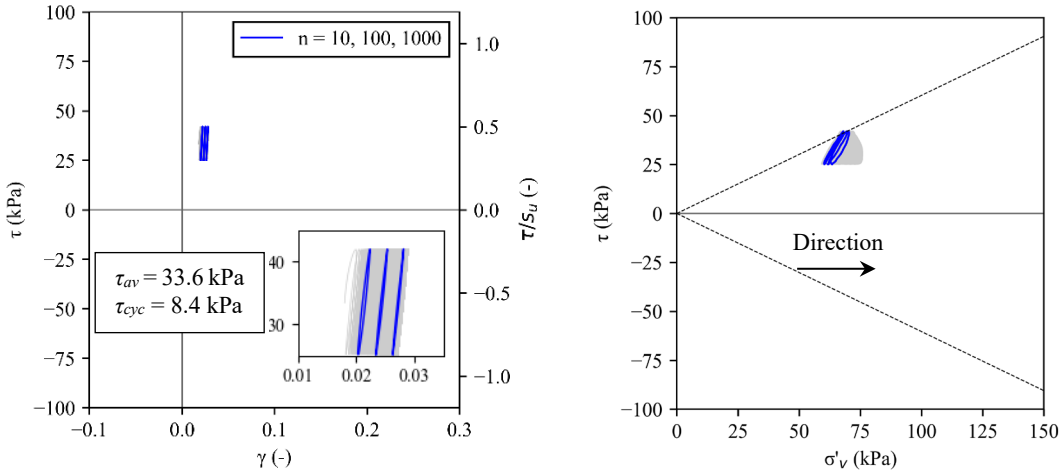
Figure 6-9: Specimen-*CSS08* (*a*) Cyclic stress-strain behaviour (*b*) Cyclic effective stress path



(*a*) (*b*)

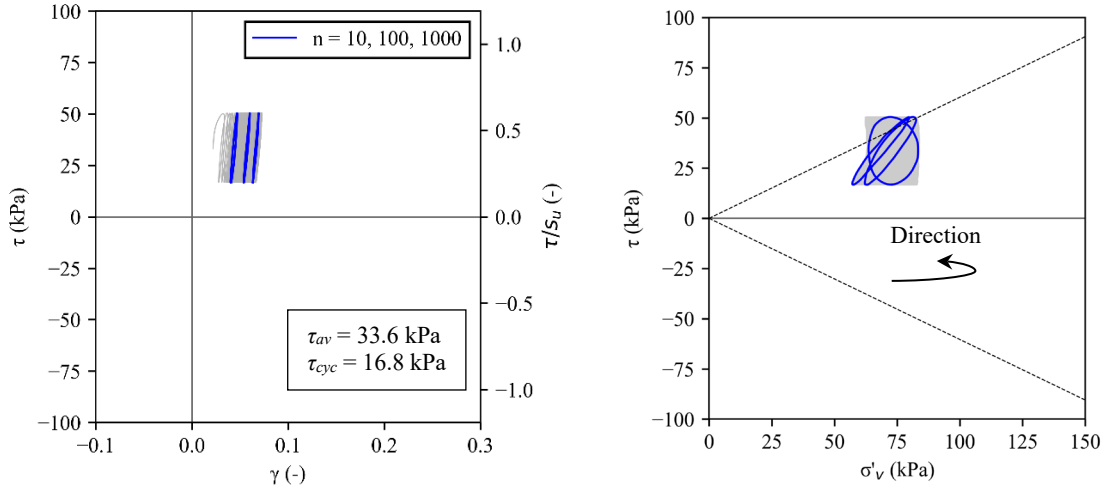
Figure 6-10: Specimen-*CSS09* (*a*) Cyclic stress-strain behaviour (*b*) Cyclic effective stress path

6.3.2.3 Cyclic simple shear (ASR = 0.4, CSR = 0.1 to 0.4)



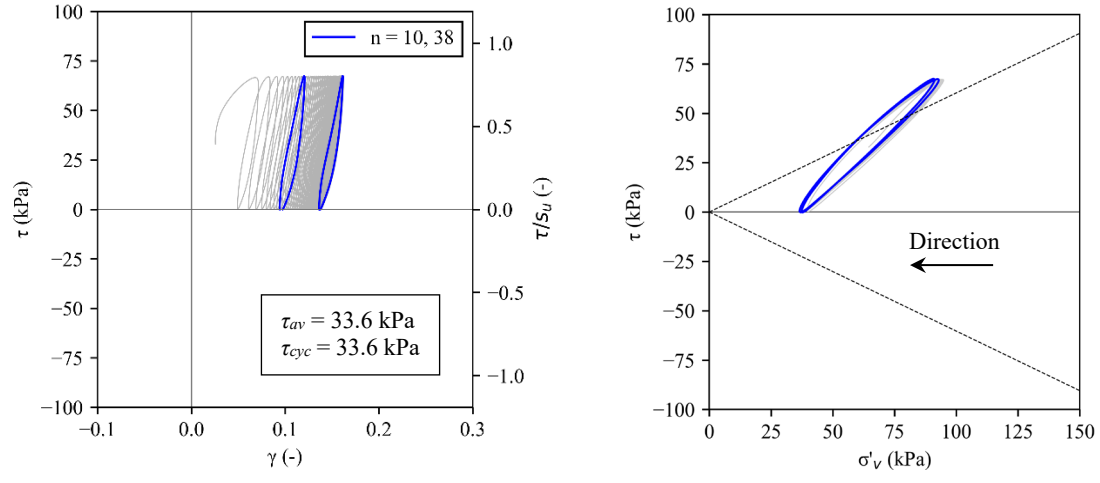
(*a*) (*b*)

Figure 6-11: Specimen-*CSS10* (*a*) Cyclic stress-strain behaviour (*b*) Cyclic effective stress path



(*a*) (*b*)

Figure 6-12: Specimen-*CSS11* (*a*) Cyclic stress-strain behaviour (*b*) Cyclic effective stress path



(*a*) (*b*)

Figure 6-13: Specimen-*CSS12* (*a*) Cyclic stress-strain behaviour (*b*) Cyclic effective stress path

6.3.2.4 Cyclic simple shear (ASR = 0.6, CSR = 0.1 to 0.2)

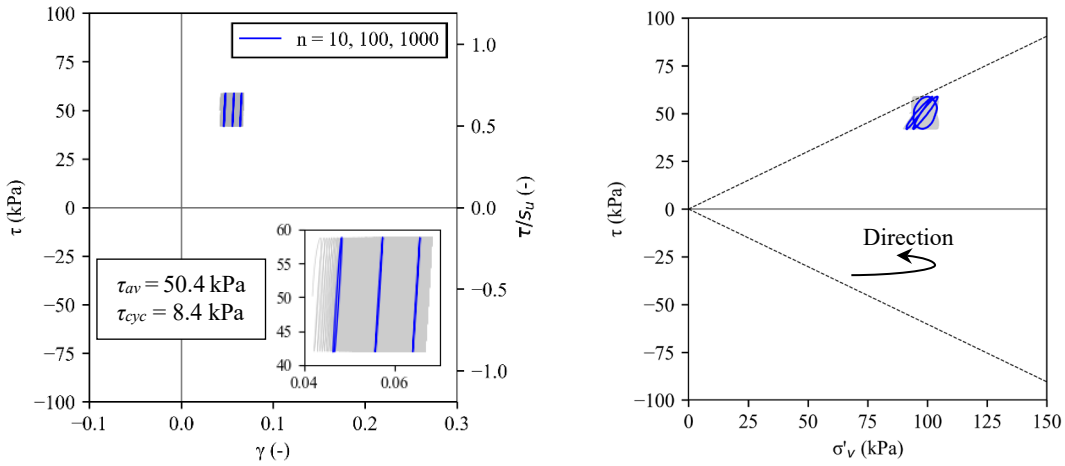


Figure 6-14: Specimen-*CSS13* (*a*) Cyclic stress-strain behaviour (*b*) Cyclic effective stress path

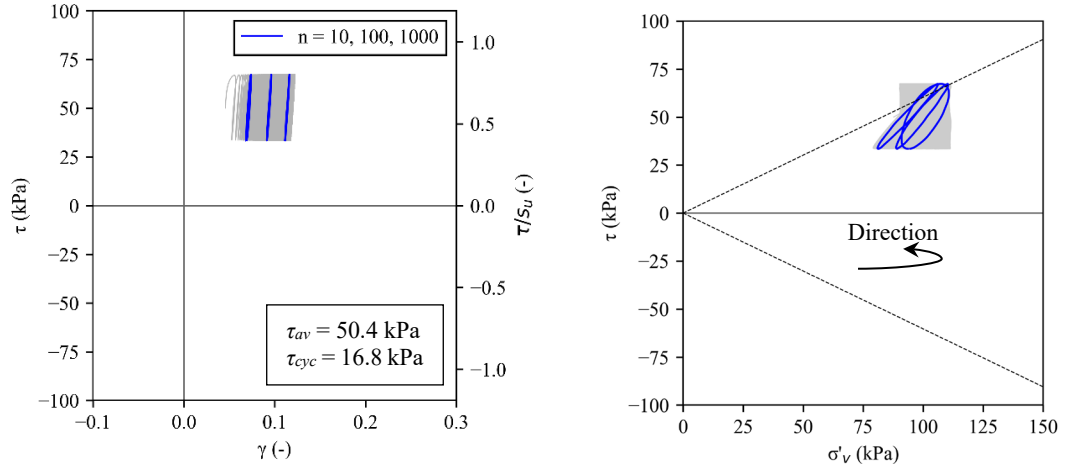


Figure 6-15: Specimen-*CSS14* (*a*) Cyclic stress-strain behaviour (*b*) Cyclic effective stress path

6.3.2.5 Cyclic simple shear (ASR = 0.8, CSR = 0.1)

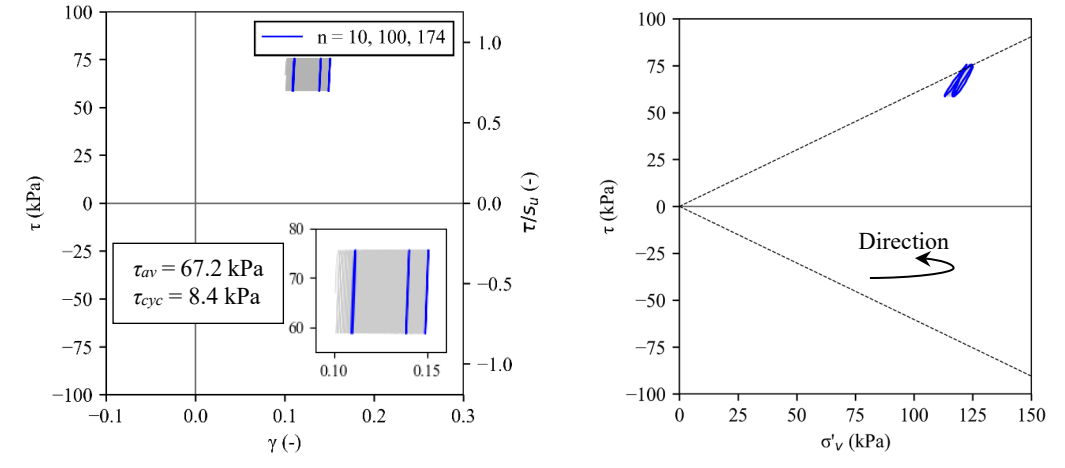


Figure 6-16: Specimen-*CSS15* (*a*) Cyclic stress-strain behaviour (*b*) Cyclic effective stress path

6.3.3 Strain accumulation and cycles to failure

The behaviour of Cowden till under constant volume cyclic loading varies markedly under different combinations of ASR and CSR, leading to variations in the accumulation of strains, stiffness degradation, and the number of cycles to failure. For all CSS tests, cycles start and finish at τ_{av}, so that, apart from the pure two-way tests (τ_{av} = 0 kPa), an additional average strain γ_{av} developed during the preshearing stage, which is included in Figure 6-18. This preshearing stage should not be confused with the preshearing cyclic stage typically referred to for sands, where a packet of small-amplitude cycles is applied before the main cycling to improve the seating between the sample and top platen, minimising stress concentrations, and increasing the horizontal effective stress (Andersen, 2015).

Tests CSS06 to CSS15 all experience a degree of ratcheting, where γ_{av} accumulates steadily with the number of cycles. The accumulation rate decreases with cycle number, as observed by the contraction of the loops for each cycle, most evident for test CSS12 in Figure 6-13. This observation was also reported by Guo et al. (2013) and Ushev (2017) for an offshore overconsolidated clay. Moreover, a number of tests show little change in accumulated cyclic shear strains γ_{cyc} with cycle number, apart from the partial two-way tests (i.e. CSS08 and CSS09). However, the higher amplitude tests (CSR > 0.6) appear to have an increased rate of accumulation, accelerating towards the onset of failure (Le et al., 2014; Ni et al., 2015). Notably, these tests fail due to large γ_{cyc} as opposed to large accumulations of γ_{av}. The accumulation of the strains γ_{av} and γ_{cyc} with cycle number for all cyclic tests is presented in Figure 6-17 and Figure 6-18. In addition, the number of cycles to failure N_f is annotated for tests that reached the failure condition.

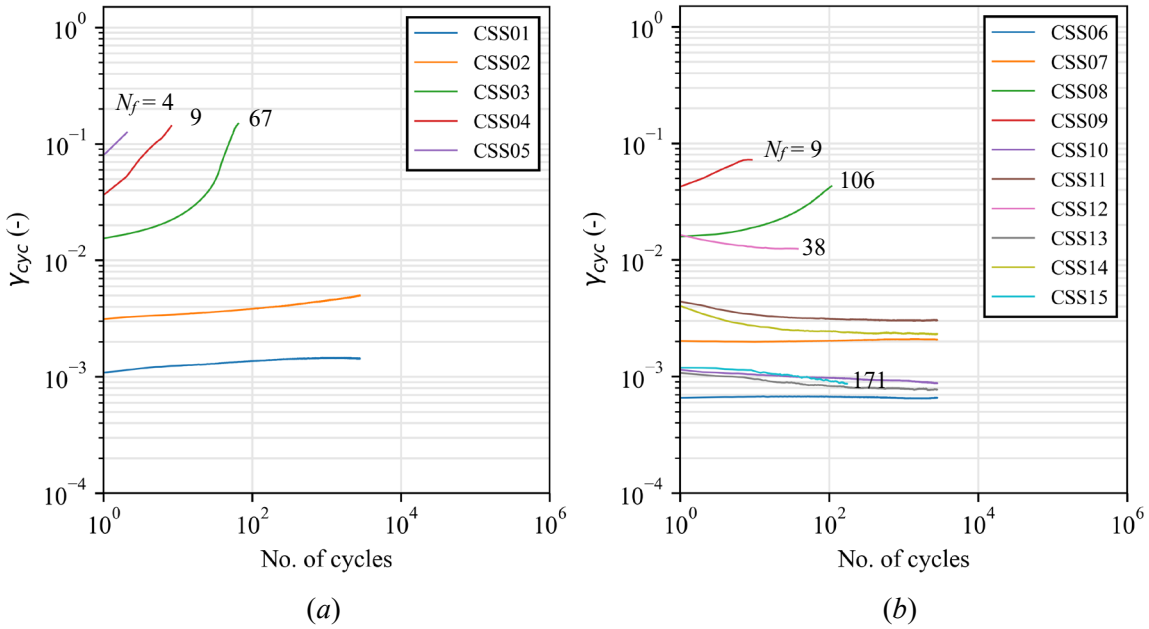


Figure 6-17: Cyclic shear strain γ_{cyc} accumulation with cycle number for (*a*) CSS01 to CSS05 (ASR = 0) and (*b*) CSS06 to CSS15 (ASR > 0)

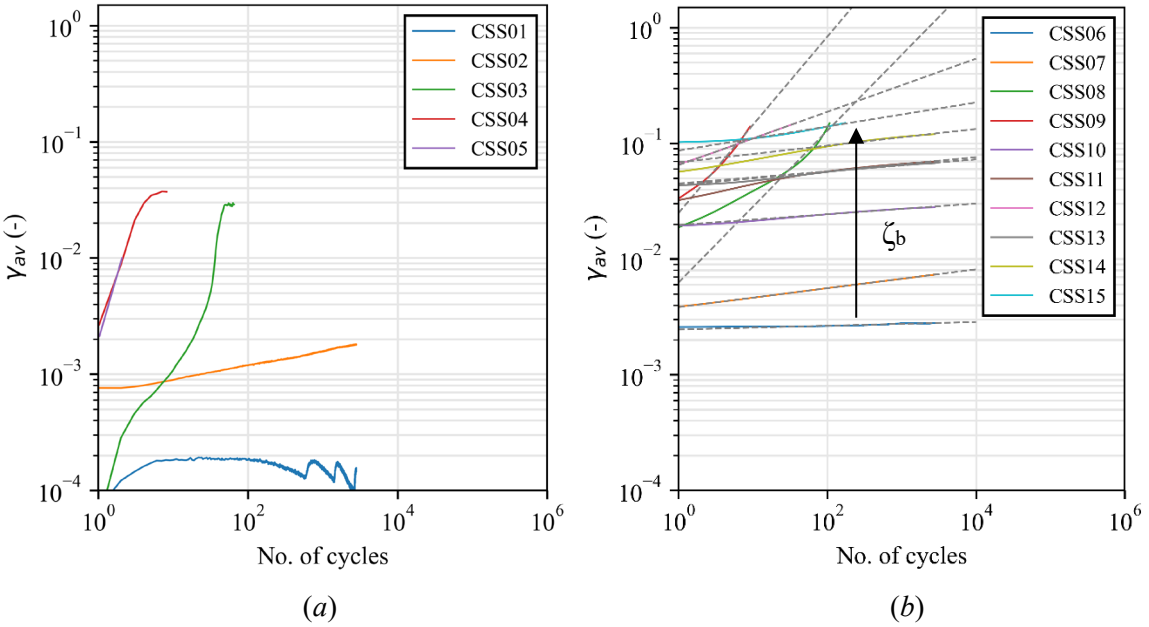


Figure 6-18: Average shear strain γ_{av} accumulation with cycle number for (*a*) CSS01 to CSS05 (ASR = 0) and (*b*) CSS06 to CSS15 (ASR > 0)

The tests which have undergone ratcheting (i.e. ASR ≠ 0 - Figure 6-18(b)) are fitted using an exponential function of the form:

$$\gamma_{av} = AN^m \tag{6-1}$$

where N is the number of cycles, and A and m are fitting parameters. The results of the fit are presented in Table 6-3. The parameters provide a characterisation of the ratcheting

behaviour, with the exponent m quantifying the rate of accumulation with cycle number. Figure 6-18(b) shows an increasing correlation between the exponent m and ζ_b. This behaviour is not unexpected considering the large strains that develop at large ζ_b. Figure 6-19 shows the increase of exponent m with increasing ζ_b, approximated by the linear fit $m = w\zeta_b$, with a mean square error (MSE) of 0.07 and $R^2 = 0.271$, denoting quite a large scatter among the dataset. Tests CSS08 and CSS09 are not included in this analysis as they are partial two-way tests which experience both stiffness degradation and ratcheting, making it difficult to distinguish the two behaviours (stiffness degradation is caused by the stress reversals, and the loading bias causes ratcheting).

Table 6-3: Fitting parameters for ratcheting

Test ID	ζ_b (-)	A (-)	m (-)
CSS06	0.3	0.470	0.016
CSS07	0.4	0.732	0.082
CSS08	0.6	1.107	0.672
CSS09	0.8	3.328	0.883
CSS10	0.5	3.752	0.0468
CSS11	0.6	8.243	0.0617
CSS12	0.8	10.979	0.265
CSS13	0.7	8.569	0.0525
CSS14	0.8	13.040	0.0727
CSS15	0.9	16.368	0.106

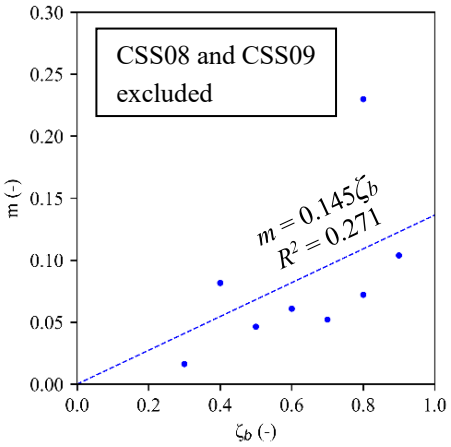


Figure 6-19: Linear fit for exponent m

Observations from the stress path plots (Figure 6-2(b) to Figure 6-16(b)) suggest that the loading characteristics (i.e. combinations of ASR and CSR) have a significant impact on the change in vertical effective stress. The failure envelope representing the upper layer tills ($\phi'_{cv,upper}$ = 31.1°), plotted on the graphs, shows that stress paths close to or crossing the failure surface (e.g. CSS08 and CSS09) lead to either a continuous drop in σ'_v or small gains before dropping. These findings agree with the behaviours observed in the triaxial compression tests reported for the PISA project (Ushev, 2017).

Cyclic loading failure is defined as either γ_{av} or γ_{cyc} exceeding 15% shear strain. The CSR is directly related to the rate at which the tests fail (Guo et al., 2013). This is observed in tests with high ASR and low CSR, by comparison to tests with low ASR and high CSR. The tests with high CSR tend to show fewer cycles to failure (e.g. CSS03 to CSS05), while conversely, an increase in ASR does not imply a decrease in N_f (Le et al., 2014). An example of this is given by CSS15 (ζ_b = ASR + CSR = 0.9). The value of N_f varies from as little as four cycles to 171 cycles recorded in Figure 6-17. This number is considered extremely small compared to the millions of cycles experienced by an operational OWT foundation over its lifetime. As a result, tests at high CSR only apply to foundation behaviour at load magnitudes associated with very severe storm loads (Le et al., 2014).

A cyclic contour plot based on the work by Andersen (2015) is given in Figure 6-20, which characterises the number of cycles to failure for all of the present CSS tests, defining failure at N_f = 10, 100 or 1000 cycles. The ζ_b = 1 line represents a failure contour for N_f =1, which can also be interpreted as the envelope defined by a representative DSS test. The contour plot also shows the contours developed from the PISA cyclic triaxial (CTX) tests, where failure was defined as the development of axial strains exceeding 10%. As a result, the contours do not intersect unity along the x-axis as the failure strains adopted for monotonic tests are larger (i.e. PISA-TXC: ε_f = 25% and PICASO-DSS: γ_f = 25%). Overall, the PISA contours lie outside those interpreted for PICASO, meaning the samples from PISA experienced less degradation and lower ratcheting rates. While $s_{u,TXC}$ for PISA was measured to be greater than $s_{u,DSS}$ (see Section 5.9), the discrepancy in contours may also be attributed to the difference in shearing rate, where cyclic tests were performed at prolonged rates (f = 3.3 × 10^{-3} Hz) for PISA and faster rates for PICASO (f = 0.1 Hz).

Interestingly, the cyclic shear strength for the first few cycles of each test surpasses the reference stress-strain curve as the CSS tests were loaded much faster than the DSS tests, indicative of rate effects (see Section 5.5.3). An example is shown in Figure 6-21, showing the first cycle for each CSS test with each exceeding the monotonic backbone curve. Note, however, that the backbone is derived from a test at a much lower strain rate.

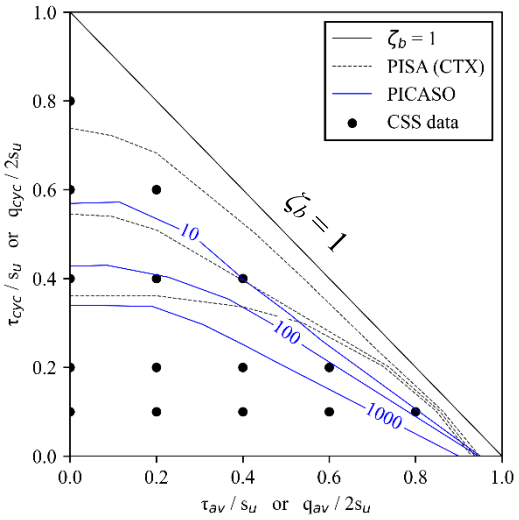


Figure 6-20: Cyclic contour highlighting number of cycles to failure

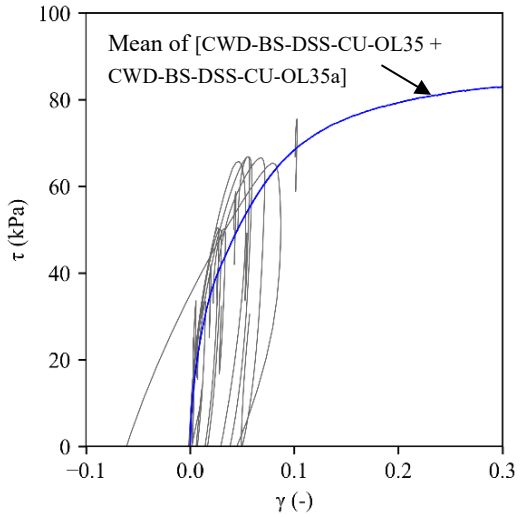


Figure 6-21: First cycles of CSS tests compared to backbone

6.3.4 Post-cyclic behaviour

There has been much discussion regarding the post-cyclic behaviour of clay. Many authors have reported decreases in strength (Lee and Focht, 1976; Yasuhara et al., 1992; Ahnberg and Larsson, 2013; Andersen, 2015; Wang et al., 2019), while some literature has suggested increases (Paramasivam and Banerjee, 2017; Ushev, 2017). Therefore, CSS test samples that had not failed under cyclic conditions were sheared monotonically to investigate the post-cyclic strength of a natural glacial till sample. Figure 6-22(a) shows the post-cyclic stress-strain curves by comparison to a monotonic backbone curve. Figure 6-22(b) shows the effective stress path in terms of τ and σ'_v. Overall, the CSS tests exhibit a larger post-cyclic s_u than the values measured from the DSS tests, with an average ratio $s_{u,post\text{-}cyclic}$ / $s_{u,DSS}$ = 1.08 (calculated from Table 6-2). The soil was observed to have large shear deformations at failure, consistent with the high failure shear strains discussed in Section 5.5.

Consequently, the ductile nature of the Cowden till suggests larger strains need to be mobilised from the cyclic loading before a reduction in strength might occur (Ahnberg et al., 2013). There exists a threshold value, where if the accumulated strain falls below it, the reduction in post-cyclic strength will be small or negligible (Meimon and Hicher, 1980). All specimens were sheared to large post-cyclic shear strains, as high as 50%. One of the tests (CSS10) exhibited larger yielding stresses, possibly due to an increase in secant stiffness caused by cycling (discussed in Section 6.3.5). Considering the high natural variability of Cowden till and its high overconsolidation ratio, the results indicate consistent post-cyclic behaviour, showing little change between the pre-cyclic and post-cyclic shear strength (Leal and Kaliakin, 2013). Further discussion on the post-cyclic stage is covered in Section 6.6.4.

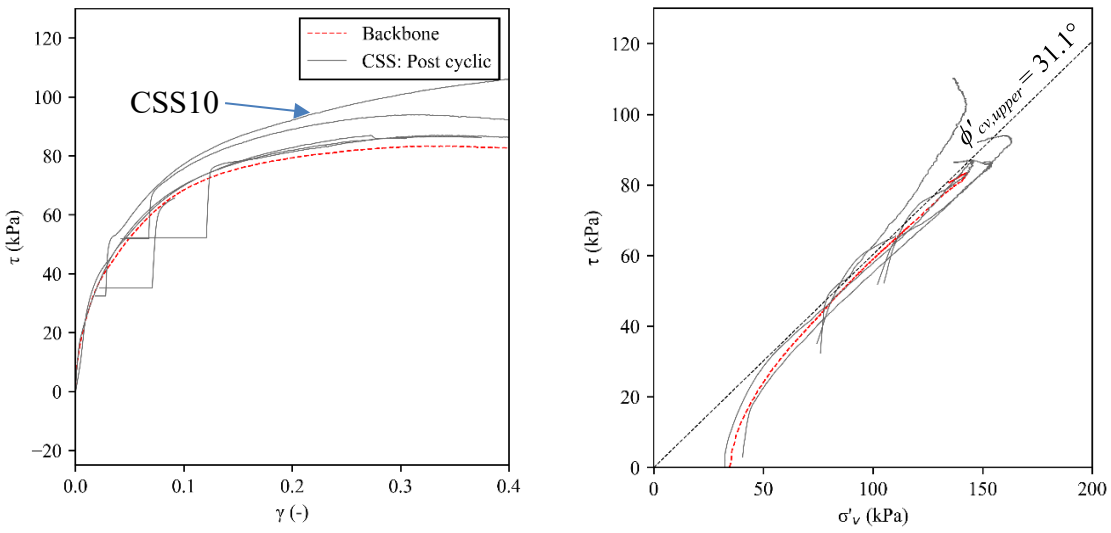


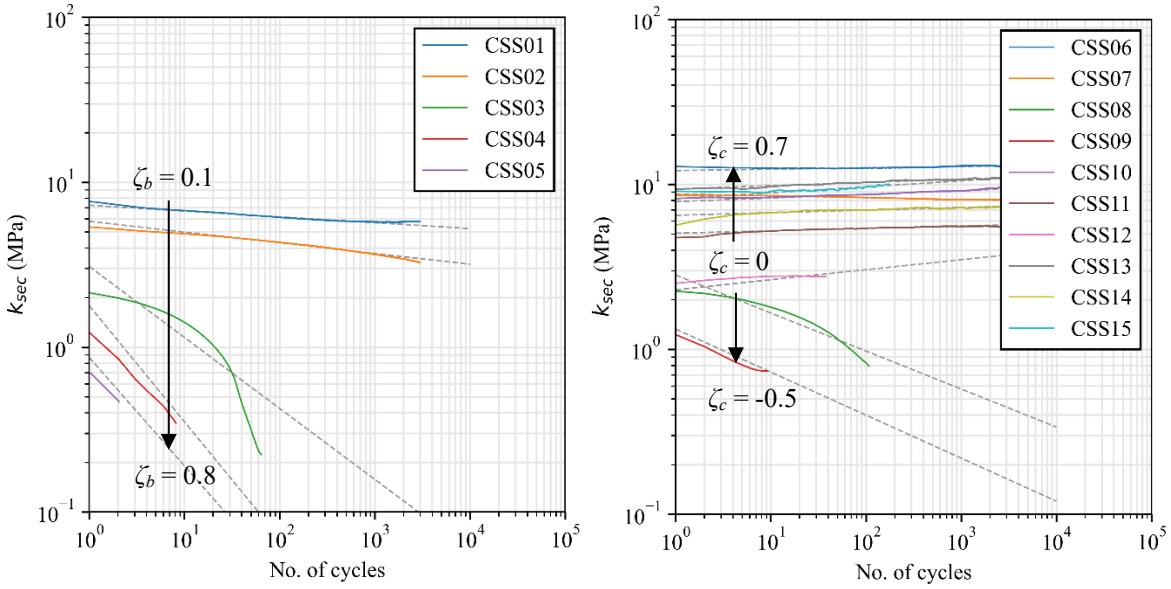
Figure 6-22: Post-cyclic (*a*) stress-strain curve and (*b*) effective stress path

6.3.5 Stiffness degradation

The central secant stiffness k_{sec} follows the definition introduced in Section 2.3.3. Secant stiffness evolution curves are plotted in Figure 6-23, as a function of cycle number. For the two-way and partial two-way cyclic tests, k_{sec} gradually decreases with increasing cycles. This behaviour can be captured using an exponential function of the form:

$$k_{sec} = BN^b \tag{6-2}$$

where N is the number of cycles and B and b are fitting parameters. The function is similar to the one in the 'Stiffness Degradation Method' suggested by Achmus et al. (2007).



(*a*) (*b*)

Figure 6-23: Evolution of secant stiffness with cycle number for tests (*a*) CSS01 to CSS05 (ASR = 0) and (*b*) CSS06 to CSS15 (ASR > 0)

In Table 6-4 and Figure 6-24 the exponent b decreases from -0.034 to -0.657 for ASR = 0 with increasing ζ_b and is generally lower for biased tests where $\zeta_c \neq -1$ (ASR > 0). This means that two-way cyclic stress reversals have a more damaging effect on the stiffness behaviour of clay compared with one-way and partial one-way tests. For similar reasons as described in Section 6.3.3, tests CSS08 and CSS09 were not included in the analysis. For ASR = 0, the exponent b appears to fit well with the dataset with MSE = 0.086 and $R^2 = 0.887$.

For all other tests (ASR > 0), little change or a slight increase in stiffness is observed (see Figure 6-24). Furthermore, initial k_{sec} values appear to be lower for smaller values of ζ_b and likewise for ζ_c. The observed behaviour indicates that the degradation of k_{sec} is strongly influenced by both ζ_b and ζ_c, where for $\zeta_c < 0$, a degradation in stiffness is likely to occur. The degradation rate also appears to be linked to the magnitude of ζ_b, where the higher the cyclic stress amplitude, the higher the rate of degradation. This is evident when comparing CSS03 and CSS04 ($\zeta_c = -1$) with CSS08 and CSS09 ($\zeta_c = -0.3$ and -0.5 respectively).

Table 6-4: Fitting parameters for stiffness degradation

Test ID	ζ_b (-)	B (-)	b (-)
CSS01	0.1	7.254	-0.034
CSS02	0.2	5.794	-0.060
CSS03	0.4	3.088	-0.428
CSS04	0.6	1.788	-0.676
CSS05	0.8	0.867	-0.657
CSS06	0.3	12.131	0.008
CSS07	0.4	8.749	-0.011
CSS08	0.6	2.823	-0.231
CSS09	0.8	1.327	-0.261
CSS10	0.5	7.858	0.022
CSS11	0.6	5.061	0.014
CSS12	0.8	2.296	0.061
CSS13	0.7	9.382	0.020
CSS14	0.8	6.500	0.016
CSS15	0.9	8.184	0.036

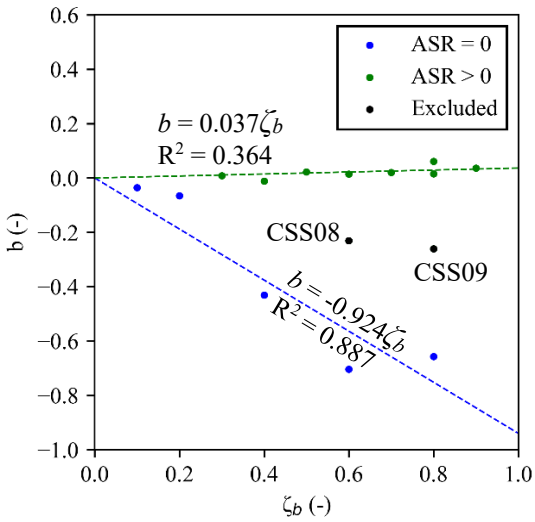


Figure 6-24: Fitting for stiffness gradient b

For tests with $\zeta_c > 0$, an increase in k_{sec} is measured even after 10^3 cycles. The tests tend to plot near the backbone (average of CWD-BS-DSS-CU-OL35 & CWD-BS-DSS-CU-OL35a), when examining the secant shear stiffness degradation with accumulated cyclic strain (Figure 6-25). In some cases, the reported results are located above the static line, indicative of rate effects, with the CSS tests carried out at a much higher rate (f = 0.1 Hz) leading to the apparent stiffening of the secant shear modulus (Robinson, 2019). Nevertheless, aside from frequency effects, CSR significantly impacts k_{sec} over many cycles, as reported by others in the literature (Teachavorasinskun et al., 2001; Lee and Sheu, 2007; Andersen, 2015).

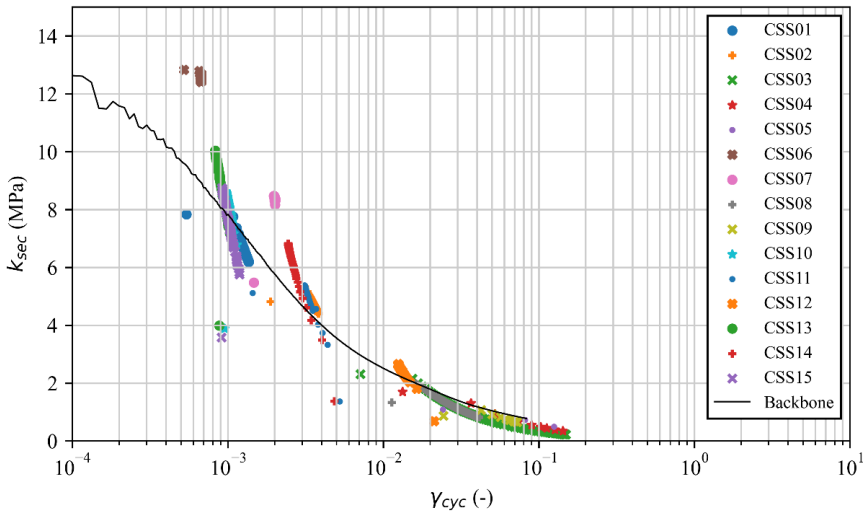


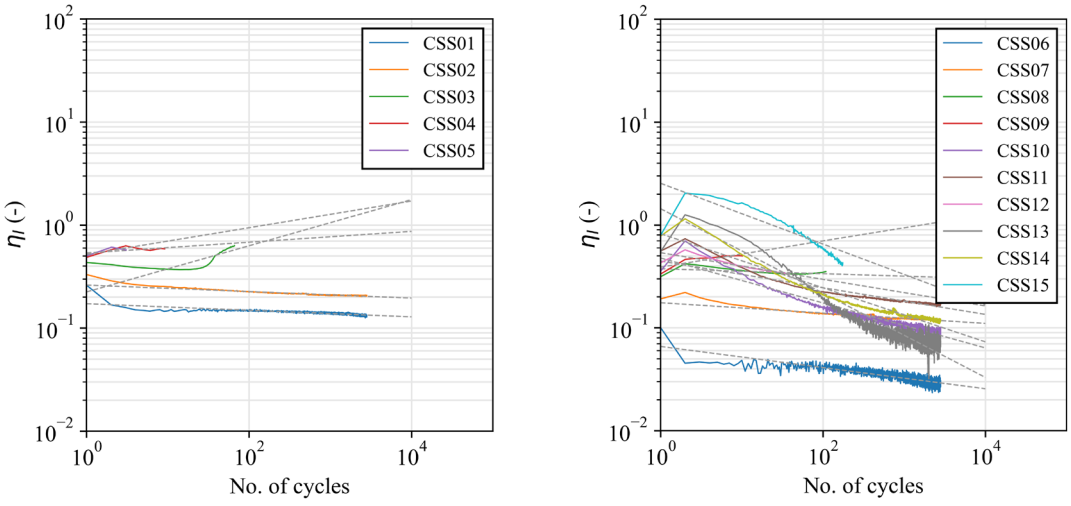
Figure 6-25: Secant stiffness k_{sec} degradation with cyclic shear strain γ_{cyc}

6.3.6 Energy loss factor (damping behaviour)

The definition for the energy loss factor η_I was given in Section 2.3.3. This factor quantifies the dissipation within each cycle, assessed as the ratio between the plastic and elastic work. Following this definition, the energy loss for each of the cyclic tests with cycle number is presented in Figure 6-26. After the first few cycles, the curves appear linear in log-log space before deviating with the onset of failure. From the plots, η_I can be seen to be a function of ζ_b and ζ_c and the number of cycles. Apart from CSS04, CSS05 and CSS09, there is an apparent decrease in η_I with the number of cycles. The dissipative behaviour is generally similar across all test types regardless of cyclic stress, and is consistent with that observed in the literature for sand (White, 2020) and clays (Ushev, 2017). For tests where ASR = 0, the dissipation reduces at a slower rate. An exponential relationship has been fitted to the development of energy loss of the form:

$$\eta_I = CN^c \tag{6-3}$$

A negative exponent indicates a decrease in the energy loss with cycle number. For the CSS tests, the exponent c reduces with cyclic stress but increases with bias ($\zeta_c \neq$ -1), indicating an inversely proportional relationship with the stiffness evolution exponent b given in Equation (6-2) (Huang et al., 2021). The fitted parameters are summarised in Table 6-5.



(*a*) (*b*)

Figure 6-26: Energy loss with number of cycles for (*a*) CSS01 to CSS05 and (*b*) CSS06 to CSS15

The behaviour, shown in Figure 6-27, indicates that if considerable stiffness degradation occurs (large negative *b*), the energy loss (i.e. dissipation) will increase relative to the elastic energy (Balaam, 2021).

Table 6-5: Fitting parameters for energy loss factor

Test ID	ζ_b (-)	C (-)	c (-)
CSS01	0.1	0.170	-0.034
CSS02	0.2	0.258	-0.034
CSS03	0.4	0.229	0.217
CSS04	0.6	0.506	0.074
CSS05	0.8	0.548	0.070
CSS06	0.3	0.069	-0.111
CSS07	0.4	0.178	-0.053
CSS08	0.6	0.427	-0.051
CSS09	0.8	0.492	0.066
CSS10	0.5	0.553	-0.240
CSS11	0.6	0.578	-0.167
CSS12	0.8	0.847	-0.260
CSS13	0.7	1.930	-0.454
CSS14	0.8	1.351	-0.340
CSS15	0.9	3.996	-0.361

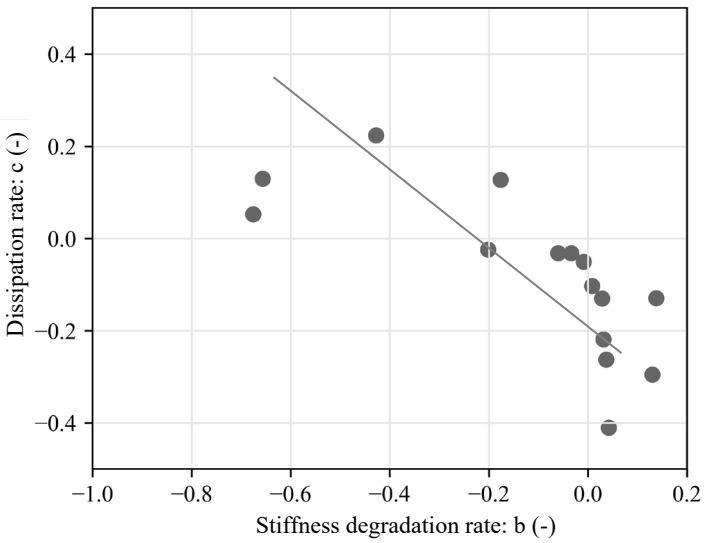


Figure 6-27: Energy loss rate versus stiffness degradation rate

6.3.7 Cyclic contour diagrams

Cyclic contour diagrams were constructed based on the CSS tests. Such diagrams have been used to inform the design of foundations for offshore structures since the 1970s (Andersen, 1976). A plot of the contours is given in Figure 6-28, describing the interaction between cyclic parameters (ASR and CSR ratios), the number of cycles to failure N_f, and the accumulation of shear strain. The plot is different from Figure 6-20 given previously, where the marked contours represent the cycles to failure. This means Figure 6-20 can be derived from plots Figure 6-28(a) to Figure 6-28(c), using the outline of each mapping. Each point (black circle) represents a single element test, with associated strain values allowing the contours to be created through linear interpolation. The strain values corresponding to γ_{av} and γ_{cyc} at 10, 100 and 1000 cycles have been summarised in Table 6-2. The generated space reveals potential failure areas, where the γ_{av} or γ_{cyc} contours bound safe zones (below 15%, which is the adopted failure strain). Contour γ_{av} = 15% does not intercept the *x*-axis at unity,

instead, it is pinned at a lower value, as the failure shear strain γ_f for a monotonic test was previously specified at $\gamma_f = 25\%$. Furthermore, the x-axis does not correspond exactly to a monotonic test but rather to the mobilised strains during the preshearing stage for tests where ASR > 0 (i.e. $\zeta_c \neq -1$). However, a monotonic test would be valid provided a comparable shearing rate was used, where the time to failure is equivalent to the preshearing stage.

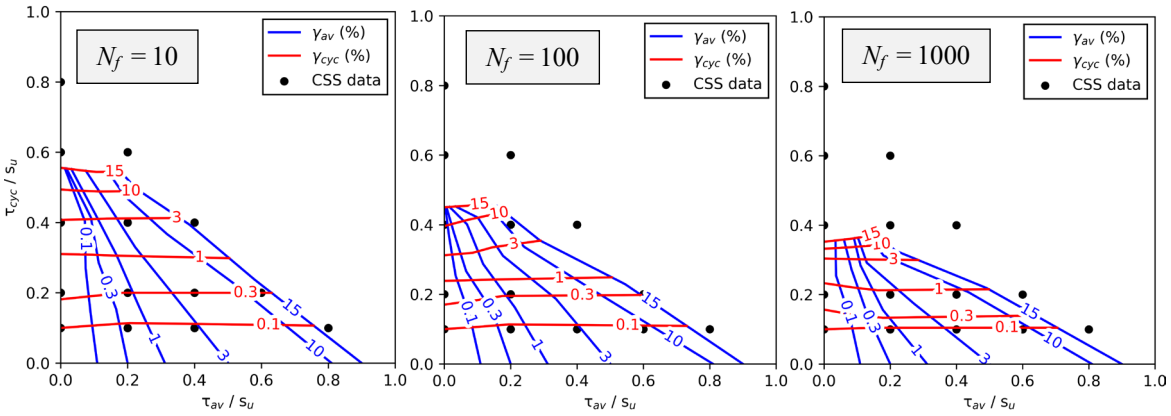


Figure 6-28: Cyclic contour diagram for (*a*) 10 (*b*) 100 and (*c*) 1000 cycles

As cycles develop, the set of contours collapses towards the origin, related to the development of the stiffness degradation and ratcheting mechanisms. The rate of reduction is highest for the γ_{cyc} contours, which is expected given the increasing rate of strain to failure observed in the high amplitude cyclic tests, as discussed in Section 6.3.3. The stiffness degradation behaviour can be isolated by evaluating a cross-section of the above contours in which ASR = 0 (ζ_c = -1), so that γ_{cyc} is a function of the number of cycles, as shown in Figure 6-29. Combining Figure 6-28 and Figure 6-29 allows a complete 3D mapping of the failure space with respect γ_{av} and γ_{cyc} to number of cycles.

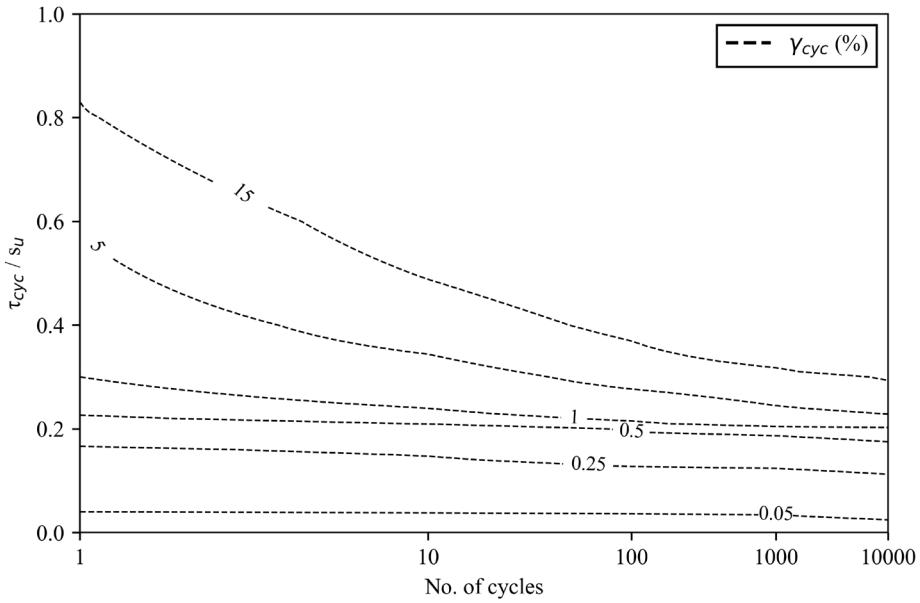


Figure 6-29: Stiffness degradation behaviour with number of cycles

6.4 Perpendicular cyclic simple shear tests (PCSS)

This section explores the response of a soil element to controlled multidirectional cyclic loading. A set of perpendicular loading tests, following Richards (2019) and Kammerer et al. (2002), were chosen and performed to isolate multidirectional cyclic behaviour and explore changes to ratcheting, stiffness degradation and energy loss. However, developing on the previous work, several more combinations of ASR_x, ASR_y, and CSR_y were used to probe the loading space. The tests represent a simplified storm idealised as uniform-amplitude cycles, whereby the loadings simulate an idealised version of misaligned wind and wave loads.

6.4.1 Test programme

The load paths of the perpendicular tests are shown in Figure 6-30, with details summarised in Table 6-6. The tests are split into two batches. Batch one features tests which are loaded by a constant stress in one direction (i.e. *x*-axis) while cyclic loading is applied in the perpendicular direction (i.e. *y*-axis). Batch two consists of multi-stage type tests, where a set is made up of three packages (similar to batch one) applied continuously and varying in terms of either ASR, CSR or direction.

For batch two, each of the tests was performed at two different frequencies, one at f = 0.1 Hz and the other at 0.01 Hz, with results presented separately within the forthcoming plots (Figure 6-32 to Figure 6-37). Each package comprised 1000 cycles to ensure behaviours at small and larger cycle counts were equally captured. Similar to the CSS tests, all PCSS tests, apart from PCSS09, were stopped when γ_{av} or γ_{cyc} reached 15%.

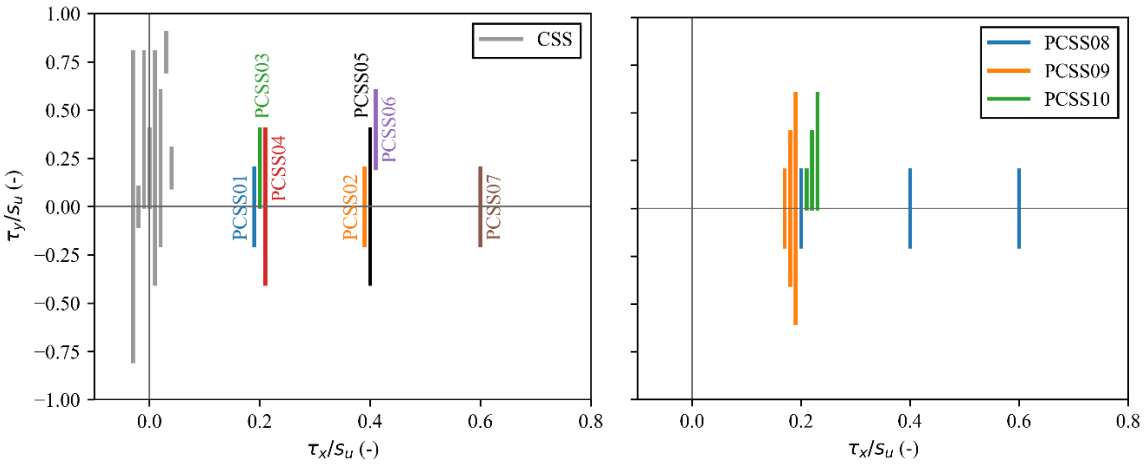


Figure 6-30: Stress path of PCSS tests for (*a*) batch one and (*b*) batch two
Note: Curves for a given τ_x / s_u have been slightly misaligned along the *x*-axis for clarity and the batch two tests are loaded in ascending order (i.e. left to right).

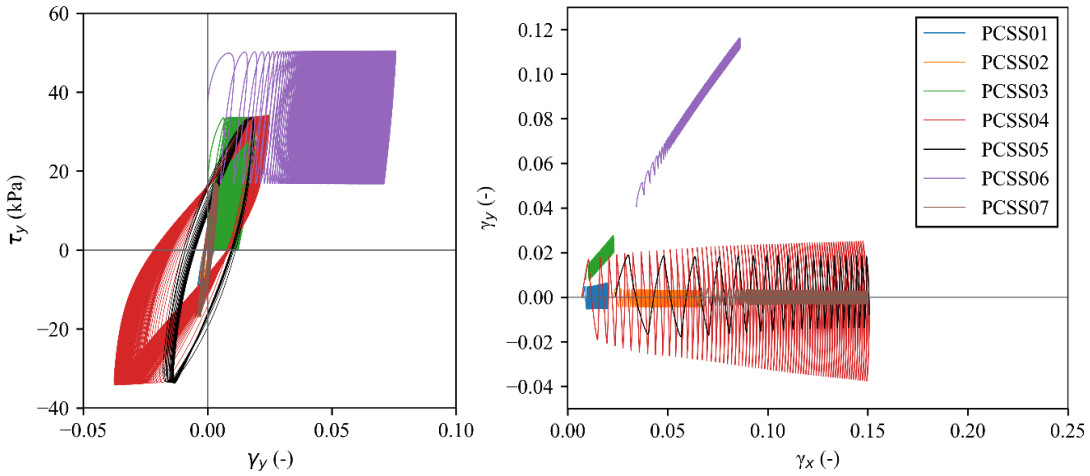
Table 6-6: PCSS test schedule

	No.	Test ID	ASR$_x$ (-)	CSR$_x$ (-)	ASR$_y$ (-)	CSR$_y$ (-)	No. of cycles (-)	Unidirectional test equivalent type
Batch 1	1	PCSS01	0.2	0	0	0.2	3000	Two-way
	2	PCSS02	0.4	0	0	0.2	3000	Two-way
	3	PCSS03	0.2	0	0.2	0.2	3000	Two-way
	4	PCSS04	0.2	0	0	0.4	74	Two-way
	5	PCSS05	0.4	0	0	0.4	20	Two-way
	6	PCSS06	0.4	0	0.4	0.2	3000	Partial one-way
	7	PCSS07	0.6	0	0	0.2	2208	Two-way
Batch 2	8	PCSS08	0.2-0.6	0	0	0.2	3000 (3000)	Varied mean load (Two-way)
	9	PCSS09	0.2	0	0	0.2-0.6	2041(1138)	Multi-amplitude (Two-way)
	10	PCSS10	0.2	0	0.2-0.6	0.2-0.6	3000 (3000)	Multi-amplitude (One-way)

Note: Tests PCSS08 to PCSS10 were performed at both f = 0.1 Hz and 0.01 Hz (N_f given in brackets)

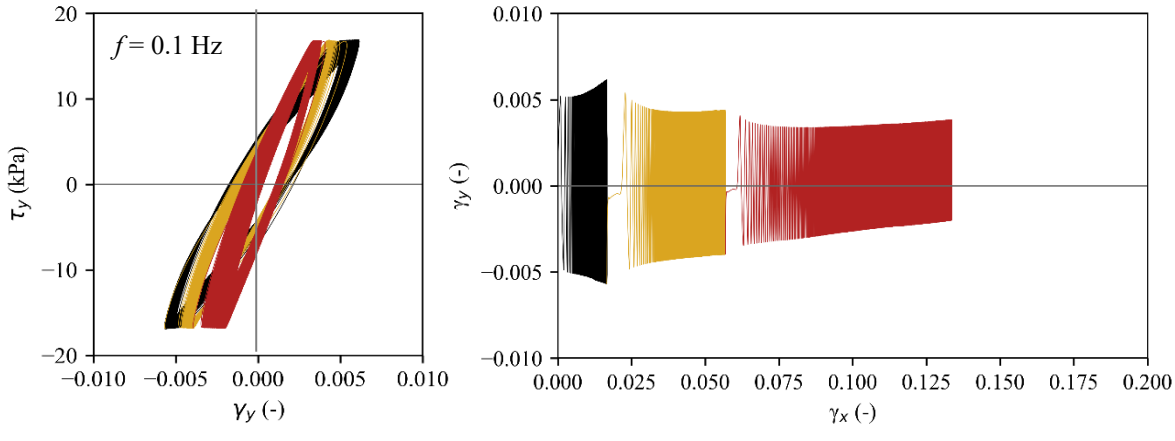
6.4.2 Test schedule results and general observations

The results of the unidirectional CSS tests suggest that loading characteristics play an essential role in the driving mechanisms for stiffness degradation and ratcheting. Therefore, PCSS tests involving comparable loading combinations are explored. The results of the batch one PCSS tests are plotted in Figure 6-31, covering the cyclic stress-strain behaviour and the strain developments in the *x*-*y* plane. As a result of the load bias, all seven tests experience a ratcheting movement along the *x*-axis. The batch two test results (Figure 6-32 to Figure 6-37) reveal the different cyclic mechanisms and how they evolve with increasing magnitude in load bias and cyclic stress amplitude, with or without an offset, as well as changes in frequency.



(*a*) (*b*)

Figure 6-31: PCSS01 to PCSS07 - (*a*) Stress-strain behaviour and (*b*) strain path



(*a*) (*b*)

Figure 6-32: PCSS08 (*f* = 0.1 Hz) - (*a*) Stress-strain behaviour and (*b*) strain path

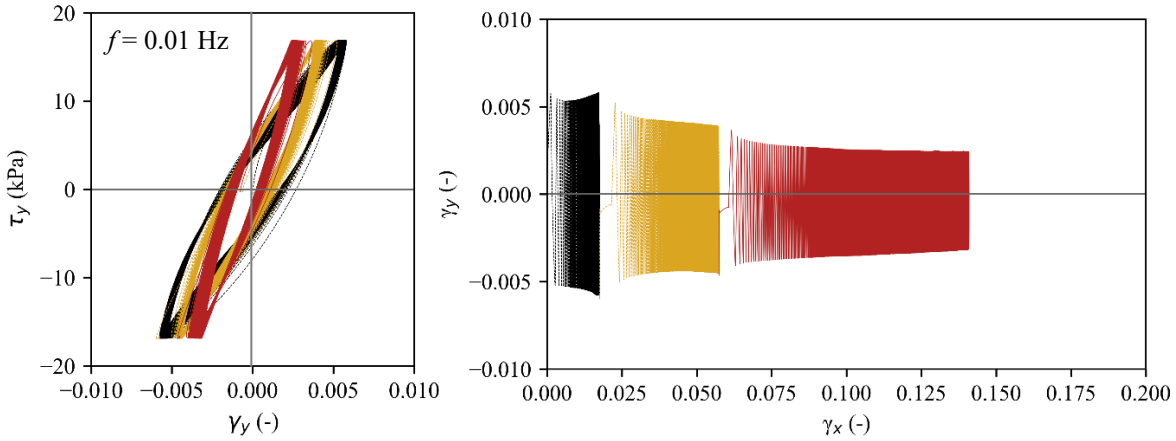


Figure 6-33: PCSS08 ($f = 0.01$ Hz) - (*a*) Stress-strain behaviour and (*b*) strain path

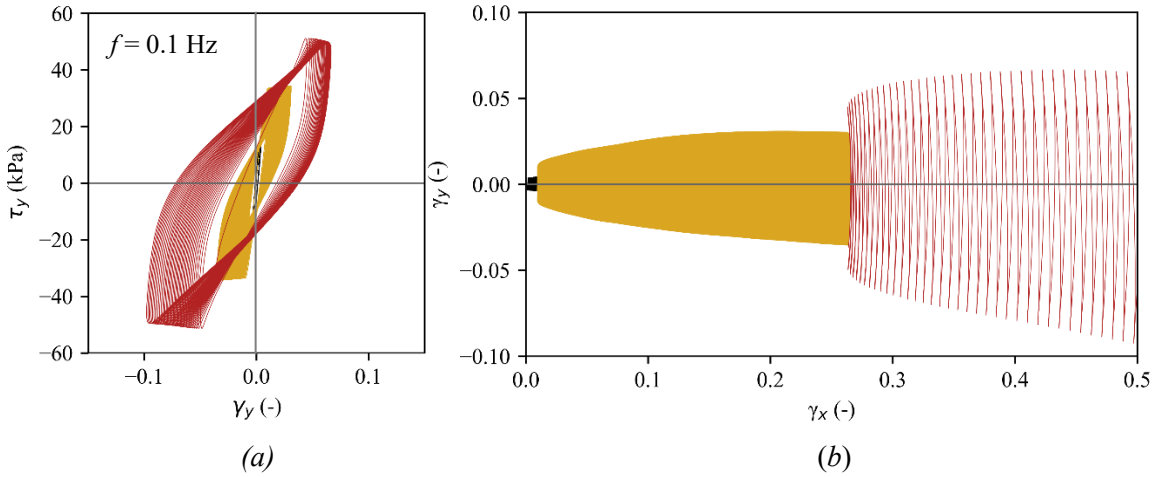


Figure 6-34: PCSS09 ($f = 0.1$ Hz) - (*a*) Stress-strain behaviour and (*b*) strain path

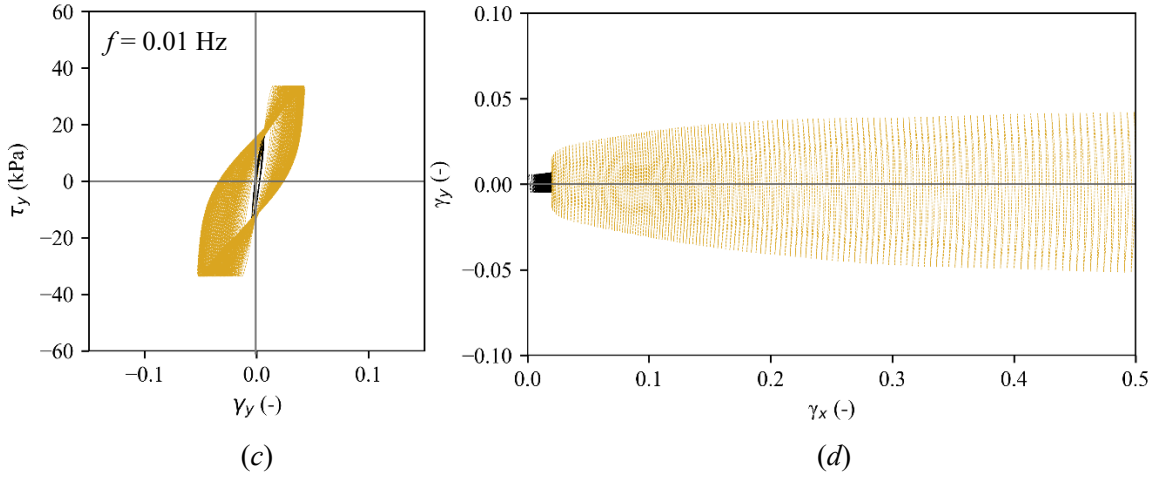


Figure 6-35: PCSS09 ($f = 0.01$ Hz) - (*a*) Stress-strain behaviour and (*b*) strain path

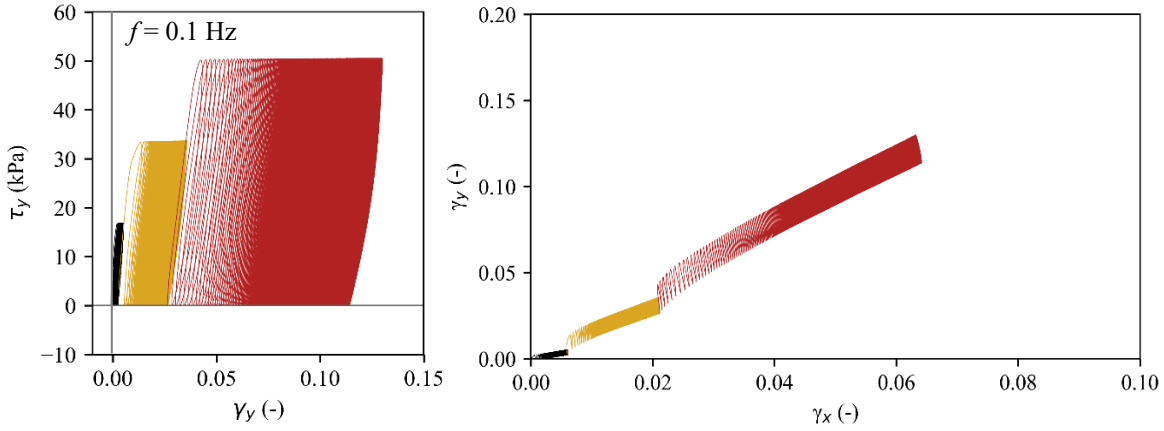


Figure 6-36: PCSS10 (f = 0.1 Hz) - (a) Stress-strain behaviour and (b) strain path

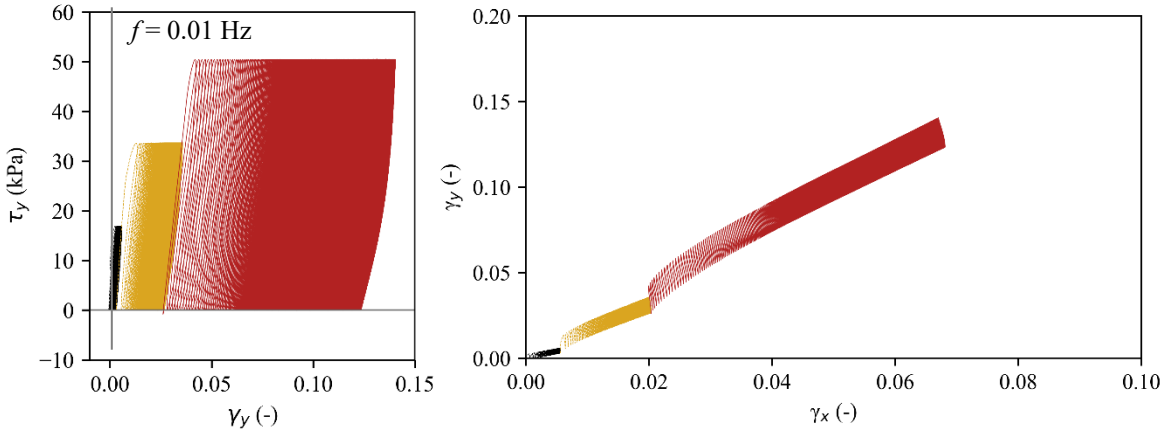


Figure 6-37: PCSS10 (f = 0.01 Hz) - (a) Stress-strain behaviour and (b) strain path

6.4.3 Strain accumulation

6.4.3.1 Batch one

Figure 6-31(b) shows the accumulation of ratcheting strain occurring in the direction of $\tau_{av,x}$. This is consistent with the findings of Richards (2019), who performed similar macro-scale model tests on piles in sand. The slope of the ratcheting rate is assessed in Figure 6-38, where all the tests represent two-way tests, apart from PCSS03 and PCSS06 which involve one-way and partial one-way cyclic loading. Using Equation (6-1), the ratcheting evolution appears to be similar for perpendicular tests with CSR_y = 0.2 with exponent m ranging from 0.07 to 0.10, while tests PCSS04 and PCSS05 give ratcheting slopes far higher for CSR_y = 0.4 (m = 0.37 to 0.57). It is interesting to note that the slopes do not appear to increase with

increasing τ_{av} but rather with τ_{cyc}. For model piles in sand, the direction of ratcheting was found to be independent of cyclic amplitude but rather a function of mean load (Richards, 2019). The current results indicate that the magnitude of the applied average load in the *x*-direction does not influence the slope of the ratcheting rate but affects the amount of total ratcheting strain accumulated. Figure 6-39 shows the development of $\gamma_{cyc,y}$ with the number of cycles. For tests PCSS02, and PCSS05 to PCSS07, the cyclic strain decreases, thus following a stiffening type progression. This is discussed further in Section 6.4.4.

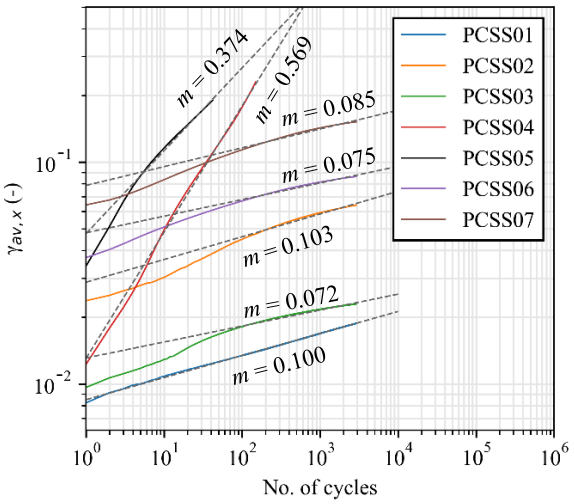


Figure 6-38: Accumulation of average strain with number of cycles

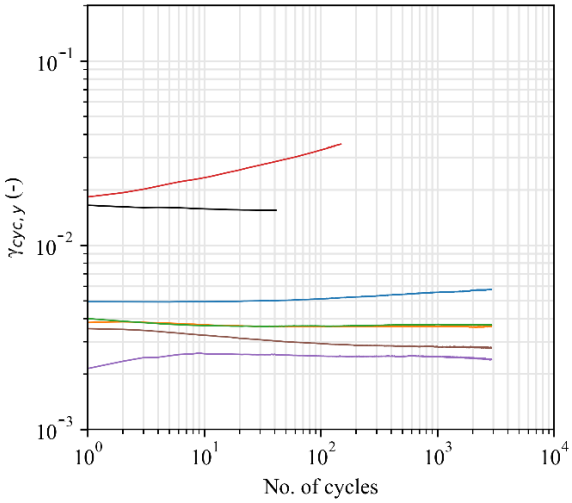
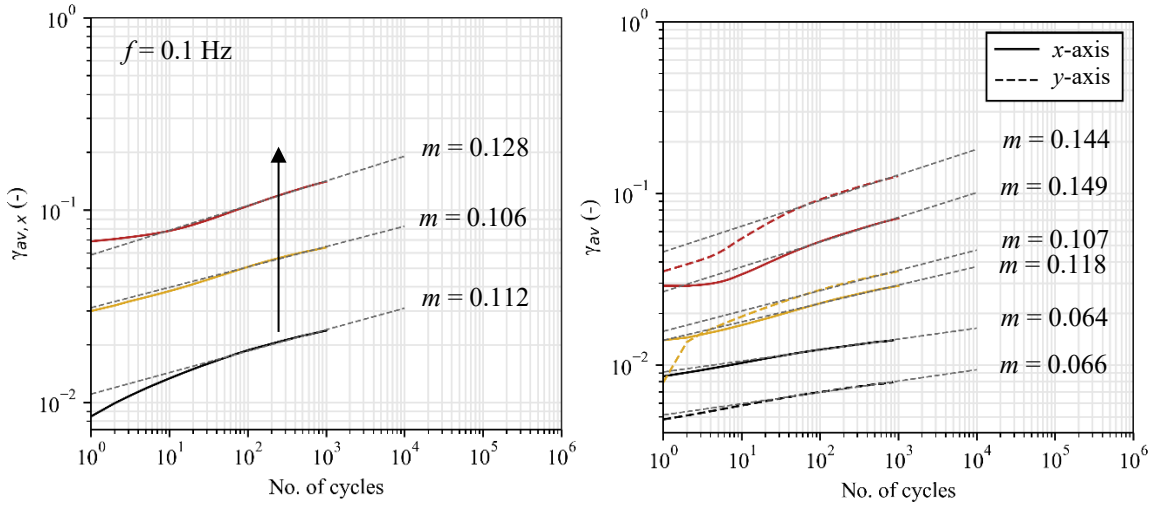


Figure 6-39: Accumulation of cyclic strain with number of cycles

6.4.3.2 Batch two

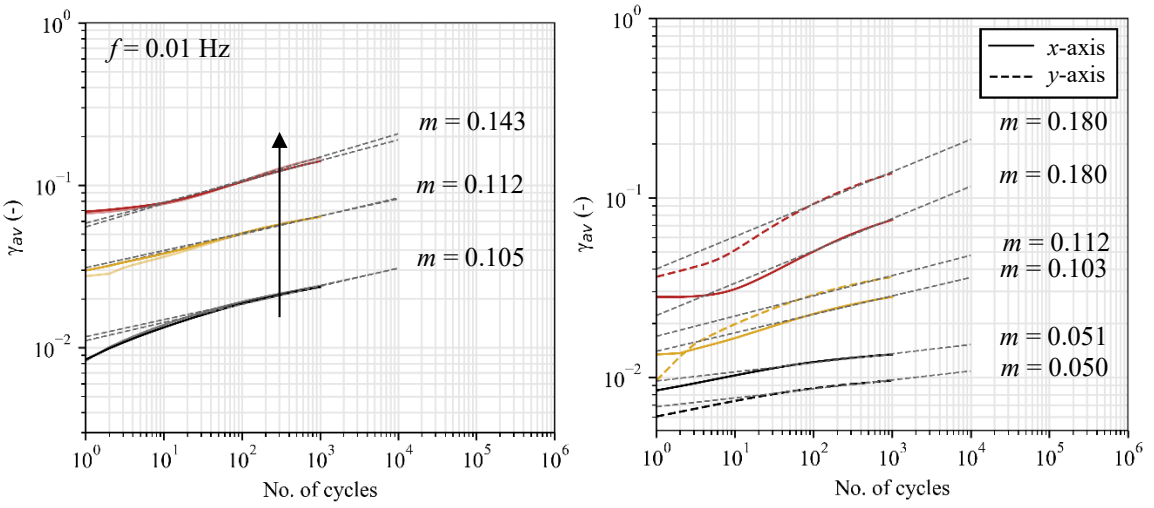
From tests PCSS08 and PCSS10, the permanent strain accumulation is observed to be a function of stress level with a minor dependency on frequency, where the slope of the ratcheting rate (denoted by exponent *m*) is continuous for a constant cyclic amplitude (CSR_y = 0.2) but it increases with the increasing cyclic amplitude in each packet. This complements the findings made in Section 6.3.3 where the value of CSR_y greatly affected the ratcheting slope, showing how a single multi-amplitude test reproduces the outputs from multiple single-amplitude CSS or PCSS tests. Furthermore, for test PCSS10, the exponent *m* is consistent in both directions. However, the magnitude of the effect is significantly lower than those measured for PCSS04 and PCSS05 in Figure 6-38. This is because, in this case,

the ratcheting is compounded by the stiffness degradation mechanism caused by the stress reversals. In terms of frequency, both sets of results (f = 0.1 and 0.01 Hz) yield similar ratcheting slopes, with the lower frequency dataset yielding slightly higher rates as demonstrated by Figure 6-40 and Figure 6-41. Although, in terms of final accumulated strain, it is not surprising to see higher amounts of strain for lower frequencies due to the lower mobilised strength caused by rate effects.



(*a*) (*b*)

Figure 6-40: Shear strain (f = 0.1 Hz) with number of cycles (*a*) PCSS08 and (*b*) PCSS10



(*a*) (*b*)

Figure 6-41: Shear strain (f = 0.01 Hz) with number of cycles: (*a*) PCSS08 and (*b*) PCSS10

6.4.3.3 Post-cyclic analysis

For several tests which did not reach failure, a post-cyclic monotonic shearing stage was introduced. From Figure 6-42, there is no clear indication of whether the original backbone curve is susceptible to softening. Instead, it seems to undergo little to no change despite large changes in secant stiffness, an observation comparable to the CSS test findings (Section 6.4).

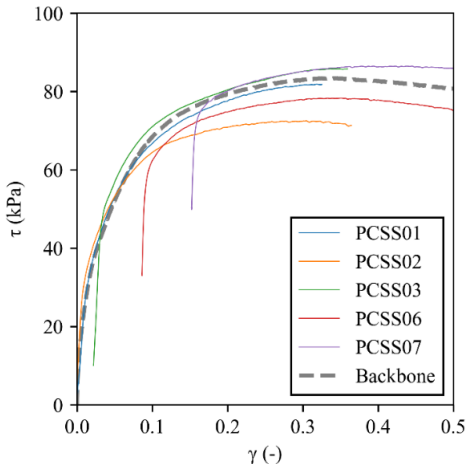


Figure 6-42: Post-cyclic response for PCSS tests

6.4.4 Stiffness degradation and energy loss factor

6.4.4.1 Batch one

Tests PCSS02 and PCSS05 to PCSS07 show an increase in k_{sec} (i.e. stiffening) compared with the other tests (Figure 6-43), a behaviour commonly observed in sand tests (Richards, 2019). Similar behaviours were observed for CSS tests with a combination of high ASR and low CSR (e.g. CSS11), where a stiffening-type progression was observed. The same findings were reported for batch two test PCSS08 and those reported by Ushev (2018) for comparable cyclic triaxial tests, which was said to be caused by slight changes in the soil's stress contact fabric at large strains, presumably meaning a dilative type behaviour caused by coarser material within the clay matrix. In contrast, Figure 6-43 shows that PCSS01, PCSS03, and PCSS04 behave closely to a two-way cyclic test for clay with the development of stiffness degradation. The average load ($\tau_{av,x}$) in the x-axis was low enough to allow stiffness degradation of the material yet large enough to provide a biased ratcheting direction.

Although using a different material, Kammerer et al. (2002) reached the same conclusion for dense Monterey 0/30 sand under multidirectional cyclic loading. For stiffness degradation behaviour, a power-law function given by Equation (6-1) was used to capture the evolution of k_{sec} under perpendicular cyclic loading, with exponents showing a decreasing or increasing behaviour depending on the combination of ASR and CSR. Figure 6-44 depicts the evolution of the energy loss factor η_I with number of cycles, with trends moving down and to the right with a tendency to stabilise past 10^2 cycles. This behaviour is identical to the CSS tests. However, at a lower number of cycles, test PCSS06 which is at the largest τ_{cyc} yields a far greater η_I than the rest. It is thought that the load bias in the cycling direction likely affected the dissipation behaviour, increasing the size of the hysteresis loops.

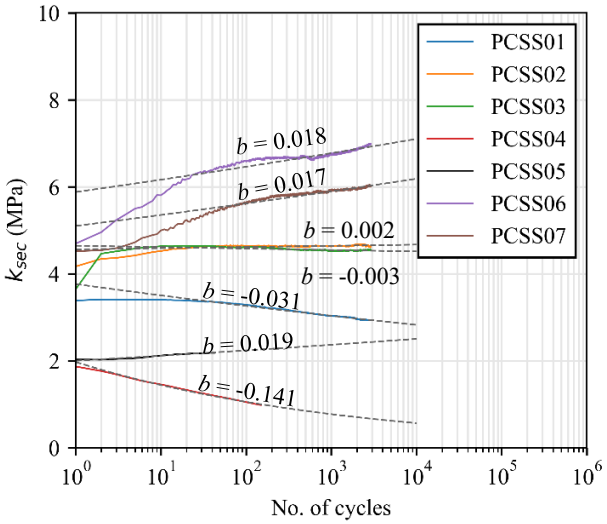


Figure 6-43: Evaluation of stiffness degradation with number of cycles

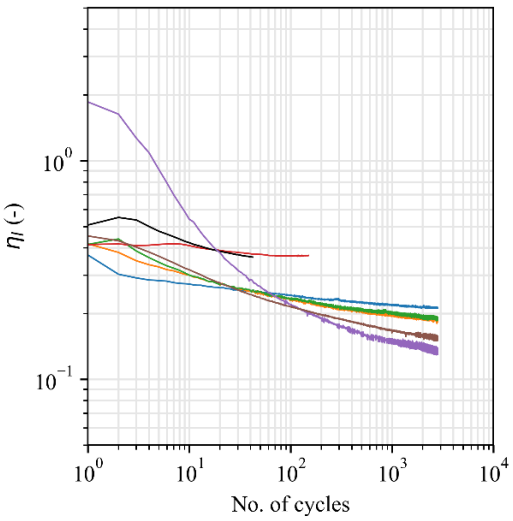
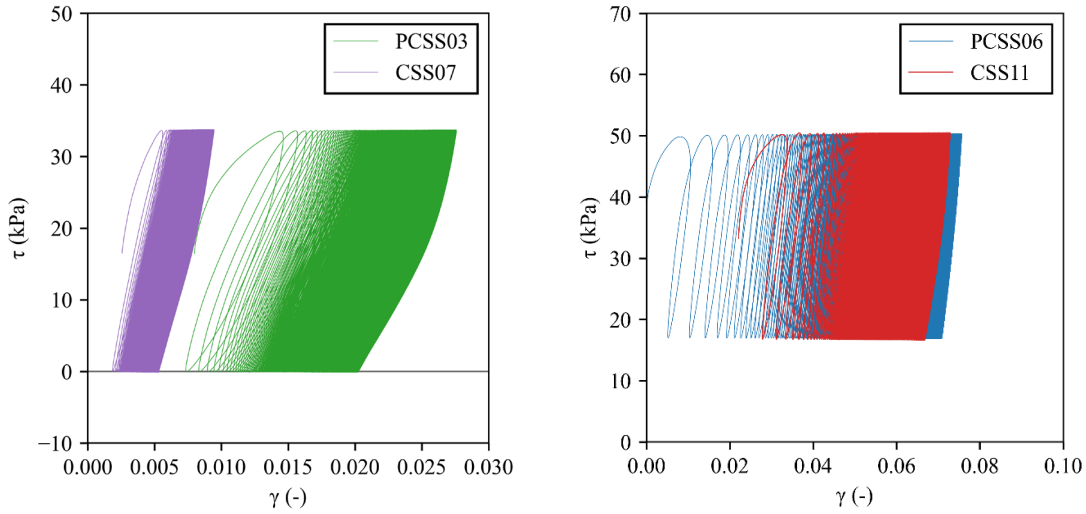


Figure 6-44: Evolution of energy loss factor

For the perpendicular tests, η_I is greater than the equivalent unidirectional tests (Section 6.3.6). While not as apparent for the two-way tests, the one-way tests shown in Figure 6-45 reveal a noticeable change in the loop area, equivalent to hysteretic energy loss E_H. The loop area for CSS07 (ASR = 0.2, CSR = 0.2) and CSS11 (ASR = 0.4, CSR = 0.2) contracts at a much quicker rate over a smaller number of cycles when compared with PCSS03 and PCSS06. The increase in η_I can be explained by the additional τ_{av}, increasing the amount of mobilised strain, thus increasing dissipation (Richards, 2019).

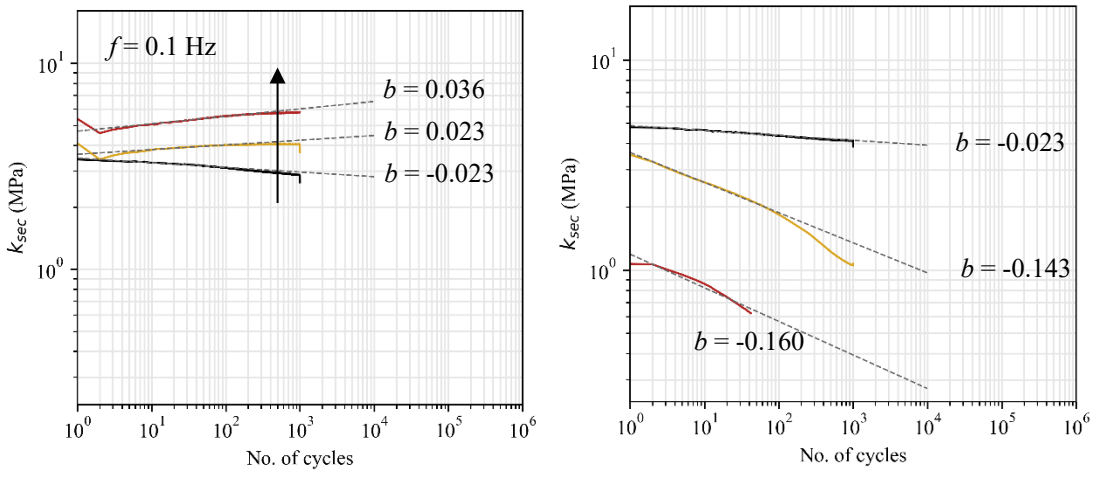


(*a*) (*b*)

Figure 6-45: Evolution of loop shape with number of cycles for (*a*) PCSS03 and CSS07, and (*b*) PCSS06 and CSS11

6.4.4.2 Batch two

As already described in Section 6.3.5, the stiffness degradation rate appears to increase with increasing cyclic amplitude for test PCSS09, with the exponent *b* ranging from -0.023 to -0.16 as shown in Figure 6-46(b). Interestingly, similar to the batch one tests, test PCSS08 shows that the stiffness behaviour progresses from a degradation to stiffening type evolution (see Figure 6-46(a)). Following the ratcheting observation, the stiffness degradation behaviour in terms of frequency are relatively similar, with larger differences observed for PCSS09 caused by mobilisation of larger strains (compare Figure 6-46 and Figure 6-47).



(*a*) (*b*)

Figure 6-46: Stiffness evolution ($f = 0.1$ Hz) with number of cycles: (*a*) PCSS08 and (*b*) PCSS09

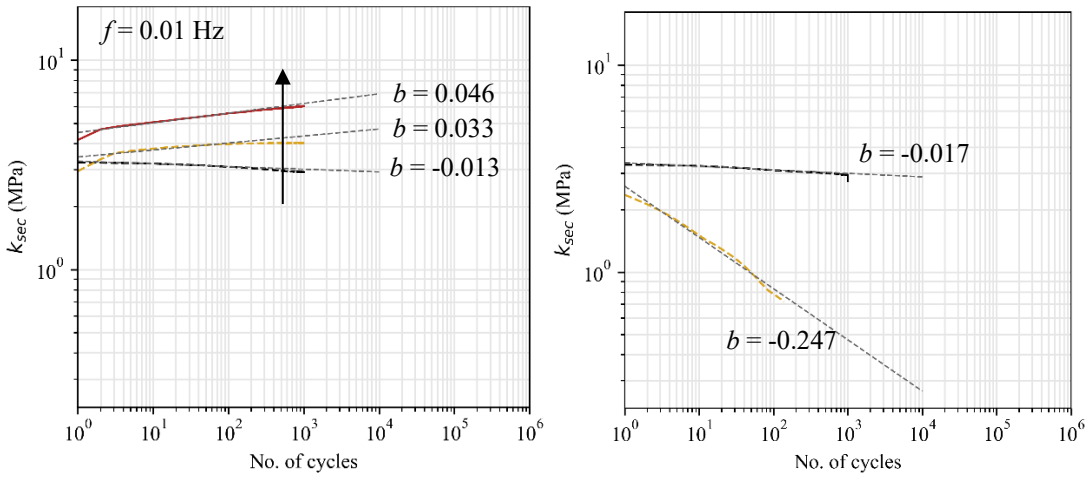


Figure 6-47: Stiffness evolution (f = 0.01 Hz) with number of cycles: (a) PCSS08 and (b) PCSS09

6.5 Random loading cyclic simple shear tests (RCSS)

The random cyclic simple shear tests aimed to investigate the impact of realistic wind and wave loading histories on the response of Cowden till soil at element level. The random amplitude tests followed a similar consolidation procedure to the unidirectional constant amplitude tests; however, the loading simulated the pattern for (1) an idling low storm phase, (2) an operational low storm phase, (3) a mid-storm phase for wind or wave, (4) a mid-storm phase which was predominantly wind-driven, (5) a high storm event driven by wind or wave before finally returning to (6) a mid-storm event. The details of the load stages are summarised in Table 6-7 and Table 6-8, and their time histories are plotted in Figure 6-48. The load data was based on information provided by Ørsted given different design scenarios, as part of the PICASO project, but suitably normalised and anonymised to reflect generic pseudo-random loading sequences, but with the appropriate characteristics. Comparisons, discussed in Section 6.8, are drawn between the medium-scale field testing (Martin, 2023), which followed similar loading histories, and the tests at soil element level. Additionally, the test programme includes an element-level version of a multidirectional pile load test, i.e. with an out-of-plane loading.

6.5.1 Test programme

The programme involved three variations of random cyclic simple shear (RCSS) tests, following the loading time histories in Figure 6-48. The mapping of the loads in normalised stress space counts the number of half-cycles $n_{0.5}$ within each bin throughout the stress space. From the distributions, a load bias exists which is scaled based on the reference s_u (~84 kPa). Furthermore, initial predictions were made using the Bi-HYP model implemented in Chapter 7 to verify the magnitudes of the loads used for the testing, to ensure large strain behaviour could be captured without tests failing prematurely.

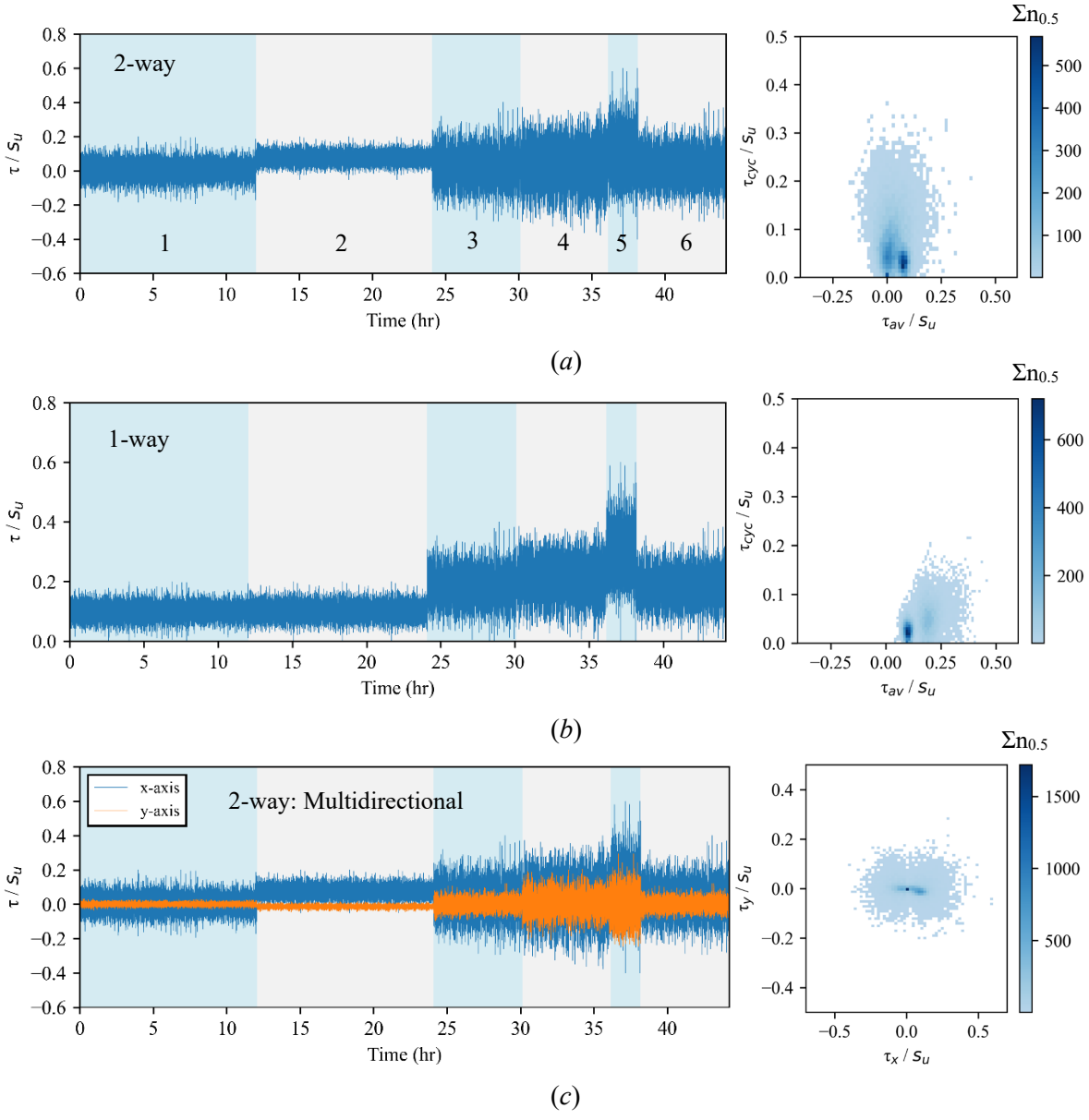


Figure 6-48: Storm load history for (*a*) RCSS01, (*b*) RCSS02 and, (*c*) RCSS03

Table 6-7: Test loading schedule for RCSS01 and RCSS03

Load Stage	$\Delta\tau_x/s_u$	$\Delta\tau_y/s_u$	$\tau_{av,x}/s_u$	$\tau_{av,y}/s_u$	$\tau_{min,x}/ s_u \rightarrow \tau_{max,x}/ s_u$	$\tau_{min,y}/ s_u \rightarrow \tau_{max,y}/ s_u$	No. cycles	Time (hr)
1	0.393	0.067	0.004	0.000	-0.193 to 0.2	-0.034 to 0.033	3618	12
2	0.251	0.063	0.076	-0.014	-0.051 to 0.2	-0.046 to 0.017	3334	12
3	0.695	0.218	0.026	0.001	-0.295 to 0.4	-0.098 to 0.120	1798	6
4	0.776	0.416	0.030	0.005	-0.376 to 0.4	-0.210 to 0.206	1903	6
5	1.001	0.538	0.103	0.002	-0.401 to 0.6	-0.244 to 0.294	646	2
6	0.695	0.218	0.026	0.001	-0.295 to 0.4	-0.098 to 0.120	1800	6

Table 6-8: Test loading schedule for RCSS02

Load Stage	$\Delta\tau_x/s_u$	$\tau_{av,x}/s_u$	$\tau_{min,x}/ s_u \rightarrow \tau_{max,x}/ s_u$	No. cycles	Time (hr)
1	0.2	0.099	0 to 0.2	3618	12
2	0.2	0.102	0 to 0.2	3334	12
3	0.4	0.184	0 to 0.4	1798	6
4	0.4	0.209	0 to 0.4	1903	6
5	0.6	0.302	0 to 0.6	323	2
6	0.4	0.184	0 to 0.4	1800	6

6.5.2 Test schedule results and general observations

The results for RCSS01 and RCSS02 are plotted in Figure 6-49 and are distinguished as blue and red curves, respectively. In addition, the backbone curve for each test is plotted for comparison, serving as a reference to assess the shape of the hysteretic loops. The hysteretic responses are generally consistent with those observed for the standard CSS tests. However, a more significant cyclic response (i.e. cycles surpassing the backbone) was detected due to the rate effects discussed in Section 6.3.3.

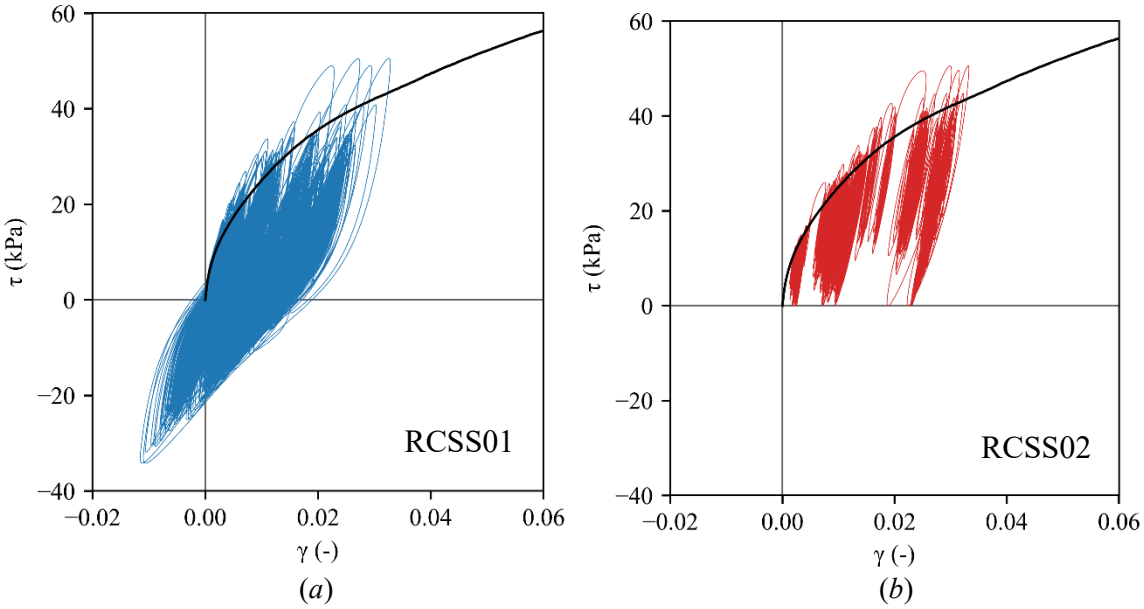


Figure 6-49: Stress-strain plot for (*a*) RCSS01 and (*b*) RCSS02

The results for the multidirectional test (RCSS03) are plotted in Figure 6-50, with the in-plane (*x*-axis) and out-of-plane (*y*-axis) loads depicted in orange and purple, respectively. The in-plane loads are identical to those applied in RCSS01, so this test explores the impact of out-of-plane loads on the in-plane strain. The magnitude of the out-of-plane loads is smaller, hence there is a bias in the strain accumulation direction, discussed further in Section 6.5.3.

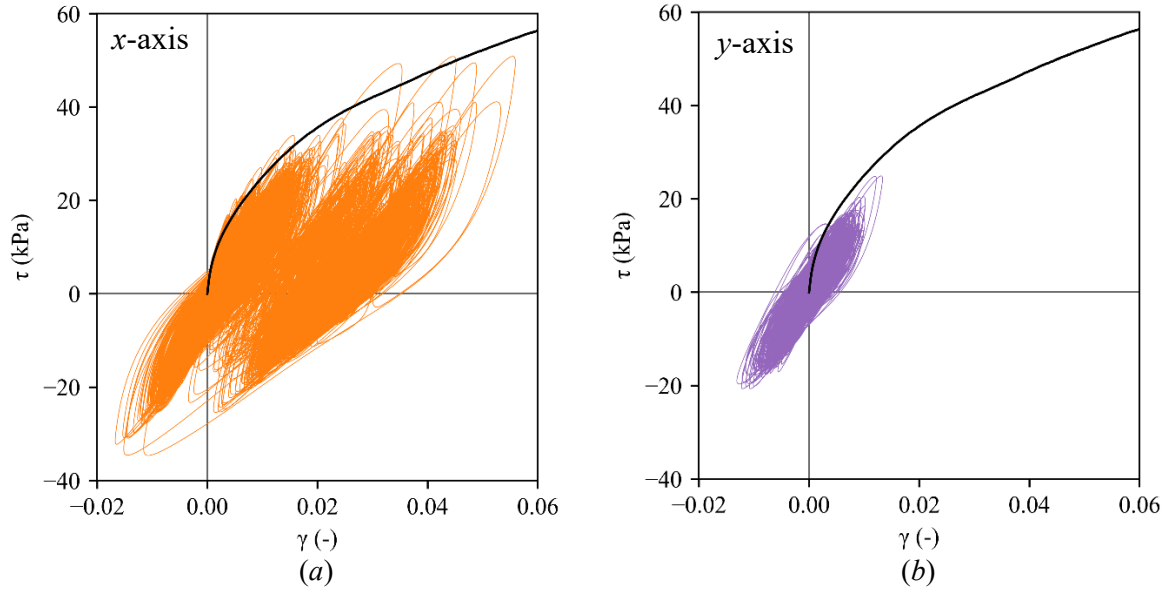


Figure 6-50: Stress-strain plot for RCSS03 in the (*a*) *x*-axis and (*b*) *y*-axis

6.5.3 Strain accumulation

Under irregular cyclic simple shear loading, the accumulated strains for both RCSS01 and RCSS02 are dominated by the large load events, in agreement with observations from LeBlanc et al. (2010), Abadie (2015) and Richards (2019) for regular multi-amplitude cyclic loading. Furthermore, the ratcheting type behaviour is consistent with the interpretations made for regular cyclic loading (in Section 6.3), where ratcheting occurs under biased cyclic loading ($\zeta_c \neq -1$), with the behaviour (i.e. magnitude and rate of evolution) dependent on the loading characteristics (i.e. ASR and CSR).

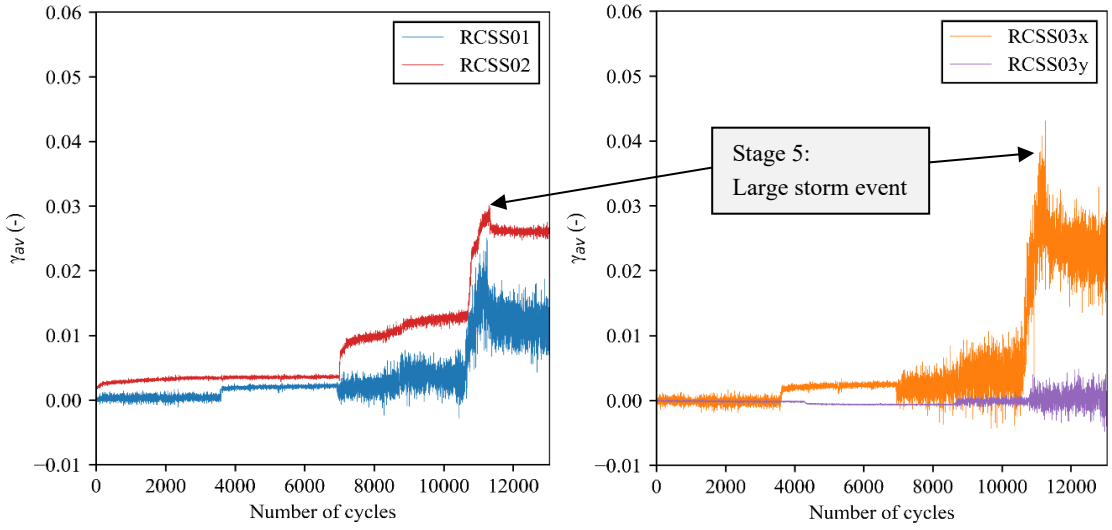


Figure 6-51: Evolution of average strain for (*a*) RCSS01 and RCSS02, and (*b*) RCSS03

As a result, the 1-way test (RCSS02) accumulates more permanent strains than the two-way test (RCSS01) despite similar ratios for τ_{max}/s_u. For RCSS03, the strain accumulation behaviour is consistent with the behaviours observed in the PCSS tests, where the out-of-plane loading increases the overall amount of strain accumulated. This is observed in Figure 6-49(a), Figure 6-50(a), and Figure 6-51(a) and (b), where larger strains are recorded for RCSS03 by comparison with RCSS01, which is a direct result of multidirectional loading (Rudolph et al., 2014; Jin et al., 2022). For each loading stage in RCSS01 and RCSS02, a ratio of accumulated strain ($\Delta\gamma_{av}$) proportional to the total amount of permanent strain at the

end of the load history is calculated, and the results are presented in Figure 6-52. The strain accumulation ratio is most significant for stages with an overall load bias coupled with high cyclic amplitudes. It is interesting to note the drop in permanent strains for all RCSS tests at the start of the sixth loading stage. This can be explained by the change in frequency, and in τ_{max}/s_u, between loading stages five and six. Here, the drop in frequency allows the sample to recover some of the strains accumulated due to rate effects (and presumably the equalisation of excess pore water pressure, although the latter is not measured). The difference in frequency is further discussed in Section 6.6.

An interesting observation is the small amount of strain accumulated from stages with little to no bias and small cyclic amplitudes. In the tests performed here, this includes stages 1 to 4 for RCSS01, stages 1, 2, 4 and 6 for RCSS02, and stages 1 to 4 for RCSS03*x*. Each stage contributes < 10% of the total amount of shear strain developed, meaning these stages are essentially redundant and can be removed for faster analysis. At a minimum, cycles with amplitudes < $0.2s_u$ can certainly be removed, allowing for the testing time to be reduced. Still, extra attention should be given to moments of transition between stages, where an offset and ramp-up to τ_{av} is likely to cause the largest change in strain, rather than the leading cycles within the subsequent package with magnitudes of similar load order. For the multidirectional test (RCSS03), the strain path is given in Figure 6-53, showing a bias in the positive *x*-direction.

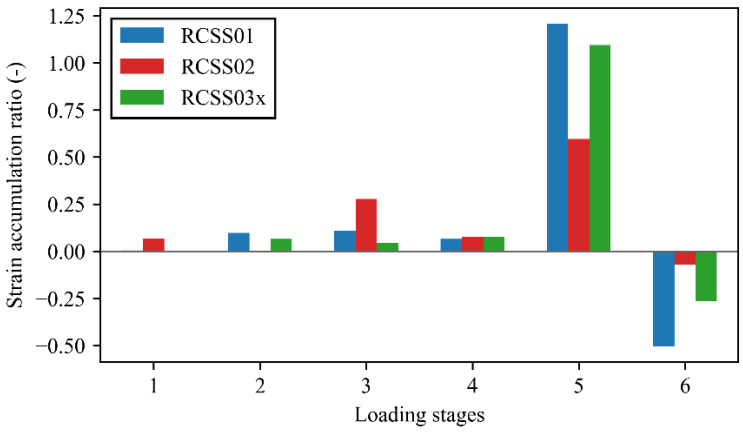


Figure 6-52: Strain accumulation ratio for each loading stage

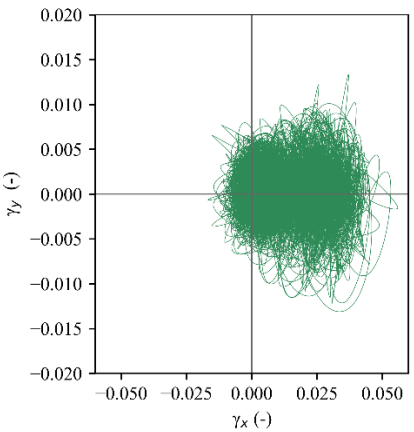


Figure 6-53: RCSS03 strain path

6.5.4 Stiffness degradation

An attempt at evaluating the evolution of stiffness is presented here. In contrast to the regular CSS tests, changes in the stiffness are conflated with the more significant impact of cyclic load amplitude, making it challenging to assess k_{sec} as it varies from cycle to cycle. Nonetheless, the plots obtained using the definition of k_{sec} in Section 2.3.3 are presented below, and the backbone (average of CWD-BS-DSS-CU-OL35 & CWD-BS-DSS-CU-OL35a) serves as a reference. Due to the amount of scatter present, fitting a function would not fully capture the evolution of k_{sec} and even less so when k_{sec} is plotted against the number of cycles. However, the k_{sec} response appears to be bounded by the monotonic backbone despite the influence of rate effects, in agreement with the standard CSS observations and those previously reported in the literature (Ushev, 2017).

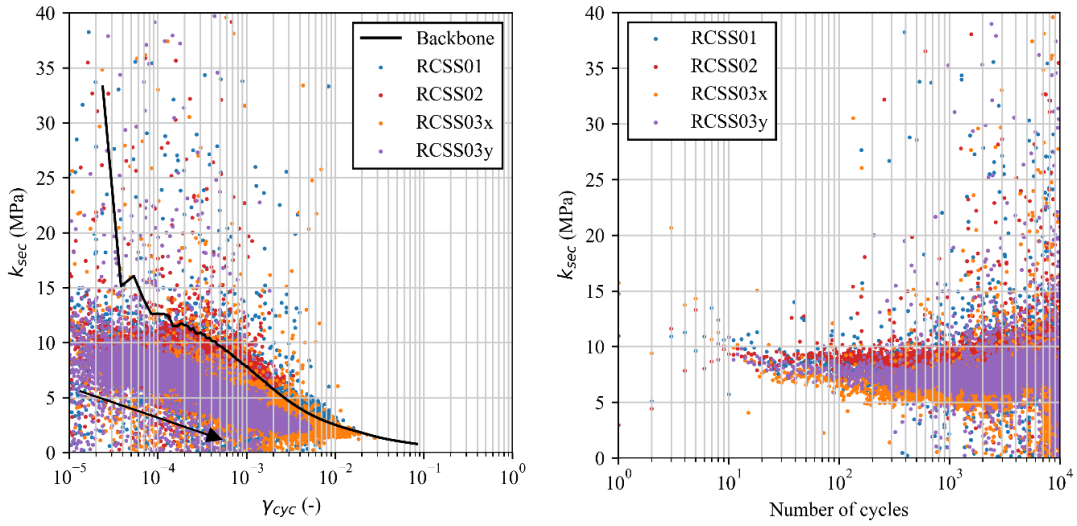


Figure 6-54: Stiffness degradation with (*a*) cyclic shear strain and (*b*) number of cycles

6.6 Random packaged cyclic simple shear tests (RPCSS)

Building on the RCSS tests, the storm load histories were discretised into packages of an equivalent number of cycles following a modified NGI cycle counting procedure (Norén-Cosgriff et al., 2015; Skau et al., 2022). The investigation involves the feasibility of different idealised load compositions and how they may be employed to simplify cyclic loading design for realistic storm load histories (Note: Multidirectional loading not considered here).

6.6.1 Test programme

The storm loads were separated into parcels based on the magnitude of the cyclic amplitude for each of the half cycles during the cycle counting procedure. Each parcel contains cycles of fixed cyclic amplitude (CSR), computed average stress (ASR), and mean frequency (f_p). Normalised cyclic load increments of 0.05 were used for each load parcel to simplify the problem. The method of counting cycles from random loading is illustrated in Figure 6-55 below, highlighting τ_{av}, τ_{cyc} and duration dt for each half-cycle.

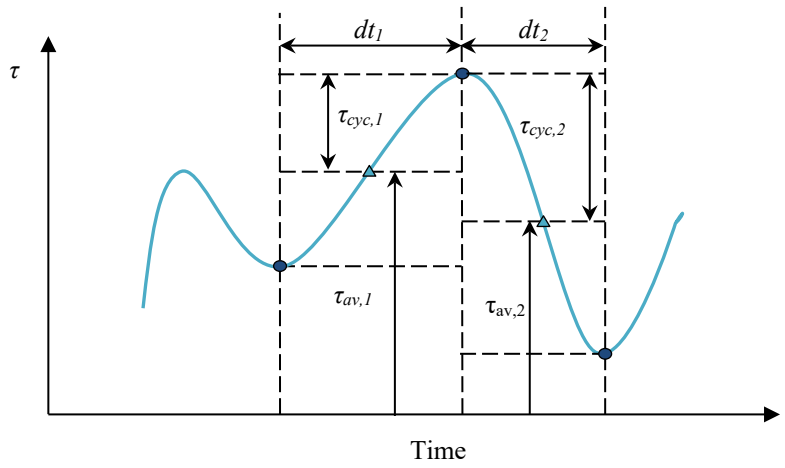


Figure 6-55: Cycle counting (based on the NGI method)

The procedure implemented here differs from the NGI method, where an average frequency across all parcels is obtained from a power spectral density approach (Skau et al., 2022). It is understood that the NGI approach allows for a more simplified application of idealised loads. A variable rate from parcel to parcel means that the contour diagrams would require scaling, or the path in the accumulation procedure would need to be adjusted (Skau et al., 2022). For this research, the mean frequency f_p is based on the accumulation of dt for each half cycle $n_{0.5}$ within the allotted parcel (e.g. $f_p = \frac{\sum n_{0.5}}{\sum dt_n}$).

The approach adopted showed that the calculated f_p yielded a testing time close to the storm history duration, and was a better representation of the overall loading behaviours. This is best argued from the application of parcels with high cyclic amplitudes paired with a high frequency. Considering the influence of the cyclic amplitude on the accumulation of

strains as already seen in CSS, PCSS, and RCSS tests, a frequency which is underestimated would mean an overprediction of the strains (owing to rate effects), hence the need for a modified NGI approach. This is also seen in the work by Wu (2022) who performed cyclic model pile tests on identical Cowden till material, recording lower angles of permanent rotation for tests at higher frequency. Tests RPCSS01 and RPCSS02 have identical parcels but are arranged in ascending and descending order respectively. RPCSS03 has fewer parcels but has a higher load bias as this is based on the one-way RCSS02 test. Figure 6-56 to Figure 6-58 show the applied load sequences.

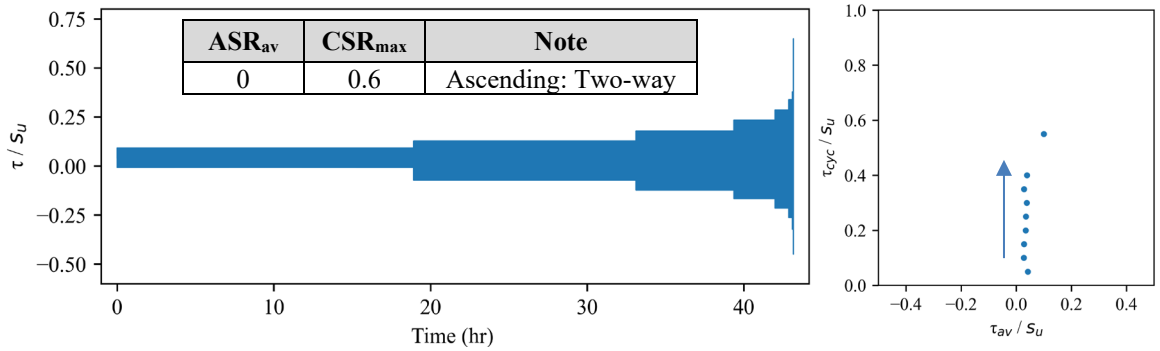


Figure 6-56: Load sequence for RPCSS01

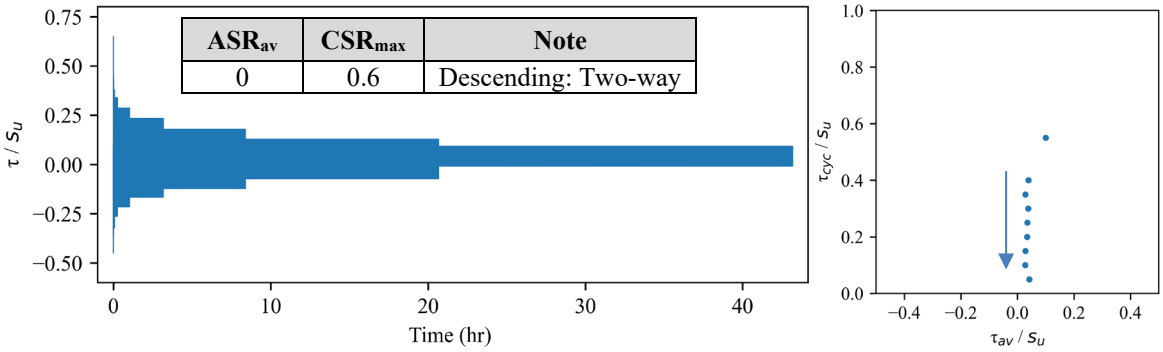


Figure 6-57: Load sequence for RPCSS02

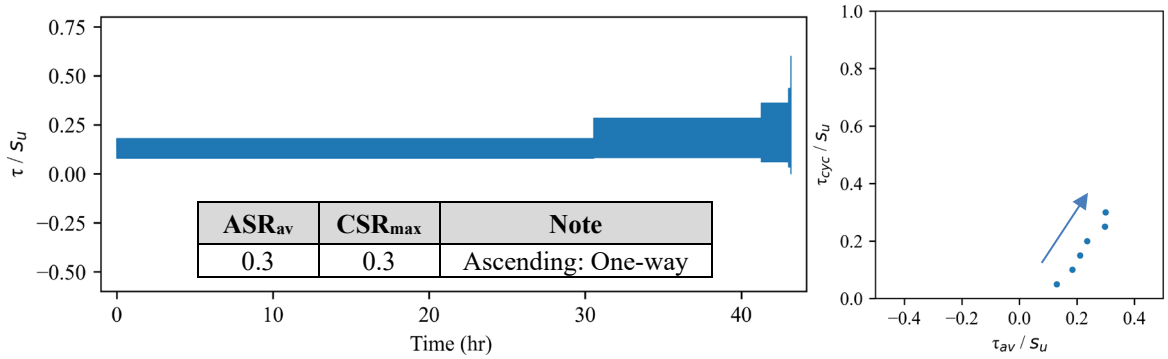


Figure 6-58: Load sequence for RPCSS03

The details of the cyclic loading parameters are given in Table 6-9 and Table 6-10. Due to the load increment size for each parcel (~0.5) and upper bound load selection, cycles from the storm history may have been assigned amplitudes higher than the original. For example, a storm load cycle with CSR = 0.51 would be allocated into a parcel ranging from 0.5 to 0.55, and since the upper bound load is selected, the CSR of that cycle is now 0.55. This conservative approach was taken to cover the higher-end shear strains that would develop during cyclic loading, noting that the largest strains occur at the largest load events. An unconservative process, selecting the lower bound or mean value, would underpredict the amount of ratcheting. While feasible, the large strain behaviours would be less pronounced, making it more difficult to assess the contributions from the larger loading cycles. The assigned frequencies are in line with known wave loading values, which usually have a dominant cyclic component with a frequency of around 0.1 Hz (Richards, 2019).

Table 6-9: Loading sequence for RPCSS01 and RPCSS02

Parcel no.	ASR	CSR	No. of cycles (-)	f_p (Hz)
1	0.043	0.05	6159	0.090
2	0.029	0.1	3939	0.076
3	0.031	0.15	1758	0.075
4	0.039	0.2	748	0.073
5	0.044	0.25	279	0.078
6	0.051	0.3	74	0.075
7	0.038	0.35	21	0.077
8	0.055	0.4	4	0.084
9	0.100	0.55	2	0.155

Table 6-10: Loading sequence for RPCSS03

Parcel no.	ASR	CSR	No. of cycles (-)	f_p (Hz)
1	0.132	0.05	9407	0.085
2	0.189	0.1	2987	0.074
3	0.222	0.15	533	0.075
4	0.256	0.2	52	0.070
5	0.297	0.25	4	0.170
6	0.300	0.3	2	0.155

6.6.2 Test schedule results and general observations

The results of all three RPCSS tests are presented in Figure 6-59, along with the monotonic backbone curve (average of CWD-BS-DSS-CU-OL35 & CWD-BS-DSS-CU-OL35a).

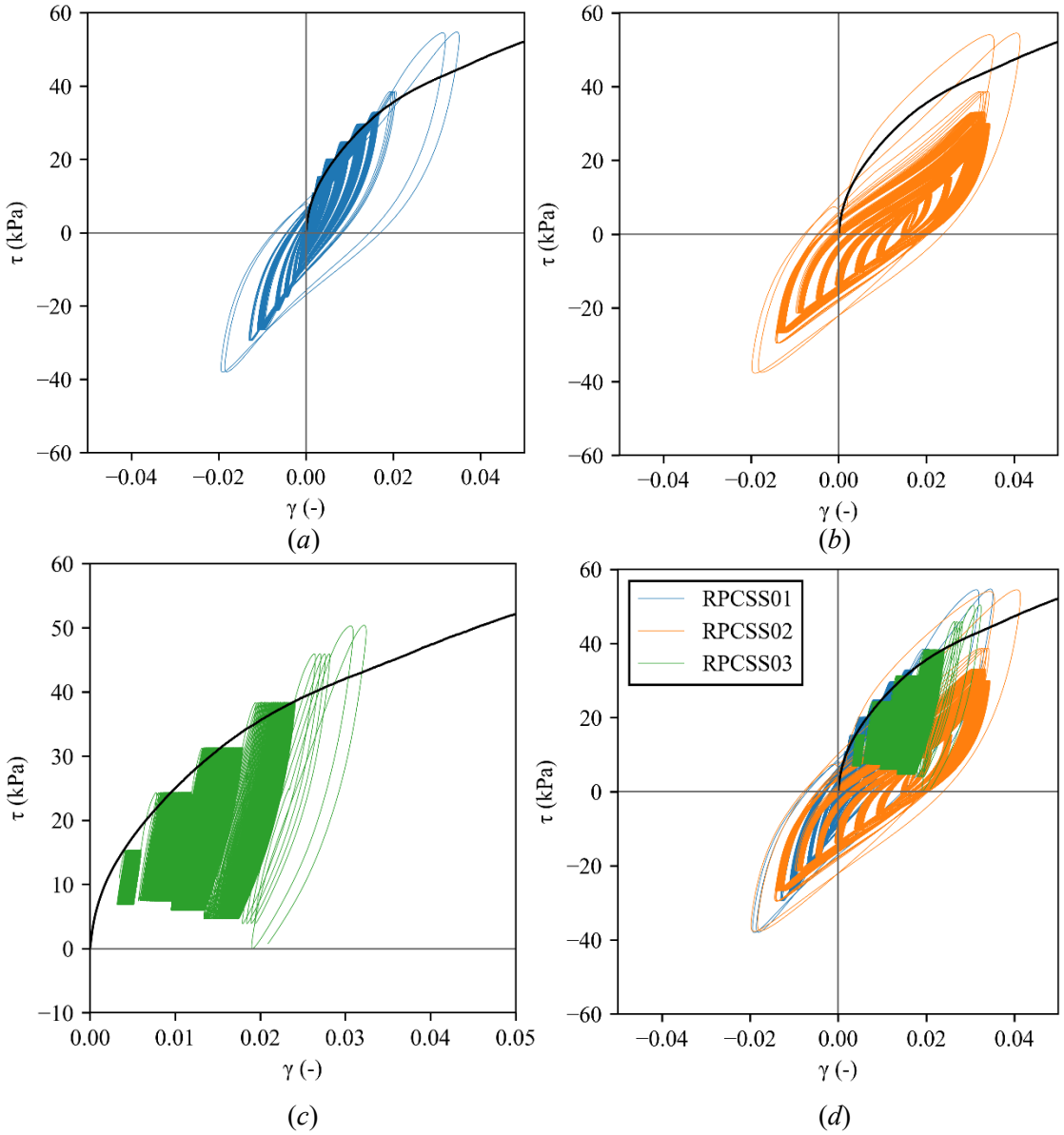


Figure 6-59: Stress-strain response for (a) RPCSS01, (b) RPCSS02, (c) RPCSS03, and (d) combined tests

6.6.3 Strain accumulation

As expected, the three loading sequences give different strain behaviours. Like the CSS tests, the two-way ascending package test (RPCSS01) shows little accumulation in γ_{av} but the highest in γ_{cyc}. RPCSS02, the descending variant, shows the opposite: an increase in γ_{av} and a decrease in γ_{cyc}. The loading bias can explain the behaviour due to the large load cycle at

the start, which causes large shear strains to develop in the direction of the initial load. Similar to observations made in the previous section for RCSS tests, after the large load cycle, the next package of smaller cycles recovered a portion of the average strains γ_{av}. As expected, the one-way test (RPCSS03) shows a larger accumulation in γ_{av} with number of cycles, but this effect is less noticeable for γ_{cyc}.

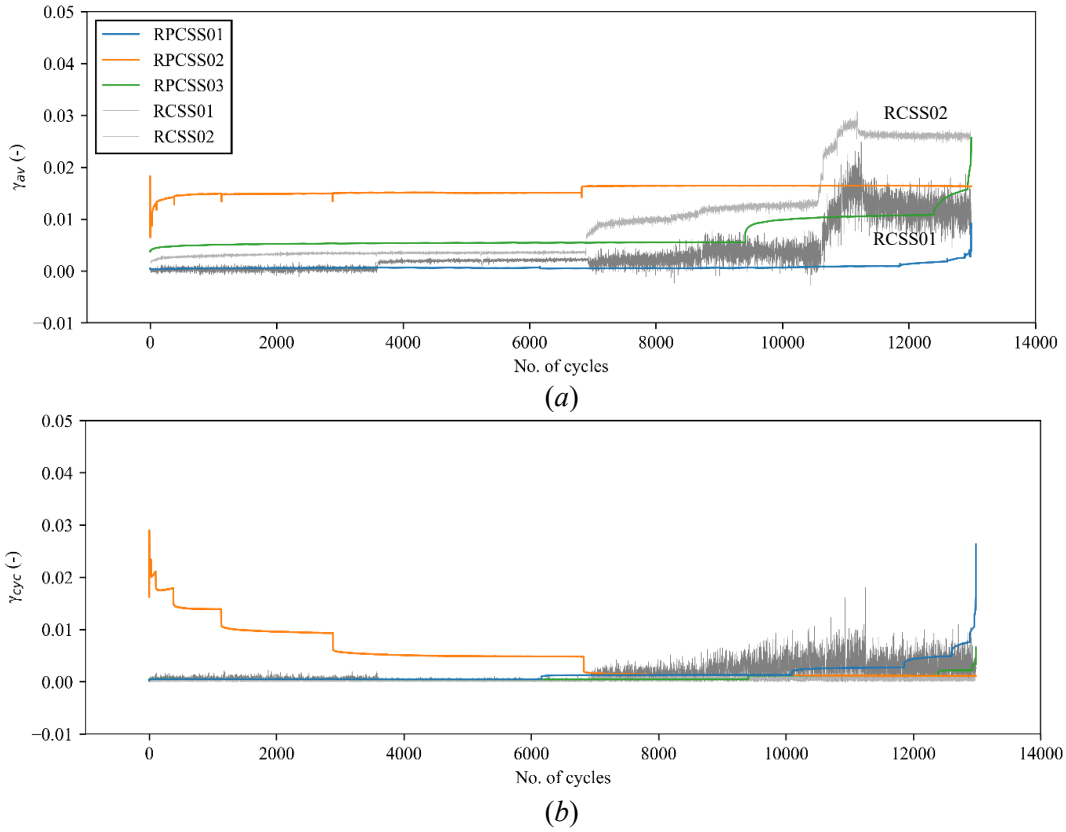


Figure 6-60: (*a*) Average strain accumulation and (*b*) Cyclic strain accumulation

When comparing the two-way tests with their relevant RCSS counterparts, their total strain responses appear to agree. With reference to Table 6-11, RPCSS01 and RPCSS02 give a final γ_{av} equal to 0.0093 and 0.0163 respectively. Surprisingly, RPCSS01 gives a very similar value to that measured for RCSS01 (γ_{av} = 0.0095). Equally, for RPCSS03 (γ_{av} = 0.0257), the values were in close agreement with the RCSS02 one-way test (γ_{av} = 0.0262). The shear strain difference demonstrates the impact of the method used to idealise loads and parcel sequence or arrangement. In this case, it makes sense for packages to be arranged in ascending rather than descending order to avoid an over-conservative design. The findings

are similar to those made by Skau et al. (2022), who demonstrated that the translation of irregular time histories into idealised load packages using an NGI-type rainflow counting method is a reasonable engineering approach to account for cyclic loading in design.

It can also be postulated that tests RPCSS01 and RPCSS02 serve as lower and upper bounds with regards to the stiffness degradation response, γ_{cyc}, as seen in Figure 6-60(b), where the final cyclic strain is considerably higher for the former. In terms of cyclic design with representative stiffness degradation, it would be sensible to adopt a descending order package arrangement similar to RPCSS02 as it gives γ_{cyc} values far closer to RCSS01 compared to RPCSS01.

Table 6-11: Summary of final average and cyclic strain accumulation values

Test ID	Test type	γ_{av} (-)	γ_{cyc} (-)
RPCSS01	Two-way ascending	0.0093	0.0263
RPCSS02	Two-way descending	0.0163	0.0011
RPCSS03	One-way ascending	0.0257	0.0066
RCSS01	Two-way	0.0095	0.0026
RCSS02	One-way	0.0262	0.0003

6.6.4 Post-cyclic behaviour

When performing idealised cyclic loading tests, it is important to check that the final strain and stiffness response is reasonably approximated when compared to the storm load tests they were derived from. After the application of the cycles, a post-cyclic monotonic loading stage was introduced to deduce the change in the ultimate capacity of the specimen. Following the cyclic stage, the specimens were sheared at the same rate as the DSS tests at a shear strain rate of 3% per hour. The post-cyclic response of the RPCSS tests is shown in Figure 6-61, along with the monotonic backbone curve and the post-cyclic results for the RCSS tests. Similar to the CSS post-cyclic response in Section 6.3.4, some of the tests show slight changes (< 12%) in s_u, with no indication of a dominant softening or hardening behaviour. It appears the capacity of the cyclic tests is fairly consistent, which is similar to the findings by Wu (2022) and Martin (2023) for model pile tests and medium-scale field

tests on Cowden till, respectively. These observations have important implications for design. An example includes the *p-y* method (Section 1.4.1), where the capacity of the pile is considered to be reduced due to cyclic loading.

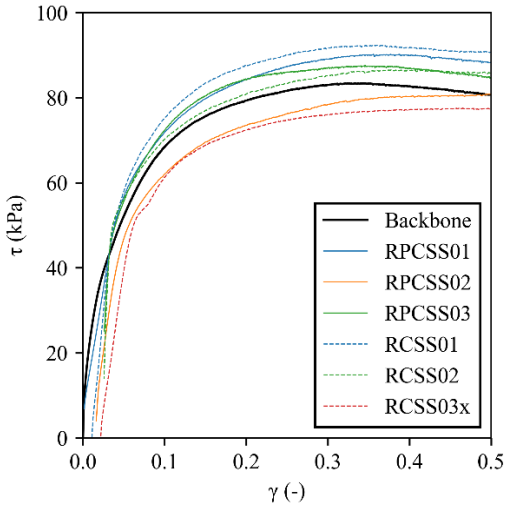


Figure 6-61: Post-cyclic monotonic stage for RCSS and RPCSS tests

The post-cyclic response of the RPCSS tests is similar to the RCSS tests. While this is expected, considering the above reasons, this may explain the validity of idealising the loads into packages as demonstrated by Norén-Cosgriff et al. (2015) and Skau et al. (2022).

6.6.5 Stiffness degradation

From Figure 6-62, the secant stiffness k_{sec} decreases with increasing cyclic shear strain γ_{cyc}, consistent with the CSS tests (Section 6.3.5). The ascending two-way (RPCSS01) and one-way (RPCSS03) tests appear to overlie one another, while following a degradation path close to the backbone curve. At small constant amplitudes, RPCSS03 shows an increasing secant stiffness with number of cycles before dropping due to a change in parcel amplitude. For RPCSS02, the large cycles at the start of the history mean lower stiffnesses are observed, falling well below the other two tests. While stiffnesses increase as the cyclic amplitudes become smaller, they fail to reach the levels seen in the other two tests. This is probably attributable to the large deformations experienced by the sample at the start, revealing the importance of stress history.

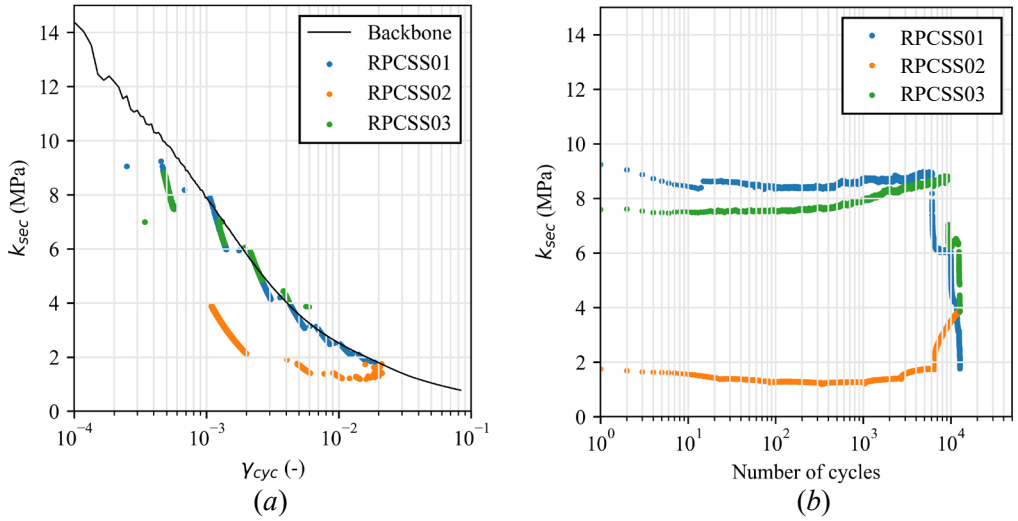


Figure 6-62: Stiffness degradation for RPCSS tests with (*a*) cyclic shear strain and (*b*) number of cycles

6.7 Challenge cyclic simple shear tests (CCSS)

The performance of a constitutive model (implementation discussed in Chapter 7) was evaluated using challenge tests; (a) a spiral type and (b) a figure-8 loop type test. The tests were not intended for calibration, but to assess how well the model captures multidirectional loading. Therefore, only the strain path outputs are presented in this section for clarity.

6.7.1 Test programme

The loadings for each axis and the resulting load paths are illustrated in Figure 6-63. The spiral loads show the stresses increasing at a constant rate, with the resultant loading direction moving through 360° per cycle. A total of five cycles were applied up to CSR = 0.6. The figure-8 loop test involves a stress history with different constant load amplitudes (CSR = 0.4 and 0.6) and offset at different frequencies (f = 0.1 and 0.2 Hz) in the x and y directions. A summary of the cyclic loading parameters is given in Table 6-12.

Table 6-12: CCSS test schedule

No.	Test ID	ASR_x (-)	CSR_x (-)	ASR_y (-)	CSR_y (-)	Time (s)	Notes
1	CCSS01	0	0.6	0	0.6	50	Spiral
2	CCSS02	0	0.6	0	0.4	1000	Figure-8

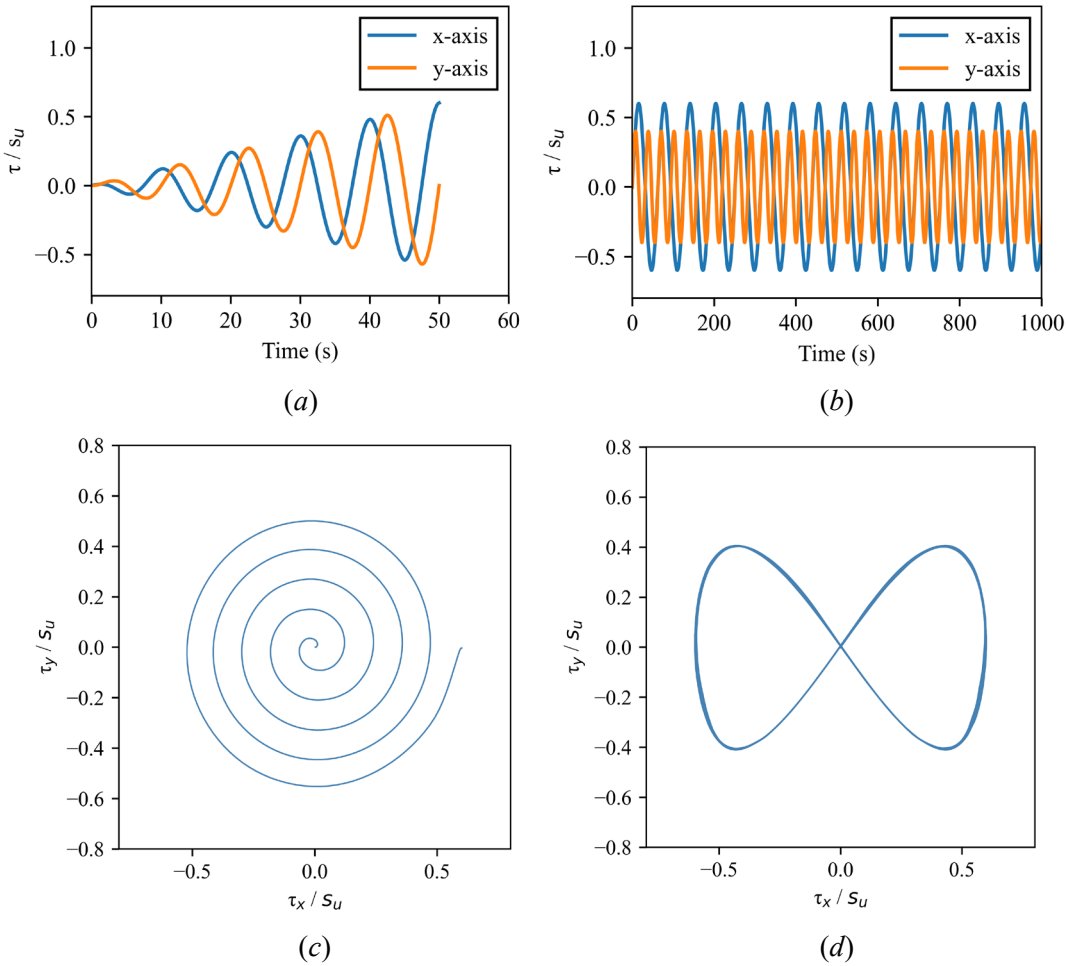
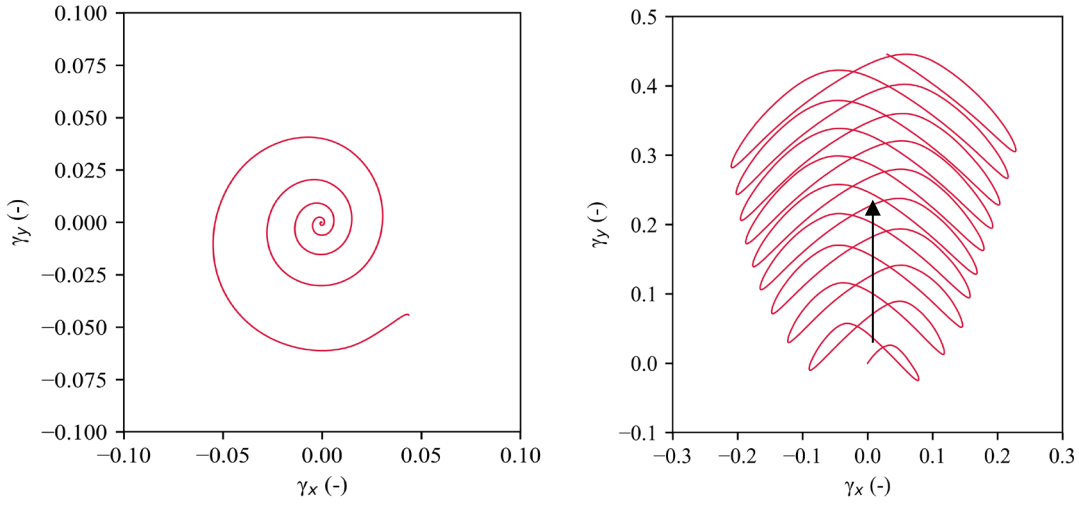


Figure 6-63: Stress history for (*a*) + (*c*) spiral loading and (*b*) + (*d*) figure-8 loop

6.7.2 Test schedule results

Qualitatively, the strain response traces a similar path to the input stress histories as shown in Figure 6-64. For the spiral loop, the response seems identical in both directions, indicating a homogenous sample. For the figure-8 loop in Figure 6-64(b), ratcheting behaviour is observed in the *y*-direction, which agrees with the previous ratcheting behaviours observed in the PCSS and RPCSS tests, where ratcheting occurs in the direction of the applied mean load (Kammerer et al., 2002; Rutherford, 2012). Unlike the spiral response, the figure-8 loop reaches high shear strains more quickly, which is expected considering the repeated loadings at $CSR_x = 0.6$. Nonetheless, the test was prematurely stopped at $\gamma_y = 0.45$ as it was close to reaching the limit of the VDDCSS device.



(*a*) (*b*)

Figure 6-64: Shear strain response for (*a*) spiral loading and (*b*) figure-8 loop

6.8 Comparison of the VDDCSS tests with medium-scale field test results

6.8.1 Outline

As part of the PICASO project a programme of medium-scale field tests on laterally loaded monopiles was performed at the Cowden site (Byrne et al., 2020). Notably, the element test programme presented in Chapters 5 and 6 used material from the same location, thus allowing for direct comparison. One of the objectives of this research has been to investigate the mapping/scaling of cyclic behaviours from element scale to full-scale tests. The tests presented in this section compare some of the standard CSS tests carried out in the laboratory with those performed at medium-scale for PICASO, hereafter referred to as 'field' tests. The cyclic parameters investigated include the accumulation of strains with number of cycles (i.e. ratcheting), changes in stiffness (i.e. degradation/stiffening), and changes in energy loss factor. Most of these curves can be reasonably approximated using the exponential functions previously defined in Section 6.3, where:

$$\gamma_{av} = AN^m \text{ or } k_{sec} = BN^b$$

Here, the exponents m and b represent the rate of change for each of these parameters, which is essential in informing the calibration of soil constitutive models for cyclic loading (see Chapter 7). For the comparison, four PICASO tests are chosen, all with a common aspect ratio $L / D = 3$, as presented in Table 6-13. The full results and details of the medium-scale field tests can be found in Martin (2023). The monotonic lateral pile test (P02) is also provided for reference, with an initial stiffness measured as $k_{max} = 133$ MN/m. For this test, loads were applied incrementally and held until the ground-level displacement v_G exceeded $v_{G,0.1D} = 122$ mm. The monotonic test took approximately $T = 305$ minutes to complete before the final unloading stage corresponding to $v_G \approx 187$ mm. This gives an average displacement rate estimated to be $\dot{v}_G \approx 0.61$ mm/min. The horizontal load at $0.1D$ was measured to be $H_{0.1D} = 0.92H_{ult}$. The unidirectional cyclic loading field tests each consisted of three loading stages varying in ASR and CSR. Their parameters and positions within the stress contour space are presented in Figure 6-65, along with the equivalent CSS tests indicated by empty circles with matching colours.

Table 6-13: PICASO medium-scale lateral pile test parameters
Source: (Martin, 2023)

Pile name	Test type	L (m)	D (m)	h (m)	t (mm)	k_{max} (MN/m)
*P02	Monotonic	3.66	1.22	4.88	13	133
P04	One-way	3.66	1.22	4.88	13	89
P08	One-way	3.66	1.22	4.88	13	54
R12	Two-way	3.66	1.22	4.88	13	178

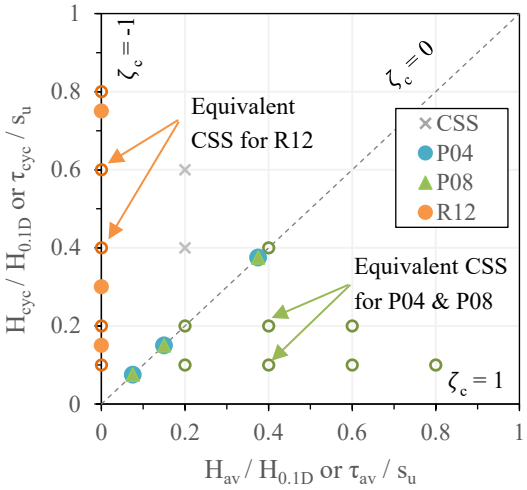


Figure 6-65: Location of PICASO cyclic tests

6.8.2 Ratcheting comparison

Previous attempts have been made to link laterally loaded pile tests to element tests (McClelland and Focht, 1958; Zhang and Andersen, 2017). While these authors mainly focused on monotonic loading, their findings required both data sets to be dimensionally consistent and normalised for comparison. Therefore, in this work the ground displacements v_G and shear strains γ were normalised by reference values v_{Gref} and γ_{ref}, respectively. It should be noted that the field tests are not necessarily normalised to failure, since defining 0.1D as failure is arbitrary. For this research, v_{Gref} and γ_{ref} are defined in Figure 6-66(a) and (b) respectively.

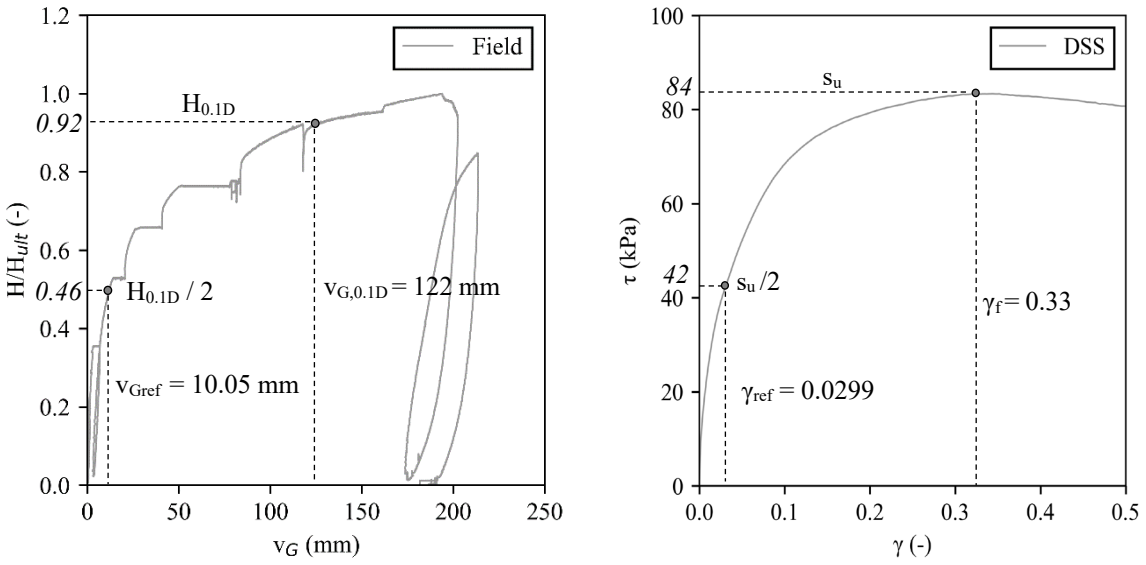


Figure 6-66: Normalisation of strains for (*a*) field tests and (*b*) laboratory DSS tests

Once normalised, the strain outputs from the two different datasets can be compared, as shown in Figure 6-67. While the accumulation of strain (denoted by exponent m) increases with ζ_b for both datasets, the rates of increase are different, as observed by the linear fit (e.g. $m = w\zeta_b$) in Figure 6-68. The field tests demonstrate an exponent m 4.3 times higher than the CSS tests. While both groups show a similar response, the discrepancies probably result from two sources: (a) the dimensional difference in soil masses involved and (b) the differences in the system of loading (McClelland and Focht, 1958). As a result, the factor

needed to transpose a CSS test curve to a field test curve is more complex than anticipated. While the factor is probably dependent on the soil characteristics, a global scaling factor encompassing all behaviours (e.g. soil type, pile dimensions and loading conditions) will need to be applied. Furthermore, the factor that has been derived does not permit direct determination of the strain accumulation across the depth of a pile in a given soil condition. Instead, it provides a means by which CSS data, applicable to a given soil depth, can be converted to pile deflection or stiffness data (next section) at a specific depth. Realistically, a similar set of CSS tests would be needed across the corresponding length to fully scale the ratcheting or stiffness behaviour along the pile length.

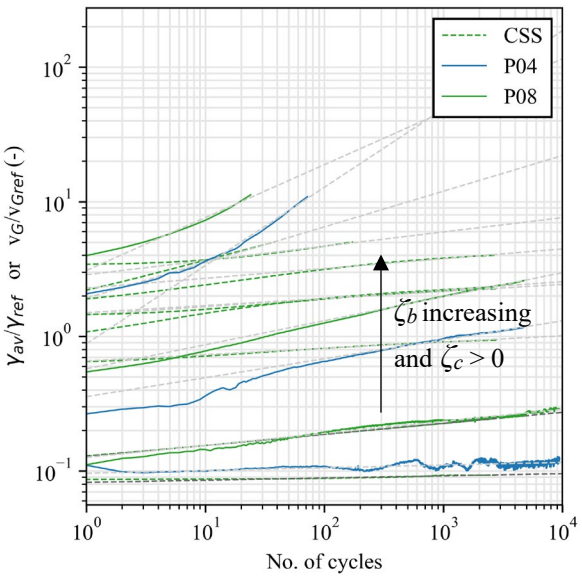


Figure 6-67: Normalised strain with number of cycles

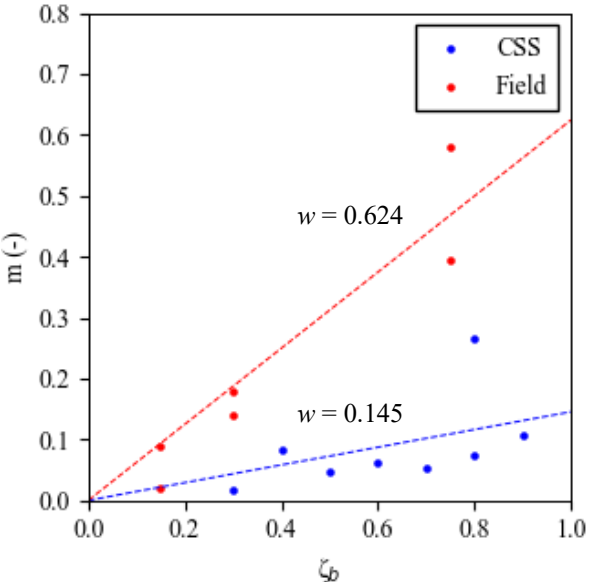


Figure 6-68: Slope of ratcheting rate with ζ_b

6.8.3 Stiffness degradation comparison

The secant hysteresis loop stiffnesses k_{sec} for both datasets were normalised using G_0 for CSS and k_{max} for the field tests. Here, k_{sec} refers to $\Delta\tau_n/\Delta\gamma_n$ for the former and $\Delta H_n/\Delta v_{G,n}$ for the latter. Again, only two-way cyclic tests were used, which show a decrease in stiffness with number of cycles (i.e. degradation). Like the ratcheting behaviour, a correlation was observed between the stiffness degradation rate and ζ_b. Here, the CSS tests degrade at a higher rate than the field tests by a factor of 1.92.

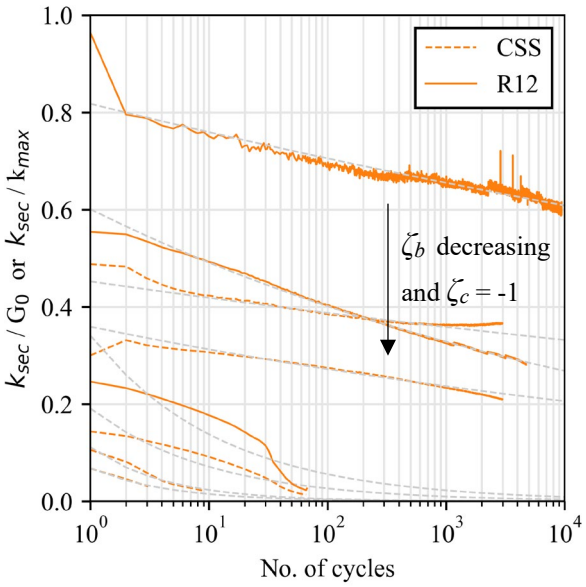


Figure 6-69: Normalised stiffness with number of cycles

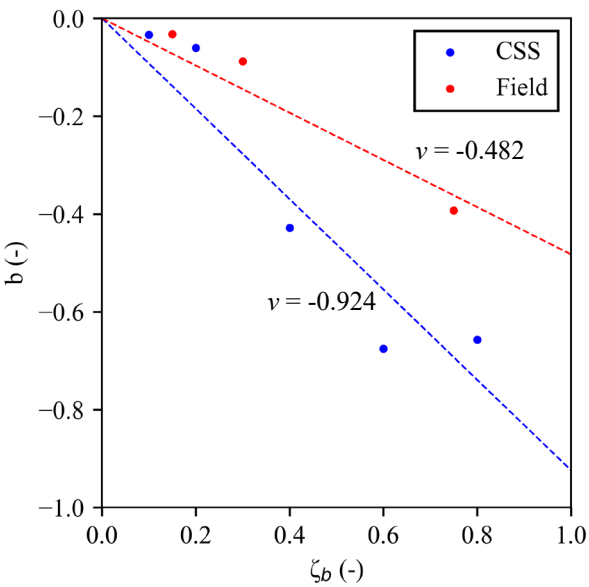


Figure 6-70: Stiffness degradation rate with ζ_b

6.8.4 Energy loss comparison

The change in energy loss factor with number of cycles is shown in Figure 6-71. Unlike ratcheting or stiffness degradation, a dependency on ζ_b is not as apparent. Instead, both CSS and field tests show a general downward trend before plateauing at 10^2 cycles. Furthermore, the energy loss generally increases with cycle amplitude.

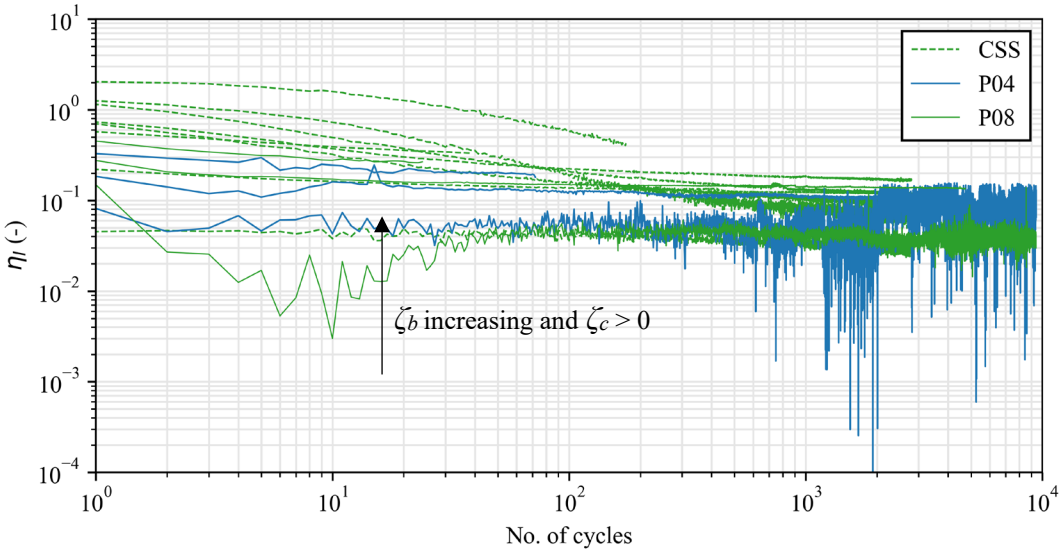


Figure 6-71: Energy loss factor with number of cycles

6.8.5 Random loading tests

Following the RCSS tests discussed in Section 6.5, identical load histories were used for the pile tests (performed before the RCSS testing) but at different magnitudes. For each of the six load stages, they were scaled up to [0.2, 0.2, 0.4, 0.4, 0.6, 0.4] of s_u for the RCSS tests and [0.15, 0.15, 0.3, 0.3, 0.75, 0.3] of H_{ult} for the field tests. The magnitude of the RCSS tests were different as these were based on the CSS tests to ensure the specimens would not prematurely fail due to excessive loading. Regardless of these magnitudes, the underlying behaviour is expected to be quite similar on a qualitative level. Comparisons were made by normalising the relevant strains and stiffnesses, similar to the normalisation procedures used for the ratcheting and stiffness degradation in Section 6.8.2 and 6.8.3, respectively.

Table 6-14: PICASO medium-scale lateral pile test parameters
Source: (Martin, 2023)

Pile name	Test type	L (m)	D (m)	h (m)	t (mm)	k_{max} (MN/m)
P10	Random two-way	7.5	2.5	10	36	413
P11	Random one-way	7.5	2.5	10	36	333
P09	Random two-way (multidirectional)	7.5	2.5	10	36	272

For the random amplitude tests, similar behaviour is observed compared to the PCSS tests. Here, the strain accumulated is higher for the one-way over the two-way test, as seen in both cases (Figure 6-72 (a) and (b)). Interestingly, a similar drop in strain after the fifth loading stage (i.e. the large storm event) is also noted, supporting the rate effect and change in pore pressure argument raised previously in Section 6.5. However, the number of cycles across the two scales does not completely match, as the medium-scale field test data was processed differently with cycles considered as noise filtered out. The details of the filtering process for the field tests are covered by Martin (2023).

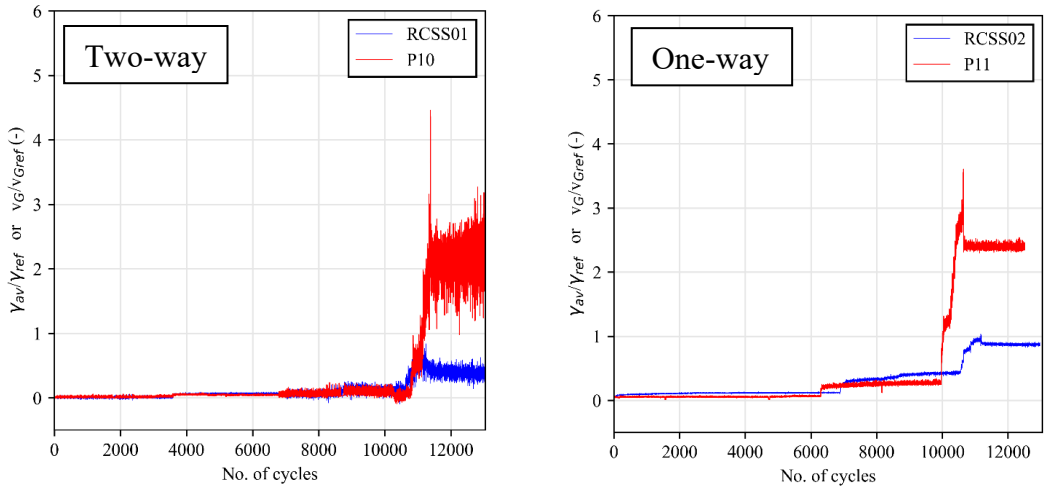


Figure 6-72: Accumulation of strains with number of cycles for (*a*) two-way and (*b*) one-way tests

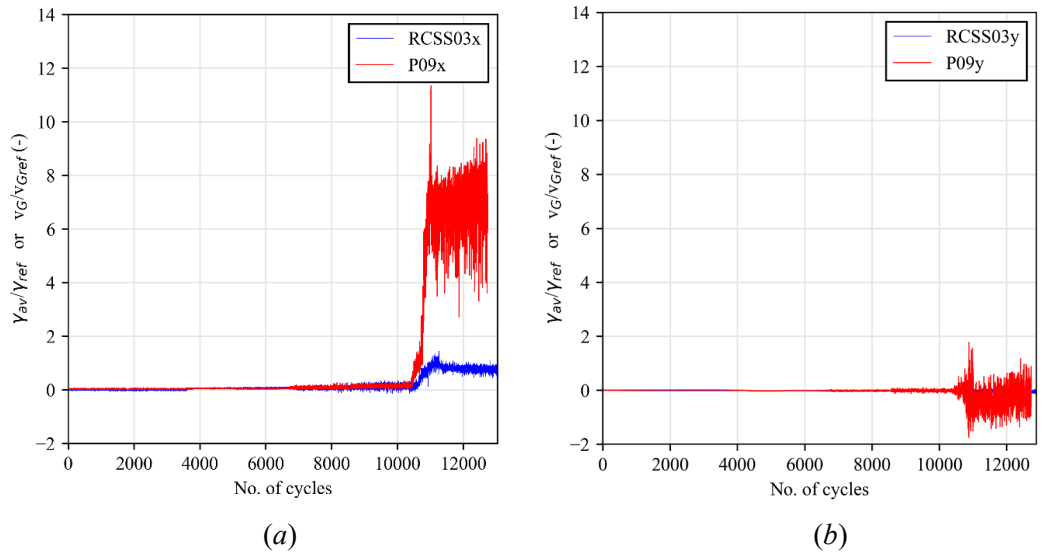
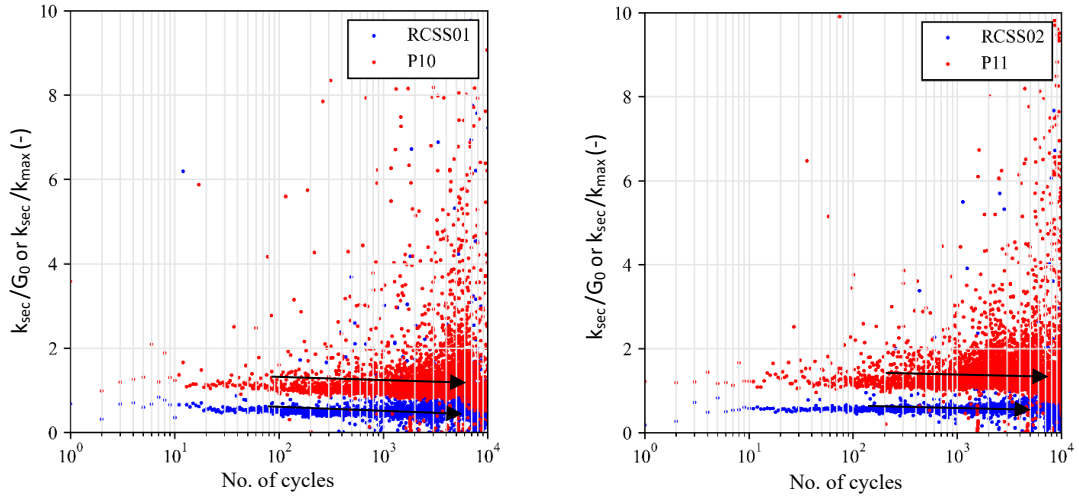


Figure 6-73: Accumulation of strains with number of cycles for multidirectional loading in (*a*) *x*-axis and (*b*) *y*-axis

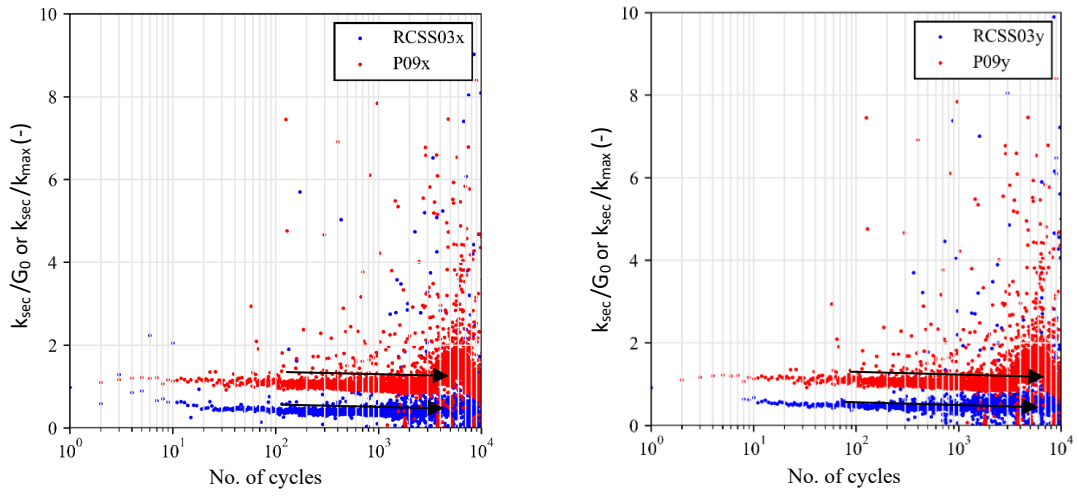
For the first few loading stages, the normalisation procedure appears adequate with similar increases in accumulated strain. However, once the larger cyclic packages were introduced, the field tests accumulated strain much faster. This is expected since the field tests apply a larger normalised load (e.g. stage 5- RCSS: CSR = 0.6 and field test: CSR = 0.75) leading to larger strains. The final strain discrepancy between the field and lab tests is a factor of 5 (= 1.71/0.341) for the two-way test and 2.7 (= 2.398/0.876) for the one-way test, bounding the factor of 4.3 measured from the ratcheting comparison in Section 6.8.2.

For the evolution of stiffnesses, a comparison is made across the two scales as given in Figure 6-74 and Figure 6-75. For all three comparisons, the field tests plot higher than the laboratory tests, which is not surprising considering the normalisation parameters, where G_0 from the CSS tests is likely to be higher than the k_{max} from the field tests as the presumed linear elastic range in the laboratory element tests is evaluated over a smaller scale and with higher fidelity. Nonetheless, the different scales agree well, with comparable downward trends despite the scatter.



(*a*) (*b*)

Figure 6-74: Degradation of stiffness with number of cycles for (*a*) two-way and (*b*) one-way tests



(a) (*b*)

Figure 6-75: Degradation of stiffness with number of cycles for multidirectional loading in (*a*) *x*-axis and (*b*) *y*-axis

6.8.6 Scaling potential

The findings in this section show a tentative relationship between the cyclic behaviours observed at element level and those observed in medium-scale pile tests. However, direct scaling of the rates of change for ratcheting and stiffness degradation with number of cycles is not yet possible as they differ in magnitude and may require a soil-specific conversion to be applied. Furthermore, several physical properties of the pile have been ignored, such as its material type and dimensions, accounting for pile stability. To fully capture the cyclic behaviour of the pile, several element tests would be needed along the length of the pile, as the behaviours for ratcheting, stiffness evolution, and energy loss may vary. To this extent, the constants that have been determined are currently only applicable to ground-level predictions for piles installed at the Cowden site.

6.9 Summary

The chapter has explored the effect of cyclic loading on Cowden till. The material was subjected to complex loadings, from simple unidirectional to more complex random amplitude tests. From the CSS tests, the behaviours can be divided into distinct groups, those that experience pure stiffness degradation (i.e. two-way), some that experience pure ratcheting (i.e. one-way or partial one-way), and those which show a combination of both (i.e. partial two-way). As a result, the ASR and CSR significantly influence the behaviour of the cycles, including the stiffness, where a stiffening type of behaviour is observed for high ASR and low CSR. In contrast, the opposite is seen for low ASR and high CSR.

The batch one and two PCSS tests show that ratcheting occurs in the direction of the mean load and the magnitude of the mean load influences the overall strain accumulation. The stiffness degradation behaviour follows the behaviour of the CSS tests, where either a degradation or stiffening response is recorded depending on the loading characteristics. The RCSS tests show a large increase in permanent strains corresponding to the large cyclic events within the loading history. Furthermore, larger permanent strains are recorded for the

multidirectional loading tests, suggesting that the out-of-plane load also influences the overall accumulated strain. The RPCSS tests were used to investigate the impact of converting the RCSS loads into idealised load histories. The parcel arrangement in ascending order gives comparable values of accumulated strain and stiffness degradation compared to the RCSS tests. For the descending order variation, much lower values are measured.

The research also evaluates cyclic loading behaviour across different scales (i.e. laboratory element tests to field pile tests). There is a link between these two scales, and this is investigated further in Chapter 7 when evaluating the cyclic parameters for the soil constitutive model.

Chapter 7

Soil constitutive modelling

7.1 Introduction

Constitutive models describing the stress-strain response of soils are widely used in the design of OWT foundations. Some models, of higher level of complexity, are able to predict key cyclic loading characteristics commonly observed in cyclic element testing of cohesive soils. In this chapter, a new model, consisting of a rate-dependent bi-directional multi-surface kinematic hardening model, formulated in the Hyperplasticity framework (Bi-MSHYP), is implemented following the formulation described in Chapter 2. The model is of the *g-w* type formulation (see Section 2.4.2) and arranged in a parallel configuration only (i.e. series configuration is not explored). The road map of the model implementation is highlighted in Figure 7-1, covering the relevant sections and their contribution.

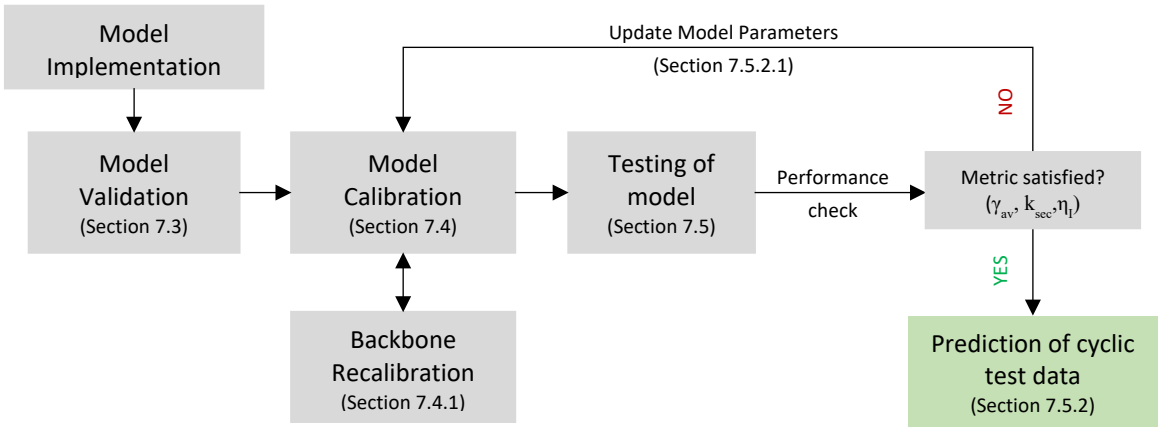


Figure 7-1: Road map of Bi-MSHYP model implementation

Following model implementation and validation (i.e. checking model against a similar model implemented by Balaam (2021)), the model is calibrated using unidirectional constant amplitude cyclic (CSS) tests. This stage requires the recalibration of the monotonic backbone while calibrating for each of the different additional mechanisms (i.e. rate effects, softening and ratcheting). Once calibrated, the model is then tested against more complex cyclic tests (e.g. PCSS tests from Section 6.4). If it fails to meet the performance metrics, the model parameters are updated and recalibrated using the complex cyclic tests (i.e. Section 7.5.2.1: model calibration using PCSS tests). Once performance is acceptable, the model is used to make final predictions of the experimental tests from Section 6.5 to 6.7.

7.2 Numerical implementation

The selected soil constitutive model has been implemented as a single element model in Python. The model requires the constitutive equations to be solved using an appropriate integration scheme. This involved integrating the constitutive relations over a finite strain increment $\Delta\varepsilon$ to determine the updated stress state σ. A stress point algorithm approach was used to determine the updated strain state. The approach can have either an implicit or explicit integration scheme. An example of the latter, and preferred approach, includes a scheme with automatic sub-stepping and error control, adopted by many (Sloan, 1987; Sloan et al., 2001; Seidalinov, 2018; Whyte, 2020) and found to yield more accurate results than an implicit scheme, as pointed out by Potts and Ganendra (1994). The scheme integrates the constitutive equation by dividing strain increments into smaller sub-increments (i.e. substeps). To ensure the model is implemented in a consistent environment, the Modified Euler integration scheme was used.

The Bi-MSHYP model was implemented in Python with an automated sub-stepping scheme. With each increment, smaller strain steps are required to achieve convergence. However, the smaller the steps, the greater the computational effort required. For this research, increments were split into a 1000 substeps to maintain accuracy and efficiency.

7.3 Validation of model

The Bi-MSHYP model detailed in Chapter 2 (Section 2.4) was implemented and benchmarked against a similar model produced by Balaam (2021) for Cowden till. The constitutive equations and required derivations for the rate-dependent multi-surface multi-axial kinematic hardening model are presented in Table 7-1. A visual representation of the model can be found in Figure 2-16(c), where a set of springs (k_n) and sliders (H_n) are arranged in a parallel configuration.

Table 7-1: Constitutive relations for Bi-MSHYP model

Governing equation	Eqn.
Energy Function:	
$$g = -\frac{1}{2E_0}\left(\left(\sigma_x + \sum_{n=1}^{N_s} H_n\alpha_{nx}\right)^2 + \left(\sigma_y + \sum_{n=1}^{N_s} H_n\alpha_{ny}\right)^2\right)$$ $$-\sigma_x\alpha_{rx} - \sigma_y\alpha_{ry} + \sum_{n=1}^{N_s}\frac{H_n}{2}\left(\alpha_{nx}^2 + \alpha_{ny}^2\right)$$	(7-1)
Constitutive behaviour:	
$$\varepsilon_x = -\frac{\partial g}{\partial \sigma_x} = \frac{\sigma_x + \sum_{n=1}^{N_s} H_n\alpha_{nx}}{E_0} + \alpha_{rx} \qquad \varepsilon_y = -\frac{\partial g}{\partial \sigma_y} = \frac{\sigma_y + \sum_{n=1}^{N_s} H_n\alpha_{ny}}{E_0} + \alpha_{ry}$$	(7-2)
$$\bar{\chi}_{nx} = -\frac{\partial g}{\partial \alpha_{nx}} = H_n\left(\frac{\sigma_x + \sum_{n=1}^{N_s} H_n\alpha_{nx}}{E_0}\right) - H_n\alpha_{nx} = H_n(\varepsilon_x - \alpha_{nx} - \alpha_{rx})$$ $$\bar{\chi}_{ny} = -\frac{\partial g}{\partial \alpha_{ny}} = H_n\left(\frac{\sigma_y + \sum_{n=1}^{N_s} H_n\alpha_{ny}}{E_0}\right) - H_n\alpha_{ny} = H_n(\varepsilon_y - \alpha_{ny} - \alpha_{ry})$$	(7-3)
$$\bar{\chi}_n = \sqrt{\bar{\chi}_{nx}{}^2 + \bar{\chi}_{ny}{}^2}$$	
$$\bar{\chi}_{rx} = -\frac{\partial g}{\partial \alpha_{rx}} = \sigma_x \qquad \bar{\chi}_{ry} = -\frac{\partial g}{\partial \alpha_{ry}} = \sigma_y$$	(7-4)
$$\bar{\chi}_r = \sqrt{\bar{\chi}_{rx}{}^2 + \bar{\chi}_{ry}{}^2} = \sqrt{\sigma_x{}^2 + \sigma_y{}^2} = \sigma_n$$	(7-5)
Flow potential:	
$$w = \sum_{n=1}^{N_s}\frac{k_n\eta}{t_{ref}}\left(\cosh\left(\frac{\langle|\chi_n| - k_n + R_n(|\chi_r| - |\sigma_n|)\rangle}{k_n\eta}\right) - 1\right)$$	(7-6)
$$d\alpha_{nx} = \frac{\partial w}{\partial \chi_{nx}}dt = \frac{\left(\frac{\chi_{nx}}{\chi_n}\right)}{t_{ref}}\sinh\left(\frac{\langle|\chi_n| - k_n + R_n(|\chi_r| - |\sigma_n|)\rangle}{k_n\eta}\right)$$ $$d\alpha_{ny} = \frac{\partial w}{\partial \chi_{ny}}dt = \frac{\left(\frac{\chi_{ny}}{\chi_n}\right)}{t_{ref}}\sinh\left(\frac{\langle|\chi_n| - k_n + R_n(|\chi_r| - |\sigma_n|)\rangle}{k_n\eta}\right)$$	(7-7)

Notes:

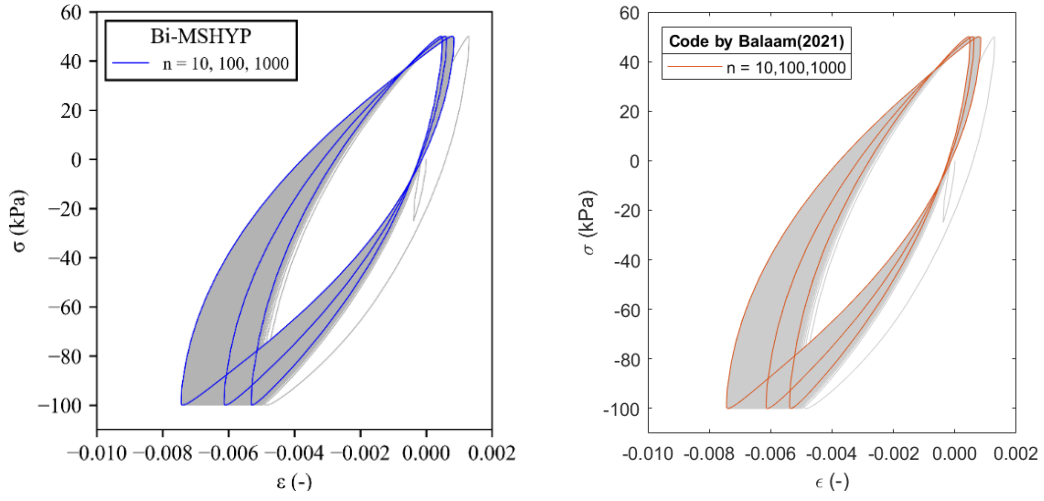
E_0	=	Initial stiffness: Stiffness based on bender element or resonant column tests
$\bar{\chi}_n$	=	Normalised generalised stress
α	=	Internal strain variable, where α_r relates to the ratcheting strain
t_{ref}	=	Reference time to failure for a slow experimental test
R	=	Ratcheting constant
η	=	Viscous constant: Defined as the increase in strength per log strain rate (η_{10}=ln(10)η)

The monotonic, rate effect, and softening parameters used by Balaam (2021) to model Cowden till triaxial compression tests at 0D are given in Table 7-2. The ratcheting mechanism parameters were included in the validation (i.e. model in Balaam (2021) for parallel configuration did not include ratcheting mechanism), and the softening refers to a soil sample's stiffness degradation when $F_\kappa = 1$, both discussed further in Section 7.4.1.

Table 7-2: Parameters used for model validation

Monotonic				**Rate**		**Softening**				**Ratcheting**				
Eq. (7-8)				Eq. (7-7)		Eq. (7-14) and (7-15)				Eq. (7-18)				
ε_f (-)	s_u (kPa)	E_0 (MPa)	α (-)	t_{ref} (hrs)	η_{10} (-)	F_κ (-)	κ_{ref} (-)	F_β (-)	m_k (-)	R_0 (-)	m_s (-)	m_r (-)	R_{ref} (-)	$F_{\beta,R}$ (-)
0.15	125	250	2.11	1000	0.1	1	0.7	20	0.1	0.01	5	2	0.007	65

The implementation using the given parameters allowed a simulation of a load path following one of the triaxial cyclic compression tests (q_{av} = -25 kPa and q_{cyc} = 75 kPa) performed for PISA (Ushev, 2017; Balaam, 2021). The results are plotted in Figure 7-2, indicating good agreement between the multiaxial model implemented for this research and the one by Balaam (2021). The reference plots were reproduced using MATLAB code provided by Balaam (2021). The addition of rate effects, softening and ratcheting mechanisms, requires the monotonic backbone to be recalibrated, as described in Section 7.4.1. For simplicity, the recalibration process was not used in the bench-marked prediction.



(*a*) (*b*)

Figure 7-2: Stress-strain response for (*a*) Bi-MSHYP model [*Python*] and (*b*) model implemented by Balaam (2021) [*MATLAB*]

7.4 Calibration of model

7.4.1 Calibration procedure

Monotonic response:

The monotonic behaviour can be captured by multiple linear surfaces of varying stiffness (H_n) and yield strength (k_n) as reviewed in Section 2.4. These parameters can be found by either deriving them directly from monotonic data or by fitting an expression to the data and extracting the values at selected points. Both approaches were attempted but the former, referred to as the data-driven approach, had shortcomings related to the quality of the data, making calibration difficult. Sparse data points meant only a limited number of surfaces can be selected, which leads to an inadequate capturing of the non-linear response. If a higher quality dataset were used, the method would be more robust. However, it would be difficult for other users to reproduce the plots in this research if a data-driven approach was followed. As a result, calibration using a fitted function was preferred.

Fitting an expression to the monotonic curve allows for a more straightforward calibration process, since the curve's optimal parameters can be found using a least-squares regression method. The main drawback lies with the overall fit, where the curve may fit the test data better in certain areas compared to others, depending on the weighting and quality of the data. However, the method eliminates noise in the data and ensures H_n and k_n are well defined.

For all monotonic tests, a higher sampling frequency was implemented at the start (i.e. small strain range) up to $\gamma = 0.1$ before reverting to a lower sampling rate for the rest of the test. This allowed the fitted function, a hyperbolic tangent function referred to as the Jeanjean equation (Jeanjean et al., 2017), to capture the behaviour well at both small and large strain ranges. Furthermore, the backbone was limited to $N_s = 40$ surfaces following Section 2.4.2. Each surface was evenly distributed along the y-axis as shown by the targeted backbone points in Figure 7-3(a) to better capture the shape of the backbone. The initial

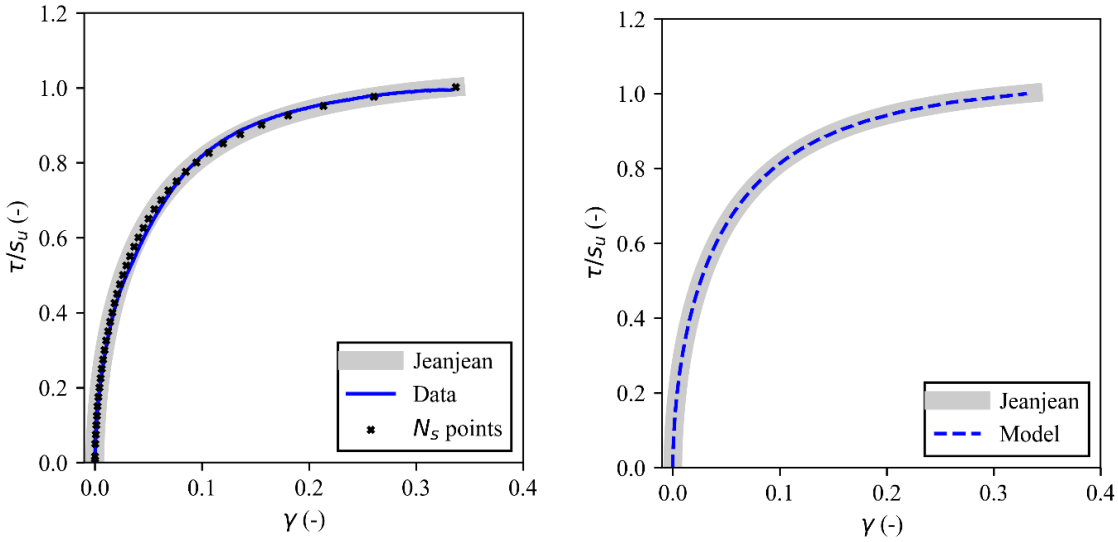
point for N_s =1 was also adjusted to account for a more accurate initial stiffness G_0 (Balaam, 2021). The implemented Jeanjean equation is described in the shear stress τ – shear strain γ space as:

$$\frac{\tau}{s_u} = \frac{\tanh\left(a\left(\frac{\gamma - \frac{\tau}{G_0}}{\gamma_f - \frac{s_u}{G_0}}\right)^{0.5}\right)}{\tanh(a)} \tag{7-8}$$

Here, parameters G_0 (E_0 = for triaxial), s_u, and γ_f (ε_f = for triaxial) are fixed and can be obtained from the reference monotonic DSS tests (CWD_BS_DSS_CU_OL35 and CWD_BS_DSS_CU_OL35a combined), and a is the optimised curvature parameter. The derived backbone parameters are as follows:

Table 7-3: Derived backbone parameters

γ_f (-)	s_u (kPa)	N_s (-)	G_0 (MPa)	α (-)
0.33	84	40	250	1.95



(*a*) (*b*)

Figure 7-3: (*a*) Discretisation of experimental backbone and Jeanjean function fit, and (*b*) Backbone model prediction

Rate effects:

The introduction of rate effects requires the backbone to be recalibrated such that surface strengths (k_n) and stiffnesses (H_n) are derived from the response at a shear strain rate $\dot{\gamma} \to 0$.

In addition to the recalibration of the backbone due to rate effects, the selection of parameters for softening and ratcheting alters the calibrated backbone response as soon as plastic strains develop. The recalibration procedure initially adopted a function fit approach using the Jeanjean function, and a curve-fit optimisation scheme (e.g. Scipy package in Python). However, this was found to be inefficient due to the number of iterations required. An improved approach was developed, leading to significant reductions in computational time, as highlighted in Appendix A (Crispin et al., 2022). Rate Process Theory (RPT) sets out that:

$$k_{d,n} = k_n \left(1 + \eta \, sinh^{-1}\left(\frac{\dot{\varepsilon}}{\dot{\alpha}_{qs}}\right)\right) \tag{7-9}$$

Where η is the viscous constant and k_n asymptotically approaches a strength $k_{d,n}$, which is a function of the strain rate $\dot{\varepsilon}(=\dot{\gamma})$. As a result, $\bar{k}_n$ must be selected such that $k_{d,n} = k_n$. Once rate-dependency is introduced into the model, the amount of change for each spring and slider can be computed using the equation:

$$\bar{k}_n = \frac{H_n \varepsilon_n}{1 + \eta \, sinh^{-1}\left(\frac{\dot{\varepsilon}}{\dot{\alpha}_{qs}}\right)} \tag{7-10}$$

This is observed in Figure 7-4, showing the original and recalibrated response.

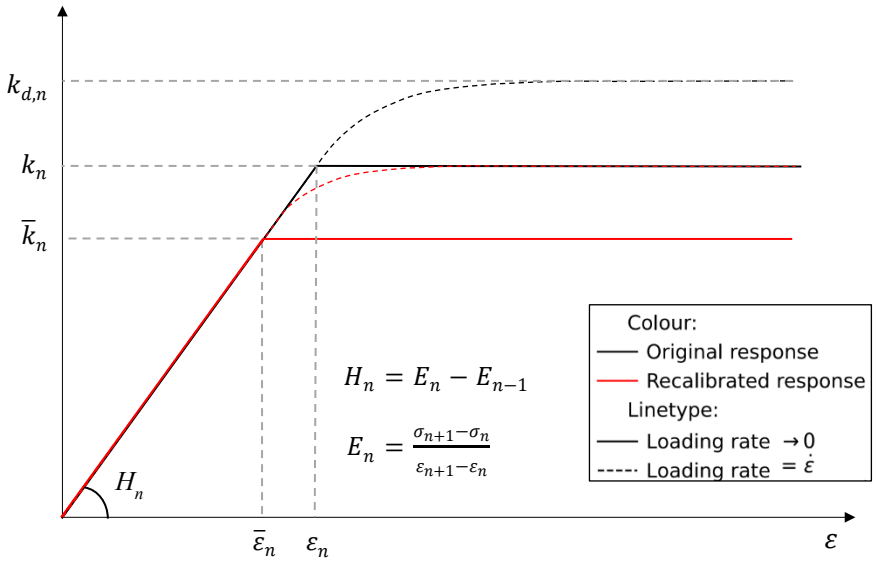


Figure 7-4: Recalibration of backbone for rate effects

The recalibration function is significantly faster than the function optimisation approach. However, one drawback is that the calibration can only be done using strain control for a constant rate test. Conversely, the optimisation of the Jeanjean function allows for both stress and strain control (Balaam, 2021).

Softening:

The softening behaviour is calibrated against cyclic tests, where $\zeta_b \neq 0$ and $\zeta_c = 0$. This follows the proposed stiffening or hardening model suggested by Abadie (2015) and Beuckelaers (2017), where the strength of each yield surface changes as a function of the hardening parameter β and is expressed in terms of κ such that:

$$\kappa = \frac{k_{sec}}{k_{sec,0}} = f(\beta) \tag{7-11}$$

where k_{sec} is the secant stiffness of a cycle. Since the model is intended to predict clay behaviour, the surfaces are likely to soften, where $f(\beta) < 1$, causing yield strengths and the secant stiffness to decrease. To capture the change in secant stiffness k_{sec} under cyclic loading, the relationship between κ and k_{sec} is explored, where the decrease in k_{sec} for a given κ can be approximated using the analytical Jeanjean expression:

$$\frac{k_{sec,\kappa}}{k_{sec,0}} = \frac{\varepsilon_{cyc,\kappa}}{\varepsilon_{cyc,0}} = \frac{2\left(\varepsilon_f - \frac{\sigma_u}{E_0}\right)\left(\frac{atanh\left(\left(\frac{\sigma_{cyc}}{2\sigma_u}\right)tanh(\alpha)\right)}{\alpha}\right)^2 + \frac{\sigma_{cyc}}{E_0}}{2\kappa\left(\varepsilon_f - \frac{\sigma_u}{E_0}\right)\left(\frac{atanh\left(\left(\frac{\sigma_{cyc}}{2\kappa\sigma_u}\right)tanh(\alpha)\right)}{\alpha}\right)^2 + \frac{\sigma_{cyc}}{E_0}} \tag{7-12}$$

where $\varepsilon_{cyc} = \gamma_{cyc}$, $\sigma_u = s_u$, $\varepsilon_f = \gamma_f$, $E_0 = G_0$, and $\sigma_{cyc} = \tau_{cyc}$. Richards (2019) and Balaam (2021) used a modified power law function to predict the softening behaviour as a function of the hardening parameter β, which can take the form of either strain or work-type quantities, for example – strain: $\dot{\beta} = \sum|\dot{\alpha}_n|$ and work: $\dot{\beta} = \sum k_n|\dot{\alpha}_n|$. However, a work-type quantity is preferred here as this allows for the evolution functions and parameters to be comparable

between series and parallel model configurations. Furthermore, the hardening parameter is chosen to evolve with plastic strain α_n, rather than the ratcheting strain α_r as implemented by Abadie (2015) and Beuckelaers (2017). The latter causes difficulties with calibration where softening and ratcheting are coupled. In the model, there is also an option to either locally soften the surfaces $f(\beta_n)$ or soften all surfaces equally $f(\beta_G)$, which is controlled by the switch parameter F_κ:

$$\kappa = \frac{k_{sec}}{k_{sec,0}} = \kappa_L^{F_\kappa} \kappa_G^{1-F_\kappa} \tag{7-13}$$

To clarify, local softening (F_κ = 1) represents the stiffness degradation experienced by a sample with cycle number while global softening (F_κ = 0) refers to the reduction in strength of the monotonic backbone curve. In this work, local softening is chosen (F_κ = 1), ensuring minimal post-cyclic softening as indicated by the cyclic test data (Sections 6.3.4 and 6.6.4). Furthermore, local softening assists with the decoupling of the ratcheting behaviour, allowing for a simpler calibration process. The suggested power law function for softening is of the form:

$$\kappa_L = \left[1 + \frac{\beta_n}{\beta_{ref}}\left(\kappa_{ref}^{-\frac{1}{m_k}} - 1\right)\right]^{-m_k} \quad : \quad \kappa_G = \left(1 + \frac{\beta_G}{\beta_{ref,G}}\left(\kappa_{ref}^{-\frac{1}{m_k}} - 1\right)\right)^{-m_k} \tag{7-14}$$

where m_k controls the rate of softening, comparable to the exponent b used in Section 6.3.5. β_{ref} and κ_{ref} correspond to a fixed point on the curve, which is used to pin the curve for a more convenient calibration process (see Figure 7-5). As a result, the choice of β_{ref} should reflect the magnitude of plastic strain on each surface such that:

$$\beta_{ref} = F_\beta \frac{k_{Ns}}{H_n} k_n \tag{7-15}$$

where F_β is the dimensionless factor for all surfaces, k_{Ns} / H_n is the plastic strain α_n expected on the surface, and k_n the surface yield strength, which ensures a work quantity. Here, F_β controls the translation of the function as illustrated in Figure 7-5.

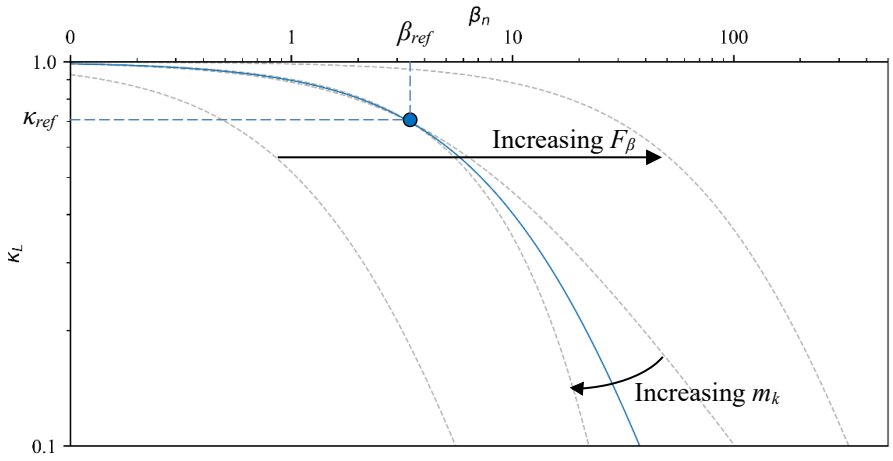


Figure 7-5: Calibration of softening function

The calibration process described here is different to the method followed by Balaam (2021), where a set of parameters, F_β and m_k, are optimised for the softening function using the 'pattern search' optimisation tool in MATLAB. In Section 6.3.5, a slope for the stiffness degradation rate m specific to the Cowden till material was determined. The softening rate was found to change with ζ_b, such that a set value of m_k does not adequately predict the change in softening across all stress levels. This contrasts with Balaam (2021) where a fixed m_k was found to be well suited for a range of soil conditions. Nonetheless, the softening function can easily be modified such that m_k is a function of stress level but this approach is not explored any further here.

Following the implementation of the model, no changes were made to the softening function, instead, the calibration was defined for tests over a mean range, where an average m of all two-way CSS tests was considered. This has limitations covered in Section 7.5 and is investigated further in the sensitivity study in Section 7.4.2. The addition of softening has the undesired side effect of changing the resulting backbone curve for the model. Like the rate effect calibration, a recalibration must be carried out to select a new set of springs k_n and sliders H_n to match the original backbone curve. Similar to the rate effect recalibration approach, the softening recalibration method follows the solution produced internally at Oxford by Crispin et al. (2022) and detailed in Appendix A. To fit a backbone curve with

known points $(\sigma_n, \varepsilon_n)$ or (τ_n, γ_n), the stress $\sigma_{ss,n}$ of the parallel spring-slider element at each point, absent the softening function, must be calculated. The final solution, in the form of an initial value problem, is given in Equation (7-16).

$$\frac{d\sigma_{ss}}{d\varepsilon} = \frac{E_n - \sum_{i=0}^{n-1} \frac{d\kappa_i(\varepsilon)}{d\varepsilon} k_{i,0} - E_{ss,n-1}\varepsilon_n \frac{d\kappa_n(\varepsilon)}{d\varepsilon} \frac{1}{\kappa_n(\varepsilon_n)}}{1 - \varepsilon_n \frac{d\kappa_n(\varepsilon)}{d\varepsilon} \frac{1}{\kappa_n(\varepsilon_n)}} \tag{7-16}$$

where $k_{i,0}$ is the initial slider strength (prior to softening), κ_i is the softening factor, and subscript n = [1, N_s]. The above equation is an effective approach, as it allows for the recalibration of the backbone in a single step. Furthermore, the method limits the amount of uncertainty introduced by users and their choice of optimisation.

Ratcheting:

The model up to this point can produce ratcheting-type behaviours due to creep (rate-dependency) and softening. However, the ratcheting movements are often underpredicted, so an additional ratcheting strain α_r is required (Abadie, 2015; Beuckelaers, 2017; Houlsby et al., 2017). The ratcheting strain is defined by:

$$\dot{\alpha}_r = S(\sigma) \sum_{n=1}^{N_s} R_n |\dot{\alpha}_n| = R \sum_{n=1}^{N_s} \frac{k_n}{\sigma_u} |\dot{\alpha}_n| \tag{7-17}$$

where S(σ) ensures the increment of α_r is in the same direction of the current load, therefore developing in the direction of the load bias, and $\sigma_u = s_u$. The added strain was found to be necessary, notwithstanding some predictions by Balaam (2021) demonstrating that softening alone in a rate-dependent model was able to capture the strain accumulation behaviour for Cowden till. The ratcheting function R controls the rate of ratcheting, which Richards (2019) and Balaam (2021) define as:

$$R = R_0 \left(1 + \frac{\sum \beta_n}{\beta_{ref,R}} \left(\left(\frac{R_0}{R_{ref} \left(\frac{|\sigma|}{\sigma_u} \right)^{m_s}} \right)^{\frac{1}{m_r}} - 1 \right) \right)^{-m_r} \tag{7-18}$$

where R_0 controls the magnitude of the function, m_r decreases R with the hardening parameter, and m_s increases R with current stress level. Additionally, similar to the softening relationship, $\beta_{ref,R}$ and R_{ref} act as a pin on the power-law relationship of R versus β. To ensure consistency, $\beta_{ref,R}$ is formulated as a factor of the expected β, similar to the softening approach, strain: $\beta_{ref,R} = F_{\beta,R}\frac{2A}{k_{N_s}}$ and work: $\beta_{ref,R} = F_{\beta,R}2A$.

The work-type quantity is preferred as it ensures models are consistent for both series and parallel configurations. Here, A is the area beneath the backbone curve and $F_{\beta,R}$ is a dimensionless parameter. Furthermore, β_n now becomes a work-type quantity allowing the evolution functions to be comparable across series and parallel configurations. The ratcheting behaviour is dependent on the hardening, the stress level and the plastic strain or work $\Sigma\beta_n$, with the ratcheting and softening behaviours intrinsically coupled (Balaam, 2021). For example, as the secant stiffness reduces with the number of cycles, the plastic strain also increases. However, the impact of the coupling between ratcheting and softening can be reduced by opting for local softening ($F_\kappa = 1$).

For parameters R_0, m_s, m_r, and $F_{\beta,R}$, Richards (2019) suggests m_s could be provisionally derived from experimental exponents and fixing $R_0 = 1$ (see Section 6.3.3). The other parameters can be determined using an optimisation routine or by trial and error, minimising the difference between measured and modelled γ_{av} (i.e. ratcheting) or k_{sec} (i.e. softening). Like the softening procedure, the addition of ratcheting changes the original backbone response. If the changes in strain are known, the model can be corrected to fit the backbone, with the goal to match each point provided. The calibration solution for ratcheting alone is given below (detailed in Appendix A):

$$\frac{d\varepsilon_{ss}}{d\varepsilon} = \frac{1+R\frac{E_n\varepsilon_{ss,n}}{\sigma_u}}{1+R\sum_{i=1}^{n-1}\frac{k_i}{\sigma_u}+R\frac{E_{ss,n-1}\varepsilon_{ss,n}}{\sigma_u}} \tag{7-19}$$

To further simplify the calibration procedure, the ratcheting correction was combined with the softening correction for the spring slider, given as:

$$\frac{d\varepsilon_{ss}}{d\varepsilon} = \frac{1 + \dfrac{R\dfrac{E_n}{\sigma_u}}{\dfrac{\kappa_n(\varepsilon_n)}{\varepsilon_{ss,n}} + \dfrac{d\kappa_n(\varepsilon_{ss})}{d\varepsilon_{ss}}}}{1 + R\displaystyle\sum_{i=1}^{n-1} \frac{k_{i,0}}{\sigma_u}\left[1 - \dfrac{\dfrac{d\kappa_i(\varepsilon_{ss})}{d\varepsilon_{ss}}}{\dfrac{\kappa_n(\varepsilon_n)}{\varepsilon_{ss,n}} + \dfrac{d\kappa_n(\varepsilon_{ss})}{d\varepsilon_{ss}}}\right] + \dfrac{R\dfrac{E_{ss,n-1}}{\sigma_u}}{\dfrac{\kappa_n(\varepsilon_n)}{\varepsilon_{ss,n}} + \dfrac{d\kappa_n(\varepsilon_{ss})}{d\varepsilon_{ss}}}} \tag{7-20}$$

The function is solved using the Runga-Kutta method to obtain $\varepsilon_{ss,j+1}$. Then following Equation (7-16), and replacing ε with ε_{ss}, σ_{ss} can be related to ε_{ss} by:

$$\frac{d\sigma_{ss}}{d\varepsilon_{ss}} = \frac{E_{\varepsilon ss,n} - \displaystyle\sum_{i=0}^{n-1} \frac{d\kappa_i(\varepsilon_{ss})}{d\varepsilon_{ss}} k_{i,0} - \dfrac{E_{ss,n-1}\varepsilon_{ss,n}}{\kappa_n(\varepsilon_n)} \dfrac{d\kappa_n(\varepsilon_{ss})}{d\varepsilon_{ss}}}{1 - \dfrac{\varepsilon_{ss,n}}{\kappa_n(\varepsilon_n)} \dfrac{d\kappa_n(\varepsilon_{ss})}{d\varepsilon_{ss}}} \tag{7-21}$$

The strain accumulation behaviour is calibrated against cyclic tests where $\zeta_c > 0$. To visualise the changes in the backbone due to the softening or ratcheting mechanism, a simplified illustration is given in Figure 7-6. The backbone is translated to the left to account for ratcheting moving the backbone to the right or shifted upwards to account for softening moving the backbone downwards. For softening and ratcheting the correction is achieved by feeding the shifted points (e.g. $\varepsilon_{ss,n}$) through Equation (7-20) to calculate the correction required to shift the backbone back onto points ε_n, i.e. to restore it to its initial position.

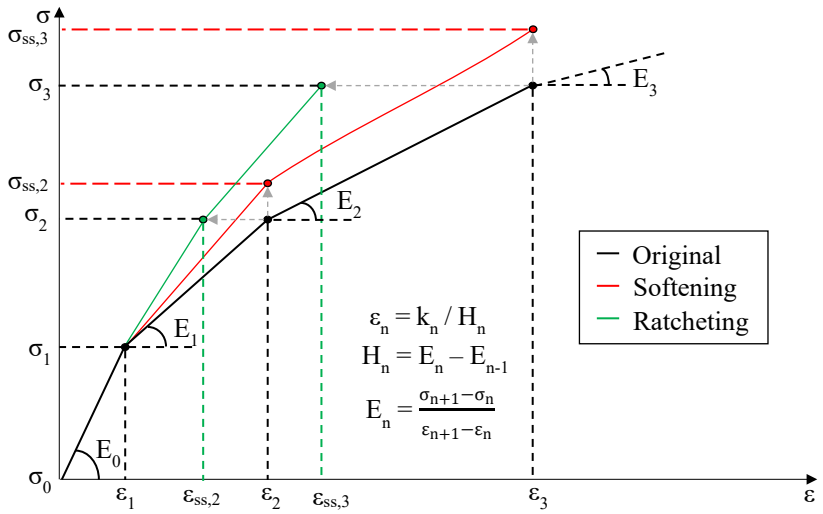


Figure 7-6: Recalibration of backbone for softening and ratcheting

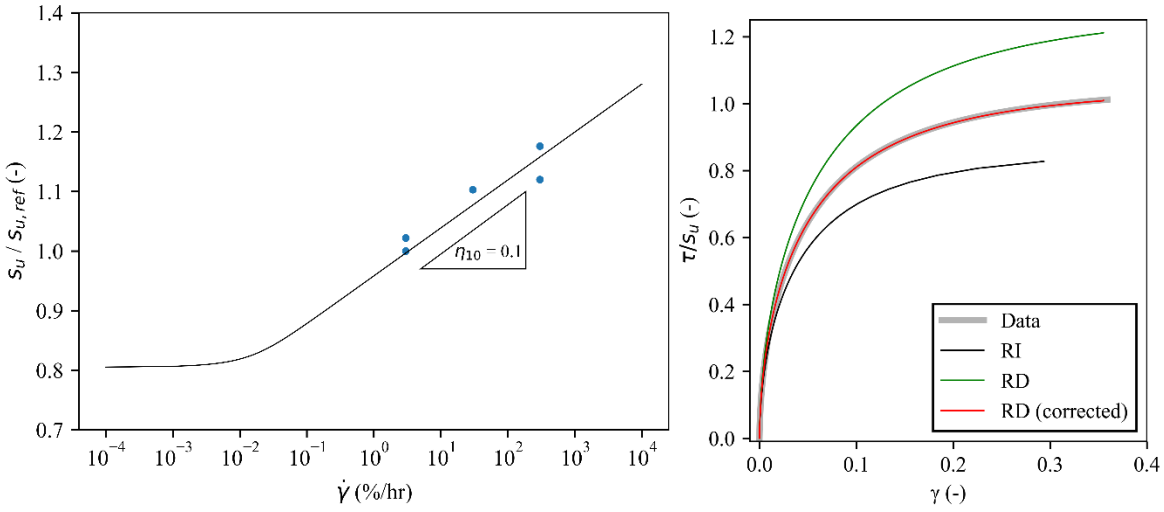
7.4.2 Sensitivity study

Like the parameters for the validation stage, a number of tests were selected to calibrate the model. A sensitivity study was carried out to quantitatively identify the number of tests needed to achieve optimal results. The number of tests required was varied for each of the key behaviours, which included rate effects, softening and ratcheting. Furthermore, the sensitivity study looked at the impact of adjusting each of the cyclic calibration parameters.

Rate effects:

The results highlighted in Section 5.5.3 indicate that a total of four tests can be used to calibrate the rate process theory function. This includes one multi-rate test and three tests at different constant shearing rates (i.e. $\dot{\gamma}$ = 3, 30 and 300 %/hr). Figure 7-7(a) shows the RPT function fitted to the test data, assuming a mean $\eta_{10} = \ln(10)\eta = 0.1$ and a $\dot{\alpha}_{qs}$ = 0.025 %/hr (t_{ref} = 1000 hours). Here, η_{10} is the normalised viscous parameter, where η_{10} = 0.1 represents a 10% increase in strength per order of magnitude increase in rate. The selected $\dot{\alpha}_{qs}$ represents a near zero-rate backbone experiment, where the test is rate-independent (RI), and completed at an extremely slow rate such that the time to failure is approximately 1000 hours. Whilst the glacial till has a high natural variability, the determined η_{10} fits the points well (R^2 = 0.9), suggesting that calibrating using a single multi-rate test would be sufficient. Nonetheless, for a robust implementation of the model, all points were used.

Following the calibration procedure detailed in Section 7.4.1, the addition of rate dependency (RD) causes the backbone to change (green line) as observed in Figure 7-7(b). To counter this, the original set of springs (k_n) and sliders (H_n) are pulled down to the rate-independent (RI) model (black line), so that the output shifts back onto the original dataset (red line).



(*a*) (*b*)

Figure 7-7: (*a*) Rate Process Theory calibration and (*b*) recalibration of backbone due to rate dependency

Following selection of the rate-effect parameters, the RD model is implemented to predict the multi-rate test, as shown in Figure 7-8. The model is in close agreement with the data, considering a mean η_{10} was used.

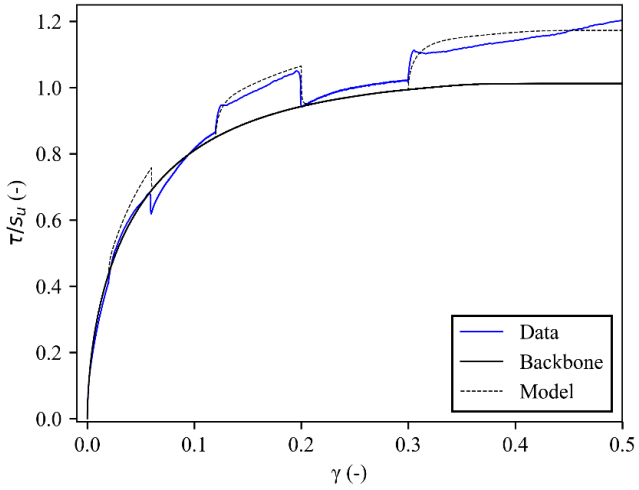


Figure 7-8: Fitting of model to multi-rate test data

Softening:

The softening function could be calibrated against a total of five two-way cyclic tests at varying amplitudes. Using Equation (7-12) and the derived backbone parameters from Table 7-3, the experimental development of κ with number of cycles can be computed. The loaded cycles appear to have higher softening rates for high ζ_b as observed in Figure 7-9(a). As

discussed in Section 7.4.1, the softening rate is governed by the exponent m_k, which is set as a constant based on the experimental data (Richards, 2019; Balaam, 2021). This is a limitation of the current model; a modification of the softening function for stress dependency is possible, but not pursued further here. An iterative process involving different combinations of two-way cyclic tests, demonstrated that a mean value of the exponent would be more representative of the softening behaviour despite the large range evident in Figure 7-9(a).

This calibration exercise did not identify the minimum number of tests required to calibrate the softening behaviour for general clay behaviour, with all two-way tests used, two at low CSR and three at high CSR. This ensured variations across stress level were captured, with a mean m_k = -0.37. Setting F_β = 0.3, F_κ = 1, and κ_{ref} = 0.7, the rate of softening simulated by the model, compared with the experimental data is presented in Figure 7-9(b). As expected, the model overpredicts the amount of softening for tests CSS01 to CSS02 and underpredicts for tests CSS03 to CSS05. The model fit appears to be poorer at high cycle numbers for high-intensity tests. This calibration was deemed an appropriate starting point but could be optimised, as developed in Section 7.5.2.1 using the PCSS tests.

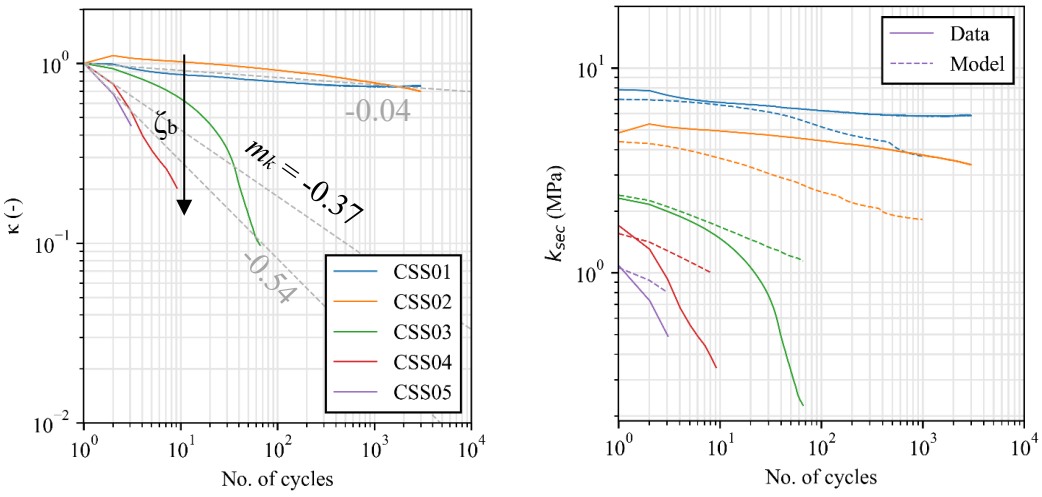


Figure 7-9: (*a*) Softening rate calibration for m_k and (*b*) model predictions for two-way CSS tests

Ratcheting:

The ratcheting behaviour could be calibrated from a total of eight tests with $\zeta_b > 0$, however, only four were used. Across the three calibration stages, calibration for ratcheting is the most cumbersome due to the coupling with softening, although this is partially limited with $F_\kappa = 1$. While the order of calibration has a negligible impact on the final calibration, the parameters for softening can differ depending on whether ratcheting has been calibrated before or after.

For consistency with previous work (e.g. Balaam (2021) and Richards (2019)), calibration of softening is followed by ratcheting, where the value for $R_{ref} / R_0 = 0.7$ is fixed and $R_0 = 1$ is set, with the parameters m_s, m_r and $F_{\beta,R}$ optimised. Parameters m_s and m_r can be provisionally derived from the analysis of the experimental data. In the case of $F_{\beta,R}$, which controls the ratcheting magnitude, a convenient value of $F_{\beta,R} = 1$ was found to work well. This may not always be the case, and may vary for different soil types and scales.

Like softening, ratcheting begins as soon as plastic strains start to develop. As a result, the backbone recalibration procedure, as described previously, must be followed. It is also possible that the inclusion of softening alone is enough to capture the ratcheting response. To demonstrate this, the model is used to simulate four random CSS tests (CSS10, CSS13, CSS14 and CSS15), with the results plotted in Figure 7-10, shown with and without ratcheting. In all cases, the inclusion of ratcheting is required to ensure the final strain is in line with those measured experimentally. The model predictions, where appropriate, were limited to 1000 cycles for ease of computation. The parameters were optimised so that the rate of ratcheting closely matched the experimental data according to stress level (i.e. ζ_b), similar to the analysis performed in Section 6.3.3 (Figure 6.19).

Qualitatively, it appears that softening alone is enough. However, the experimental data shows that the rate of strain accumulation starts to decrease with increasing number of cycles. As a result, softening alone would not be sufficient, where plastic strains accumulate at a constant rate. Further enhancements can be made to the model by modifying both the softening and ratcheting to suitably capture the observed behaviour. Moreover, the choice of locally or globally softening the surfaces may be improved by taking a combination, for instance, setting $F_\kappa = 0.9$, but this approach is not pursued further here.

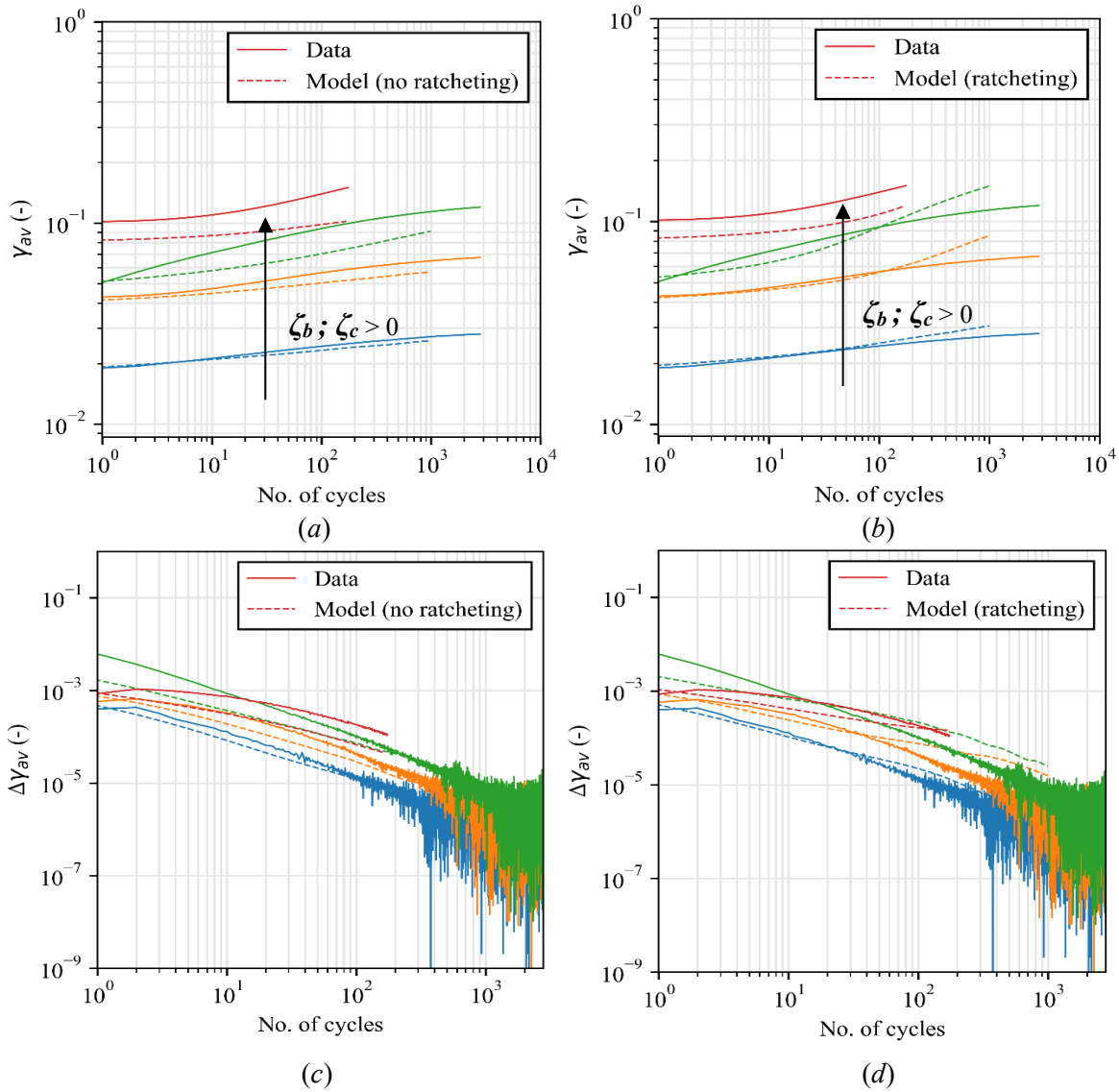


Figure 7-10:Model (*a*) + (*c*) without ratcheting and (*b*) + (*d*) with ratcheting

Overall:

The optimal results are based on three performance metrics set out in Table 7-4, with the final outputs for comparison based on an 'unseen' partial two-way test (CSS08). The outputs of the model are revealed in Figure 7-11, covering the performance of the model with respect to final average shear strain $\gamma_{av,F}$, secant stiffness $k_{sec,F}$ and energy loss factor $\eta_{I,F}$ at the end of the test (i.e. N_f = 106). The model approximately follows the experimental outputs for the first few cycles, with ratcheting being underpredicted at large number of cycles.

Table 7-4: Performance of model against experimental data for CSS08

Performance metric	Symbol	Data	Model
Final average strain (-)	$\gamma_{av,F}$	0.149	0.062
Final stiffness (MPa)	$k_{sec,F}$	0.785	0.711
Final energy loss factor (-)	$\eta_{I,F}$	0.352	0.324

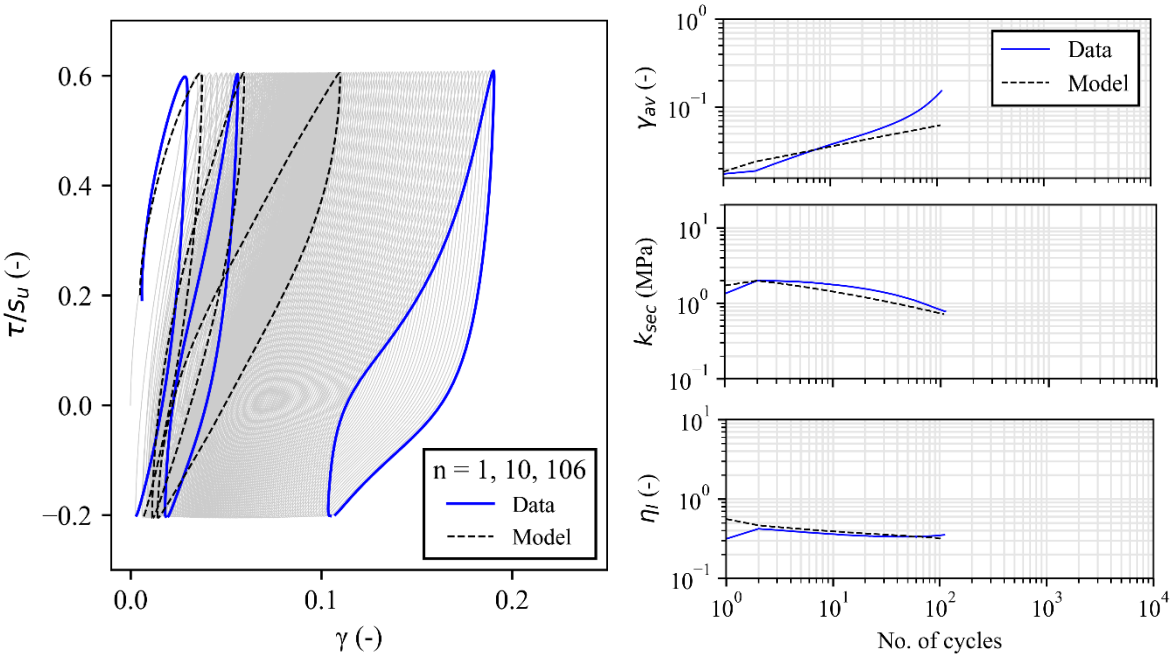


Figure 7-11: CSS08 - (*a*) Model stress-strain behaviour and (*b*) prediction of performance metrics

To further evaluate the model, the sensitivity study was extended to evaluate the effect of each of the model parameters on the three performance metrics, see Table 7-5.

Table 7-5: Sensitivity of parameter choice

Stage	Parameter	Unit	Min:Max	$\gamma_{av,F}$ (-)	$k_{sec,F}$ (MPa)	$\eta_{l,F}$ (-)
Monotonic	G_0	MPa	125:375	0.060:0.058	0.74:0.79	0.30:0.33
	N_s	-	20:60	0.063:0.060	0.71:0.75	0.32:0.32
	s_u	kPa	$0.8s_u$: s_u	0.041:0.062	0.64:0.71	0.24:0.32
	γ_f	-	-	-	-	-
	α	-	-	-	-	-
Rate	η_{10}	-	0.05:0.15	0.071:0.057	0.62:0.79	0.31:0.32
	t_{ref}	hours	100:10000	0.063:0.062	0.68:0.75	0.32:0.32
Softening	F_κ	-	0.5:1	0.081:0.062	0.78:0.71	0.46:0.32
	κ_{ref}	-	0.5:1	0.072:0.033	0.61:2.42	0.28:0.44
	$F_{\beta,l}$	-	0.1:10	0.070:0.038	0.61:1.74	0.29:0.41
	m_k	-	0.1:0.5	0.046:0.070	1.39:0.58	0.41:0.29
Ratcheting	R_0	-	0.1:1	0.043:0.062	0.71:0.71	0.32:0.32
	m_s	-	0.1:10	1.080:0.046	0.69:0.74	0.39:0.32
	m_r	-	1:10	0.057:0.094	0.71:0.72	0.32:0.32
	R_{ref}	-	0.1:1	0.047:0.068	0.71:0.71	0.32:0.32
	$F_{\beta,R}$	-	0.5:10	0.052:0.201	0.71:0.71	0.32:0.33

7.4.3 Selected calibration parameters

The parameters used for the Cowden till model predictions are detailed in Table 7-6. The recalibration of the Bi-MSHYP backbone parameters (i.e. k_n and H_n) have not been included here but the parameters have been altered to match the specified curve from the monotonic parameters. The performance of the model using these parameters is covered in Section 7.5 and the parameters are likely to change should certain performance metrics not be met. A summary of the calibration procedure is given in Figure 7-12, which is suggested as the preferred approach for modelling an overconsolidated glacial till.

Table 7-6: Final parameters for Bi-MSHYP model

Stage	Parameter	Unit	Value
Monotonic	G_0	MPa	250
	N_s	-	40
	s_u	kPa	84
	γ_f	-	0.33
	α	-	1.95
Rate	η_{10}	-	0.1
	t_{ref}	hours	1000
Softening	F_k	-	1
	κ_{ref}	-	0.7
	$F_{\beta,l}$	-	0.3
	m_k	-	0.37
Ratcheting	R_0	-	1
	m_s	-	6.5
	m_r	-	1.4
	R_{ref}	-	0.7
	$F_{\beta,R}$	-	1

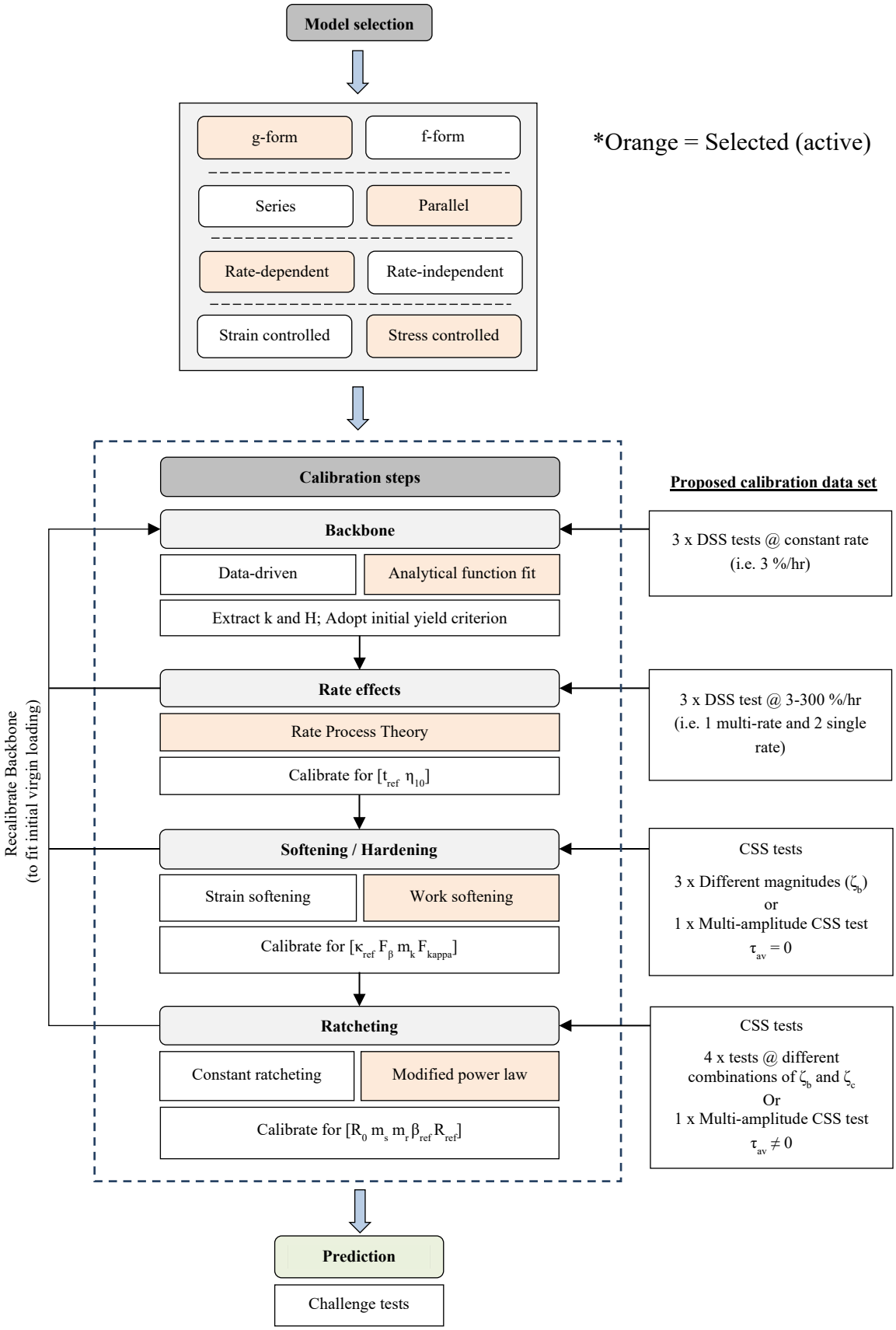


Figure 7-12: Overview of Bi-HYP implementation

7.5 Performance and predictions of model

To assess the calibrated model's performance, it is evaluated against a range of 'unseen' cyclic tests. This includes multidirectional and multi-amplitude cyclic tests under well-defined load paths. In addition, cyclic contour plots are reproduced to showcase the model's overall ability to simulate the experimental data.

7.5.1 Synthesising cyclic contour plots

While the model has been optimised against unidirectional CSS tests, the variability of the data can lead to discrepancies between some of the experimental data. For example, the reproduced cyclic contour plots in Figure 7-13, following the NGI method covered in Section 6.3.7, appears only to partially capture the experimental data. At the lower stress levels, the strain contours are underpredicted. This is the outcome of calibrating softening against all two-way CSS tests, illustrating that the choice of optimisation can be weighted depending on purpose. For this research the aim was to predict a range of complex cyclic tests across different stress magnitudes. Figure 7-13 demonstrates that the model can reproduce a convincing set of contour diagrams that capture the overall Cowden till behaviour.

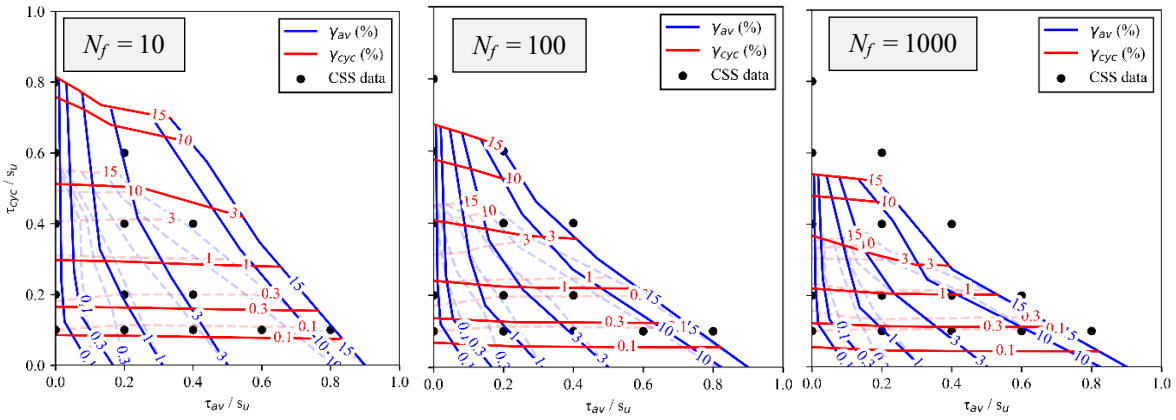


Figure 7-13: Reproduced cyclic contour plots (— model ---data)

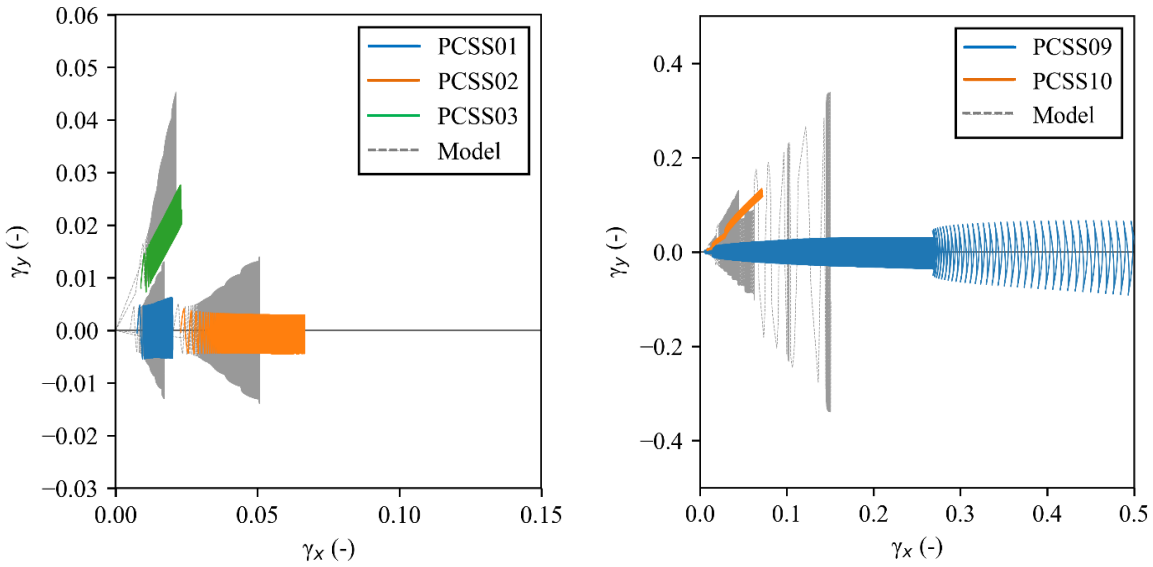
7.5.2 Complex cyclic loading predictions

The cyclic loading predictions for the more complex experiments follow the order of experiments described in Chapter 6. The discrepancies between the model and experimental data are discussed in terms of the key cyclic behaviours (i.e. strain accumulation and stiffness change). Additionally, comparisons also include loading bias, frequency, pseudo-random loading, idealised load effects, and unique load paths. Following the process described in Section 7.1 (Figure 7-1), the model is tested against the more complex cyclic tests and the model parameters are updated where necessary, to improve performance.

7.5.2.1 Perpendicular cyclic simple shear tests (PCSS)

Model predictions for batch one experimental tests (PCSS01 to PCSS03), consisted of a monotonic loading stage followed by a symmetric cyclic stage in the perpendicular direction. The model captures the ratcheting behaviour reasonably well as shown in Figure 7-14(a). The results support the findings made in Section 6.4.3, where the magnitude of the applied average load influenced the amount of ratcheting but at a constant ratcheting rate (i.e. findings from PCSS08). However, due to compromising for a softening over hardening approach, predictions for ratcheting were often overpredicted for a given number of cycles.

Although, the model simulates the ratcheting motion in the x-direction well it performs less well in capturing the softening type response observed in the y-direction. This is indicated in Figure 7-14(a) where the cyclic strains along the y-axis are far greater than the experimental outputs, suggesting that softening is overestimated by the model. Furthermore, in several cases (i.e. PCSS02, PCSS07 and PCSS08), an increase in stiffness was observed experimentally. This may be due to slight changes in the soil's stress contact fabric at large strains (Ushev, 2017). The model's current formulation would not capture these behaviours without reconfiguration to capture both hardening, where $m_k < 0$, and softening. Therefore, ratcheting was underpredicted in most cases, likely due to the calibration with unidirectional CSS tests instead of more complex and representative tests.



(*a*) (*b*)

Figure 7-14: Strain path for (*a*) PCSS01 to PCSS03 and (*b*) PCSS09 to PCSS10

Model predictions were also carried out for batch two tests (PCSS09 and PCSS10). These tests provide further insight into the influence of ASR and CSR, most notably the increase in ratcheting rate along the *x*-axis with increasing CSR in the *y*-direction, discussed in 6.4.3. In general, the model predicted too much softening for all complex cyclic loading cases, including those described in Sections 7.5.2.2 to 7.5.2.4. Therefore, it may be more appropriate for the model to be calibrated with multi-amplitude type (i.e. PCSS09 and PCSS10) tests to capture, consistently, the change in softening or ratcheting with number of cycles under a range of stress magnitudes. The softening parameters were recalibrated according to test PCSS09 to demonstrate the improved response using a single element test instead of several. In terms of ratcheting, the preliminary calibrated model greatly underpredicted the response for both batches of tests as shown in Figure 7-14. Therefore, similarly, the ratcheting parameters needed to be recalibrated and this was done using test PCSS10. Additionally, this step was necessary as the softening and ratcheting mechanisms are intrinsically coupled. The new softening and ratcheting parameters are given in Table 7-7. For simplicity, only parameters m_k, m_s, and m_r were modified, given in green.

Table 7-7: Final softening and ratcheting parameters for Bi-MSHYP model

Stage	Parameter	Unit	Final
Softening	F_k	-	1
	κ_{ref}	-	0.7
	$F_{\beta,l}$	-	0.3
	m_k	-	0.11
Ratcheting	R_0	-	1
	m_s	-	3.9
	m_r	-	0.7
	R_{ref}	-	0.7
	$F_{\beta,R}$	-	1

The predictions in Sections 7.5.2.2 to 7.5.2.4 are based on the updated (final) parameters. It is noted that, although the predicted cyclic contour plots in Section 7.5.1 have not been recalculated, the mapping would elongate further along the *y*-axis (i.e. stiffening) with the updated parameters. The new predictions for the PCSS tests are given in Figure 7-15 and Figure 7-16. For PCSS01 to PCSS03, the softening magnitude appears to be reasonably predicted as opposed to the amount of ratcheting, which has been overpredicted for PCSS02 and PCSS03. This is a direct consequence of calibrating the model using test PCSS09, which demonstrated a dominant softening behaviour, with no hardening present.

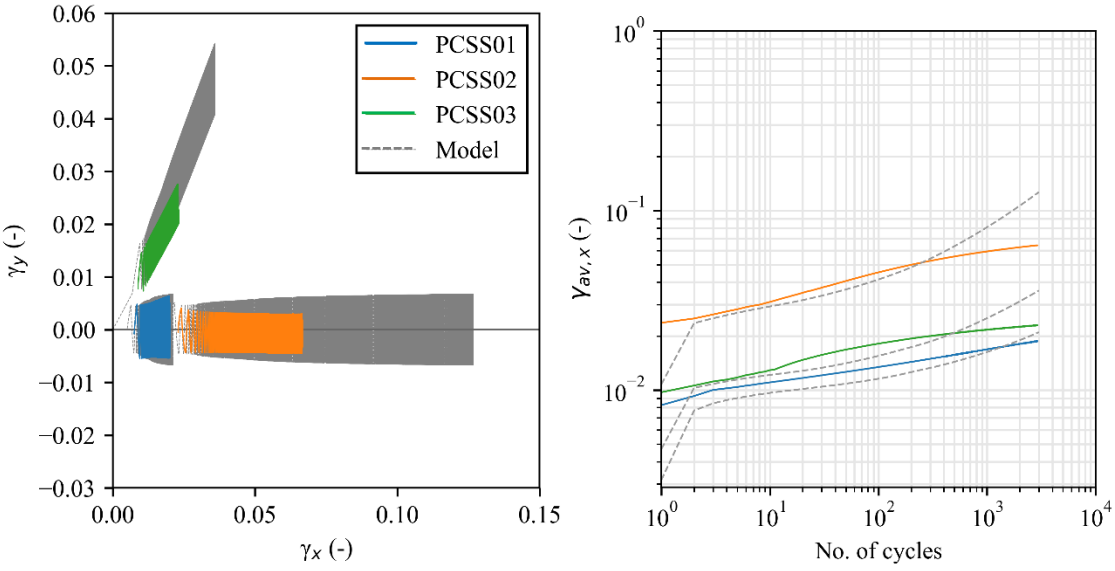


Figure 7-15: Model predictions for PCSS01 to PCSS03 - (*a*) Strain path and (*b*) strain accumulation evolution

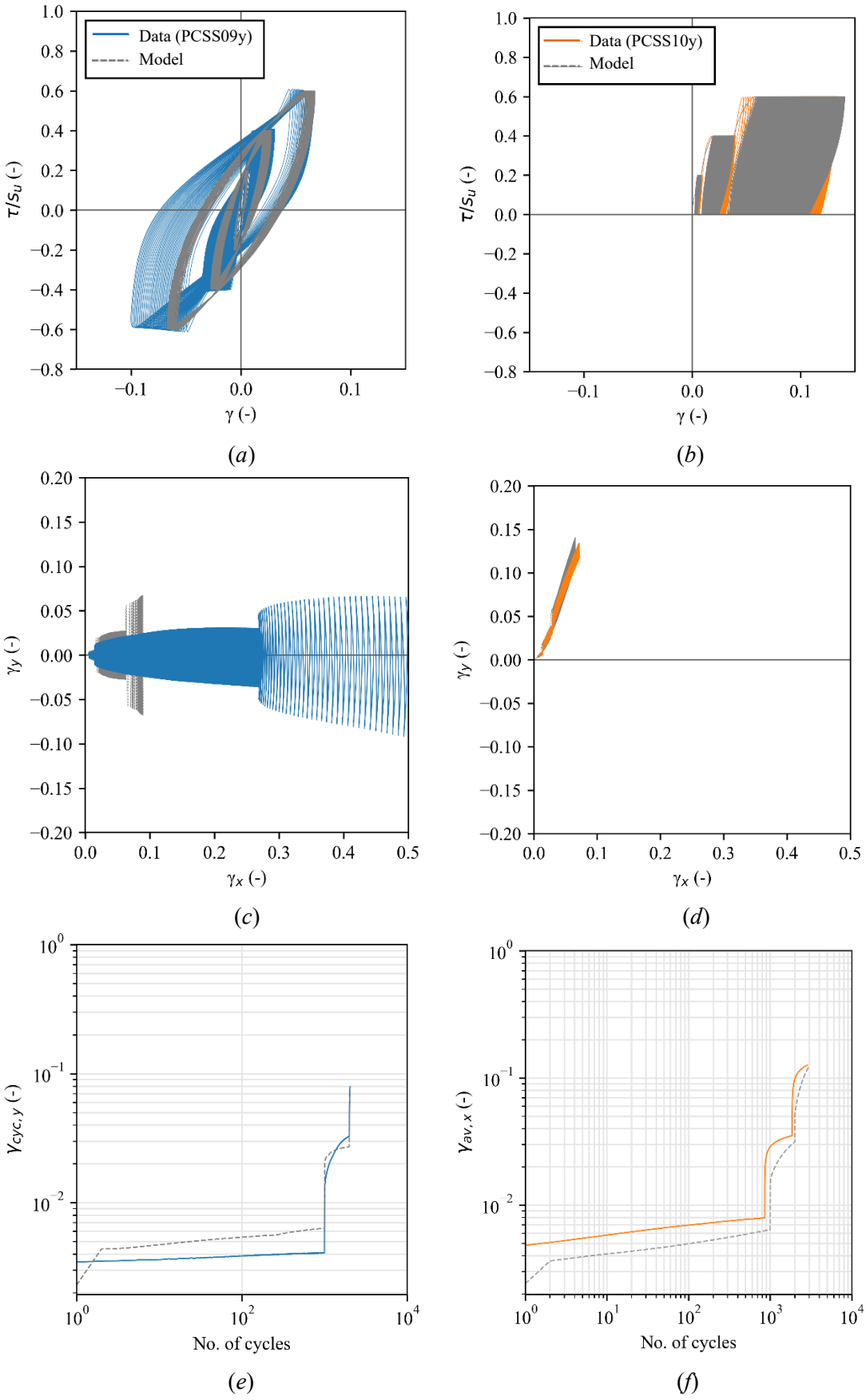


Figure 7-16: Stress-strain in *y*-axis for (*a*) PCSS09 and (*b*) PCSS10, strain path for (*c*) PCSS09 and (*d*) PCSS10, and strain accumulation for (*e*) PCSS09 and (*f*) PCSS10

For PCSS09 and PCSS10 the overall response is well captured when examined in a single direction, though the strain path for PCSS09 signals an inadequate response in the orthogonal *x*-direction, where not enough movement is captured. This is probably caused by the coupling of *x* and *y* components combined with an inadequate softening function for this specific material.

7.5.2.2 Random loading cyclic simple shear tests (RCSS)

In this section, model predictions (based on the updated (final) softening parameters) for three examples of storm loads, RCSS01 to RCSS03 from Section 6.5, are presented. The results are compared to the experimental responses in Figure 7-17. The computations are based on the same parameters set out in Table 7-7 for the PCSS loading responses. These parameters are preferred as they better reflect the realistic storm loads.

In general, the model predictions have captured the key features of the soil-element response to storm loading. Here, ratcheting is observed during the application of cycles under biased loading, with the overall response dominated by the large load events. For RCSS01 and RCSS03 the accumulated shear strain is slightly underpredicted but could be better predicted by adjusting the evolution of k_h with m_k or R with m_r. The experimental outputs show RCSS03 (γ_{av} = 0.023) to have a much higher γ_{av} compared to RCSS01 (γ_{av} = 0.012), which is caused by the additional out-of-plane storm load history. This is also captured by the model but at a lower magnitude. For RCSS02, all three performance metrics appear to be well captured.

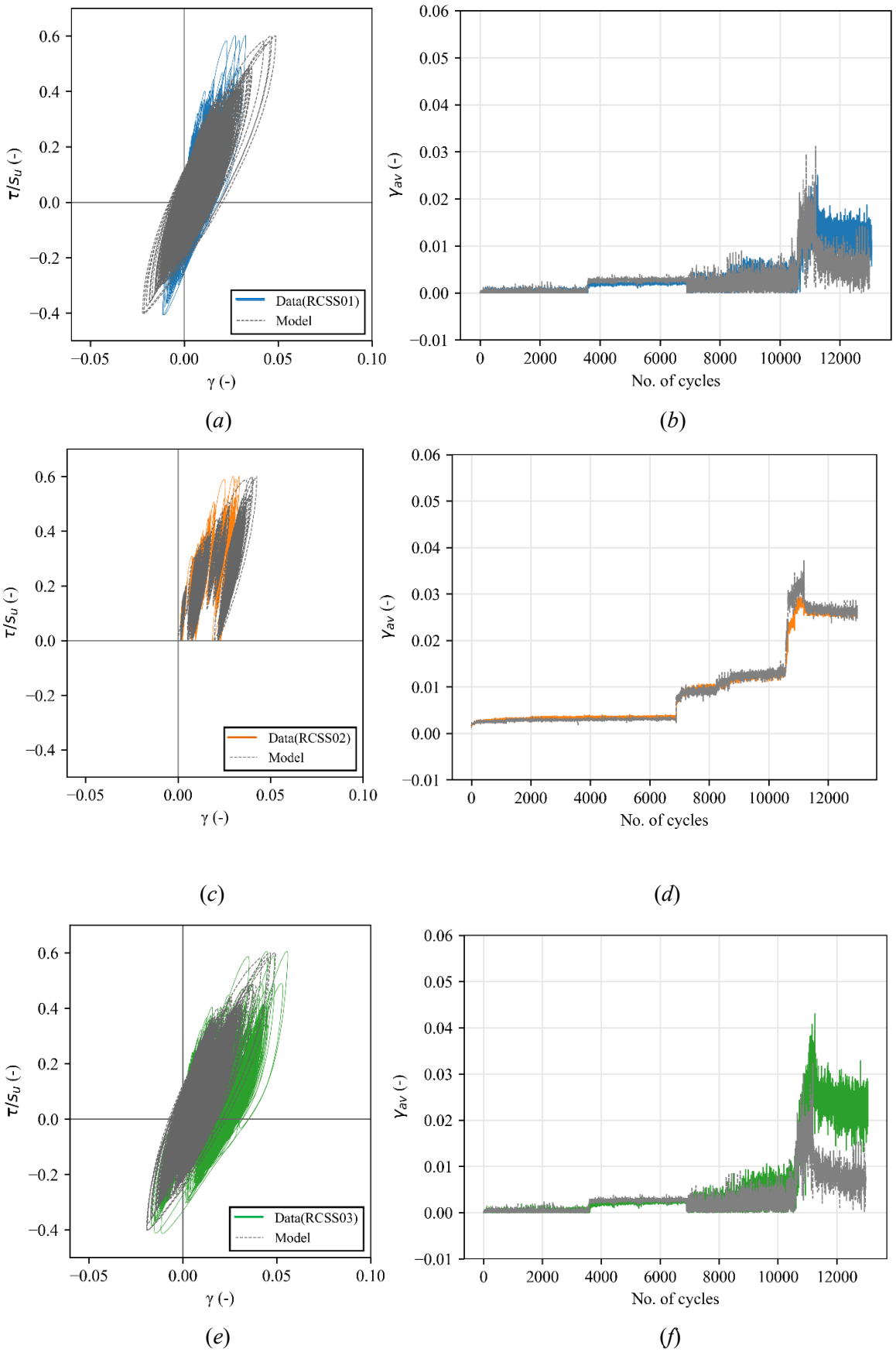


Figure 7-17: Stress-strain response and strain accumulation for (*a*) + (*b*) RCSS01, (*c*) + (*d*) RCSS02, and (*e*) + (*f*) RCSS03

7.5.2.3 Random packaged cyclic simple shear tests (RPCSS)

The Bi-MSHYP model was used to predict the idealised load packages employed in Section 6.6. All three multi-amplitude datasets were applied to show the model's ability to capture the hysteresis loop shape, stiffness and strain accumulation. From Figure 7-18(a) to (f), the model's calculated accumulated strain for all cases closely resembles the direction and magnitude of the experimental results.

However, it appears the model overpredicts the softening response, even at larger amplitudes despite the use of the optimised parameters from the batch two PCSS tests. This is probably linked to the absence of stress dependency in the softening function. Nonetheless, creating a multi-amplitude load dataset for model calibration was preferred. Reasons include limiting sample variability and a simpler calibration process (i.e. only one complex multi-amplitude test is needed instead of several CSS tests at different stress levels). The multi-amplitude tests can be set up as a two-way test to capture softening or as a one-way loading test to capture ratcheting.

Provided the model is well calibrated, the use of idealised storm loads can inform users on the effectiveness of the discretisation into load parcels and how closely they might resemble the experimental storm load response. Concerns around frequency, package arrangement, and equivalent number of cycles can be better explored. Additionally, an advantage includes the influence of cycle amplitude type, where the model could suggest that a larger number of cycles within the history can be discarded, as they contribute little to the overall strain and stiffness behaviour.

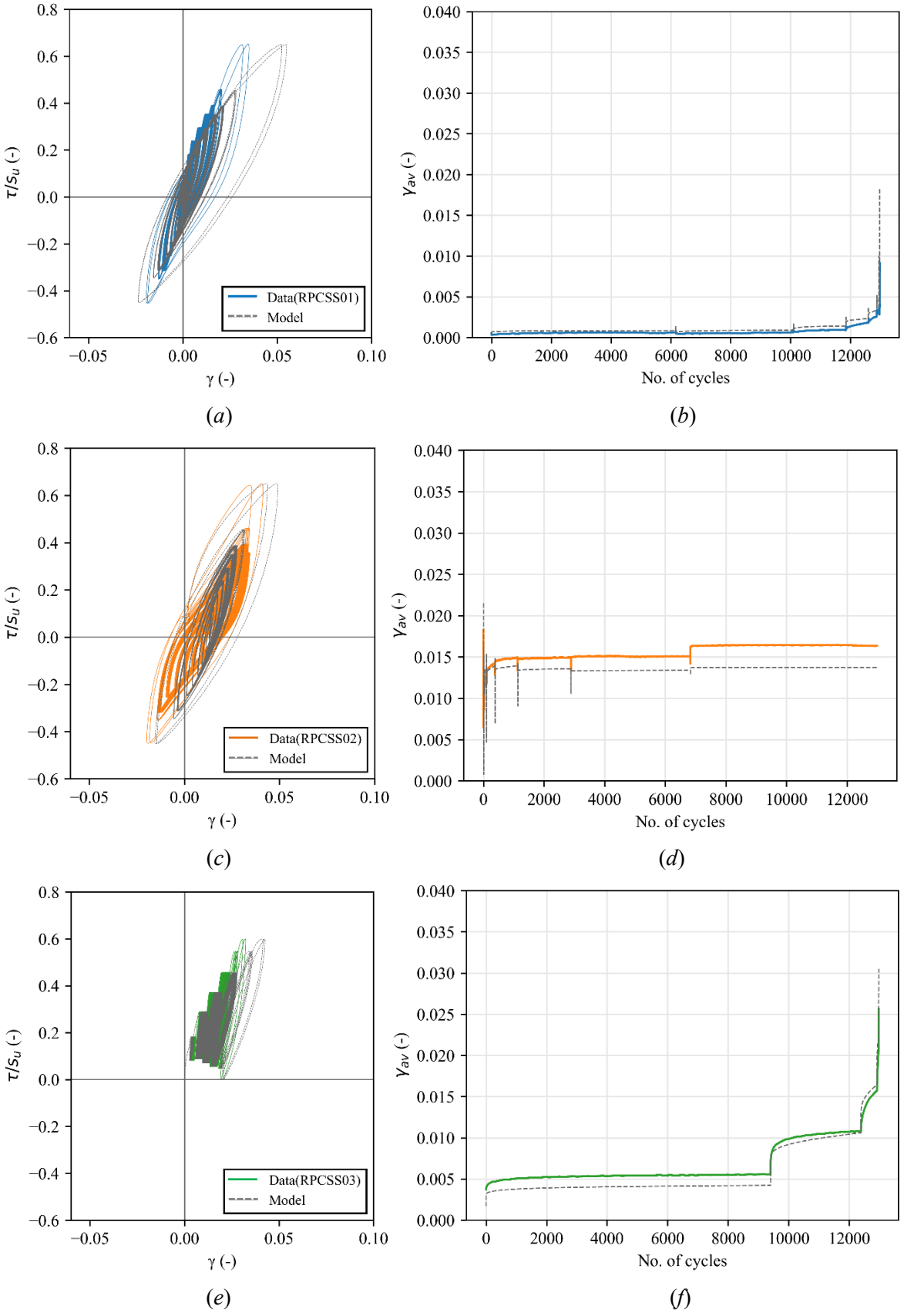
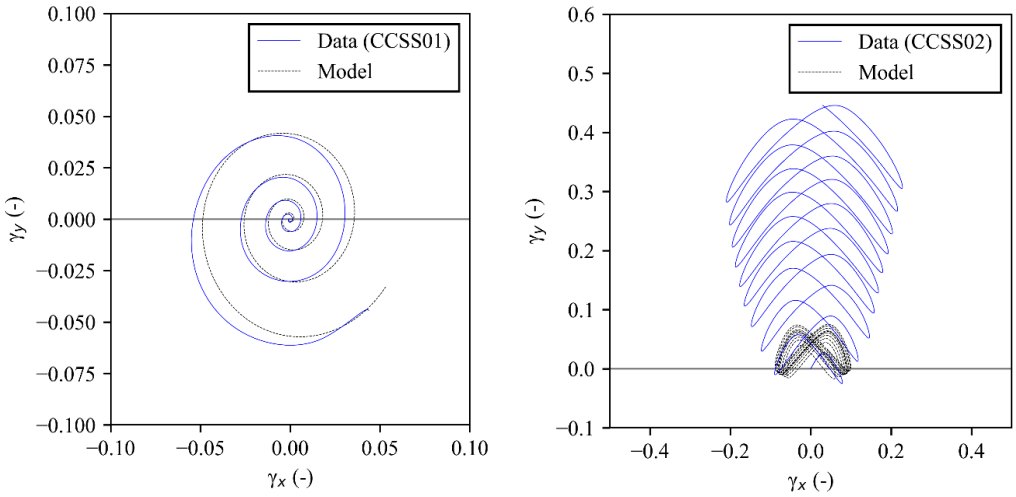


Figure 7-18: Stress-strain response and strain accumulation for (*a*)+(*b*) RPCSS01, (*c*)+(*d*) RPCSS02, and (*e*)+(*f*) RPCSS03

7.5.2.4 Challenge cyclic simple shear tests (CCSS)

Figure 7-19 shows the performance of the Bi-MSHYP model (based on Table 7-7) under multidirectional spiral loading and figure-8 loop type loading. Although these types of loads are not realistic, the experimental data represents a robust challenge for the model. The strain response for the spiral test (CCSS01) is well captured but less so for CCSS02 due to the large deformations. As described in Section 7.4.2, this is caused by the softening calibration of the model against PCSS09 over the test's stress range, overpredicting the stiffness at small amplitudes and underpredicting at large amplitudes. As a result, for a test with $CSR_x = 0.6$, the model is likely to underpredict the softening, leading to lower predictions of strain. While this is a product of the calibration stage, the model could be recalibrated for a better fit. This highlights the flexibility of the model and its ability to predict multidirectional loading.



(*a*) (*b*)

Figure 7-19: Model prediction for (*a*) CCS01: Spiral loop tests and (*b*) CCSS02: Figure-8 loop test

From the different evaluations and analysis, it is evident the modular type Bi-MSHYP model is capable of reproducing the many cyclic behaviours observed experimentally. The variability of Cowden till has affected the accuracy of the results in some instances, where rates for softening and ratcheting are notably different across the ζ_b range. However, considering the targeted calibration range, it is reasonable to conclude that the model predicts the cyclic behaviour better at low to medium (CSR < 0.4) cyclic stress magnitudes.

7.5.3 Discussion

The Bi-MSHYP model is a powerful numerical approach for predicting the cyclic behaviour of clay in a single element. While the model can be fully defined using two functions, an energy and dissipation function, and conforms to the laws of thermodynamics, it is not without limitations in its current form. The model consists of softening and ratcheting mechanisms embedded as evolution functions, with various choices, which in some cases may be considered more complex than is necessary. Further work is needed to explore the form of the model and most rigorous means of calibration to capture the range of behaviour for different clays under the various loading conditions.

7.5.3.1 Unidirectional loading response

For unidirectional constant amplitude cyclic loading, the model can reproduce all key cyclic behaviours (e.g. loop shape, softening and ratcheting) observed from the CSS tests with reasonable accuracy for all metrics. The formulation of the model means the cycles closely follow the shape of the original backbone. Therefore, since the softening and ratcheting elements are adequately calibrated, the energy loss over number of cycles is reasonably approximated. The reproduced contour plots highlight the applicability (i.e. to current industry design procedures) of the model following a robust calibration procedure. Sample variability likely affected the performance of the model, with notable differences observed for softening behaviour across different combinations of ζ_b and ζ_c.

7.5.3.2 Multidirectional loading response

The predictions for multidirectional loading were limited to PCSS, RCSS, and CCSS tests. The majority of the multidirectional behaviour can be interpreted from the PCSS tests, which explored different areas within the multidirectional stress space, uncovering behaviours associated with stress amplitude, load bias, frequency and direction. The model predicts these behaviours with acceptable accuracy, most notably, ratcheting occurring in the mean

load direction, stiffness evolution at small strains, and dependency of ratcheting on stress magnitude. In terms of limitations, the model overpredicted the amount of softening in unidirectional tests but better captured it for the multidirectional tests. Based on the predictions of the more complex cyclic tests, calibration using the PCSS tests yielded improved results, showing that the conservatism related to unidirectional constant amplitude tests. As a result, the calibration should follow a less conservative approach, using tests that are more representative of storm loads (i.e. multidirectional and multi-amplitude).

7.5.3.3 Multi-amplitude loading response

Multi-amplitude type loading tests were best defined by the PCSS and RPCSS tests. The packages of varying amplitudes can be used for a more streamlined calibration process. Calibrating the model using these outputs ensures behaviours across the different stress levels are addressed. The model predicts the multi-amplitude loading tests with adequate accuracy, showing the greatest accumulation of strain at the largest cycles and changes in stiffness associated with frequency and cyclic amplitude. It also demonstrated that the evolution of these outputs are independent of frequency, as evidenced by the small changes in k_{sec} and γ_{av} for the batch two tests.

7.5.3.4 Overall state of model implementation and repeatability

The hyperplastic model is mechanistic and modular, with each added mechanism building upon the previous one. It is clear that small changes in the backbone during recalibration have a large effect on all metrics of monotonic and cyclic behaviour. Concurrently, the intention of the model implementation is to ensure any user can reproduce the model predictions given a set of parameters. Variations in predictions are generally attributed to the choice of optimisation function and associated error tolerance. Therefore, the backbone recalibration functions for rate effects, softening and ratcheting covered in Section 7.4.1, are advantageous as they remove user variability, while also considerably reducing the

computational time into a single step instead of an iterative optimisation. The recommendations can also be applied by extending the 0D element model to a 0D macro-element model, as seen in the model predictions by Martin (2023).

7.5.3.5 Targeted data calibration

As with most soil constitutive models, there is a heavy emphasis on ensuring the number of elements tests needed to calibrate a model is not excessive and overly complicated. Interaction diagrams (shown in Figure 6.1) provide a useful pictorial for assigning tests. The normalisation further assists in the magnitude selection, allowing for the model to be fitted and most accurate in desired stress levels if required (e.g. Low stress → $\zeta_b < 0.5$).

7.6 Summary

The model presented in this chapter is a rate-dependent kinematic hardening model formulated with softening and ratcheting evolution functions. Based on the experimental results, a local surface-specific softening approach was preferred and where applicable, the softening and ratcheting mechanisms were a function of a work quantity rather than strain. In this case, the secant stiffness reduction is limited and can be inaccurate at larger strains. The model calibration process has been streamlined following a more rigorous calibration method, where changes in the original monotonic backbone from softening or ratcheting are corrected as an initial value problem (Appendix A).

It was demonstrated that the model overpredicted the amount of softening for each of the more complex cyclic tests (PCSS, RCSS, RPCSS, and CCSS) when parameters derived from the unidirectional CSS tests were used. Therefore, the model was further optimised by recalibrating the softening and ratcheting parameters using more complex multidirectional and multi-amplitude tests (based on the PCSS experiments). The optimised model captured several cyclic features which included, the non-linear hysteresis loop shape, accumulated strains with loading bias for both unidirectional and multidirectional variations, softening

evolution with number of cycles, and strain-rate dependency where an increase in strength and stiffness was observed at higher strain rates. The predictions were found to be satisfactory but of course could be improved through tailored evolution functions or targeted calibration tests, where for unidirectional or multidirectional, selected tests could be allocated to specific zones within the cyclic stress space. This allows for the better derivation of the parameters towards specific stress ranges while also addressing possible limitations.

Chapter 8

Conclusions and recommendations

8.1 Introduction

This section draws conclusions across the different core chapters, detailing key findings and their effect within the wider framework. Shortcomings and areas of improvement are also covered, making appropriate recommendations to overcome some of the challenges faced in this research.

8.2 Major contributions

Site characterisation of PICASO Cowden site

The site was fully characterised using the in-situ CPT measurements described in Chapter 2 and the monotonic test results in Chapter 5. The findings complement the already successful PISA project, adding to the database of tests and supporting previous findings. Furthermore, the data was used in different work packages, which were part of the greater PICASO project; this included soil constitutive model calibration, 3D finite element analysis (FEA) calculations, and assigning load magnitudes for the medium-scale field tests. The tests were also necessary for some of the pre-test model pile predictions. This was done in combination with the PISA data to check for consistency across the two sites. It was found that the PICASO site bears many similarities with the PISA site. Most notably in terms of index properties, compression behaviour, undrained shear strength, and stress-strain behaviour.

Improvement of direct simple shear (DSS) apparatus

The VDDCSS device that was used in this research was capable of performing a range of complex cyclic tests. However, modifications were made to the system to understand the stresses and strains governing the mechanisms observed. This included the installation of a lateral stress sensor, the replacement of the LVDT armature, and the use of stainless-steel thick rings for the specimen. The sensor gave reasonable results but could be improved following the drift correction and sensitivity limitations, the armature greatly improved the accuracy of the axial displacement measurements, and the thick rings ensured a more consistent failure mechanism through better interface contact.

Monotonic response of an overconsolidated glacial till

A total of 88 completed monotonic (19 oedometer, 55 DSS and 14 triaxial) tests are presented in this research. The monotonic results revealed further insight into the behaviour of Cowden till. Highlighting its swelling potential when exposed to water (Section 5.3.3), the advantage of overloading DSS specimens during consolidation (Sections 5.4), the increase in strength (~10%) due to rate effects (Section 5.5.3), and the relation between the triaxial and DSS results, where $s_{u,DSS}$ / $s_{u,TX}$ = 0.711 (Section 5.7.4 and 5.9). While a library of triaxial tests already exists for Cowden till (Ushev, 2017), the conducted DSS experiments add value to the database as a complementary pair.

Cyclic load response of clay

In total, 36 cyclic simple shear tests were completed (15 CSS, 13 PCSS, 3 RCSS, 3 RPCSS, and 2 CCSS) in this research, starting from unidirectional constant amplitude and building up to multidirectional and multi-amplitude cyclic simple shear tests. It is apparent that the simpler CSS tests do not provide a full representation of realistic load histories. This was shown in Section 6.4, which highlighted the impact of biased loading in opposing directions, where ratcheting was observed in the direction of the applied mean load and stiffness changes varying between stiffening and degrading depending on the loading characteristics.

Application of realistic storm loading and idealised load packages

The application of realistic storm loads shows that large increases in permanent strains occur at large cyclic events (Section 6.5: RCSS). This finding was coupled with the observation that a large proportion of the strains accumulated were contributions from the average shear strain $\gamma_{av,}$ induced by loading to the average stress τ_{av} for each of the stages. It also shows that a large proportion of the load history could be disregarded given a certain cyclic amplitude ($< 0.2s_u$). Under multidirectional storm loading, it also suggests that the out-of-plane load (y-axis) also influences the accumulated permanent strain (x-axis) irrespective of the magnitude. The storm loads were further idealised into load packages (Section 6.6: RPCSS). The packages which were arranged in ascending order give comparable values of accumulated strain and stiffness degradation compared to the realistic storm load tests. For the descending order variation, much lower values are measured. Furthermore, similar to the storm load tests (RCSS), the mean load applied for each of the packages appears to dominate the amount of overall strain accumulated. In terms of post-cyclic response, Cowden till experiences little change in its ultimate capacity (s_u) for all cyclic tests.

Implementation and optimisation of a constitutive model at element scale

In the past, variations of the implemented constitutive model (Bi-MSHYP) were used to predict the behaviour of clays, mainly under unidirectional and multi-amplitude loading. The model in this research incorporated the evolution functions from these variations into a multi-axial formulation to further understand the impact of directionality. The model was found to capture adequately the hysteresis, rate dependency, softening and ratcheting behaviours for unidirectional loading, but could be further improved by developing some of the evolution functions. In particular, for a sample that experiences both stiffness degradation and softening, the model will need to be modified such that local softening or hardening can be implemented as a function of either stress level or the amount of work done (β).

Furthermore, the multidirectional experimental results indicate mechanisms which could be better accounted for in multiaxial space such as the increased amount of ratcheting caused by the additional out-of-plane load (Section 6.4) and a better evolution of the softening function with stress level and cycle number. In terms of calibration methods, an improved approach has been adopted, where a single step backbone correction was used instead of a function optimisation approach. Furthermore, the multi-amplitude tests from the PCSS tests proved to be an effective dataset to calibrate the softening and ratcheting mechanisms.

8.3 Future work

Soil characterisation

A large number of monotonic tests were performed on natural Cowden till samples. However, to investigate the intrinsic compression and strength properties of the material, it would be recommended to have a parallel set of reconstituted or remoulded tests. Such tests have already been carried out by Ushev (2017) for the PISA site, however, additional tests would improve the confidence in the results. It would also clarify the importance of the clay matrix and how it dominates the strength behaviour while also providing information on the sensitivity of the clay.

Improved direct simple shear testing

The direct simple shear test kit has had a number of modifications to improve the measured outputs. However, several more variations and modifications can be made to understand the shearing mechanisms further. This includes the use of different platen ends (i.e. pinned or grooved), improved LVDT instrumentation, installation of a pore pressure transducer, and the use of a lateral stress sensor with a better sensitivity range. Alternatively, other variations of the direct simple shear apparatus can be explored, such as the confined variable direct simple shear (VDDCSS-CON) produced by GDS instruments.

Alternative soil constitutive models

The principal focus of this thesis has been the development of an experimental database. However, the data have also been compared with a theoretical model. A multi-surface kinematic hardening model formulated in the Hyperplasticity framework was used in this research. However, implementing a critical-state type model (e.g. SANICLAY) based on the experimental results (Section 5.10) would provide for useful comparison, giving insight into the cyclic mechanisms best captured by the respective models or showing what mechanisms need to be included. Similarly, a comparable model in a different framework (e.g. Hypoplasticity) would also provide detail in terms of how mechanisms are accommodated when not bounded by the laws of thermodynamics.

Model calibration

Although the model has been well implemented for clays in general, following Balaam (2021), the implemented Bi-MSHYP model can be further improved. It is suggested that the softening function be modified to accommodate the behaviours observed for the Cowden till material. Most notably, ensuring the softening is load magnitude dependent, modifying the function to accommodate the transition from softening to hardening, and ensuring multi-directionality is well represented through better normalisation of the generalised stress or strain components. This would allow for the effects of the varied direction of true offshore loads to be better predicted, further reducing conservatism.

Scaling of element tests to monopile design

Efforts were made to normalise element test parameters to the pile scale, but due to the complexity of cyclic loading in soils, simplifications were necessary to analyse observed behaviours. Different normalisation procedures need to be applied and evaluated to understand differences in the backbone response (e.g., initial stiffness, backbone curvature, and failure shear strain) and identify the most suitable scaling constants. Nevertheless, these findings pave the way for continued exploration and understanding of the intricate relationship between soil element and pile-scale responses.

References

4C Offshore. 2019. *Global Offshore Wind Farms*. Available: https://www.4coffshore.com/windfarms/ [2019, September 20].

Abadie, C.N. 2015. Cyclic Lateral Loading of Monopile Foundations in Cohesionless Soils. DPhil Thesis, University of Oxford.

Acharya, B. & Airey, D. 2017. Effect of Specimen Confinement Method on Simple Shear Test of Clay. In *Springer Series in Geomechanics and Geoengineering*. Springer Verlag. 247–254.

Achmus, M., Abdel-Rahman, K. & Kuo, Y.-S. 2007. Behaviour of Large Diameter Monopiles Under Cyclic Horizontal loading. In *12th International Colloquium on Structural and Geotechnical Engineering*. Cairo.

Ahnberg, H. & Larsson, R. 2013. Strength Degradation of Clay Due to Cyclic Loadings and Enforced Deformation. In *Proceedings of the 18th International Conference on Soil Mechanics and Geotechnical Engineering*. Linkoping. 1411–1414.

Airey, D.W. 1984. Clays in Circular Simple Shear Apparatus. PhD Thesis, University of Cambridge.

Airey, D.W. & Wood, D.M. 1987. An Evaluation of Direct Simple Shear Tests on Clay. *Geotechnique*. 37(1):25–35.

Airey, D.W., Budhu, M. & Wood, D.M. 1985. Some Aspects of the Behaviour of Soils in Simple Shear. In *Developments in Soil Mechanics and Foundation Engineering*. V. 2. P.K. Banerjee & R. Butterfield, Eds. London: Elsevier Applied Science Publishers. 185–213.

Andersen, K.H. 1976. Behaviour of Clay Subject to Cyclic Loading. In *Proceedings of the International Conference on The Behaviour of Offshore Structures*. Trondheim. 392–403.

Andersen, K.H. 2009. Bearing Capacity Under Cyclic Loading -Offshore, Along the Coast, and on Land. *Canadian Geotechnical Journal*. 46(5):513–535.

Andersen, K.H. 2015. Cyclic Soil Parameters for Offshore Foundation Design. In *Frontiers of Offshore Geotechnics III*. Taylor & Francis Group. 5–82.

API. 2011. Geotechnical and Foundation Design Considerations. *IS0 19901-4:2003*.

ASTM D2435/D2345M-11. 2011. *Standard Test Methods for One-Dimensional Consolidation Properties of Soils Using Incremental Loading*.

ASTM D6528-17. 2017. *Standard Test Method for Consolidated Undrained Direct Simple Shear Testing of Fine Grain Soils*. West Conshohocken.

ASTM D8296-19. 2019. *Standard Test Method for Consolidated Undrained Cyclic Direct Simple Shear Test under Constant Volume with Load Control or Displacement Control*.

Atkinson, J.H. 2000. Non-Linear Soil Stiffness in Routine Design. *Geotechnique*. 50(5):487–508.

Atkinson, J.H. & Bransby, P.L. 1978. *The Mechanics of Soils*. London: McGraw-Hill.

Atkinson, J.H. & Viggiani, G. 1995. Interpretation of Bender Element Tests. *Géotechnique*. 45(1):149–154.

Atkinson, J.H., Lau, W.H.W. & Powell, J.J.M. 1991. Measurement of Soil Strength in Simple Shear Tests. *Canadian Geotechnical Journal*. 28(2):255–262.

Bailey, H., Brookes, K.L. & Thompson, P.M. 2014. Assessing Environmental Impacts of Offshore Wind Farms: Lessons Learned and Recommendations for the Future. *Aquatic Biosystems*. 10(1).

Balaam, T.D. 2021. Calibration of Cyclic Loading Models for Monopile Foundations. DPhil Thesis, University of Oxford.

Baxter, C.D.P., Bradshaw, A.S., Ochoa-Lavergne, M. & Hankour, R. 2010. DSS Test Results Using Wire-Reinforced Membranes and Stacked Rings. In *GeoFlorida 2010: Advances in Analysis, Modeling, and Design*. 600–607.

Been, K. & Jefferies, M.G. 1985. A State Parameter for Sands. *Géotechnique*. 35(2):99–112.

Beuckelaers, W.J.A.P. 2017. Numerical Modelling of Laterally Loaded Piles for Offshore Wind Turbines. DPhil Thesis, University of Oxford.

Bicalho, K. V, Gomes Correia, A., Ferreira, S. & Marinho, F.A.M. 2006. Filter Paper Method of Soil Suction Measurement. In *XIII Panamerican Conference on Soil Mechanics and Geotechnical Engineering*. Margarita.

Bishop, A.W. 1972. Shear Strength in Undisturbed and Remoulded Soil Specimens. In *Stress-Strain Behaviour of Soils*. R.H.G. Parry, Ed. Cambridge, UK: G.T. Foulis & Co Ltd. 3–58.

Bjerrum, L. & Landva, A. 1966. Direct Simple-Shear Tests on a Norwegian Quick Clay. *Géotechnique*. 16(1):1–20.

Boulanger, R.W. & Seed, R.B. 1995. Liquefaction of Sand under Bidirectional Monotonic and Cyclic Loading. *Journal of Geotechnical Engineering*. 121(12):870–878.

British Standards Institution. 2017. Geotechnical Investigation and Testing- Laboratory Testing of Soil-Part 5: Incremental Loading Oedometer Test. (BS EN ISO 17892-5: 2017).

British Standards Institution. 2020. Petroleum and Natural Gas Industries — Specific Requirements For Offshore Structures-Part 4: Geotechnical and Foundation Design Considerations. (BS EN ISO 19901-4:2016).

Brosse, A., Kamal, R.H., Jardine, R.J. & Coop, M.R. 2017. The Shear Stiffness Characteristics of Four Eocene-to-Jurassic UK Stiff Clays. *Geotechnique*. 67(3):242–259.

Budhu, M. 1979. Simple Shear Deformation of Sands. PhD Thesis, University of Cambridge.

Budhu, M. 1984. Nonuniformities Imposed by Simple Shear Apparatus. *Canadian Geotechnical Journal*. 21(1):125–137.

Budhu, M. 1988. Failure State of a Sand in Simple Shear. *Canadian Geotechnical Journal*. 25:395–400.

Burd, H.J., Byrne, B.W., McAdam, R.A., Houlsby, G.T., Martin, C.M., JAP Beuckelaers, W., Zdravković, L., Taborda, D.M., et al. 2017. Design Aspects for Monopile Foundations. *TC 209 workshop on foundation design for offshore wind structures,19th ICSMGE*. 35–44.

BVG Associates. 2019. *Guide to an Offshore Wind Farm*.

Byrne, B.W., McAdam, R., Burd, H.J., Houlsby, G.T., Martin, C.M., Zdravkovic, L., Taborda, D.M.G., Potts, D.M., et al. 2015. New Design Methods for Large Diameter Piles Under Lateral Loading for Offshore Wind Applications. In *Frontiers in Offshore Geotechnics III:Proceedings of the 3rd International Symposium on Frontiers in Offshore Geotechnics (ISFOG 2015)*. Leiden. 705–710.

Byrne, B.W., McAdam, R.A., Burd, H.J., Houlsby, G.T., Martin, C.M., Gavin, K., Doherty, P., Igoe, D., et al. 2015. Field Testing of Large Diameter Piles under Lateral Loading for Offshore Wind Applications. In *Proceedings of XVI ECSMGE: Geotechnical Engineering for Infrastructure and Development*. ICE. 1255–1260.

Byrne, B.W., McAdam, R.A., Burd, H.J., Houlsby, G.T., Martin, C.M., Beuckelaers, W.J.A.P., Zdravkovic, L., Taborda, D.M.G., et al. 2017. PISA: New Design Methods for Offshore Wind Turbine Monopiles. In *Proceedings of the 8th International Conference of Offshore Site Investigation and Geotechnics*. London. 142–161.

Byrne, B.W., Aghakouchak, A., Buckley, R.M., Burd, H.J., Gengenbach, J., Houlsby, G.T., McAdam, R.A., Martin, C.M., et al. 2020. PICASO: Cyclic Lateral Loading of Offshore Wind Turbine Monopiles. In *4th International Symposium on Frontiers in Offshore Geotechnics*. Austin.

Byrne, B.W., Houlsby, G.T., Burd, H.J., Gavin, K.G., Igoe, D.J.P., Jardine, R.J., Martin, C.M., McAdam, R.A., et al. 2020. PISA Design Model for Monopiles for Offshore Wind Turbines: Application to a Stiff Glacial Clay Till. *Géotechnique*. 70(11):1030–1047.

Casagrande, A. 1936. The Determination of the Pre-Consolidation Load and its Practical Significance. In *Proceedings of the International Conference on Soil Mechanics and Foundation Engineering*. Harvard University Cambridge. 60–64.

Chandler, R.J. & Gutierrez, C.I. 1986. The Filter-Paper Method of Suction Measurement. *Geotechnique*. 36(2):265–268.

Cole, E.R.L. 1967. The Behaviour of Soils in the Simple-Shear Apparatus. PhD Thesis, University of Cambridge.

Collins, I.F. & Houlsby, G.T. 1997. Application of Thermomechanical Principles to the Modelling of Geotechnical Materials. *Proceedings of the Royal Society of London. Series A: Mathematical, Physical and Engineering Sciences*. 453(1964):1975–2001.

Craig, R.F. & Knappett, J.A. 2012. *Craig's Soil Mechanics*. V. 8. New York: Spon Press.

Crispin, J., Houlsby, G.T. & Qiu, Z. 2022. *Calibration Procedure for HARM Models*. Private Communication.

Dahl, K.R., Boulanger, R.W., Dejong, J.T. & Driller, M.W. 2010. Effects of Sample Disturbance and Consolidation Procedures on Cyclic Strengths of Intermediate Soils. In *Fifth International Conferences on Recent Advances in Geotechnical Earthquake Engineering and Soil Dynamics*. San Diego, California. 1–21.

Das, B.M. 2011. *Geotechnical Engineering Handbook*. B.M. Das, Ed. J.Ross Publishing.

Davies, B.J., Roberts, D.H., Bridgland, D.R., Cofaigh, C.Ó. & Riding, J.B. 2011. Provenance and Depositional Environments of Quaternary Sediments from the Western North Sea Basin. *Journal of Quaternary Science*. 26(1):59–75.

Davis, R.O. & Selvadurai, A.P.S. 2002. *Plasticity and Geomechanics*. Cambridge: Cambridge University Press.

Degroot, D.J., Germaine, J.T. & Ladd, C.C. 1994. Effect of Nonuniform Stresses on Measured DSS Stress-Strain Behavior. *Journal of Geotechnical Engineering*. 120(5):892–912.

DNVGL-ST-0126. 2016. *Support Structures for Wind Turbines*.

Donohue, S. & Long, M. 2009. Suction Measurements as Indicators of Sample Quality in Soft Clay. *Geotechnical Testing Journal*. 32(3):286–296.

Duncan, J.M. & Seed, H. 1966. Strength Variation Along Failure Surfaces in Clay. *Journal of Soil Mechanics and Foundations Division*. 92(SM6):81–104.

Dyvik, R., Berre, T., Lacasse, S. & Raadim, B. 1987. Comparison of Truly Undrained and Constant Volume Direct Simple Shear Tests. *Geotechnique*. 37(1):3–10.

Erten, D. & Maher, M.H. 1995. Cyclic Undrained Behaviour of Silty Sand. *Soil Dynamics and Earthquake Engineering*. 14(2):115–123.

Fischer, T., de Vries, W. & Schmidt, B. 2010. *Upwind Design Basis- WP4: Offshore Foundations and Support Structures-UpWind Project*. Universität Stuggart.

Fugro. 2020. Private communication.

Ghionna, V.N. & Porcino, D. 2006. Liquefaction Resistance of Undisturbed and Reconstituted Samples of a Natural Coarse Sand from Undrained Cyclic Triaxial Tests. *Journal of Geotechnical and Geoenvironmental Engineering*. 132(2):194–202.

Gregory, A.S., Whalley, W.R., Watts, C.W., Bird, N.R.A., Hallett, P.D. & Whitmore, A.P. 2006. Calculation of the Compression Index and Precompression Stress from Soil Compression Test Data. *Soil and Tillage Research*. 89(1):45–57.

Grognet, M. 2011. The Boundary Conditions in Direct Shear Tests: Development of Peat Testing at Low Vertical Stress. MSc Thesis, Delft University of Technology.

Guo, L., Wang, J., Cai, Y., Liu, H., Gao, Y. & Sun, H. 2013. Undrained Deformation Behavior of Saturated Soft Clay Under Long-Term Cyclic Loading. *Soil Dynamics and Earthquake Engineering*. 50:28–37.

Hight, D.W. 1983. Laboratory Investigations of Sea Bed Clays. PhD Thesis, Imperial College London.

Hosseini Kamal, R. 2012. Experimental Study of the Geotechnical Properties of UK Mudrocks. PhD Thesis, Imperial College London.

Houlsby, G.T. 1981. A Study of Plasticity Theories and Their Applicability to Soils. PhD thesis, University of Cambridge.

Houlsby, G.T. & Puzrin, A.M. 2006. *Principles of Hyperplasticity:An Approach to Plasticity Theory Based on Thermodynamic Principles*. London: Springer.

Houlsby, G.T., Abadie, C.N., Beuckelaers, W.J.A.P. & Byrne, B.W. 2017. A Model for Nonlinear Hysteretic and Ratcheting Behaviour. *International Journal of Solids and Structures*. 120:67–80.

Housel, W.S. 1960. Dynamics and Static Resistance of Cohesive Soils 18-46-1958. In *Papers on Soils-1959 Meetings, Symposium on Time Rates of Loading in Soil Testing*. Philadelphia. 4–35.

Huang, J., Chen, J., Ke, W., Zhong, Y., Lu, Y. & Yi, S. 2021. Damping Ratio Evolution of Saturated Ningbo Clays Under Cyclic Confining Pressure. *Soil Dynamics and Earthquake Engineering*. 143.

Inman, D.J. 2014. *Engineering Vibration*. 4th ed. Boston: Pearson.

IRENA. 2019. *Future of Wind: Deployment, Investment, Technology, Grid Integration and Socio-Economic Aspects*.

Ishihara, K. & Yamazaki, F. 1980. Cyclic Simple Shear Tests on Saturated Sand in Multi-Directional Loading. *Japanese Society of Soil Mechanics and Foundation Engineering*. 20(1):45–59.

Iwan, W.D. 1967. On a Class of Models for the Yielding Behavior of Continuous and Composite Systems. *Journal of Applied Mechanics*. 34(3):612–617.

Jana, A. & Stuedlein, A.W. 2021. Monotonic, Cyclic, and Postcyclic Responses of an Alluvial Plastic Silt Deposit. *Journal of Geotechnical and Geoenvironmental Engineering*. 147(3).

Jardine, R.J. & Standing, J.R. 2012. Field Axial Cyclic Loading Experiments on Piles Driven in Sand. *Soils and Foundations*. 52(4):723–736.

Jardine, R.J., Gens, A., Hight, D.W. & Coop, M.R. 2004. Developments in Understanding Soil Behaviour. In: Advances in Geotechnical Engineering. In *Proceedings of the Skempton Conference*. London: Thomas Telford. 103–206.

Jardine, R.J., Chow, F.C., Overy, R. & Standing, J.R. 2005. *ICP Design Methods for Driven Piles in Sands and Clays*. London: Thomas Telford.

Jeanjean, P., Zhang, Y., Zakeri, A., Andersen, K.H., Gilbert, R. & Senanayake, A.I.M.J. 2017. A Framework for Monotonic P-Y Curves in Clays. *Proceedings of the 8th International Conference of Offshore Site Investigation and Geotechnics*. 108–142.

Jin, H., Guo, L., Sun, H., Wu, T., Shi, L. & Cai, Y. 2022. Energy-Based Evaluation of Undrained Cyclic Behavior of Marine Soft Clay Under Multidirectional Simple Shear Stress Paths. *Acta Geotechnica*. 18(2):1–16.

de Josselin de Jong, G. 1971. Discussion Session 2. Stress-Strain Behaviour of Soils. In *Proceedings of Roscoe Memorial Symposium*. R.H.G. Parry, Ed. Henley-on-Thames, United Kingdom. 258–261.

Kammerer, A.M., Pestana, J.M. & Seed, R.B. 2002. *Behavior of Monterey 0/30 Sand under Multidirectional Cyclic Simple Shear Loading Conditions*. California.

Karlsrud, K. & Hernandez-Martinez, F.G. 2013. Strength and Deformation Properties of Norwegian Clays from Laboratory Tests on High-Quality Block Samples. *Canadian Geotechnical Journal*. 50(12):1273–1293.

Keller, T., Lamandé, M., Schjønning, P. & Dexter, A.R. 2011. Analysis of Soil Compression Curves from Uniaxial Confined Compression Tests. *Geoderma*. 163(1–2):13–23.

Kjellman, W. 1951. Testing the Shear Strength of Clay in Sweden. *Geotechnique*. 2(3):225.

Klar, A., Roed, M., Rocchi, I. & Paegle, I. 2019. Evaluation of Horizontal Stresses in Soil during Direct Simple Shear by High-Resolution Distributed Fiber Optic Sensing. *Sensors*. 19(3684):3684.

Kulhawy, F.H. & Mayne, P.W. 1990. Manual of Estimating Soil properties for Foundation Desgin. Cornell University.

Ladd, C.C. 1991. Stability Evaluation During Staged Construction. *Journal of Geotechnical Engineering*. 117(4):560–615.

Ladd, C.C. & Degroot, D.J. 2003. Recommended Practice for Soft Ground Site Charaterisation. In *12th Panamerican Conference on Soil Mechanics and Geotechnical Engineering*. Cambridge, MA USA.

Ladd, C.C. & Foott, R. 1974. New Design Procedure for Stability of Soft Clays . *Journal of the Geotechnical Engineering Division*. 100(7):763–786.

Lade, P. V. 2016. *Triaxial Testing of Soils*. Wiley Blackwell.

Lagioia, R. & Panteghini, A. 2016. On the Existence of a Unique Class of Yield and Failure Criteria Comprising Tresca, Von Mises, Drucker-Prager, Mohr-Coulomb, Galileo-Rankine, Matsuoka-Nakai and Lade-Duncan. *Proceedings of the Royal Society A: Mathematical, Physical and Engineering Sciences*. 472(2185).

Lau, W.H.W. 1988. The Behaviour of Clay in Simple Shear and Triaxial Tests. The City University of London, PhD Thesis.

Le, T., Airey, D. & Standing, J.R. 2022. Influence of Shearing Strain-Rate on the Mechanical Behaviour of Three Structured Clays. *Geotechnique*. (October, 24):1–51.

Le, T.M.H., Eiksund, G.R. & Strøm, P.J. 2014. Cyclic Behavior of an Overconsolidated Marine Clay at Sheringham Shoal Offshore Wind Farm. *Journal of Ocean and Wind Energy*. 1(1):59–64.

Leal, A.N. & Kaliakin, V.N. 2013. *Behavior of Cohesive Soils Subjected to Cyclic Loading : An Eextensive Review of Pertinent Literature*. Delaware,USA.

LeBlanc, C., Houlsby, G.T. & Byrne, B.W. 2010. Response of Stiff Piles in Sand to Long-Term Cyclic Lateral Loading. *Géotechnique*. 60(2):79–90.

LeBlanc, C., Byrne, B.W. & Houlsby, G.T. 2010. Response of Stiff Piles to Random Two-Way Lateral Loading. *Géotechnique*. 60(9):715–721.

Lee, C.J. & Sheu, S.F. 2007. The Stiffness Degradation and Damping Ratio Evolution of Taipei Silty Clay under Cyclic Straining. *Soil Dynamics and Earthquake Engineering*. 27(8):730–740.

Lee, K.L. & Focht, J.A. 1976. Strength of Clay Subjected to Cyclic Loading. *Marine Geotechnology*. 1(3):165–185.

Lehane, B. 1992. Experimental Investigations of Pile Behaviour using Instrumented Field Piles. PhD Thesis, Imperial College London.

Li, Y. 2016. Shear Behaviour of Sand in Bi-Directional Simple Shear Tests. PhD Thesis, University of Nottingham.

Li, Y. 2018. Test Granular Materials Failure Using Bi-Directional Simple Shear Apparatus: A Review. *Applied Sciences*. 8(7):1140.

Li, Y., Yang, Y., Yu, H.-S. & Roberts, G. 2017. Monotonic Direct Simple Shear Tests on Sand under Multidirectional Loading. *International Journal of Geomechanics*. 17(1).

Li, Y., Wu, Y. & Wang, Z. 2020. Stress State and Noncoaxiality of Leighton Buzzard Sand in NGI-Type Bi-Directional Simple Shear Tests. *Marine Georesources and Geotechnology*.

Liu, T. 2018. Advanced Laboratory Testing for Offshore Pile Foundations under Static and Cyclic Loading. PhD Thesis, Imperial College London.

Liu, T., Ushev, E.R. & Jardine, R.J. 2020. Anisotropic Stiffness and Shear Strength Characteristics of a Stiff Glacial Till. *Journal of Geotechnical and Geoenvironmental Engineering*. 146(12).

Lunne, T., Berre, T. & Strandvik, S. 1997. Sample Disturbance Effects in Soft Low Plasticity Norwegian Clay. In *Proceedings of Conference on Recent Developments in Soil and Pavement Mechanics*. 81–102.

Lunne, T., Berre, T., Andersen, K.H., Strandvik, S. & Sjursen, M. 2011. Effects of Sample Disturbance and Consolidation Procedures on Measured Shear Strength of Soft Marine Norwegian Clays. *Canadian Geotechnical Journal*. 43(7):726–750.

Martin, S. 2023. Medium Scale Field Testing of Monopile Foundations under Cyclic Lateral Loading. DPhil Thesis, University of Oxford.

Masing, G. 1926. Eigenspannungen und Verfestigung beim Messing. In *Proceedings of the 2nd International Congress of Applied Mechanics*. Zurich, Swisse.

Matešić, L. & Vucetic, M. 2003. Strain-Rate Effect on Soil Secant Shear Modulus at Small Cyclic Strains. *Journal of Geotechnical and Geoenvironmental Engineering*. 129(6):536–549.

Matlock, H. 1970. Correlations for Design of Laterally Loaded Piles in Soft Clay. In *Proceedings of the 2nd Annual Offshore Technology Conference*. V. 1. Houston, Tx, USA. 577–588.

Matsuda, H., Hendrawan, A.P., Ishikura, R. & Kawahara, S. 2011. Effective Stress Change and Post-Earthquake Settlement Properties of Granular Materials Subjected to Multi-Directional Cyclic Simple Shear. *Soils and Foundations*. 51(5):873–884.

Matsuda, H., Thanh Nhan, T. & Ishikura, R. 2013. Prediction of Excess Pore Water Pressure and Post-Cyclic Settlement on Soft Clay Induced by Uni-Directional and Multidirectional Cyclic Shears as a Function of Strain Path Parameters. *Soil Dynamics and Earthquake Engineering*. 49(2013):75–88.

Mayne, P.W. 1985. A Review of Undrained Strength in Direct Simple Shear. *Soils and Foundations: Japanese Society of Soil Mechanics and Foundation Engineering*. 25(3):64–72.

McClelland, B. & Focht Jr., J.A. 1958. Soil Modulus for Laterally Loaded Piles. *Transactions of the American Society of Civil Engineers*. 123(1).

McGuire, S. 2011. Comparison of Direct Simple Shear Confinement Methods on Clay and Silt Specimens. MSc, University of Rhode Island.

McKinlay, D.G., Tomlinson, M.J. & Anderson, W.F. 1974. Observations on the Undrained Strength of a Glacial Till. *Geotechnique*. 24(4):503–516.

Le Meil, G., Hendry, M. & Martin, D. 2016. Direct Simple Shear (DSS) Testing of a Very Stiff Glacialacustrine Clay. In *69th Canadian Geotechnical Conference*. Vancouver.

Meimon, Y. & Hicher, P.Y. 1980. Mechanical Behaviour of Clays under Cyclic Loading. In *International Symposium on Soils under Cyclic and Transient Loading*. 77–87.

Mitchell, J.K. & Soga, K. 2005. *Fundamentals of Soil Behaviour*. Wiley.

Mun, W., Teixeira, T., Balci, M.C., Svoboda, J. & McCartney, J.S. 2016. Rate Effects on the Undrained Shear Strength of Compacted Clay. *Soils and Foundations*. 56(4):719–731.

Nhan, T.T., Matsuda, H. & Sato, H. 2017. A Model for Multi-Directional Cyclic Shear-Induced Pore Water Pressure and Settlement on Clays. *Bulletin of Earthquake Engineering*. 15:2761–2784.

Ni, J., Indraratna, B., Geng, X.-Y., Carter, J.P. & Chen, Y.-L. 2015. Model of Soft Soils under Cyclic Loading. *International Journal of Geomechanics*. 15(4).

Norén-Cosgriff, K., Jostad, H.P. & Madshus, C. 2015. Idealized Load Composition for Determination of Cyclic Undrained Degradation of Soils. *Frontiers in Offshore Geotechnics III - 3rd International Symposium on Frontiers in Offshore Geotechnics*. 1097–1103.

Ochiai, H. 1975. The Behaviour of Sand in Direct Shear Tests. *Soils and Foundations*. 15(4):93–100.

Oda, M. & Konishi, J. 1974. Rotation of Principal Stresses in Granular Material During Simple Shear. *Soils and Foundations*. 14(4):39–53.

Orsted. 2019. *Making Green Energy Affordable-How the Offshore Wind Energy Industry Matured-and What we can Learn from It*.

Paramasivam, B. & Banerjee, S. 2017. Factors Affecting Post-cyclic Undrained Shear Strength of Marine Clay. *Geotechnical and Geological Engineering*. 35(4):1783–1791.

Peacock, W.H. & Seed, H.B. 1968. Sand Liquefaction under Cyclic Loading Simple Shear Conditions. In *Proceedings of the American Society of Civil Engineers*. 689–708.

Poirier, S.E., DeGroot, D.J. & Sheahan, T.C. 2005. Measurement of Suction in a Marine Clay as an Indicator of Sample Disturbance. *Site Characterization and Modeling*. (130–142):2221–2230.

Potts, D.M. & Ganendra, D. 1994. An Evaluation of Substepping and Implicit Stress Point Algorithms. *Computer Methods in Applied Mechanics and Engineering*. 119:341–354.

Powell, J. & Butcher, A. 2003. Characterisation of a Glacial Clay Till at Cowden, Humberside. *Characterisation and Engineering Properties of Natural Soils*. 2:983.

Puzrin, A.M. & Houlsby, G.T. 2001. Fundamentals of Kinematic Hardening Hyperplasticity. *International Journal of Solids and Structures*. 38(21):3771–3794.

Pyke, R.M. 1979. Nonlinear Soil Models for Irregular Cyclic Loadings. *Journal of the Geotechnical Engineering Division*. 105(6):715–726.

Pyke, R.M., Chan, C.K. & Seed, H.B. 1975. Settlement of Sands under Multidirectional Shaking. *Journal of the Geotechnical Engineering Division*. 101(4):379–398.

Reese, L.C., Cox, W.R. & Koop, F.D. 1974. Analysis of Laterally Loaded Piles in Sand. In *Proceedings of the Offshore Technology Conference (OTC)*. Houston, Texas. 473–483.

RenewableUK. 2022. *Wind Energy Statistics - RenewableUK*. Available: https://www.renewableuk.com/page/UKWEDhome [2019, September 12].

Reynolds, O. 1885. On the Dilatancy of Media Composed of Rigid Particles in Contact, with Experimental Illustrations. *Philosophical Magazine Series 5*. 20(127):469–481.

Richards, I.A. 2019. Monopile Foundation under Complex Cyclic Lateral Loading in Sand. DPhil Thesis, University of Oxford.

Richards, I.A., Byrne, B.W. & Houlsby, G.T. 2020. Monopile Rotation under Complex Cyclic Lateral Loading in Sand. *Géotechnique*. 70(10):916–930.

Robertson, P.K. 2009. Interpretation of Cone Penetration Tests-a Unified Approach. *Canadian Geotechnical Journal*. 46(11):1337–1355.

Robinson, S. 2019. Rate Effect Behaviour of Different Clays from High Speed Triaxial Testing. PhD Thesis, University of Dundee.

Roscoe, K.H. 1953. An Apparatus for the Application of Simple Shear to Soil Samples. *Proceedings of the third international conference on soil mechanics and foundation engineering*. 1:186–191.

Roscoe, K.H. & Burland, J.B. 1968. *On the Generalised Stress-Strain Behaviour of "Wet" Clay*. J. Heyman & F.A. Leckie, Eds. Cambridge University Press.

Roscoe, K.H., Schofield, A.N. & Thurairajah, A. 1963. Yielding of Clays in States Wetter than Critical. *Géotechnique*. 13(3):211–240.

Rowe, P.W. 1962. The Stress-Dilatancy Relation for Static Equilibrium of an Assembly of Particles in Contact. In *Proceedings of the Royal Society A*. 500–527.

Rudolph, C., Bienen, B. & Grabe, J. 2014. Effect of Variation of the Loading Direction on the Displacement Accumulation of Large-Diameter Piles under Cyclic Lateral Loading in Sand. *Canadian Geotechnical Journal*. 51(10):1196–1206.

Rutherford, C.J. 2012. Development of a Multi-Directional Direct Simple Shear Testing Device for Characterization of the Cyclic Shear Response of Marine Clays. Texas A&M University.

Schnaid, F. 1990. A Study of the Cone-Pressuremeter Test in Sand. DPhil Thesis, University of Oxford.

Schofield, A. & Wroth, P. 1968. *Critical State Soil Mechanics*. McGraw-Hill.

Seed, H.B. & Lundgren, R. 1954. Investigation of the Effect of Transient Loading on the Strength and Deformation Characteristics of Saturated Sands. In *Proceedings of American Society for Testing and Materials 54*. 1288–1306.

Seidalinov, G. 2018. Constitutive and Numerical Modeling of Clay Subjected to Cyclic Loading. PhD Thesis, University of British Columbia.

Sha'al, B.Z. 1972. The Behaviour of Cohesionless Soils in Simple Shear under Cyclic Loading. PhD Thesis, The University of London.

Sheahan, T.C., Ladd, C.C. & Germaine, J.T. 1996. Rate-Dependent Undrained Shear Behavior of Saturated Clay. *Journal of Geotechnical Engineering*. 122(2):99–108.

Skau, K.S., Dahl, B.M., Jostad, H.P., Suzuki, Y., Sordi, J. De & Havmøller, O. 2022. Response of Lightly Over-Consolidated Clay Under Irregular Cyclic Loading and Comparison with Predictions from the Strain Accumulation Procedure. *Géotechnique*. 73(5):1–44.

Sloan, S.W. 1987. Substepping Shcemes for the Numerical Integration of Elastoplastic Stress-Strain Relations. *International Journal for Numerical Methods in Engineering*. 24(5):893–911.

Sloan, S.W., Abbo, A.J. & Sheng, D. 2001. Refined Explicit Integration of Elastoplastic Models with Automatic Error Control. *Engineering Computations (Swansea, Wales)*. 18(1–2):121–154.

Stroud, M.A. 1971. The Behaviour of Sand at Low Stress Levels in the Simple Shear Apparatus. PhD Thesis, University of Cambridge.

Sun, M. & Biscontin, G. 2019. The Development of Shear Strain in Undrained Multi-Directional Simple Shear Tests. In *7th International Conference on Earthquake Geotechnical Engineering*. 5136–5142.

Taborda, D.M.G., Potts, D.M. & Zdravković, L. 2016. On the Assessment of Energy Dissipated Through Hysteresis in Finite Element Analysis. *Computers and Geotechnics*. 71:180–194.

Tatsuoka, F., Di Benedetto, H., Enomoto, T., Kawabe, S. & Kongkitkul, W. 2008. Various Viscosity Types of Geomaterials in Shear and their Mathematical Expression. *Soils and Foundations*. 48(1):41–60.

Taylor, D.W. 1948. *Fundamentals of Soil Mechanics*. John Wiley & Sons.

Teachavorasinskun, S., Thongchim, P. & Lukkunaprasit, P. 2001. Shear Modulus and Damping Ratio of Clay during Undrained Cyclic Loading. *Geotechnique*. 51(5):467–470.

Terzaghi, K. 1944. Ends and Means in Soil Mechanics. *Engineering Journal*. 27(12):608–615.

Terzaghi, K. & Peck, R.B. 1948. *Soil Mechanics in Engineering Practice*. New York: John Wiley & Sons.

Terzaghi, K., Peck, R.B. & Mesri, G. 1996. *Soil Mechanics in Engineering Practice*. New York: John Wiley & Sons.

Thian, S.Y. & Lee, C.Y. 2017. Cyclic Stress-Controlled Tests on Offshore Clay. *Journal of Rock Mechanics and Geotechnical Engineering*. 9(2):376–381.

Thian, S.Y. & Lee, C.Y. 2018. Simplified Constant Volume Simple Shear Tests on Clay. *KSCE Journal of Civil Engineering*. 22(8):2834–2842.

United Nations. 2015. *Framework Convention on Climate Change - Paris Agreement*.

Ushev, E. 2017. Laboratory Investigation of the Mechanical Properties of Cowden Till under Static and Cyclic Conditions. PhD Thesis, Imperial College London.

Ushev, E. & Jardine, R. 2020. The Behaviour of Bolders Bank Glacial Till Under Undrained Cyclic Loading. *Géotechnique*. 72(1):1–46.

Wai, D., Manmatharajan, M. V. & Ghafghazi, M. 2021. Effect of Imperfect Direct Simple Shear Test Boundary Conditions on Monotonic and Cylic Measurements. *Journal of Geotechnical and Geoenvironmental Engineering*. 148(1).

Wang, Y., Lei, J. & Wang, Y. 2019. A Post-Cyclic Strength Degradation Model for Saturated Soft Clay. *Ocean Engineering*. 186.

Watanabe, K. & Kusakabe, O. 2013. Reappraisal of loading rate effects on sand behavior in view of seismic design for pile foundation. *Soils and Foundations*. 53(2):215–231.

White, J.R.F. 2020. A Laboratory Investigation into the Behaviour of Sand at Low Confining Stresses. DPhil Thesis, University of Oxford.

White, J.R.F. 2021. Personal Communication (Email). 12 October.

Whyte, S. 2020. Development, Implementation, Calibration and Use of Practical Constitutive Models in Finite Element Analysis of Offshore Foundations. DEng Thesis, University of Oxford.

Wind Europe. 2019. *Wind energy in Europe in 2018 | WindEurope*. Available: https://windeurope.org/about-wind/statistics/european/wind-energy-in-europe-in-2018/ [2019, September 13].

Wind Europe. 2021a. *Setting the Course Towards Climate Neutrality*.

Wind Europe. 2021b. *Wind Energy in Europe: 2020 Statistics and the Outlook for 2021-2025*.

Wood, D.M. 1990. *Soil Behaviour and Critical State Soil Mechanics*. Cambridge: Cambridge University Press.

Wood, D.M., Drescher, A. & Badhu, M. 1979. On the Determination of Stress State in the Simple Shear Apparatus. *Geotechnical Testing Journal*. 2(4):211–222.

World Weather Online. 2021. *Cowden Monthly Climate Averages*. Available: https://www.worldweatheronline.com/cowden-weather-averages/kent/gb.aspx.

Wroth, C.P. & Bassett, R.H. 1965. A Stress–Strain Relationship for the Shearing Behaviour of a Sand. *Géotechnique*. 15(1):32–56.

Wu, K. 2022. Rate Effects of Monopile Foundations. DPhil Thesis, University of Oxford.

Yasuhara, K., Hirao, K. & FL Hyde, A. 1992. Effects of Cyclic Loading on Undrained Strength and Compressibility of Clay. *Soils and Foundations*. 32(1):100–116.

Zdravković, L., Taborda, D.M.G., Potts, D.M., Jardine, R.J., Sideri, M., Schroeder, F.C., Zdravkovi, L., Taborda, D.M.G., et al. 2015. Numerical Modelling of Large Diameter Piles Under Lateral Loading for Offshore Wind Applications. *Frontiers in Offshore Geotechnics III*. (August):759–764.

Zdravković, L., Jardine, R.J., Taborda, D.M.G., Abadias, D., Burd, H.J., Byrne, B.W., Gavin, K., Houlsby, G.T., et al. 2020. Ground Characterisation for PISA Pile Testing and Analysis. *Géotechnique*. 70(11):945–960.

Zhang, Y. & Andersen, K.H. 2017. Scaling of Lateral Pile p-y Response in Clay From Laboratory Stress-Strain Curves. *Marine Structures*. 53:124–135.

Zhang, Y., Andersen, K.H., Jeanjean, P., Mirdamadi, A., Gundersen, A.S. & Jostad, H.P. 2017. A Framework for Cyclic p-y Curves in Clay and Application to Pile Design in GoM. *OSIG: Advanced Soil Characterisation*. 431–440.

Ziegler, H. 1977. *An Introduction to Thermomechanics*. 1st ed. North-Holland, Amsterdam.

Zwanenburg, C., de Lange, D.A. & Teunissen, J.A.M. 2019. Lateral Stress Measurement in DSS Testing. In *Proceedings of the 17th European Conference on Soil Mechanics and Geotechnical Engineering*.

Appendix A

Model backbone recalibration by Crispin et al. (2022)

Softening recalibration

The recalibration method follows the solution produced internally at Oxford by Crispin et al. (2022). Assuming only softening, if plastic strain is occurring then $\dot{\varepsilon} = \dot{\alpha}$. In addition, no changes in load direction occurs on the backbone, which gives $\beta_n = k_n\dot{\varepsilon}$, allowing κ_L to be expressed as:

$$\kappa_L = \left[1 + \frac{k_n(\varepsilon - \varepsilon_n)}{\beta_{ref,n}}\left(\kappa_{ref}^{-\frac{1}{m_k}} - 1\right)\right]^{-m_k} \tag{A-1}$$

The differentiation of κ_L with respect to ε is then given by:

$$\frac{d\kappa_L(\varepsilon)}{d\varepsilon} = \frac{-m_k F_\kappa k_i}{\beta_{ref,n}}\left(\kappa_{ref}{}^{-\frac{1}{m_k}} - 1\right)\left(1 + \frac{k_n(\varepsilon - \varepsilon_i)}{\beta_{ref,n}}\left(\kappa_{ref}{}^{-\frac{1}{m_k}} - 1\right)\right)^{-m_k-1} \tag{A-2}$$

To fit the backbone curve with known coordinates (σ_n, ε_n) or (τ_n, ε_n), the stress at each spring-slider element $\sigma_{ss,n}$ for a parallel model before softening must be calculated. This is obtained using the relationship:

$$\sigma = \sigma_{ss} - \sum_{n=0}^{N_s}[1 - \kappa_n(\varepsilon)]k_{n,0}\, y_n \tag{A-3}$$

where y_n = 1 when surface n is yielding and 0 otherwise. Assuming plastic yielding up to surface j:

$$\sigma_{ss} = \sigma + \sum_{n=0}^{j}[1 - \kappa_n(\varepsilon)]k_{n,0} \tag{A-4}$$

where j = [1, N_s]. The softening parameter κ_L can be differentiated with respect to ε_{ss} and the result expressed in incremental form:

$$\dot{\sigma}_{ss} = \dot{\sigma} - \dot{\varepsilon}\sum_{n=0}^{j}\frac{d\kappa_n(\varepsilon)}{d\varepsilon}k_{n,0} = E_j\dot{\varepsilon} - \dot{\varepsilon}\sum_{n=0}^{j-1}\frac{d\kappa_n(\varepsilon)}{d\varepsilon}k_{n,0} - \dot{\varepsilon}\frac{d\kappa_n(\varepsilon)}{d\varepsilon}k_{j,0} \tag{A-5}$$

The point of yielding, based on k_j and H_j, can only be calculated once a datapoint beyond $\varepsilon_{ss,j}$ (e.g. $\varepsilon_{ss,j+1}$) is already calculated. As a result, k_j, must be removed from the sum and determined separately using the following steps:

$$\kappa_j(\varepsilon_j)k_{j,0} = H_j\varepsilon_j = \left[E_{ss,j-1} - E_{ss,j}\right]\varepsilon_j = \left[E_{ss,j-1} - \frac{\dot{\sigma}_{ss}}{\dot{\varepsilon}}\right]\varepsilon_j \tag{A-6}$$

where $E_{ss,n} = \frac{\sigma_{ss,n+1} - \sigma_{ss,n}}{\varepsilon_{n+1} - \varepsilon_n}$. Combining Equation (A-5) and (A-6) gives:

$$\dot{\sigma}_{ss} = E_j\dot{\varepsilon} - \dot{\varepsilon}\sum_{n=0}^{j-1}\frac{d\kappa_n(\varepsilon)}{d\varepsilon}k_{n,0} - \frac{d\kappa_j(\varepsilon)}{d\varepsilon}\frac{1}{\kappa_j(\varepsilon_j)}\left[E_{ss,j-1}\dot{\varepsilon} - \dot{\sigma}_{ss}\right]\varepsilon_j \tag{A-7}$$

$$\left[1 - \varepsilon_j\frac{d\kappa_j(\varepsilon)}{d\varepsilon}\frac{1}{\kappa_j(\varepsilon_j)}\right]\dot{\sigma}_{ss} = \dot{\varepsilon}\left[E_j - \sum_{n=0}^{j-1}\frac{d\kappa_n(\varepsilon)}{d\varepsilon}k_{n,0} - E_{ss,j-1}\varepsilon_j\frac{d\kappa_j(\varepsilon)}{d\varepsilon}\frac{1}{\kappa_j(\varepsilon_j)}\right]$$

This can be rearranged as an initial value problem:

$$\frac{d\sigma_{ss}}{d\varepsilon} = \frac{E_j - \sum_{i=0}^{j-1}\frac{d\kappa_i(\varepsilon)}{d\varepsilon}k_{i,0} - E_{ss,j-1}\varepsilon_j\frac{d\kappa_j(\varepsilon)}{d\varepsilon}\frac{1}{\kappa_j(\varepsilon_j)}}{1 - \varepsilon_j\frac{d\kappa_j(\varepsilon)}{d\varepsilon}\frac{1}{\kappa_j(\varepsilon_j)}} \tag{A-8}$$

Ratcheting recalibration

A recalibration approach based on work by Crispin et al. (2022) is followed. The approach is preferred as it reduces the computational time and limits the amount of user subjectivity caused by the selection and optimisation of fitted functions. Building on from Equation (7-18), $|\dot{\alpha}_n| = \dot{\alpha}_n$ for the backbone curve, which simplifies the equation to:

$$\dot{\alpha}_r = \dot{\alpha}R\sum_{n=1}^{N_s}\frac{k_n}{\sigma_u}y_n \tag{A-9}$$

where $\dot{\alpha}$ is the incremental plastic strain from the spring sliders which have yielded and y_n = 1 when surface n is yielding and 0 when not. Assuming plastic yielding up to surface j:

$$\dot{\varepsilon} = \dot{\alpha} + \dot{\alpha}_r = \dot{\alpha}\left[1 + R\sum_{n=1}^{j}\frac{k_n}{\sigma_u}\right] \tag{A-10}$$

In order to fit a backbone curve with known points $(\sigma_n, \varepsilon_n)$, the strain of the parallel spring-slider element at each point, $\varepsilon_{ss,n}$, must be calculated. Between $(0,0)$ and $(\sigma_1, \varepsilon_1)$, the behaviour is elastic and unchanged from before. This is given by:

$$\dot{\varepsilon}_{ss} = \frac{\sigma_1}{\varepsilon_1}\dot{\varepsilon} = E_0\dot{\varepsilon} \tag{A-11}$$

However, once first yielding occurs at $(\sigma_1, \varepsilon_1)$, the incremental strain $\dot{\varepsilon}_{ss}$ is equal to the incremental plastic strain $\dot{\alpha}$. Therefore, it can be related to $\dot{\varepsilon}$ using Equation (A-10):

$$\dot{\varepsilon} = \dot{\varepsilon}_{ss}\left[1 + R\sum_{n=1}^{j}\frac{k_n}{\sigma_u}\right] \tag{A-12}$$

As k_j and H_j can only be determined once a datapoint beyond $\varepsilon_{ss,j}$ (ideally $\varepsilon_{ss,j+1}$) is already calculated, k_j must be removed from the sum and calculated separately using the following steps:

$$k_j = H_j\varepsilon_{ss,j} = \left[E_{ss,j-1} - \frac{\dot{\sigma}}{\dot{\varepsilon}_{ss}}\right]\varepsilon_{ss,j} = \left[E_{ss,j-1} - E_j\frac{\dot{\varepsilon}}{\dot{\varepsilon}_{ss}}\right]\varepsilon_{ss,j} \tag{A-13}$$

where

$$E_{ss,n} = \frac{\sigma_{n+1}-\sigma_n}{\varepsilon_{ss,n+1}-\varepsilon_{ss,n}},\ E_n = \frac{\sigma_{n+1}-\sigma_n}{\varepsilon_{n+1}-\varepsilon_n} \tag{A-14}$$

Substituting this into Equation (A-12) to give:

$$\dot{\varepsilon} = \dot{\varepsilon}_{ss} + R\dot{\varepsilon}_{ss}\sum_{n=1}^{j-1}\frac{k_n}{\sigma_u} + R\frac{E_{ss,j-1}\varepsilon_{ss,j}}{\sigma_u}\dot{\varepsilon}_{ss} - R\frac{E_j\varepsilon_{ss,j}}{\sigma_u}\dot{\varepsilon} \tag{A-15}$$

Grouping similar terms and arranging it as an initial value problem gives:

$$\frac{d\varepsilon_{ss}}{d\varepsilon} = \frac{1 + R\frac{E_j\varepsilon_{ss,j}}{\sigma_u}}{1 + R\sum_{i=1}^{j-1}\frac{k_i}{\sigma_u} + R\frac{E_{ss,j-1}\varepsilon_{ss,j}}{\sigma_u}} \tag{A-16}$$

and solved in closed form with a basic forward Euler method.

Combined Ratcheting and Softening

Following the ratcheting only solution to Equation (A-12), the incremental strain $\dot{\varepsilon}_{ss}$ can be related to $\dot{\varepsilon}$:

$$\dot{\varepsilon} = \dot{\varepsilon}_{ss}\left[1 + R\sum_{i=1}^{j}\frac{k_{i,0}}{\sigma_u}\right] \tag{A-17}$$

As before, $k_{j,0}$ and H_j can only be determined once a datapoint beyond $\varepsilon_{ss,j}$ (ideally $\varepsilon_{ss,j+1}$) is already calculated, $k_{j,0}$ must be removed from the sum and calculated separately:

$$\kappa_j(\varepsilon_j)k_{j,0} = H_j\varepsilon_{ss,j} = \left[E_{ss,j-1} - \frac{\dot{\sigma}_{ss}}{\dot{\varepsilon}_{ss}}\right]\varepsilon_{ss,j} \tag{A-18}$$

Following the softening only solution to Equation (A-4) and noting that with ratcheting the softening depends on $\dot{\varepsilon}_{ss}$ rather than $\dot{\varepsilon}$, the

$$\sigma_{ss} = \sigma + \sum_{n=0}^{j}[1 - \kappa_n(\varepsilon_{ss})]k_{n,0} \tag{A-19}$$

The κ_n terms can be differentiated with respect to $\dot{\varepsilon}_{ss}$ (note these are the same as Equation (A-2) with ε_{ss} substituted in for ε) and the result expressed in incremental form:

$$\dot{\sigma}_{ss} = \dot{\sigma} - \dot{\varepsilon}_{ss}\sum_{n=0}^{j}\frac{d\kappa_n(\varepsilon_{ss})}{d\varepsilon_{ss}}k_{n,0} = \dot{\varepsilon}_{ss}\left[E_j\frac{\dot{\varepsilon}}{\dot{\varepsilon}_{ss}} - \sum_{n=0}^{j-1}\frac{d\kappa_n(\varepsilon_{ss})}{d\varepsilon_{ss}}k_{n,0} - \frac{d\kappa_j(\varepsilon_{ss})}{d\varepsilon_{ss}}k_{j,0}\right] \tag{A-20}$$

Inputting this into Equation (A-18) gives:

$$k_{j,0} = \left[E_{ss,j-1} - E_j\frac{\dot{\varepsilon}}{\dot{\varepsilon}_{ss}} - \sum_{n=0}^{j-1}\frac{d\kappa_n(\varepsilon_{ss})}{d\varepsilon_{ss}}k_{i,0} - \frac{d\kappa_j(\varepsilon_{ss})}{d\varepsilon_{ss}}k_{j,0}\right]\frac{\varepsilon_{ss,j}}{\kappa_j(\varepsilon_j)} \tag{A-21}$$

$$k_{j,0}\left[1 + \frac{\varepsilon_{ss,j}}{\kappa_j(\varepsilon_j)}\frac{d\kappa_j(\varepsilon_{ss})}{d\varepsilon_{ss}}\right] = \left[E_{ss,j-1} - E_j\frac{\dot{\varepsilon}}{\dot{\varepsilon}_{ss}} - \sum_{n=0}^{j-1}\frac{d\kappa_n(\varepsilon_{ss})}{d\varepsilon_{ss}}k_{n,0}\right]\frac{\varepsilon_{ss,j}}{\kappa_j(\varepsilon_j)} \tag{A-22}$$

$$k_{j,0} = \frac{E_{ss,j-1} - E_j \frac{\dot{\varepsilon}}{\dot{\varepsilon}_{ss}} - \sum_{n=0}^{j-1} \frac{d\kappa_n(\varepsilon_{ss})}{d\varepsilon_{ss}} k_{n,0}}{\frac{\kappa_j(\varepsilon_j)}{\varepsilon_{ss,j}} + \frac{d\kappa_j(\varepsilon_{ss})}{d\varepsilon_{ss}}} \tag{A-23}$$

Which can be in-turn substituted into Equation (A-17) as follows:

$$\dot{\varepsilon} = \dot{\varepsilon}_{ss}\left[1 + R\left[\sum_{n=1}^{j-1} \frac{k_{n,0}}{\sigma_u} + \frac{\frac{E_{ss,j-1}}{\sigma_u} - \frac{E_j}{\sigma_u}\frac{\dot{\varepsilon}}{\dot{\varepsilon}_{ss}} - \sum_{n=0}^{j-1} \frac{d\kappa_n(\varepsilon_{ss})}{d\varepsilon_{ss}}\frac{k_{n,0}}{\sigma_u}}{\frac{\kappa_j(\varepsilon_j)}{\varepsilon_{ss,j}} + \frac{d\kappa_j(\varepsilon_{ss})}{d\varepsilon_{ss}}}\right]\right] \tag{A-24}$$

Grouping similar terms:

$$\dot{\varepsilon}\left[1 + \frac{R\frac{E_j}{\sigma_u}}{\frac{\kappa_j(\varepsilon_j)}{\varepsilon_{ss,j}} + \frac{d\kappa_j(\varepsilon_{ss})}{d\varepsilon_{ss}}}\right] = \dot{\varepsilon}_{ss}\left[1 + R\sum_{n=1}^{j-1} \frac{k_{n,0}}{\sigma_u}\left[1 - \frac{\frac{d\kappa_i(\varepsilon_{ss})}{d\varepsilon_{ss}}}{\frac{\kappa_j(\varepsilon_j)}{\varepsilon_{ss,j}} + \frac{d\kappa_j(\varepsilon_{ss})}{d\varepsilon_{ss}}}\right] + \frac{R\frac{E_{ss,j-1}}{\sigma_u}}{\frac{\kappa_j(\varepsilon_j)}{\varepsilon_{ss,j}} + \frac{d\kappa_j(\varepsilon_{ss})}{d\varepsilon_{ss}}}\right]\dot{\varepsilon} = \dot{\varepsilon}_{ss}\left[1 + R\sum_{n=1}^{j} \frac{k_{n,0}}{\sigma_u}\right] \tag{A-25}$$

This can then be arranged as an initial value problem as before:

$$\frac{d\varepsilon_{ss}}{d\varepsilon} = \frac{1 + \frac{R\frac{E_j}{\sigma_u}}{\frac{\kappa_j(\varepsilon_j)}{\varepsilon_{ss,j}} + \frac{d\kappa_j(\varepsilon_{ss})}{d\varepsilon_{ss}}}}{1 + R\sum_{n=1}^{j-1} \frac{k_{n,0}}{\sigma_u}\left[1 - \frac{\frac{d\kappa_n(\varepsilon_{ss})}{d\varepsilon_{ss}}}{\frac{\kappa_j(\varepsilon_j)}{\varepsilon_{ss,j}} + \frac{d\kappa_j(\varepsilon_{ss})}{d\varepsilon_{ss}}}\right] + \frac{R\frac{E_{ss,j-1}}{\sigma_u}}{\frac{\kappa_j(\varepsilon_j)}{\varepsilon_{ss,j}} + \frac{d\kappa_j(\varepsilon_{ss})}{d\varepsilon_{ss}}}} \tag{A-26}$$

This can be solved using a Runge-Kutta method. Then, once $\varepsilon_{ss,j+1}$ (and therefore $\dot{\varepsilon}_{ss}$ between each point) has been obtained, Equation (A-18) and (A-20) can be combined to relate $\dot{\sigma}_{ss}$ to $\dot{\varepsilon}_{ss}$:

$$\dot{\sigma}_{ss} = \dot{\varepsilon}_{ss}\left[E_{\varepsilon ss,j} - \sum_{n=0}^{j-1} \frac{d\kappa_n(\varepsilon_{ss})}{d\varepsilon_{ss}} k_{n,0} - \frac{\varepsilon_{ss,j}}{\kappa_j(\varepsilon_j)}\frac{d\kappa_j(\varepsilon_{ss})}{d\varepsilon_{ss}}\left[E_{ss,j-1} - \frac{\dot{\sigma}_{ss}}{\dot{\varepsilon}_{ss}}\right]\right] \tag{A-27}$$

Grouping similar terms:

$$\dot{\sigma}_{ss}\left[1 - \frac{\varepsilon_{ss,j}}{\kappa_j(\varepsilon_j)}\frac{d\kappa_j(\varepsilon_{ss})}{d\varepsilon_{ss}}\right] = \dot{\varepsilon}_{ss}\left[E_{\varepsilon ss,j} - \sum_{n=0}^{j-1} \frac{d\kappa_n(\varepsilon_{ss})}{d\varepsilon_{ss}} k_{n,0} - \frac{E_{ss,j-1}\varepsilon_{ss,j}}{\kappa_j(\varepsilon_j)}\frac{d\kappa_j(\varepsilon_{ss})}{d\varepsilon_{ss}}\right] \tag{A-28}$$

This can then also be arranged as an initial value problem:

$$\frac{d\sigma_{ss}}{d\varepsilon_{ss}} = \frac{E_{\varepsilon ss,j} - \sum_{n=0}^{j-1} \frac{d\kappa_n(\varepsilon_{ss})}{d\varepsilon_{ss}} k_{n,0} - \frac{E_{ss,j-1}\varepsilon_{ss,j}}{\kappa_j(\varepsilon_j)}\frac{d\kappa_j(\varepsilon_{ss})}{d\varepsilon_{ss}}}{1 - \frac{\varepsilon_{ss,j}}{\kappa_j(\varepsilon_j)}\frac{d\kappa_j(\varepsilon_{ss})}{d\varepsilon_{ss}}} \tag{A-29}$$